A study of subgrid scale modelling and inflow boundary conditions for large eddy simulation of wall-bounded flows

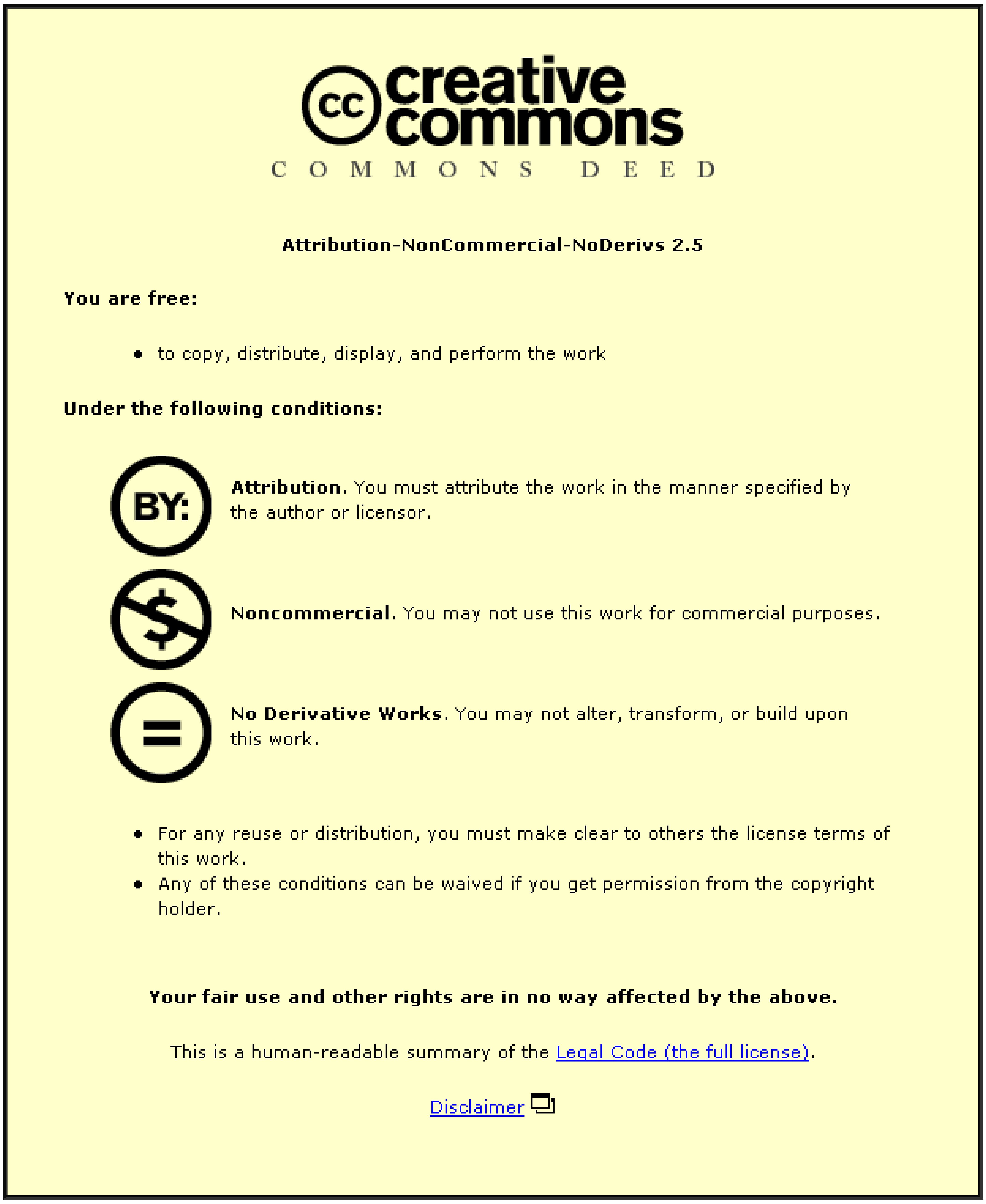

A Study of Subgrid Scale Modelling and Inflow Boundary Conditions for Large Eddy Simulation of Wall-bounded Flows

by

Ioannis Veloudis

A Doctoral Thesis

Submitted in partial fulfilment of the requirements

for the award of

Doctor of Philosophy of Loughborough University

25/09/2006

Abstract

The complicated turbulence structures in wall-bounded flows require accurate subgrid scale, SGS, modelling and realistic inlet boundary conditions for Large Eddy Simulation, LES. The present study focused on the investigation and development of transport equation SGS models and on the development of inlet conditions generation algorithms specialised for LES of wall-bounded flows.

The investigation of SGS models has been carried out in two stages. In the first stage, models based on resolved scales and models based on subgrid scales were tested on a series of channel flow cases. Among the second group of models, there was a new SGS model whose development was based on the concept of dissipation calculated from the energy spectrum. The results indicated the superiority of the models based on subgrid scales, with the new model providing the most accurate flow field in general.

The second stage involved the use of the Smagorinsky model and the Yoshizawa and Horiuti k_{sgs}-equation model on a wing body junction case. The results that indicated common general flow characteristics but also a number of flow features unique to each solution. In accordance to the results obtained by the channel flows, the wing body junction case showed the superiority of the k_{sgs}-equation model.

Finally, the second part of the present study involved the development of an inlet conditions generation algorithm capable of producing inlet data appropriate to be used for LES of wall-bounded flows. A Digital Filter based algorithm was used as a baseline for the development of a multi-filtering technique, which in combination with frequency domain convolution and data interpolation, resulted in an efficient algorithm that can provide quasi-turbulent inlet data, characterised by pre-specified turbulent scale variations.

Keywords: turbulence, wall-bounded flow, CFD, LES, inlet-boundary conditions, digital filter

Acknowledgments

The author wishes to express his appreciation to the individuals whose support was essential for the completion of the research undertaken.

I would like to thank Dr. Z.Yang and Prof. J.J. McGuirk for the honour and privilege of working with them on this project. Their help, guidance and advice was of crucial importance for the completion of the present work. I would also like to express my gratitude to Dr. G. Page who let me work with his code and offered me his help whenever I needed it.

Special thanks to the staff of the department of Aeronautical and Automotive Engineering of Loughborough University, who always provided their assistance in order to make sure that I could concentrate on my work.

I would also like to thank my parents and my brother who supported me throughout these years and helped me pursue the best of myself. Their love, encouragement and understanding was always a crucial factor to help me through this crucial stage of my life.

Furthermore, I would like to thank Miles, Indy and Ibrahim who I had the pleasure and honour to work with. Our discussions on subjects related to my project were always enlightening and helpful. Their friendship and encouragement helped me overcome the difficult stages of the present work. Special thanks also to Giorgos, Elena, Petrakis, Tasos and Ilias who were always there for me, in the good and the bad times of the past years in Loughborough.

Finally, I would like to thank my partner Christina Apostolou who showed me great love and support throughout my project. Her patience, understanding and encouragement helped me concentrate and complete the present work under the best possible environment.

Contents

List of Figures

List of Tables

List of Abbreviations

BC Boundary Conditions

CDS Central Differencing Scheme

CFD Computational Fluid Dynamics

CFL Courant Friedrich Levy

CV Control Volume

DFG Digital Filter Generator

DI Direct Interaction

DNS Direct Numerical Simulation

EDQNM Eddy-Damped Quasi Normal Markovian

ERCOFTAC European Research Community On Flow, Turbulence and Combustion

ESD Energy Spectrum Dissipation

FFT Fast Fourier Transform

FT Flow Through

FTT Flow Through Time

LDA Laser Doppler Anemometry

LES Large Eddy Simulation

LHS Left Hand Side

LSE Linear Stochastic Estimation

MP Message Passing

MPI Message Passing Interface

MS Mixed Scale

MSD Multi-scale Statistical Dynamic

NS Navier-Stokes

NWM Near-Wall Modelled

NWR Near-Wall Resolved

PBC	Periodic Boundary Conditions
POD	Proper Orthogonal Decomposition
RANS	Reynolds Averaged Navier-Stokes
RG	Renormalisation Group
RHS	Right Hand Side
RK	Runge Kutta
SGS	Subgrid Scale
SST	Shear Stress Transport
TVD	Total Variation Diminishing
UPS	Upwind Scheme
WW	Werner Wengle

Notation

Roman

$2D$ two-dimensional

$3D$ three-dimensional

A wall function constant

A area

A^+ van Driest near-wall damping function constant

A_{ij} velocity gradient tensor

B wall function constant

C subgrid scale model constant

C positive constant used in Pope's energy spectrum

C_L positive constant used in Pope's energy spectrum

C_{MTS} constant used by Inagi's SGS model

C_P pressure coefficient

C_f skin-friction coefficient

$C_{f\,Dean}$ skin-friction coefficient based on Dean's formula

C_sSmagorinsky model constant

C_{so} modified Smagorinsky model constant

C_μ k_{sgs}-equation model constant

C_η positive constant used in Pope's energy spectrum

C_1 dissipation term constant

C_2 diffusion term constant

D discriminant of velocity gradient tensor

E log-law constant

$E()$ energy spectrum function

F_{wI} Inagi's near-wall damping function

F_{wY} Yoshizawa's near-wall damping function

$G()$ convolution filter kernel

H half channel height

H boundary layer shape factor

K turbulent kinetic energy of smallest resolved scales

K_o spectrum constant

L, l length

L turbulence integral length scale

P 1st tensor invariant

Pr turbulent kinetic energy production

Pr_K K production

$Pr_{k_{sgs}} k_{sgs}$ production

$\bar{P}$ spatially filtered pressure

$\overline{P}$ modified spatially filtered pressure

Q 2nd tensor invariant

R 3rd tensor invariant

R correlation

Re Reynolds number

$\overline{S}$ characteristic filtered rate of strain

$\overline{S}_{ij}$ resolved strain rate tensor

T airfoil section thickness

T turbulence integral time scale

T_G computational time

T_s representative turbulence time scale used by Inagi SGS model

U axial time-averaged velocity component

U_{RG} velocity scale of resolved scales

U_{SG} velocity scale of subgrid scales

U_{crit} critical tangential velocity

U_t velocity tangential to the wall at the 1st internal cell-centre

V normal time-averaged velocity component

V cell volume

$Var()$ variance

W lateral time-averaged velocity component

$W()$ wake function

a_{ij} Cholesky decomposition tensor

b_{ij} anisotropic part of stress tensor

dA area element

dV volume element

$det()$ determinant of a tensor

e_{C_f} skin-friction coefficient error

$f()$ function

$f_L()$ non-dimensional function used by Pope's energy spectrum

$f_w()$ universal non-dimensional function integrated to wall

$f_\eta()$ non-dimensional function used by Pope's energy spectrum

h reference height

h grid spacing

k turbulent kinetic energy

l length scale

l_{Diss} dissipation length scale used by Norris and Reynolds algebraic model

l_m mixing length

l^* length scale used in Hassid and Poreh k_{sgs}-equation subgrid scale model

n_i unit vector in i direction

r spatial separation

r_m random data series

t time

t time scale

$tr()$ trace of a tensor

u streamwise instantaneous velocity component

u velocity scale

$\overline{u'}$ streamwise resolved velocity fluctuation component

u' streamwise subgrid scale velocity component

u_t friction velocity

$\hat{u}()$ coherent fluctuation

v normal instantaneous velocity component

$\overline{v'}$ normal resolved velocity fluctuation component

v' normal subgrid scale velocity component

w lateral instantaneous velocity component

$\overline{w'}$ lateral resolved velocity fluctuation component

w' lateral subgrid scale velocity component

x axial Cartesian coordinate

y normal Cartesian coordinate

z lateral Cartesian coordinate

Greek symbols

$\overline{\Delta}$ filter width

$\tilde{\overline{\Delta}}$ test filter width

$\overline{\Delta}_{ES}$ filter width based on energy spectrum

Δ_m filter width in m direction

Δt time step

Π wall function constant

α Mixed Scale subgrid scale model constant

β positive constant used in Pope's energy spectrum

γ Gaussian filter constant

δ boundary layer thickness

δ^* boundary layer displacement thickness

δ_ν boundary layer viscous length scale

δ_{ij} Kronecker's delta

ε rate of dissipation of turbulent kinetic energy

$\tilde{\varepsilon}$ rate of energy transfer between scales at cutoff wavenumber

ε_I rate of energy input into the system

ε_T dissipation rate of the smallest resolved scales turbulence kinetic energy

η dissipation length scale

θ boundary layer momentum thickness

κ wavenumber

κ_{vK} von Karman constant

λ characteristic length scale

λ eigen value

μ absolute viscosity

μ_e effective viscosity

ν kinematic viscosity

ν_t eddy viscosity

ξ computational space coordinate

π pi

ρ density

τ total shear stress

τ_{ij} subgrid scale stress tensor

ϕ conserved scalar

$\phi()$ variable

ω modulus of vorticity

Superscripts

$\bar{}$ spatially filtered value

$\tilde{\bar{}}$ spatially double filtered value

$\rightarrow$ vector quantity

$'$ derivative

$^+$ value non-dimensionalised by the viscous length scale

$^\circ$ angle value in degrees

^{n} iteration number

^{n} normalised value

^{r} anisotropic part

Subscripts

$_B$ bulk value

$_B$ based on bulk velocity

$_C$ value at channel centre line

$_{DFG}$ value used by the Digital Filter Generation algorithm

$_{ES}$ value based on energy spectrum

$_{G}$ grid-defined value

$_{L}$ value based on characteristic turbulence length scale

$_{L}$ value on the left

$_{LES}$ value used by the LES calculation

$_{R}$ value on the right

$_{c}$ cut-off value

$_{d}$ value at dissipation level

$_{i}$ index

$_{in}$ internal value

$_{int}$ interpolated value

$_{j}$ index

$_{k}$ index

$_{max}$ maximum value

$_{min}$ minimum value

$_{o}$ representative scale

$_{out}$ external value

$_{p}$ value at first internal cell

$_{sgs}$ subgrid scale

$_{w}$ value at wall

$_{x}$ value of component in streamwise direction

$_{y}$ value of component in normal direction

$_{z}$ value of component in transverse direction

$_{\theta}$ value based on boundary layer momentum thickness

$_{\tau}$ value based on friction velocity

Operators

$\langle\rangle$ time-averaged value

Chapter 1

Introduction

1.1 Wall-bounded flows : a physical review

With the exception of free shear flows, the majority of flows related to engineering applications are bounded by solid surfaces. Wall-bounded flows, compressible or incompressible, can be encountered in both internal and external flows, ranging from oil pipelines to gas turbine engines. Therefore, it is of great importance to study the physical phenomena and the mechanisms related to these flows, in order to understand their behaviour and form expressions that will provide us with accurate predictions.

In the case of wall-bounded flows, the presence of the solid surface and the physical implications to the flow lead to a wide range of scales that characterise the turbulence present. Close to the wall, within the viscous sublayer, the characteristic length scale is set by the friction velocity u_τ and the kinematic viscosity ν, while outside this layer the length is set by the distance from the wall. As Reynolds number, Re, increases and the viscous sublayer is suppressed, the range of turbulence scales involved becomes even larger. Fluid structures, which are formed close to the wall play an important role to the development of the whole flow field. Therefore, it is important to either capture these features or model their behaviour accurately. As the computational cost increases significantly with Re, the role of modelling becomes more significant.

1.1.1 Flow through a channel

A wall-bounded flow case of particular interest is the flow through a channel. The simplicity of the geometry in combination with the presence of a number of flow phenomena have made channel flow a very popular test case for the experimental and numerical study of turbulence and the flow behaviour close to a solid surface. In the present study, channel flows were used extensively as test cases and therefore, it was considered appropriate to present a brief introduction to the main characteristics of this flow.

A typical channel geometry comprises of two parallel walls, tangential to the freestream flow direction, separated by a distance of $2H$. The mean flow is in the axial direction, x, and varies mainly in the wall normal direction, y. In an experimental setup, the walls extend far enough in the spanwise direction, z, in order to minimise side-wall effects, resulting in a statistical independence of z. The velocity components in the x, y and z direction are given by u, v and w respectively. A schematic of a typical channel geometry can be seen in Figure 1.1.

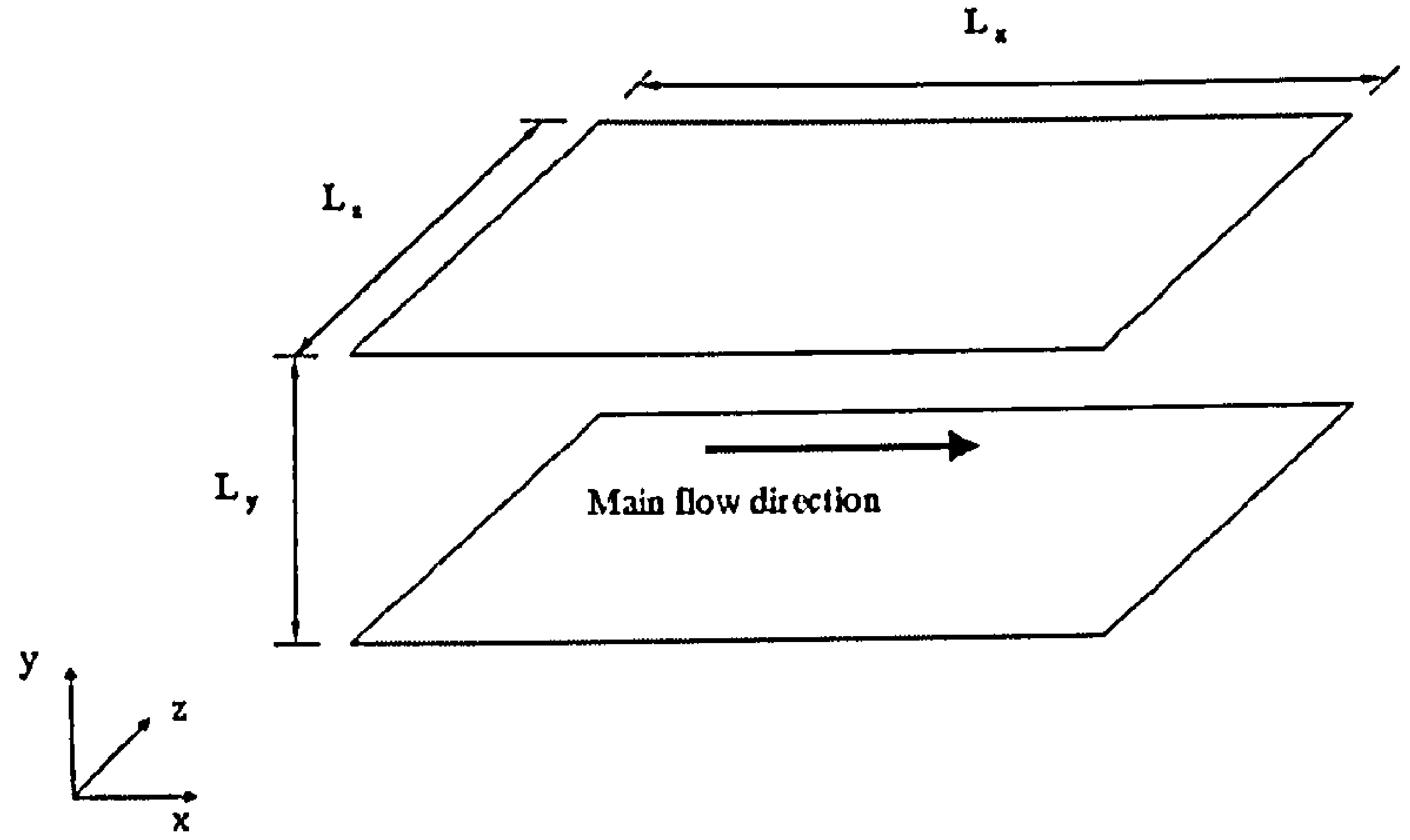

Figure 1.1: Channel geometry

The flow is laminar for $Re < 1,350$ and fully turbulent for $Re > 3,000$ [146]. When the flow has fully developed, it is statistically stationary and one-dimensional, varying only in the y direction. Since $\frac{\partial \langle u \rangle}{\partial x} = \langle w \rangle = 0$, the mass conservation equation leads to $\frac{\partial \langle v \rangle}{\partial y} = 0$. Due to the solid wall boundary condition that requires $\langle v \rangle = 0$ at the wall, $\langle v \rangle$ is also zero. Note that $\langle \rangle$ denotes time-averaged values.

The second important feature of the flow can be deducted from the lateral momentum equation, which can show that the mean pressure gradient is uniform across the flow and equal to:

$$\frac{\partial \langle P \rangle}{\partial x} = \frac{dP_w}{dx} \tag{1.1}$$

where P is the pressure and the subscript w denotes the value at the wall.

From the axial momentum equation, it can be shown that the total shear stress τ, given by the sum of viscous and Reynolds stresses as shown in Eq.1.2:

$$\tau = \rho\nu\frac{d\langle u \rangle}{dy} - \rho\left\langle u^{'}v^{'}\right\rangle \tag{1.2}$$

is related to P_w with:

$$\frac{d\tau}{dy} = \frac{dP_w}{dx} = -\frac{\tau_w}{H} \tag{1.3}$$

In Eq.1.2, ρ is the fluid density, ν is the kinematic viscosity and the superscript $'$ denotes the fluctuating velocity component.

Eq.1.3 shows that when the flow is fully developed, the driving force of the flow, which is a drop in pressure between the channel entrance and exit, is counteracted by the gradient of the total shear stress, resulting in no mean streamwise acceleration. Taking into account the antisymmetry of the shear stress with respect to the centre plane, it can be shown that the wall normal shear stress gradient equals $-\frac{\tau_w}{H}$, where τ_w is the shear stress at the wall. Hence, for a given pressure drop and channel height, the linear variation of τ is given by:

$$\tau = \tau_w\left(1 - \frac{y}{H}\right) \tag{1.4}$$

independently of the fluid properties or the state of the fluid motion [146].

Considering the solid wall boundary condition and the high shear region close to the wall, it should be expected that viscous stresses are larger closer to the wall, comparing to Reynolds stresses that should be zero at the wall, and increase in magnitude with the distance from the solid surface. This behaviour has been confirmed by DNS results for flows over a wide range of speeds. In the near-wall region, ν and τ_w are important parameters and therefore, they have been used for the definition of velocity and length scales, which are representative of those present in the region. Hence, u_τ is the friction velocity, given by:

$$u_\tau = \sqrt{\frac{\tau_w}{\rho}} \tag{1.5}$$

and δ_v is the viscous length scale, given by:

$$\delta_v = \frac{\nu}{u_\tau} \tag{1.6}$$

Finally, y^+ is the distance from the wall, non-dimensionalised by the viscous length scale, given by:

$$y^+ = \frac{y u_\tau}{\nu} \tag{1.7}$$

From the above, it is evident that a channel flow can be completely specified by a number of variables; namely ρ, ν, H and $\frac{dP_w}{dx}$ or u_τ. Using these variables, a relation can be formed for the region close to the wall, of the form:

$$\frac{d\langle u\rangle}{dy} = \frac{u_\tau}{y} f\left(\frac{y}{\delta_v}\right) = \frac{u_\tau}{y} f\left(y^+\right) \tag{1.8}$$

where $f\,()$ is a universal non-dimensional function. By defining u^+as:

$$u^+ = \frac{\langle u\rangle}{u_\tau} \tag{1.9}$$

Eq.1.8 can be written as:

$$\frac{du^+}{dy^+} = \frac{1}{y^+} f\left(y^+\right) \tag{1.10}$$

The integration of Eq.1.10 leads to the law of the wall, given by Eq.1.11.

$$u^+ = f_w\left(y^+\right) \tag{1.11}$$

where

$$f_w = \int_0^{y^+} \frac{1}{y'} f\left(y'\right) dy'$$

Hence, the estimation of f_w in the different regions of the flow near the wall can lead to the prediction of u^+. This will be explored further in the following section.

1.1.2 The boundary layer

An important feature of the flow through a channel as well as of every wall-bounded flow, is the presence of a boundary layer, which is formed over the wall. The formation of this layer is due to the viscosity of the fluid that results in zero velocity at the wall. The fluid forms a layer over the wall, through which it accelerates from zero to freestream velocity. The height of this layer is represented by δ. The form and the state of a boundary layer can significantly vary from case to case. However, some common features can be identified when the boundary layer is one-dimensional in the time-average sense, fully developed and attached to the wall. In this case, the boundary layer is called canonical [155].

A canonical boundary layer can be divided into two parts: the inner region extending from the wall to 0.2δ and the outer region. The inner region is dominated by viscous and turbulence effects, while the outer by the flow turbulence. Each of these can be subdivided into a number of layers, based on the local dynamics. In the inner region three layers can be observed.

The first layer is governed by viscous effects and forms a laminar sublayer. In this flow region $f_w(0) = 0$ and its derivative $f_w^{'}(0) = 1.0$, by considering the solid wall boundary condition and the fact that τ reduces to $\tau_w = \mu \frac{d\langle u \rangle}{dy}$ at the wall. Using a Taylor expansion for the representation of f_w and by eliminating all the higher order terms, the following equation can be obtained:

$$\left\langle u^+ \left(y^+\right)\right\rangle = y^+ \tag{1.12}$$

DNS data [78, 126] and experimental results [185] have confirmed the accuracy of this approximation for $y+ \leq 5.0$.

The third layer in the inner region of a canonical boundary layer is the Prandtl or logarithmic inertial layer. This extends in $30.0 > y^+, \frac{y}{\delta} \ll 1.0$. Within this region, fluid dynamics are governed by the flow turbulence. The dependence of f_w on y^+ vanishes and the result is that f_w obtains a constant value, given by $\frac{1}{\kappa_{vK}}$, where κ_{vK} is the von Karman constant, equal to 0.41 . Hence, Eq.1.10 becomes:

$$\frac{du^+}{dy^+} = \frac{1}{\kappa_{vK} y^+} \tag{1.13}$$

Von Karman [184] integrated Eq.1.13 and formed the *log-law*, which is given by:

$$\langle u^+ (y^+) \rangle \simeq \frac{1}{\kappa_{vK}} \ln y^+ + 5.2 \pm 0.25 \tag{1.14}$$

Eq.1.14 can be also written in the form:

$$\langle u^+ (y^+) \rangle \simeq \frac{1}{\kappa_{vK}} \ln E y^+ \tag{1.15}$$

where $E = 9.0$.

A number of researchers [23, 78, 126, 185, 149] have confirmed the validity of the log-law for boundary layers with or without pressure gradient, over a range of $2,800 < Re < 230,000$.

Between the two layers described above, lays the buffer layer. In this flow region, which extends in $5.0 < y^+ \leq 30$, fluid dynamics are affected by both viscous and turbulence effects and the flow undergoes a transition from laminar to turbulent state. The behaviour in terms of average streamwise velocity is given by:

$$\langle u^+ (y^+) \rangle \approx 5.0 \ln y^+ - 3.05 \tag{1.16}$$

The outer region of a canonical boundary layer includes part of the outer Pradtl layer and the wake region. In the outer region of the boundary layer, the characteristic length is δ and the characteristic velocity is again the friction velocity. A detailed examination of experimental data by Coles [22] indicated that the time-averaged velocity profiles are given by:

$$\langle u^+ (y^+) \rangle \simeq A \ln y^+ + B \tag{1.17}$$

for the logarithmic region and by:

$$\langle u^+ (y^+) \rangle \simeq A \ln y^+ + B + \frac{\Pi}{\kappa_{vK}} W \left(\frac{y}{\delta} \right) \tag{1.18}$$

for the wake region.

A, B and Π are constants and W is the *wake function* proposed by Coles [22] as:

$$W\left(\frac{y}{\delta}\right) = 2\sin^2\left(\frac{\pi y}{2\delta}\right) \tag{1.19}$$

All the boundary layer regions described above can be seen in Figure 1.2.

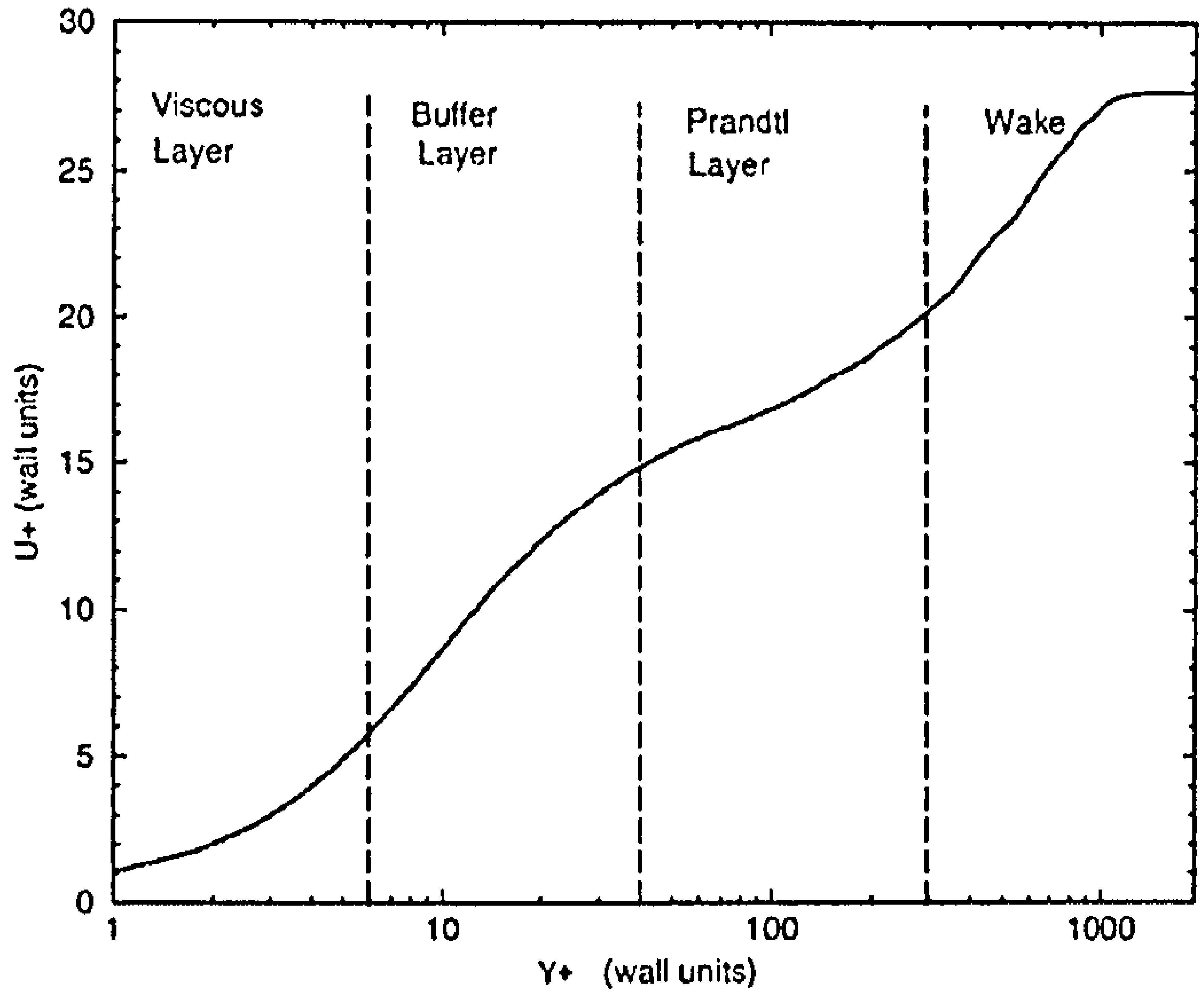

Figure 1.2: Canonical boundary layer regions

1.1.3 Boundary layer dynamic processes and fluid structures

Within a canonical boundary layer, there is a number of dynamic processes that are responsible for the fluid behaviour and the generation and development of turbulence. In the near-wall region, the flow is organised in ribbons parallel to the freestream velocity. These structures involve pockets of high and low velocity fluid that play an important role in the energy transfer between the different fluid layers.

Slow moving pockets of fluid are moving away from the wall, ejecting low velocity fluid in areas where the average fluid velocity is higher. This causes an instability that ultimately results in flow burst close to the outer part of the log-law region. Fast moving fluid is then moving closer to the wall, sweeping the near-wall region, almost parallel to it. This mechanism of fluid transfer from and towards the lower regions of the boundary layer generates strong variations in the unsteady Reynolds stresses and is responsible for large part of the turbulent kinetic energy production and dissipation. As a mechanism, it is highly anisotropic with characteristic scales of $\lambda_x^+ \approx 200 - 1000$ in the streamwise direction and of $\lambda_z^+ \approx 100$ in the transverse direction [64, 143].

The maximum energy production is observed at $y^+ \approx 15.0$ and causes high backward energy cascade, i.e. transfer of energy from small to large scales, and it is associated with the sweeping events. On the other hand, forward energy cascade is directly related to ejection effects [155]. In the wake region, the energy cascade mechanism is predominant and is associated mainly with ejections.

A series of studies by Jimenez et al. [71, 72, 73] have shown that turbulence in the near-wall region is an autonomous system that is responsible for the generation of significant part of the turbulent kinetic energy that is dissipated in the outer regions of the boundary layer. This turbulence cycle involves the formation of velocity streaks from the advection of the mean velocity profile by the streamwise vortices and the generation of vortices from the instabilities of the streaks. The presence of the wall only maintains the mean shear stress.

Using a priory tests on a plane channel flow, Hartel [64, 63] showed that the net effect of the interaction of the inner turbulence cycle and the outer flow is a forward energy cascade. Furthermore, the mean strain part is associated with forward kinetic energy cascade, while the fluctuating strain part causes a backward energy cascade in the buffer layer, with a maximum near $y^+ \approx 15.0$. This backward cascade is correlated with the presence of coherent events associated with turbulence production.

In his study, Robinson [153] presented a number of such coherent events. The buffer layer is dominated by isolated quasi-longitudinal structures that form an average angle of 5^o at $y^+ \approx 15.0$ with the wall and 15^o at $y^+ \approx 30.0$. Their diameter increases with the distance from the wall.

In the log-law region, two different types of structures can be found. The fluid dynamics are governed by quasi-longitudinal and arch structures. The quasi-longitudinal structures are occasionally connected to transverse structures and form an angle with surface between 15^o and 30^o. The span of the arch structures is of the order of the width of the slow moving fluid pockets at the bottom of the layer, and increases linearly with y. The relative number of quasi-longitudinal structures decreases with y, until it cancels out at the beginning of the wake region [155].

Finally, the wake region is populated with arch structures that form an angle of 45^o with the wall. Their x and y spacing is of the order of δ [155].

1.1.4 Variation of Reynolds stresses, kinetic energy production and rate of dissipation

All the dynamic processes described in the previous section have a direct effect on the Reynolds stresses distribution, as well as on the distribution of turbulent kinetic energy production, Pr, and rate of dissipation, ε. Knowledge of the distribution and behaviour of these parameters is of great importance for the development and testing of turbulence models. Figure 1.3 shows the distribution of $\frac{Pr}{\varepsilon}$ with respect to y^+ obtained by a DNS of a channel flow at $Re = 13,750$ [78].

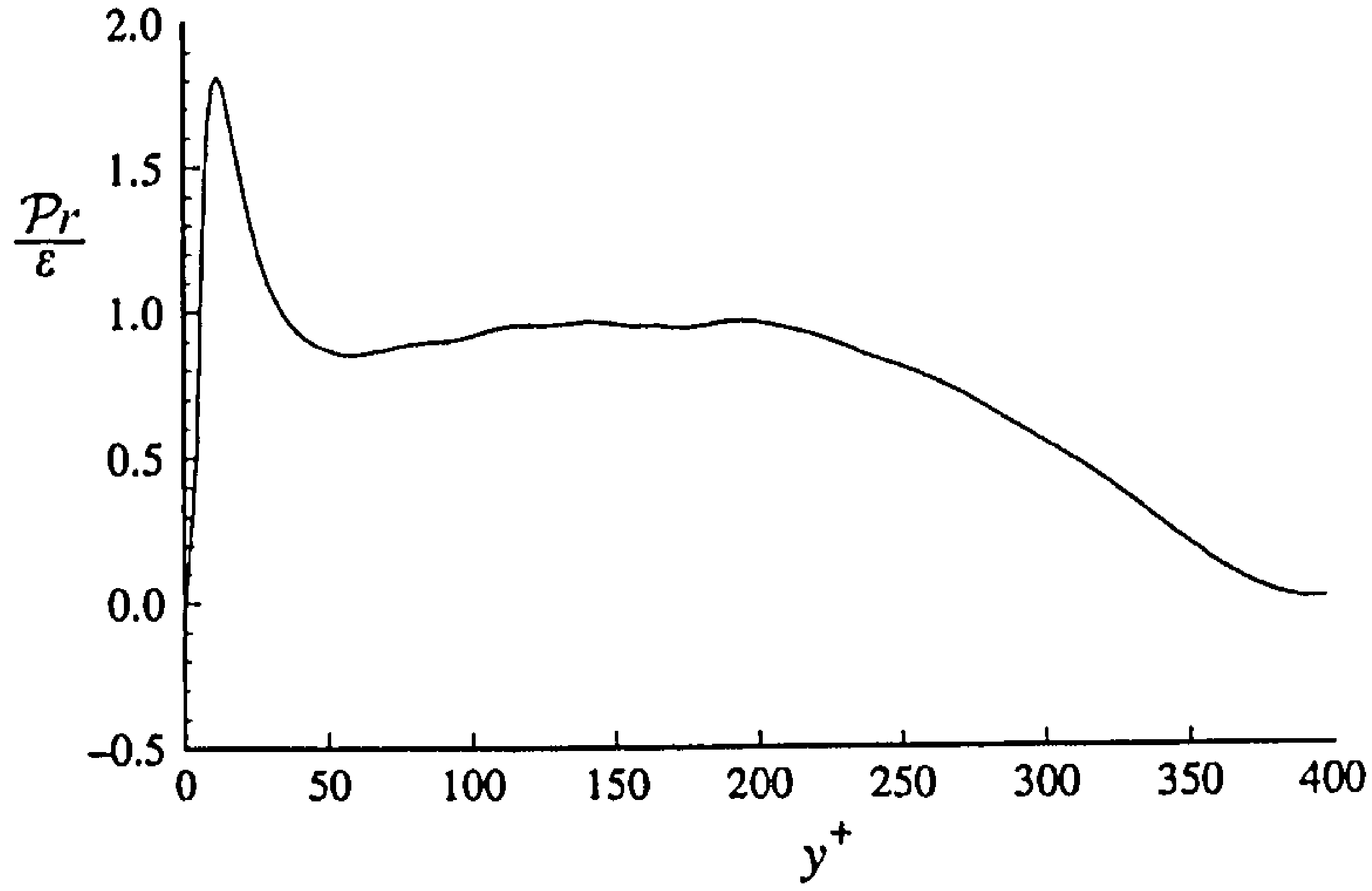

Figure 1.3: $\frac{Pr}{\varepsilon}$ vs. y^+ (source: DNS of channel flow at $Re = 13,750$ [78])

$\frac{Pr}{\varepsilon}$ is zero at the wall because of the zero production. It must be also noted that ε reaches the maximum value at the wall due to the fact that the fluctuating strain rates do not vanish at the wall. Moving away from the solid surface, ε decreases gradually, while there is an increase of Pr, proportional to y^3, until $y+ \approx 15.0$. Using Taylor expansion and taking into account the no-slip condition for the tangential velocity components and the impermability condition for the normal component, it can be shown that the variation of stresses away from the wall is:

$$\langle u^2 \rangle \propto y^2, \langle v^2 \rangle \propto y^4, \langle w^2 \rangle \propto y^2, \langle uv \rangle \propto y^3 \tag{1.20}$$

indicating that $\langle v^2 \rangle$ and $\langle uv \rangle$ increase slower. It can also be seen that the turbulent kinetic energy, k, varies as $k \propto y^2$.

In the log-law region, the production and dissipation of k are almost in an equilibrium state, while all the stresses remain constant. Finally, moving towards to the centre line region of the flow, both the gradient of the mean velocity and the shear stresses reduce to zero, resulting in zero turbulence production. Wei and Willmarth [185], in their study of channel flows up to $Re = 40,000$, observed no variation of the stresses distribution described above, for the region $y^+ < 50$, for a fully developed turbulent flow. For the rest of the boundary layer however, an increase with increased Re was observed for the normal stresses. Typical distributions of normal and shear stresses normalised by the friction velocity can be seen in Figure 1.4, obtained by a DNS of a channel flow at $Re = 13,750$ [78]. On the same graph, the turbulent kinetic energy k can also be seen.

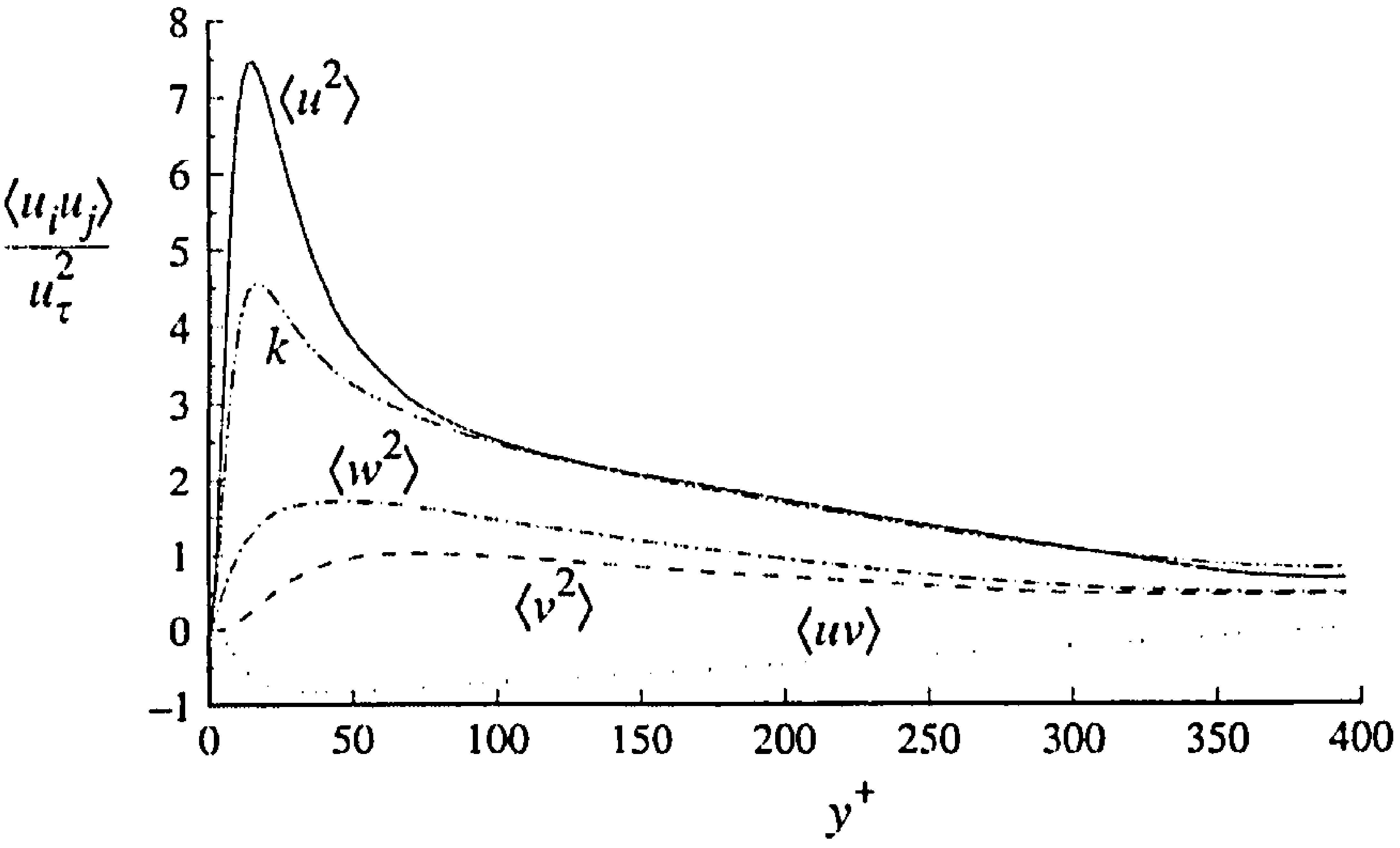

Figure 1.4: $\langle u^2 \rangle$, $\langle v^2 \rangle$, $\langle w^2 \rangle$, $\langle uv \rangle$ and k vs. y^+ (source: DNS of channel flow at $Re = 13,750$ [78])

1.2 Large Eddy Simulation

The behaviour of any Newtonian fluid can be described by the Navier-Stokes, NS, equations. Since no analytical solution is possible for the majority of the flows of interest, researchers turned into iterative, numerical solutions. Direct Numerical Simulation, DNS, i.e. a numerical solution of the exact NS equations, without modelling any term, requires a very high grid refinement as well as a very small timestep in order to capture all the time and length scales involved. As it was shown in the previous section, particularly for wall-bounded flows, this range of scales can be very wide, increasing significantly the required grid density. Furthermore, the computational requirements of DNS, can be shown to be directly related to the flow Re. Pope [146] suggests that the relation of Re and the time required for a homogeneous turbulence DNS, at a computing rate of one gigaflop, is given by:

$$T_G = \left(\frac{Re_L}{800}\right)^3 \tag{1.21}$$

where T_G is the computational time required in days and Re_L is the Reynolds number based on the characteristic turbulence length scale.

From Eq.1.21, it can be seen that even with contemporary computer technology, a simulation of a flow of $Re_L = 6,000$ would take 422 days. From this example it is clear that DNS cannot be applied widely to flows of real engineering interest. However, some successes over the recent years have been reported [50].

Due to their time averaging nature, Reynolds Averaged Navier-Stokes, RANS, equations can reduce significantly the computational time required, but the instantaneous behaviour of any turbulence present in the flow is lost. Hence, for unsteady turbulent flows, where the information of the unsteady motions is considered important, Large Eddy Simulation, LES, can provide the best available option in terms of acceptable computational cost and accuracy of the simulation.

LES is a technique that relies on the spatial filtering of the flow field. The flow field structures, which are greater than the filter size, are calculated using the exact NS equations while any flow structure smaller than the filter size, i.e. of subgrid scale, is modelled. Comparing to turbulence modelling used in RANS, subgrid scale modelling has potentially two advantages. Firstly, while the large eddies are flow dependent, smaller scale eddies tend to be more universal, as well as isotropic. Secondly, they can react more rapidly to perturbations, recovering quicker the equilibrium state [142]. Both these features can make subgrid scale modelling simpler and more accurate than that of large scale motions.

Based on the characteristics described above, LES has the potential to provide more accurate simulations than RANS, though in a higher computational cost. Still, comparing with DNS, the computational time required by LES is only a fraction, since the small scales of motions, whose resolution is the major cause of the DNS high computational requirements, are not resolved.

There are four main conceptual steps in LES:

1. The filtering operation. This operation decomposes the velocity $u(\vec{x},t)$, where $\vec{x}$ represents the position vector and t time, into the sum of the filtered component and the residual or subgrid-scale, SGS, component . This can be seen in Eq. 1.22. $\overline{u}(\vec{x},t)$ represents the motions of eddies, which are larger than the filter size while $u'(\vec{x},t)$ represents the motions of eddies which are smaller than the filter size. Note that superscript denoted spatially filtered quantity.

$$u(\vec{x},t) = \overline{u}(\vec{x},t) + u'(\vec{x},t) \tag{1.22}$$

2. The equations of the evolution of $\overline{u}(\vec{x},t)$ are derived by the NS equations. The LES NS equations of momentum contain the residual or SGS stress tensor that arises from the SGS motions. These equations are presented in sub-section 1.2.2.

3. Since the residual stress tensor is unknown, a model is employed to represent its evolution. The presentation and analysis of such models can be found in section 1.3 and in Chapter 2.

4. The filtered equations are solved numerically to give $\overline{u}(\vec{x},t)$, which provides an approximation to the large scale motions [146, 147].

Today, there are three main types of LES; the classic LES, the Monotonically Integrated LES, MILES, and the Hybrid LES. According to the classic LES, the NS equations are filtered explicitly or implicitly and a SGS model is used for the estimation of the residual or SGS stress tensor, as described by the four conceptual steps above.

MILES differs from the classic LES with respect to the SGS modelling. In MILES no SGS model is used but instead its effect is being introduced by specially designed discretisation schemes. This implicitly adopts the hypothesis that the action of the SGS scales is purely dissipative [155]. In the majority of cases, high resolution methods are used that seem to achieve many of the properties of the SGS model [42]. As a result, a number of studies have shown close agreement between MILES and classic LES solutions [43]. The approach has been widely used in cases where the use of an SGS model is difficult either due to the complexity of the flow mechanisms modelled or due to the inability of the SGS model to guarantee realisability constraints of the quantities studied [155]. For further reading on MILES approach and the schemes used, the reader can refer to [43] and [44] respectively.

Finally, Hybrid LES is effectively a combination of classic LES and RANS. In an effort to decrease the simulation cost, three approaches have emerged to combine the two techniques. According to the first, the computational space is divided into two domains. The first domain comprises of a layer over rigid surfaces present in the geometry of interest and the second domain of the rest of the flow field. During the simulation, RANS equations are being solved in the first domain, providing a form of boundary conditions for the LES equations which are used for the flow solution in the rest of the field. According to the second approach RANS are used everywhere to obtain the low frequency part of the solution and a large eddy type simulation to obtain the high frequency part. Finally, the third approach makes use of a universal turbulence-SGS model, able to introduce correct physics over a wide range of cutoff wave numbers, even outside or at the beginning of the inertial range [155].

In the present study, the interest of the author laid in the investigation and development of SGS models for wall bounded flows and therefore the classic LES approach was followed as it was considered to fit best to the given purpose of this work.

1.2.1 Filtering in LES

In order to perform the decomposition of the primitive variables, given by Eq.1.22, a filter must be used. For a space-time variable $\phi\left(\vec{x},t\right)$, the filtering procedure is defined by:

$$\overline{\phi}\left(\vec{x},t\right) = \int_{-\infty}^{+\infty} \phi\left(\vec{\xi},t\right) G\left(\vec{x}-\vec{\xi}\right) d^3\xi \tag{1.23}$$

where the convolution kernel G is the characteristic of the filter employed.

In LES, the most widely used filters are:

- Box or top-hat filter:

$$G\left(\vec{x}-\vec{\xi}\right) = \begin{cases} \frac{1}{\overline{\Delta}} \text{ for } -\overline{\Delta}/2 \leq \vec{x}-\vec{\xi} \leq \overline{\Delta}/2 \\ 0 \text{ otherwise} \end{cases} \tag{1.24}$$

where $\overline{\Delta}$ is the cutoff length associated with the filter. The box filter is described in the physical space and it is the most easy to use with the finite-difference or finite volume technique, because the filtered variable takes essentially the cell averaged value, when $\overline{\Delta}$ is equal to the cell size.

- Gaussian filter:

$$G\left(\vec{x}-\vec{\xi}\right)=\left(\frac{\gamma}{\pi\overline{\Delta}^{2}}\right)^{1/2}\exp\left(\frac{-\gamma\left|\vec{x}-\vec{\xi}\right|^{2}}{\overline{\Delta}^{2}}\right) \tag{1.25}$$

where γ is a constant taken to be equal to 6.0. The Gaussian filter can be described in both physical and spectral space.

- Spectral or sharp cutoff filter:

$$G\left(\vec{x}-\vec{\xi}\right)=\frac{\sin\left(\kappa_c\left(\vec{x}-\vec{\xi}\right)\right)}{\kappa_c\left(\vec{x}-\vec{\xi}\right)} \tag{1.26}$$

where κ_c is the cutoff wavenumber given by $\kappa_c=\frac{\pi}{\overline{\Delta}}$. The spectral filter is described in spectral space.

Filtering in LES can be explicit or implicit. When explicit, all primitive variables are convoluted by G, according to Eq. 1.23. In the latter case, the role of the filter is performed by the computational grid and the resulted filter has the form of the top-hat filter.

None of the three filters are commutative under differentiation when applied on non-uniform grids. Hence, an error of $O\left(\Delta^{2}\right)$ can be introduced [57]. This behaviour has only recently started to be investigated, giving rise to studies on commutative forms of filters [32]. Furthermore, the net effect of use of different filters on the simulation accuracy is still not clear and it is, therefore, an open area of research.

1.2.2 LES equations

The spatially filtered NS equations, adopted by LES to give the evolution of $\overline{u}\left(\vec{x},t\right)$, are obtained through the application of the filtering operation to the NS equations. The filtered continuity equation, for incompressible flow, then takes the following form:

$$\overline{\left(\frac{\partial u_i}{\partial x_i}\right)} = \frac{\partial \overline{u}_i}{\partial x_i} = 0 \tag{1.27}$$

from which it can be obtained:

$$\frac{\partial u'_i}{\partial x_i} = \frac{\partial \left(u_i - \overline{u}_i\right)}{\partial x_i} = 0 \tag{1.28}$$

Equation 1.27 indicates that both $\overline{u}\left(\vec{x}, t\right)$ and $u'\left(\vec{x}, t\right)$ are solenoidal fields. The filtered momentum equation, for incompressible flow, has the form:

$$\frac{\partial \overline{u}_i}{\partial t} + \frac{\partial \overline{u_i u_j}}{\partial x_j} = -\frac{1}{\rho}\frac{\partial \bar{P}}{\partial x_i} + \nu \frac{\partial^2 \overline{u}_i}{\partial x_j x_j} \tag{1.29}$$

where $\bar{P}$ is the spatially filtered pressure field. The main difference between Eq.1.29 and the original NS equations is the $\overline{u_i u_j}$ term. $\overline{u_i u_j}$ is different from $\overline{u}_i \overline{u}_j$, with the difference being given by the subgrid scale stress tensor τ_{ij}:

$$\tau_{ij} = \overline{u_i u_j} - \overline{u}_i \overline{u}_j \tag{1.30}$$

Eq.1.30 is attributed to Leonard [96] who expressed a formulation for its evaluation. Note that strictly the stress tensor is given by $-\rho\tau_{ij}$. The residual stress tensor is not a stress, but it is rather handled as a stress term. Physically, it expresses the large scale momentum flux caused by the action of the small unresolved scales [48]. The subgrid scale kinetic energy is given by:

$$k_{sgs} = \frac{1}{2}\tau_{ii} \tag{1.31}$$

and the anisotropic residual stress tensor is defined by:

$$\tau_{ij}^{r} = \tau_{ij} - \frac{2}{3}k_{sgs}\delta_{ij} \tag{1.32}$$

where δ_{ij} is the Kronecker's delta. The isotropic residual stress is included in the modified filtered pressure, which is given by:

$$\overline{P} = \bar{P} + \frac{2}{3}k_{sgs} \tag{1.33}$$

Using the above definitions, Eq.1.29 can be rewritten as:

$$\frac{\partial \overline{u}_i}{\partial t} + \frac{\partial \overline{u}_i \overline{u}_j}{\partial x_j} = -\frac{1}{\rho}\frac{\partial \overline{P}}{\partial x_i} + \nu \frac{\partial^2 \overline{u}_i}{\partial x_j x_j} - \frac{\partial \tau_{ij}^{r}}{\partial x_j} \tag{1.34}$$

In order to solve Eq.1.27 and 1.34, a model is required for τ_{ij}^{r}. Eq. 1.27 and 1.34 describe random, three dimensional, 3D, unsteady fields. Using a set of boundary conditions for the primitive variables and a model for the anisotropic residual stress tensor, Eq.1.27 and 1.34 can be solved numerically, to give $\overline{P}(\vec{x},t)$ and $\overline{u}(\vec{x},t)$.

From the above, it becomes clear that both boundary conditions and SGS modelling can affect significantly the calculation procedure in terms of numerical stability and accuracy of the computed flow field. Comparing to RANS, the LES technique, due to the inherent unsteadiness of the equations, introduces some further requirements related to boundary conditions and especially to those applied at the inlet of the flow domain. Unsteady boundary conditions are always required. The quality of these conditions in terms of realism of turbulence can vary, as well as the effect that it will have on the downstream flow development. There is a number of flows that can be significantly affected by the turbulence introduced at the inlet plane of the computational domain. In such cases, the inlet boundary conditions should contain as much realistic information about the primitive variables introduced, as possible. Typical examples are the flow through a channel with periodic constrictions [174], jet flows and spatially developing boundary layers [108]. However, it has been observed that for other flows, such as the flow over a cube mounted on a channel surface [88], the flow development can be dictated by the presence of geometric features, inside the flow domain, causing the inlet conditions to have little effect on the flow downstream.

While the effect of boundary conditions depends upon the flow case, the role of SGS modelling in LES depends on the computational grid refinement. The coarser the mesh, the larger the role of the SGS model, as more and more scales have to be encountered by the model. This implies that at the DNS limit, i.e. when the refinement is such that all scales are properly resolved, the effect of the SGS model should tend to zero.

1.3 Subgrid scale modelling

As mentioned in the previous section, the residual stress tensor is unknown. In order to solve the system of Eq.1.34 and 1.27, τ_{ij}^{r} has to be modelled. This is the subject of a large area of research, known as SGS modelling. The first pioneering work on LES and SGS modelling was done during the 60's and 70's. The following decade saw a decline in the field, mainly due to the lack of computational power and the attention given to developments in RANS turbulence modelling. From the early 90's, a considerable progress has been made. Today, SGS modelling is considered a very important part of the LES technique, as it can significantly affect both the cost and the accuracy of the simulation.

The main function of a SGS model is to model correctly the energy transfer among the different turbulence scales. The majority of the models that have been developed, are based on the analysis of a forward energy cascade, i.e. for the case where energy is transfered from the large, energy containing eddies, to the smaller, dissipative ones. This is because a) this direction in energy transfer represents the largest part of the total energy transfer and b) the role of backscattering, i.e. the transfer of energy from the smaller to the larger scales, is still not well understood. However, there are a number of implementations that allow for the prediction of its effect [17, 79, 95, 112].

A schematic of the energy transfer that corresponds to the forward energy cascade case can be seen in Figure 1.5. In this Figure, ε_I is the injection rate of kinetic energy into the system, $\tilde{\varepsilon}$ is the rate of kinetic energy transfer from the resolved to the subgrid scales at κ_c and ε is the rate of kinetic energy dissipated by the viscous effects.

In the following sections, the main philosophy and the principal ideas behind SGS modelling, will be presented. Different trends will be critically described, providing a picture of the subject, as it stands today. Description and detailed analysis of the typical models from every category of SGS models will be given in Chapter 2.

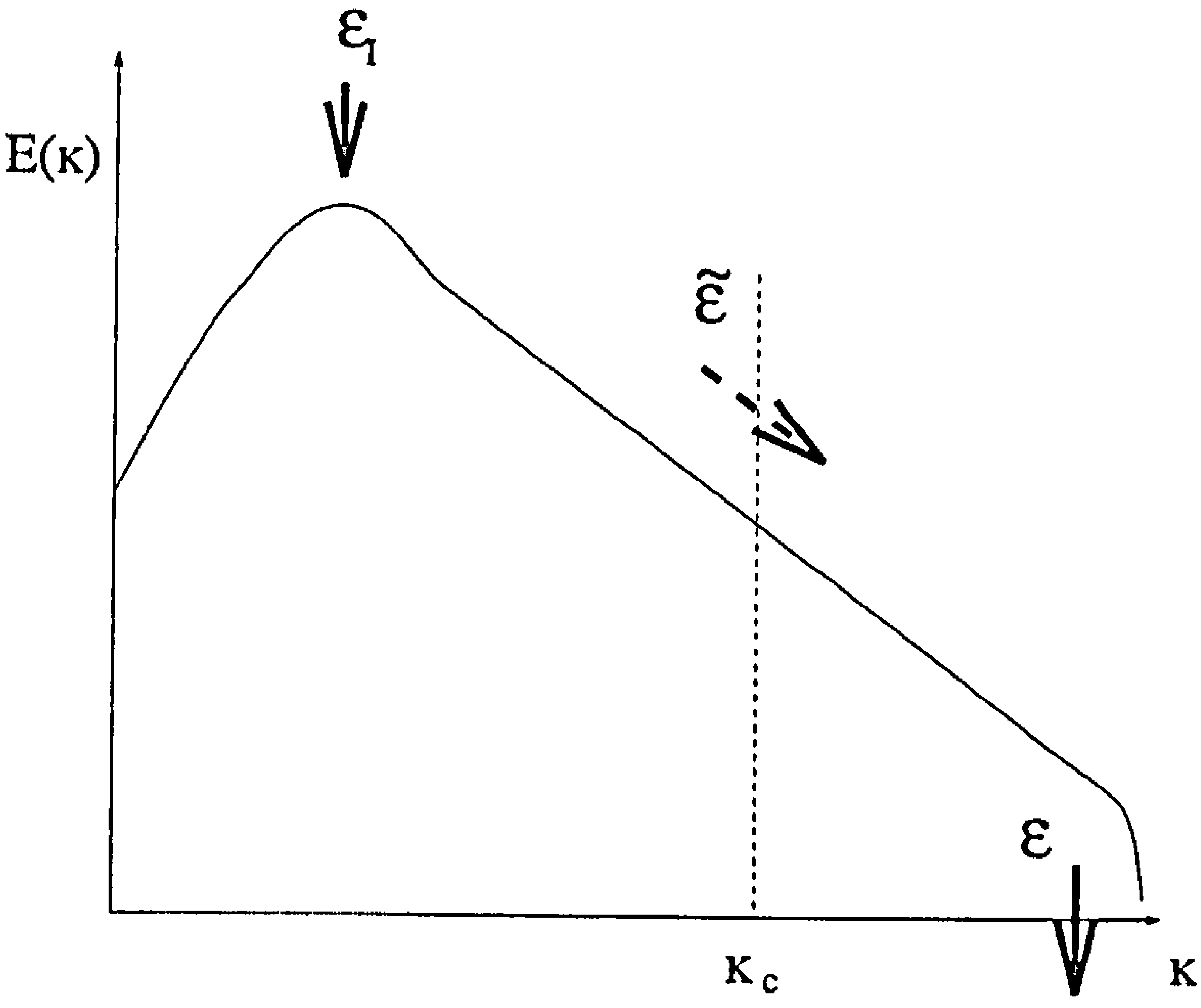

Figure 1.5: Schematic of kinetic energy transfer in forward energy cascade case (ε_I: injection rate of kinetic energy into the system, $\tilde{\varepsilon}$: kinetic energy transfer rate from the resolved to the subgrid scales at κ_c, ε: dissipation rate of kinetic energy by viscous effects)

1.3.1 The Boussinesq assumption

Although not without its shortcomings [146], the majority of the SGS models make use of the Boussinesq assumption and express τ_{ij}^r as a function of the resolved strain-rate tensor $\overline{S_{ij}}$, and a proportionality constant in the form of eddy viscosity ν_t.

$$\tau_{ij}^r = \tau_{ij} - \frac{1}{3}\tau_{kk}\delta_{ij} = -2\nu_t\overline{S_{ij}} \tag{1.35}$$

Eq.1.35 assumes that the energy transfer mechanism from the resolved to the subgrid scales is analogous to the molecular mechanism, represented by the diffusion term, in the NS equations [155]. Hence, the same mathematical structure is employed with the kinematic viscosity replaced by ν_t. With the adoption of Eq.1.35, the closure consists of determining an expression for ν_t.

From the dimensional point of view, ν_t can be expressed as:

$$\nu_t \propto l_o \cdot u_o \text{ or equivalently } \nu_t \propto l_o^2 \cdot \frac{1}{t_o}$$

where l_o, u_o and t_o are the representative length, velocity and time scales.

The formulation that will lead to the calculation of these parameters forms the core of SGS modelling. Based upon different approaches to the problem, four main categories of models have emerged over the years. According to the first approach, the scales of interest are computed from global quantities related to the resolved scales, by making use of a number of assumptions. According to the second approach, ν_t is deduced from SGS variables without the requirement of any assumption. Therefore, in theory, the second approach can produce more realistic models.

The third category comprises of models based on the energy at the cutoff scale. Finally, the fourth category has models, which are founded on the assumption that the most energetic of the subgrid-scales are those closer to the cutoff scale and that they interact primarily with the smallest resolved scales. The resulted models are called scale-similarity models.

Most of the models of all but the third category, have been developed in the physical space. However, in the third category we can find a number of models that originally were developed in wavenumber space and later were modified or extended to be applied in the physical space.

1.3.2 Models based on resolved scales

The first category of models consists of models that use information from the resolved scales for the modelling of ν_t. Dimensional analysis shows that:

$$\nu_t \propto \bar{\varepsilon}^{1/3} \cdot \overline{\Delta}^{4/3} \tag{1.36}$$

Assuming that the energy spectrum takes the form of the Kolmogorov's spectrum extending to infinity, given by:

$$E(\kappa) = K_o \langle \varepsilon \rangle^{2/3} \kappa^{-5/3} \tag{1.37}$$

where κ is the wavenumber $K_o = 1.4$, we can deduce:

$$\nu_t = \frac{A}{K_o \pi^{4/3}} \langle \bar{\varepsilon} \rangle^{1/3} \overline{\Delta}^{4/3} \tag{1.38}$$

where $A \simeq 0.44$ by the Eddy-Damped Quasi Normal Markovian, EDQNM, theory.

In order to proceed further, an assumption has to be made related to $\tilde{\varepsilon}$. This is the *Local Equilibrium Hypothesis*, according to which

> *"the flow is in constant spectral equilibrium, so there is no accumulation of energy at any frequency and the shape of the spectrum remains invariant with time"* [155]

Mathematically, *Local Equilibrium Hypothesis* is described as:

$$\varepsilon_I = \tilde{\varepsilon} = \varepsilon \tag{1.39}$$

Based on Eq.1.37 and assuming isotropic homogeneous flow, where [13, 155, 146]:

$$2\overline{S}_{ij}\overline{S}_{ij} = \int_0^{\kappa_c} 2\kappa^2 E(\kappa)\, d\kappa \tag{1.40}$$

ε can be estimated as:

$$\varepsilon = \frac{1}{\pi^2}\left(\frac{3K_o}{2}\right)^{-3/2} \overline{\Delta}^2 \left(2\left|\overline{S}\right|^2\right)^{3/2} \tag{1.41}$$

where $\left|\overline{S}\right|^2 = 2\overline{S}_{ij}\overline{S}_{ij}$. Full derivation of Eq. 1.40 can be found in [13]. Substitution of Eq.1.41 in Eq.1.38 leads in:

$$\nu_t = \left(C_s\overline{\Delta}\right)^2 \left(2\left|\overline{S}\right|^2\right)^{1/2} \tag{1.42}$$

where

$$C_s = \frac{\sqrt{A}}{\pi\sqrt{K_o}}\left(\frac{3K_o}{2}\right)^{-1/4} \tag{1.43}$$

Eq.1.42 describes the Smagorinsky model [163], which is the most widely used SGS model. Detailed discussion on this model will follow in Chapter 2.

According to another approach by Lilly [100], which uses Eq.1.42 as a starting point, the equality of energy production and dissipation that is implied by Eq.1.39 leads to:

$$\varepsilon = -\overline{S}_{ij}\tau_{ij} = 2\nu_t\overline{S}_{ij}\overline{S}_{ij} \tag{1.44}$$

Equating Eq.1.44 to Eq.1.41, results in the following expression for C_s:

$$C_s = \frac{1}{\pi}\left(\frac{3K_o}{2}\right)^{-3/4} \tag{1.45}$$

As it can be seen from the above, the value of C_s can be estimated for some flow cases, but it is significant to note that its value can vary considerably for different flows. The presence of shear or the transition from laminar to turbulent flow are two of the factors that can affect its value [139]. A priori knowledge of C_s is important for the correct behaviour of the model and it is this feature that can potentially limit its application to flows that have not been studied before. This limitation gave rise to the dynamic procedure, which is described in section 1.3.7.

Another important issue of these models is that the resulted formulation of ν_t is a function of the velocity gradients of the resolved flow field. Hence, even in a laminar flow, ν_t can potentially take non-zero value even if the flow is fully resolved. This feature limits the capabilities of such models only to fully turbulent, under-resolved flows.

1.3.3 Models based on subgrid scales

The second category comprises of models based on subgrid scales. Using dimensional analysis, ν_t can be expressed as a function $\overline{\Delta}$, ε and k_{sgs}. The employment of a combination of these three variables has two main advantages: firstly the resultant models have a direct relation to the SGS scales and should result in zero eddy viscosity when the flow is fully resolved or laminar. Secondly, it is possible to avoid the use of the equilibrium hypothesis that limits the generality of the model.

There is a number of possible formulations, but only the ones related to our study will be described here. For further reading, the reader can reference to Sagaut [155]. One option is to use dimensional analysis and form an equation in terms of $\overline{\Delta}$ and ε, similar to Eq.1.38. Then, the solution of the integral of the energy spectrum with respect to ε, leads to the derivation of an expression of the following form:

$$\nu_t = C\varepsilon^{\alpha/3} k_{sgs}^{(1-\alpha)/2}\overline{\Delta}^{1+\alpha/3} \tag{1.46}$$

where

$$C = \frac{A}{K_o\pi^{4/3}}\left(\frac{3K_o}{2}\right)^{(\alpha-1)/2}\pi^{(1-\alpha)/3} \tag{1.47}$$

Eq.1.46 can give rise to three different SGS models, based on the value of the parameter α. For $\alpha = 1$ the resulted model is equivalent to the resolved scales model given by Eq.1.42. For $\alpha = -3$ the resulted model is only a function of k_{sgs} and ε, in a form similar to the $k - \varepsilon$ turbulence model of RANS. Finally, for $\alpha = 0$, takes the form:

$$\nu_t = \sqrt{\frac{2}{3}} \frac{A}{\pi K_o^{3/2}} k_{sgs}^{1/2} \overline{\Delta} \tag{1.48}$$

In Eq.1.48, k_{sgs} is not known a priori. It can be calculated by solving the transport equation of k_{sgs}, which is presented in section 1.3.4. For the expressions that involve ε, either an assumed energy spectrum can be used for its calculation, as shown above, or its transport equation. The last approach has not been preferred since the exact equation of ε introduces a number of terms that have to be modelled [146], reflecting on the complexity and the accuracy of the resulted model.

Although the requirement for the calculation of a coefficient is present in this category of models as well, the main advantage of formulations based on information from the subgrid scales is the physical realisability, which has the potential, theoretically, to be improved compared to models based on resolved scales.

1.3.4 The transport equation of k_{sgs} and the gradient diffusion hypothesis

The transport equation of k_{sgs} can be directly derived from the Navier Stokes equation in two steps: a) multiply each momentum equation with the corresponding component of u_i and filter the resulted equation b) multiply each filtered momentum equation with the corresponding component of $\overline{u_i}$ and subtract the resulted equation from the equation obtained by the first step [25]. This leads to the following equation:

$$\begin{aligned} \frac{\partial k_{sgs}}{\partial t} + \frac{\partial \overline{u}_j k_{sgs}}{\partial x_j} = & -\tau_{ij} \frac{\partial \bar{u}_i}{\partial x_j} - \frac{1}{2} \frac{\partial}{\partial x_j} \left(\overline{u_i u_i u_j} - \bar{u}_j \overline{u_i u_i} \right) - \frac{\partial}{\partial x_j} \left(\overline{P u_j} - \bar{P} \bar{u}_j \right) \\ & + \frac{\partial}{\partial x_j} \left(\nu \frac{\partial k_{sgs}}{\partial x_j} \right) + \frac{\partial}{\partial x_j} \left(\tau_{ij} \overline{u_i} \right) - \nu \left(\overline{\frac{\partial u_i}{\partial x_j} \frac{\partial u_i}{\partial x_j}} - \frac{\partial \bar{u}_i}{\partial x_j} \frac{\partial \bar{u}_i}{\partial x_j} \right) \end{aligned} \tag{1.49}$$

In Eq. 1.49:

$\frac{\partial \overline{u}_j k_{sgs}}{\partial x_j}$ (Term 1) is the advection term

$\frac{1}{2}\frac{\partial}{\partial x_j}\left(\overline{u_i u_i u_j} - \bar{u}_j \overline{u_i u_i}\right)$ (Term 2) is the turbulent transport term

$\frac{\partial}{\partial x_j}\left(\overline{P u_j} - \bar{P}\bar{u}_j\right)$ (Term 3) is the term representing the diffusion due to pressure effects

$\frac{\partial}{\partial x_j}\left(\nu \frac{\partial k_{sgs}}{\partial x_j}\right)$ (Term 4) is the term representing the diffusion due to viscous effects

$\frac{\partial}{\partial x_j}\left(\tau_{ij}\overline{u_i}\right)$ (Term 5) is the term representing the diffusion due to the subgrid modes

$\nu\left(\overline{\frac{\partial u_i}{\partial x_j}\frac{\partial u_i}{\partial x_j}} - \frac{\partial \bar{u}_i}{\partial x_j}\frac{\partial \bar{u}_i}{\partial x_j}\right) = \varepsilon$ (Term 6) is the SGS viscous dissipation term and

$\tau_{ij}\frac{\partial \bar{u}_i}{\partial x_j} = Pr$ (Term 7) is the production by the resolved modes.

The diffusion terms 2 and 3 and the SGS viscous dissipation term cannot be calculated directly and have to be modelled. As far as the viscous dissipation term is concerned, it is usually modelled based on dimensional analysis [155], as:

$$\varepsilon = C_1 \frac{k_{sgs}^{3/2}}{\overline{\Delta}} \tag{1.50}$$

However, in some recent work by De Lange [90], ε was computed by the solution of an extra transport equation using the Renormalisation Group, RG, theory.

Regarding the diffusion terms, an approach proposed by Lilly [100] and discussed by McComb [114], is to use the *gradient diffusion hypothesis* according to which:

> *"the turbulent transport of a conserved scalar ϕ, given by $\left\langle \vec{u}\phi' \right\rangle$, is in the direction of the mean scalar gradient $-\nabla \langle\phi\rangle$. Hence there is a positive scalar $\Gamma(\vec{x},t)$ such that $\left\langle \vec{u}\phi' \right\rangle = -\Gamma(\vec{x},t)\,\nabla\langle\phi\rangle$"* [146]

Hence, by assuming that the non-linear term inside the spatial derivative is proportional to the gradient of k_{sgs}, terms 2, 3 and 5 can be modelled as:

$$\frac{\partial}{\partial x_j}\left[-\frac{1}{2}\left(\overline{u_i u_i u_j} - \bar{u}_j \overline{u_i u_i}\right) - \left(\overline{p u_j} - \bar{p}\bar{u}_j\right) + \left(\tau_{ij}\overline{u_i}\right)\right] = C_2 \frac{\partial}{\partial x_j}\left(k_{sgs}^{1/2}\overline{\Delta}\frac{\partial k_{sgs}}{\partial x_j}\right) \tag{1.51}$$

In Eq.1.50 and 1.51, C_1 and C_2 are constants to be determined.

Term 7 represents the production of k_{sgs} and acts as a source in Eq.1.49. It is important to note that the same term can be found in the transport equation of the resolved turbulent kinetic energy, where it is acting as a sink [118], draining energy from the large scales, down to the subgrid dissipative scales.

1.3.5 Models based on the energy at the cutoff scale

The models that belong to this category are based on the assumption that if the energy at the cutoff scale is not zero, then subgrid scales exist and have to be modelled. The first model of this kind was developed for calculations that were performed in wavenumber space [84, 19]. However, the limitations of this approach regarding the applicability to finite differences, finite volumes codes and to more complex geometries, led to an extension of the main idea to the physical space [113].

A number of ways have been proposed for the calculation of $E(\kappa_c)$. Working in Fourier space, Kraichnan [84] used two-point correlations while Chollet and Lesieur [19] employed the EDQNM theory [98], to derive similar expressions.

In terms of physical space, formulation of such models can be based on Eq.1.38. Assuming that the cutoff lays in the inertial region of a Kolmogorov energy spectrum, given by Eq.1.37, it can be deduced the following expression for ν_t:

$$\nu_t = \frac{A}{\sqrt{K_o}}\sqrt{\frac{E(\kappa_c)}{\kappa_c}} \tag{1.52}$$

The adoption of other forms of the energy spectrum are also possible, leading to other similar expressions.

The main difficulty of these models is the accurate calculation of $E(\kappa_c)$ in the physical space [155]. However, if this problem is overcome, then the resulted expression will have a physical consistency, since it will generate zero values of ν_t in highly resolved or laminar regions of the flow.

1.3.6 Scale similarity models

The studies of Clark et al. [21], McMillan & Ferziger [116] and Lieu et al. [102] indicated that there is very little correlation between the subgrid-scale stress tensor and the resolved strain rate tensor, widely used in models based on resolved scales. This provided an explanation for the lack of accuracy of these models, regarding the correct representation of the subgrid scale stresses. Furthermore, it gave rise to another category of models, which were based on the idea that the important interactions between the resolved and unresolved scales involve the smallest eddies of the former and the largest eddies of the later [48]. Based on the observation that the smallest resolved scales are similar to the largest subgrid scales, which are modelled, Bardina et al [12] proposed the following expression:

$$\tau_{ij} = \overline{\overline{u}_i \overline{u}_j} - \overline{\overline{u}}_i \overline{\overline{u}}_j \tag{1.53}$$

where the double overline indicates a quantity that has been filtered twice.

Although the residual stress tensor given by Eq.1.53 correlates very well with the actual τ_{ij} [12, 102], it hardly dissipates any energy. Therefore, it cannot serve on its own as a SGS model. In order to correct the lack of dissipation, it is necessary to combine the model with the Smagorinsky model, to produce a mixed model, which has been reported to improve the quality of the results. According to another approach, the lack of dissipation can be corrected by the replacement of the second filter with spatial averaging [60] or with a filter of different width [102]. This last idea is conceptually close to the dynamic procedure that is presented in the following section.

1.3.7 The dynamic procedure

As it was mentioned in section 1.3.2, the variation of C_s based on the flow conditions constitutes one of the most important problems of the Smagorinsky model. The dynamic procedure provides a methodology that allows the calculation of the local value of C_s, avoiding in this way a priori definition to a single value. The dynamic procedure was introduced by Germano et al. [55] in 1991 and it was modified and extended by Lilly [101] and Meneveau [119] in 1992 and 1996 respectively. Models that make use of the dynamic procedure involve the use of two filters of different widths. The grid filter has width $\overline{\Delta}$, which is proportional to the grid spacing h. The test filter has width $\tilde{\overline{\Delta}}$, which is usually taken to be twice $\overline{\Delta}$. In practice, the test filter is applied to $\overline{u}(\vec{x},t)$, giving $\tilde{\overline{u}}(\vec{x},t)$. Hence, Eq.1.22 can be extended as follows:

$$u(\vec{x},t) = \overline{u}(\vec{x},t) + u'(\vec{x},t) = \tilde{\overline{u}}(\vec{x},t) + \left(\overline{u}(\vec{x},t) - \tilde{\overline{u}}(\vec{x},t)\right) + u'(\vec{x},t) \tag{1.54}$$

The SGS stresses based on single and double filtering operations can be defined as:

$$\tau_{ij} = \overline{u_i u_j} - \overline{u}_i \overline{u}_j \tag{1.55}$$

and

$$T_{ij} = \widetilde{\overline{u_i u_j}} - \tilde{\overline{u}}_i \tilde{\overline{u}}_j \tag{1.56}$$

The identity proposed by Germano [54] can then be obtained by applying the test filter on τ_{ij} and subtracting the result from T_{ij}.

$$L_{ij} \equiv T_{ij} - \tilde{\tau}_{ij} = \widetilde{\overline{u}_i \overline{u}_j} - \tilde{\overline{u}}_i \tilde{\overline{u}}_j \tag{1.57}$$

The significance of L_{ij} is that it can be calculated from $\overline{u}\,(\vec{x}, t)$, while τ_{ij} and T_{ij} cannot. In physical terms, L_{ij} can be loosely interpreted as a representation of the contribution to the SGS stresses from the largest unresolved motions.

Recalling Eq.1.35 and 1.42, the deviatoric part of τ_{ij} can be written as:

$$\tau^r_{ij} = -2c_s \overline{\Delta}^2 \overline{S}\,\overline{S}_{ij} \tag{1.58}$$

where c_s has replaced C_s^2 to allow negative values that represent energy backscatter. The same model equation written using the test filter gives:

$$\tilde{T}_{ij} = -2c_s \tilde{\overline{\Delta}}^2 \tilde{\overline{S}}\,\tilde{\overline{S}}_{ij} \tag{1.59}$$

where $\tilde{\overline{S}}$ and $\tilde{\overline{S}}_{ij}$ are defined using $\tilde{\overline{u}}\,(\vec{x}, t)$. Taking c_s to be uniform and defining:

$$M_{ij} = 2c_s \overline{\Delta}^2 \widetilde{\overline{S}\,\overline{S}_{ij}} - 2c_s \tilde{\overline{\Delta}}^2 \tilde{\overline{S}}\,\tilde{\overline{S}}_{ij} \tag{1.60}$$

Eq.1.58and Eq.1.59 lead to:

$$L_{ij}^{S} = T_{ij}^{d} - \tilde{\tau}_{ij}^{r} = c_s M_{ij} \tag{1.61}$$

Eq.1.61 gives the Smagorinsky model for the deviatoric part of L_{ij}, which is given by:

$$L_{ij}^{d} = L_{ij} - \frac{1}{3} L_{kk} \delta_{ij} \tag{1.62}$$

Since LES can provide directly M_{ij} and L_{ij}^{d}, these can be used to determine the value of c_s for which L_{ij}^{S} can give the best approximation to L_{ij}^{d}. The single value of c_s cannot be chosen to match the five independent components of L_{ij}^{S} and L_{ij}^{d}. Therefore, the mean square error is minimized by specifying c_s as:

$$c_s = \frac{M_{ij} L_{ij}}{M_{kl} L_{kl}} \tag{1.63}$$

Because the use of Eq.1.63 was proved to destabilise the calculation, an averaging operation was proposed by Germano [56] and Piomelli [138], leading to:

$$c_s = \frac{(M_{ij} L_{ij})_{average}}{(M_{kl} L_{kl})_{average}} \tag{1.64}$$

This resulted in stable calculations and correct c_s variation. In some implementations where negative c_s values caused instability of the calculations, c_s was either bounded [11] or clipped [106], i.e. it was set zero when a negative value would arise. From the description given, it can be seen that the dynamic procedure can be applied on a variety of eddy viscosity based SGS models [188, 199].

1.4 Inflow conditions for LES

In section 1.2.2, it was pointed out that for a number of flows, the realistic behaviour of inlet boundary conditions can play an important role in accuracy of the LES performed. It has been shown by Klein et al. [80, 81], Stanley et al. [171], and Lund et al. [108] that

DNS and LES results for a plane jet, a spatially developing boundary layer and the breakup of a liquid sheet are very sensitive to the inlet conditions. Le et al. [93] demonstrated in a backward facing step flow simulation that, if the inflow information did not contain the phase information of realistic turbulent eddies, the turbulence level in the separated shear layer decayed rapidly and a relatively long inlet section was needed to develop physically acceptable inlet profiles. Furthermore, Maruyama [111] performed LES of a high Reynolds number turbulent boundary layer and found that the inflow turbulence characteristics had a significant impact on the downstream flow field.

From the examples given above, it is clear that for a number of turbulent flows, the flow downstream is highly influenced by the conditions at the inlet. This constitutes a vicious circle where turbulence has to be prescribed at the inflow in order to simulate turbulence [82]. In many cases, realistic time series that fulfill the NS equations, have to be specified. This implies that a separate simulation might be required. However, this introduces a further increase in cost and therefore, a number of approaches have been developed over the years as possible alternatives. These are discussed in the following sections. For further reading, the reader can reference to [155, 108, 82, 124].

1.4.1 Domain enlargement

Probably the simplest approach in generating inlet data is to introduce the inlet plane far upstream of the flow domain of interest. A laminar profile with some disturbance can then be specified and the flow can go through a natural transition to turbulence. This method has been used in the past, in flows focusing in transition process [150], but it has some major disadvantages.

Firstly, it can significantly increase the computational cost. This is because there is an increase of the flow domain that has to be accounted for and furthermore, because the correct simulation of transition can be very costly. Secondly, it provides no control over the resulted flow characteristics.

1.4.2 The "precursor" method

The so-called precursor method, where a separate LES calculation is performed to generate unsteady inlet conditions, is perhaps the most accurate technique currently. According to this method, the precursor calculation is performed using the same timestep as the main simulation. At the end of each iteration, the velocity field at a plane of a desired streamwise location is saved. Then this information can be imposed to the inlet plane of the main simulation as a boundary condition. This procedure produces realistic turbulent structures at the inlet plane and is the only way of allowing the LES method to capture the correct flow physics in the domain of interest [4].

According to Lund [108], the simplest approach for the generation of inflow data for wall-bounded flows is to use a fully developed "parallel flow" with streamwise and spanwise periodicity for the precursor simulation. An example of such practice was given by Kaltenbach [75]. The idea can be extended further for generation of inlet data for spatially developing boundary layer flows with the employment of a stress-free boundary condition for the upper boundary of the precursor simulation [107].

Despite the advantages of the method in terms of inflow data realism, the cost of an additional simulation remains a critical issue. With the adoption of periodic boundary conditions for the precursor simulation, the cost can be reduced but still, in many cases, it remains higher than other approaches discussed in the following sections.

1.4.3 Periodic boundary conditions

In flows that are fully developed, or take place in streamwise repeating geometries, the issue of generating inlet conditions is circumvented by the use of periodic boundary conditions, where information about the velocity field is taken from the outflow plane and is introduced to the inlet plane of the flow. As long as the length of the flow domain is larger than the largest anticipated flow structures, this method has the potential to provide realistic, self-sustained turbulent inflow conditions for a number of flows, where streamwise homogeneity exist. A number of researchers have successfully used this method, both in DNS and LES [78, 174]. However, for flows with no direction of statistical homogenity, or for non-periodic geometries, this method cannot be applied.

1.4.4 Spalart's method

Spalart [167] extended the idea of outlet/inlet linkage to a turbulent boundary layer simulation by using a coordinate transformation technique. The main advantages of the method are that it is capable of producing an equilibrium spatially evolving boundary layer with direct control of the momentum thickness and the skin friction coefficient [108]; Na and Moin [127] employed a similar procedure on DNS of attached and separated boundary layers. The method proved useful, although a development section was required for the cases of strongly sheared flow. Lund and Moin [107] used Spalart's method for a simulation of a boundary layer of a concave wall, observing no transient downstream of the inlet plane.

Despite its advantages, the method is complex and restricted to flows where mean streamwise variations are small compared with transverse variations. Lund et al. [108] presented a similar method for generating turbulent inflow data for the simulation of spatially developing boundary layers. Their approach was to recycle the turbulent velocity field to the inlet from predictions at a station near the domain exit after appropriate scaling. The method was applied successfully on a flat-plate boundary layer. Unfortunately, this method relies on self-similarity assumptions and can introduce same spurious couplings inside the flow domain [155].

Spille-Kohoff and Kaltenbach [170] proposed an improved method, which uses a buffer region near the inlet plane, where body forces are applied in order to produce the target profiles of the velocity field at a location further downstream. The body forces required are calculated using closed-loop control theory and the method has the potential to reproduce both single and two-point statistics and integral properties of the boundary layer.

1.4.5 The signal superposition method

A large number of algorithms for the generation of unsteady inflow conditions for DNS and LES is based on the superposition of a disturbance signal on a time or/and spatially averaged velocity profile, as described by Eq.1.65.

$$\vec{u}\left(\vec{x},t\right)=\left\langle u\left(\vec{x}\right)\right\rangle +u^{'}\left(\vec{x},t\right) \tag{1.65}$$

where $\left\langle u\left(\vec{x}\right)\right\rangle$ is a time-averaged profile and $u^{'}\left(\vec{x},t\right)$ is the disturbance signal.

The disturbance can be a white noise signal that can be adjusted to produce the desired set of one-point, second-order statistics. However, the lack of any phase information results in incorrect higher order correlations and hence, unrealistic flow structures. As a consequence, the single and two-point correlations are not reproduced correctly and a rapid decay of the input disturbance can be observed [94, 110].

The inability of white noise to generate a realistic turbulent field led researchers to more sophisticated approaches for the generation of the disturbance signal. Lee et al. [94] generated the disturbance signal by making use of a prescribed energy spectrum and a time varying function in order to produce non periodic inflow conditions. However, the application to turbulent flows did not give satisfactory results. Le et al. [93] extended the idea by superimposing fluctuations with given second moments and spectral shape onto a mean velocity profile and applied this method to a backward facing step flow simulation. It was found that this method was not very satisfactory as the turbulence level still decayed rapidly.

Based on the observation that different turbulence scales are present in the inner and outer part of a turbulent boundary layer, Yao and Sandham [192] proposed a method, where two disturbance signals are produced for different regions of the flow. Both signals were given by products of exponential and trigonometric functions of wall distance, desired wave numbers and phase shifts.

Klein et al. [82] have recently developed a promising method. According to this approach, a digital filtering procedure is employed to generate velocity time series at each point in the inlet (Digital Filter Generator - DFG); these manipulated time series reproduce pre-specified first and second moment single point statistics as well as a locally prescribed autocorrelation function. Turbulence length (or time) scales are used as input to make the non-dimensional assumed shape of the autocorrelation function dimensional at each point. Klein et al. have demonstrated their DFG procedure in two test cases: DNS of a plane turbulent jet and 2D DNS of the primary break up of a liquid jet. The method seems flexible as it does not suffer from any restrictions regarding the nature of the flow considered.

Recently, Batten et al. [14] proposed a new method to generate synthetic inflow turbulence based on the superposition of sinusoidal modes with random frequencies and wave numbers, constructing a field with given moments and spectra. Keating and Piomelli [77] applied this method to a spatially developing duct flow and a boundary layer on a flat plate. Their study showed that the method proposed by Batten et al. does display advantages over other methods based on random number sequences. However, a relatively long transition distance was still required for the turbulence structure in the inlet profile to become self-consistent.

Furthermore, Druault et al. [45] have employed Proper Orthogonal Decomposition [103], POD, and Linear Stochastic Estimation [2], LSE, to generate realistic unsteady velocity profiles, based on experimental data and correlation functions. According to this method, the velocity field comprises of the time-averaged component, $\langle u(\vec{x})\rangle$, the coherent fluctuation component, $\hat{u}(\vec{x},t)$, and the incoherent fluctuation component, $u'(\vec{x},t)$, as described by Eq.1.66.

$$\vec{u}\left(\vec{x},t\right) = \left\langle u\left(\vec{x}\right)\right\rangle + \hat{u}\left(\vec{x},t\right) + u^{'}\left(\vec{x},t\right) \tag{1.66}$$

The method was applied on 2D plane mixing layer at low and high Re and the results indicated that the generated data corresponded to real turbulent flow from the inlet plane with no transitional distance required. However, the necessity and the cost of producing the experimental data required to obtain $\hat{u}\left(\vec{x},t\right)$ can be an issue.

With the recent developments in the field and the increased level of sophistication introduced in the generation of the disturbance signal, the signal superposition method has shown that it has the potential to produce realistic turbulent inflow conditions. The cost for most of the algorithms is less than a precursor simulation and in addition, there is the possibility to have direct control over a number of important flow parameters.

1.5 Aims and objectives of this study

Section 1.1 indicated that the study of wall-bounded flows is very important as they are present in the majority of the engineering applications. A brief description of the structure and the dynamics of the flow as it passes over a solid surface indicated a variety of phenomena that need to be accounted for. Turbulence scales and variations of the characteristics of the flow from one region to another, made clear the challenges for any attempt to simulate accurately these effects.

In section 1.2, LES was presented as one of the relatively new numerical techniques that has the potential to provide a useful tool for the prediction and study of wall-bounded flows. Referring to the governing equations of this technique, the filtered NS equations, it was shown that there are two factors that can be very important for the accuracy and the cost of every LES; the modelling of the subgrid scale stress term and the inlet boundary conditions.

Section 1.3 presented the basic ideas that support SGS modelling and the main four schools of thought. It was shown that models based on resolved scales are lacking in generality and can introduce non-physical behaviour in parts of the flow. The dynamic procedure discussed at the end of this section indicated a way to improve such models and make them more generally applicable. As far as scale similarity models is concerned, despite their improved physical behaviour, they do not produce enough dissipation and therefore, practice has shown that they can perform well when combined with models based on resolved scales. Models based on energy at the cutoff scale can perform well in spectral space, but when extended to physical space, difficulties arise related to the computation of the cutoff energy. Models based on the subgrid scales seem to have a direct connection with the phenomena that take place beyond the cutoff length. Difficulties in calculating the correct behaviour of SGS variables do exist but, when overcome, the resulted models can be more accurate, theoretically, because they use information directly from these scales.

Another major factor for the LES accuracy of many flows, namely the inlet boundary conditions, was discussed in section 1.4. Five different approaches were presented, reflecting the methodology of majority of the work that has been done in the field. A common characteristic of all the techniques is a trade off between realism of the produced data and computational cost. As it was discussed, algorithms based on disturbance superposition upon a time-averaged signal have the potential to produce realistic turbulent velocity fields with prespecified characteristics in terms of first and second order statistics. This feature can be particularly useful for engineering applications, where the flow downstream can be significantly affected.

Considering the issues presented and discussed in these sections, the aim of this study is:

> To explore the possibilities of improvement of SGS modelling and inlet boundary conditions for LES of wall-bounded flows.

More specifically, the two major tasks involved are:

1. The investigation of the potential of SGS models based on the information estimated from the subgrid scales.
2. The identification and development of a cost effective algorithm for the generation of realistic inflow boundary conditions.

The first task requires the formulation and implementation of a transport equation model, which will make use of transport equations in order to solve directly for a SGS variable of interest. A good candidate for such a variable could be the subgrid scale kinetic energy since it can provide a representative velocity scale of the subgrid scales. Although in a number of works k_{sgs} is approximated by the employment of a double filtering operation on the velocity field, the computed variable might not be representative, due to the modification of the energy spectrum because of the filtering operation [139]. A typical example is the case where a box filter is employed and the simulation is performed in the physical space. A more reliable method, which is not affected to the same extent by the filtering operation, is the solution of the transport equation of k_{sgs}. A transport equation for another variable such as ε could also be used but the number of terms to be modelled in that case, would be larger, compromising the accuracy and generality of the model. Therefore, alternative formulations should be explored that could potentially alleviate such issues. Furthermore, the particular interest of this study to wall-bounded flows imposes one more requirement related to the SGS modelling. The models considered have to account for the flow phenomena in the near-wall region.

Finally, the models under investigation have to be tested on wall-bounded flow cases that will be able to show any differences from others in terms of the accuracy of the computed flow field. Considering these issues, the following objectives have to be met:

1. Implementation of a transport equation model that allows for near-wall effects.
2. Exploration of alternative SGS model formulations and investigation of their potential to improve the accuracy of LES of wall-bounded flows.
3. Testing and comparison of the implemented models with others on a number of flow cases that will indicate the advantages and disadvantages of their use.

As far as the generation of inlet conditions is concerned, an algorithm of the signal superposition method should be employed, as this approach seems to have certain advantages over the others, especially for wall-bounded flows and applications of industrial interest, where computational cost is a critical factor and control over some inlet flow parameters is desired.

A critical study related to the performance of the algorithm has to be carried out and any areas, where further improvement is possible, have to be identified. Application and testing of the resulted method has to follow, in order to access the importance of the new features. Therefore, the objectives are:

1. Identification of an appropriate method
2. Identification and development of areas where further improvement is possible.
3. Testing and comparison of the original and final method.

The rest of this thesis describes the work that has been done in order to achieve the aim of this study and meet the objectives set. In the second Chapter, the reader will go through a detailed description of the models used for the present study; namely the Smagorinsky model, the Mixed Scale model proposed by Sagaut and the k_{sgs}-equation model. A review of near-wall treatment is also be given. Chapter 3 describes in detail the code development required for the introduction of the SGS models used in the present study. Furthermore, the formulation of a new SGS model is presented, introducing a new approach to SGS modelling. Chapter 4 presents a comparative study of the models implemented, on a series of channel flow test cases. This study continues to Chapter 5, where the application of Smagorinsky and k_{sgs}-equation model on the ERCOFTAC wing-body junction case is described, followed by a detailed discussion. Chapter 6 presents the work that was performed on the implementation, development and testing of an algorithm for the generation of unsteady inlet data. Finally, the conclusions of this work as well as suggestions for future studies are given in chapter 7.

Chapter 2

Subgrid Scale Models

2.1 The Smagorinsky model

The most widely used model based on the resolved scales was formulated by Smagorinsky [163] back in 1963. Using the Boussinesq assumption, it expresses the subgrid scale viscosity ν_t as:

$$\nu_t = l^2 \overline{S} = \left(C_s \overline{\Delta}\right)^2 \overline{S} \tag{2.1}$$

where l is the length scale, an idea based on Prandtl's mixing length hypothesis. l is given by the product of the Smagorinsky constant C_s and the filter width $\overline{\Delta}$. $\overline{S}$ is the characteristic filtered rate of strain given by

$$\overline{S} \equiv \left(2\overline{S}_{ij}\overline{S}_{ij}\right)^{1/2} \tag{2.2}$$

The Smagorinsky model can be formulated by many approaches: heuristically, from the application of the equilibrium hypothesis to the dynamic equations for the SGS stresses, or from various turbulence theories such as the Renormalisation Group, RG, theory [190], or from the adaption of the equilibrium hypothesis, the assumption of homogeneous and isotropic flow and the assumption of the Kolmogorov energy spectrum. Hence, it is no surprise that the Smagorinsky model does not perform well in cases, where these assumptions do not apply.

Pope [146] points out the importance of both the flow *Re* and the filter length used, for the performance of the model. When the model is applied to high *Re* cases, the cutoff length is located at the inertial subregion of the spectrum, where there is an equilibrium between turbulence production and dissipation and hence, the assumption made in the derivation of the model is indeed valid. In low *Re* cases however, the filter may lay in the region of the spectrum where there is an overlap between the energy-containing and dissipative scales. In this case, the equilibrium hypothesis could fail, resulting in a degraded performance of the model.

There are three major issues with the model. The first is the value of the constant C_s. As discussed in section 1.3.2, there are many different ways to calculate C_s, giving a range of values. Unless $\overline{\Delta}$ is contained well inside an ideal inertial range of isotropic and homogeneous turbulence, C_s cannot be universal for all flows [118]. The importance of this observation became clear from the first applications of the model. Deardorf [28] employed the Smagorinsky model for an LES calculation of a fully turbulent channel flow. In order to avoid the excessive damping of turbulent fluctuations, instead of the theoretical value of $C_s = 0.17$ (see section 1.3.2 for the derivation of this value), a lower value of 0.1 was adopted. However, a priori testing of the model on homogeneous turbulence, performed by McMillan and Ferziger [115], indicated that the best correlation achieved between Smagorinsky and DNS predicted τ^r_{ij} was with $C_s = 0.17$. That was an indication of the validity of the assumptions made by Lilly [100] in the derivation of this value for C_s, for this flow case. In a channel flow, where shear and flow anisotropies are present, Moin and Kim [123] adopted the van Driest damping function [181], to be discussed in detail in section 2.4.2, in an effort to reduce the near-wall eddy viscosity. From these applications and many others, it was realised that some flow features such as shear or anisotropy can have a significant effect on C_s. Although this behaviour of C_s has not been fully understood, it is believed that it is related to the increase of backscatter of energy in flows with mean shear or strain [116].

The second issue is the selection of the length scale. Ferziger suggests [48] that the length scale should be of the form:

$$l = \left(L\overline{\Delta}^2\right)^{1/3} \tag{2.3}$$

where L is the turbulence integral length scale. However, the difficulty in obtaining L has led to the use of $C_s\overline{\Delta}$ as the representative length scale.

In the case of an isotropic filter, applied in isotropic flows, the representation of l by $C_s\overline{\Delta}$ may be adequate. However, in anisotropic flows the choice of the length scale becomes a much more complicated issue. Although an adjustment of C_s can in some cases resolve the problem, this is not always possible. A classic example is the application of the model to wall-bounded flows. In such flows, the flow structures in the near-wall regions tend to be very anisotropic, and hence, the choice of a representative length scale is much less clear.

In practical LES, it is very common to use anisotropic grids, in order to achieve higher refinement in particular regions. If implicit filtering is used, the filter is going to be an anisotropic box filter. Scotti et al. [160] showed that for such a case, $\overline{\Delta}$ should be based on the cell volume as:

$$\overline{\Delta} = (\Delta x \Delta y \Delta z)^{1/3} \tag{2.4}$$

where $\Delta x, \Delta y$ and Δz is the size of the cell in the corresponding direction. It is worth noting that Eq.2.4 is the same as that proposed empirically by Deardorff [29] back in 1974.

Another proposal for the calculation of $\overline{\Delta}$ was made by Unger and Friedrich [180], in an effort to take into account the variation of the representative length scale in the near-wall region of wall-bounded flows. According to this approach, $\overline{\Delta}$ is computed as:

$$\overline{\Delta} = min\left(\frac{\kappa_{vK} y}{C_s}, (\Delta x \Delta y \Delta z)^{1/3}\right) \tag{2.5}$$

where κ_{vK} is the von Karman constant and y is the distance from the wall.

The adoption of $\kappa_{vK} y$ as a length scale in the near-wall region resulted from the experimental studies of Nikuradse [129], who observed the presence of such scales in this region. This formulation was used for a pipe flow simulation [180]. However, Friedrich and Nieuwstadt [51] reported that this formulation failed to reproduce the experimental results due to the inability of the model to represent accurately the energy transfer mechanisms near the wall. Other formulations have also been proposed [155] but they have not been used as much.

The introduction of the dynamic procedure alleviated the problems related to the length scale definition, increasing even more the popularity of Smagorinsky model. Apart from the pioneers of the method, already mentioned in section 1.3.7, a large number of researchers used the dynamic procedure, in low and high Reynolds numbers, with fine or coarse grids

[128, 156, 109]. A general trend of these studies is that the use of the model decreased the wall stress . In low Re, the grid spacing is very important for the capturing of the turbulence production mechanisms. In high Re, the dynamic procedure is affected by the numerical implementation and the grid size [109].

The third issue of the Smagorinsky model is related to the physical realisability. As pointed out in section 1.3.2, the model produces non-zero values of ν_t, even in laminar, fully resolved flows.

Furthermore, its action is purely dissipative. This can be demonstrated by considering the SGS turbulence production, given by:

$$Pr \equiv -\tau_{ij}^{r}\overline{S}_{ij} \tag{2.6}$$

Using the Smagorinsky model formulation of τ_{ij} in Eq.2.6 gives:

$$Pr \equiv -\tau_{ij}^{r}\overline{S}_{ij} = 2\nu_t\overline{S}_{ij}\overline{S}_{ij} = \nu_t\overline{S}^2 \tag{2.7}$$

Eq.2.7 shows that the production term is always positive, indicating no capability for the prediction of backscatter.

This purely dissipative behaviour becomes more pronounced in cases of inhomogeneous and transitional flows, where decreased values of C_s are usually employed in order to improve the results. In wall-bounded flows, while τ_{ij}^{r} should drop to zero at the wall as y^3, the Smagorinsky predicted τ_{ij}^{r} remains finite due to the presence of the mean shear, requiring some short of near-wall damping. The ability of the dynamic procedure to automatically adjust this value according to the flow conditions, is the main reason for its success.

In addition to the features described above, another shortcoming related to physical realisability of the model is the poor correlation of τ_{ij}^{r} and $\overline{S}_{ij}$, described in section 1.3.6. This comes in contrast with the Smagorinsky formulation that suggests that the two tensors are almost perfectly correlated.

Despite the shortcomings, the Smagorinsky model has been widely used in a number of flow cases due to its simplicity and numerical robustness [118]. The model was also used in the present study for comparison purposes.

2.2 The Mixed Scale model

The Mixed Scale model, MS, was proposed by Sagaut [154]. The development of the model was based on two fundamental constraints; one imposed by the physics of turbulence and one by the numerics. The physical constraint would ensure that the model would obey the Galilean invariance, produce zero τ_{ij}^{r} when the exact solution exhibits no scales corresponding to subgrid scales, generate the same effect as the term it models and finally does not affect adversely the dynamics of the resolved scales. The numerical constraint would make sure that the model would not be inhibited by discretisation errors, would not destabilise the simulation and that its numerical implementation would not increase significantly the computational cost [154].

Taking into account the shortcomings of the models based solely on the resolved scales, and the fact that models, which make use of information from the subgrid scales, can fulfill all the requirements imposed by the physical constraints, Sagaut proposed a mixed scale formulation for ν_t. In an attempt to take into account the effect of both the filtered flow field and the energy content of the subgrid scales, the MS model computes the eddy viscosity using a weighted geometric mean of the velocity scales generated by these two factors. The resulted formulation reads as:

$$\nu_t = C_m \left|F\left(\bar{u}_i\left(\vec{x},t\right)\right)\right|^{\alpha} \left(k_{sgs}\right)^{\frac{1-\alpha}{2}} \overline{\Delta}^{1+\alpha} \tag{2.8}$$

where C_m is the model coefficient and α is a constant, which controls the weighting of the scales. $F\left(\bar{u}_i\left(\vec{x},t\right)\right)$ is either $\overline{S}$ or $\nabla \times \bar{u}_i\left(\vec{x},t\right)$.

C_m can be evaluated theoretically by analytical theories of turbulence for homogeneous isotropic case. Sagaut [155] suggests that:

$$C_m = 0.2^{1-\alpha} C_s^{2\alpha} \tag{2.9}$$

where C_s is the Smagorinsky constant, evaluated theoretically in section 1.3.2.

Instead of using the transport equation of k_{sgs}, Sagaut approximated the value of k_{sgs}, using a double filtering procedure, as:

$$k_{sgs} \simeq \frac{1}{2} \left(\bar{u}_i\left(\vec{x},t\right)\right)' \left(\bar{u}_i\left(\vec{x},t\right)\right)' \tag{2.10}$$

where $\left(\bar{u}_i\left(\vec{x},t\right)\right)'$ is is given by:

$$\left(\bar{u}_i\left(\vec{x},t\right)\right)' = \bar{u}_i\left(\vec{x},t\right) - \tilde{\bar{u}}_i\left(\vec{x},t\right) \tag{2.11}$$

In Eq.2.11 , the tilde symbol designates the test filter.

Eq.2.11 shows that $\left(\bar{u}_i\left(\vec{x},t\right)\right)'$ represents the high frequency component of the resolved velocity field and is defined using a second filter, the so called test filter. This approximation is based on the same idea that scale similarity models used, described in section 1.3.6.

It is worth noting that different values of the constant α result in different models. $\alpha = 0.0$, gives the k_{sgs}-equation model given by Eq.1.48, if the value of k_{sgs} evaluated by the transport equation is used instead of the approximation suggested by Sagaut. $\alpha = -1.0$ gives the hybrid k_{sgs}/Smagorinsky model and $\alpha = 1.0$ results in the Smagorinsky model.

Sagaut applied the model to a backward facing step 2D flow simulation with $\alpha = 0.5$ [154]. In two test cases, with different values of C_m, it was found that with $C_m = 0.1$ the model generated a flow field in good agreement with the experimental data by Eaton and Johnston [47], both qualitatively and quantitatively. Some discrepancies in the prediction of longitudinal turbulent intensity were attributed to the fact that the simulation was 2D and therefore, some k_{sgs} redistribution mechanisms were not captured at all.

In the development of the MS model, the flow was assumed to be turbulent, fully developed and isotropic. In order to improve the model performance in flow cases that depart from these conditions, two techniques were adopted. The selective function and the accentuation technique proposed by Ducros [46]. The selective function, also known as structural sensor, checks the structural properties of the test field $\left(\bar{u}_i\left(\vec{x},t\right)\right)'$ and turns the model off when these do not correspond to a fully turbulent field. Regarding the accentuation technique, the subgrid scale viscosity is evaluated using a modified flow field, obtained from the resolved flow field through the use of a high-pass filter, which magnifies the contribution of the highest resolved frequencies [154].

In a comparative study of self-adaptive SGS models on wall-bounded flows, Sagaut [156] studied the MS model with these two techniques. The results indicated that the selective function implementation of the model was sensitive to the grid resolution and the flow Re, especially regarding the near-wall behaviour. The Ducros filtering procedure was not that sensitive either to the grid or the Re. The results were better when a coarser grid was used but overall the performance was inferior to that obtained when a selective function was used.

More recently, Yoshizawa et al. [196] used the MS model with $\alpha = -2.0$ and a near-wall damping function, to be discussed in section 2.4.2, in order to achieve the correct near-wall behaviour. The model performed well in channel flows of $Re_\tau = 180$ and $Re_\tau = 395$, where Re_τ is the Reynolds number based on u_τ. Finally, Tsubokura [179] used the MS model with $\alpha = -1.0$, resulting in a formulation independent of $\overline{\Delta}$.

2.3 The k_{sgs}-equation model

The k_{sgs}-equation model is a one transport equation model that solves explicitly the transport equation of k_{sgs} and uses this information to obtain a subgrid velocity scale for the formulation of ν_t, which is computed as:

$$\nu_t = C_\mu \overline{\Delta} \sqrt{k_{sgs}} \tag{2.12}$$

As discussed in section 1.3.4, a number of terms of the exact transport equation have to be modelled. Using the approach introduced in section 1.3.4, the modelled transport equation for k_{sgs} reads:

$$\frac{\partial k_{sgs}}{\partial t} + \frac{\partial \overline{u}_j k_{sgs}}{\partial x_j} = -\tau_{ij}\overline{S}_{ij} - C_1 \frac{k_{sgs}^{3/2}}{\overline{\Delta}} + C_2 \frac{\partial}{\partial x_j}\left(\overline{\Delta}\sqrt{k_{sgs}}\frac{\partial k_{sgs}}{\partial x_j}\right) + \nu \frac{\partial^2 k_{sgs}}{\partial x_j \partial x_j} \tag{2.13}$$

In Eq.2.13,

$+\frac{\partial \overline{u}_j k_{sgs}}{\partial x_j}$ (Term 1) is the advection by the resolved modes

$-\tau_{ij}\overline{S}_{ij}$ (Term 2) is the production by the resolved modes

$-C_1 \frac{k_{sgs}^{3/2}}{\overline{\Delta}}$ (Term 3) is the turbulent dissipation

$+C_2\frac{\partial}{\partial x_j}\left(\overline{\Delta}\sqrt{k_{sgs}}\frac{\partial k_{sgs}}{\partial x_j}\right)$ (Term 4) is the turbulent diffusion

$+\nu\frac{\partial^2 k_{sgs}}{\partial x_j \partial x_j}$ (Term 5) is the dissipation due to viscous effects and

C_μ, $C_1$and C_2 are coefficients that have to be computed.

The model, as described by Eq.2.13, was originally used for LES by Schumann [158], who applied it to plane channel and annuli flow. Schumann used a splitting method for the isotropic and anisotropic part of the SGS stresses, modelling the first by the k_{sgs}-equation model and the latter by the mixing length model. As far as the boundary conditions at the wall, he employed the log-law for the calculation of velocities at this flow region. The results of this approach were satisfactory, indicating independence of the grid resolution and anisotropies. Similar quality of the predicted flow field had been obtained by Deardorff [28], in the first effort to calculate a channel flow, using the Smagorinsky model. However, Yoshizawa and Horiuti [195] pointed out that both models gave approximately the same results due to the treatment of the near-wall region. In both cases, this region was not resolved properly and the log-law was imposed instead of the no-slip condition. Hence, the area, where the equilibrium hypothesis breaks down was not considered properly and therefore the advantage of the k_{sgs}-equation model was not pointed out.

Deardorff [30] used the model for a channel flow, in order to decrease the complexity and cost of the model he proposed a few years earlier [29], based on transport equations for τ_{ij}^{r}. However, he made use of a modified length scale definition, instead of Eq.2.4, in the formulation of ν_t and ε, in order to improve the representation of subgrid scales in stably stratified regions. Furthermore, he was the first to model Term 4 as:

$$\text{Term 4} = 2\nu_t\frac{\partial k}{\partial x_j} \tag{2.14}$$

implying that $C_\mu = 0.5C_2$. Moeng [122] worked also with this model, on the same case as Deardorff, but employing a mixed pseudo-spectral finite difference method in order to take advantage of the speedup provided by the fast Fourier transform algorithm.

Yoshizawa and Horiuti [195] used the Direct Interaction, DI, theory [193, 194] to derive the k_{sgs}-equation model and the values of the constants C_μ, $C_1$and C_2. In their derivation, an extra term is present, related to the anisotropic part of the SGS stress tensor. Horiuti [66] used this model without the extra term, in combination with no-slip boundary conditions at the wall, for a channel flow at $Re = 27,550$. The Smagorinsky model was also employed for comparison purposes. The results of the two simulations indicated little difference in terms of the mean flow quantities. However, in terms of the turbulence intensities and the flow behaviour in the near-wall region, where the equilibrium hypothesis breaks down, the superiority of the k_{sgs}-model was clear. The dissipative nature of the Smagorinsky model resulted in an over-prediction of mean spacing between the flow streaks formed next to the wall.

More recently, Dejoan [31] used the k_{sgs}-equation model of Hassid and Porch [65] in order to explore the behaviour of a transport equation model on an unsteady turbulent channel flow and compared it with the Smagorinsky model. In this form of the model, the length scale in the formulation of ν_t was given by Eq.2.15.

$$l_{sgs} = \left[\Pi\left(\Delta_m, l^*\right)\right]^{1/3} \tag{2.15}$$

where $l^* = 0.1\delta/C_s$ for $y \leq 0.1\delta/\kappa_{vK}$ and $l^* = \kappa_{vK}y/C_s$ for $y \geq 0.1\delta/\kappa_{vK}$ and Δ_m denotes the filter length in the m direction. Furthermore, a form of damping function in terms of the turbulent Reynolds number Re_t, was employed for ν_t and ε.

In this work [31], Dejoan and Schiestel showed that while in plane channel flow the behaviour of the two models was similar, when applied to a turbulent pulsed flow in a plane channel, the performance of the k_{sgs}-equation model was superior. The phase-shifts linked to the lag effects produced by unsteadiness were much better captured by the transport equation model and this was due to the ability of the model to incorporate turbulence history effects.

Comparing to zero equation models such as the Smagorinsky model, the k_{sgs}-equation model can introduce the turbulence history effect in the calculation of ν_t, and theoretically it has the potential for a more accurate representation of this parameter as it uses directly subgrid scale quantities. One of the most important advantages however, is its ability to provide a formulation of ν_t without the use of the assumption that the rate of dissipation of k_{sgs} is equal to the production of the turbulent kinetic energy at the cut off scales.

2.3.1 The dynamic procedure and the k_{sgs}-equation model

In recent years, there is an effort to combine the advantages of the k_{sgs}-equation model with the dynamic procedure. This is because the k_{sgs}-equation model involves the specification of at least two coefficients; C_μ and C_1. This is the case if an equation of the form of Eq.2.14

is adopted for the turbulent diffusion term in the modelled equation for k_{sgs}. Otherwise, C_2 has also to be computed. The use of the dynamic procedure can alleviate this problem as it can be used to calculate dynamically both C_μ and C_1.

The first formulation for a dynamic k_{sgs}-equation model was presented by Wong [188], who used the Multi-scale Statistical Dynamic, MSD, closure method to obtain dynamically C_μ for linear and non-linear eddy viscosity SGS models with or without a transport equation for k_{sgs}. The method is in-line with that proposed by Germano and Lilly, with the main difference being that v_t is expressed in terms of k_{sgs}, according to Eq.2.12. Hence, τ_{ij} and T_{ij} become:

$$\tau_{ij} = \frac{2}{3}\delta_{ij}k_{sgs} - 2C_\mu\overline{\Delta}\sqrt{k_{sgs}}\,\overline{S}_{ij} \tag{2.16}$$

$$T_{ij} = \frac{2}{3}\delta_{ij}K - 2C_\mu\widetilde{\overline{\Delta}}\sqrt{K}\,\widetilde{\overline{S}}_{ij} \tag{2.17}$$

where $K = T_{kk}/2$.

For the calculation of C_1, Wong defines ε and the dissipation rate of K, ε_T, as follows:

$$\varepsilon \equiv \nu\left(\overline{\frac{\partial u_i}{\partial x_j}\frac{\partial u_i}{\partial x_j}} - \frac{\partial \overline{u}_i}{\partial x_j}\frac{\partial \overline{u}_i}{\partial x_j}\right) = C_1\frac{k_{sgs}^{3/2}}{\overline{\Delta}} \tag{2.18}$$

$$\varepsilon_T \equiv \nu\left(\widetilde{\overline{\frac{\partial u_i}{\partial x_j}\frac{\partial u_i}{\partial x_j}}} - \frac{\widetilde{\partial \overline{u}_i}}{\partial x_j}\frac{\widetilde{\partial \overline{u}_i}}{\partial x_j}\right) \simeq C_1\frac{K^{3/2}}{\widetilde{\overline{\Delta}}} \tag{2.19}$$

Then, by subtracting Eq.2.18 from Eq.2.19, the following expression is deduced:

$$\frac{C_1}{\overline{\Delta}} \simeq \frac{\nu\left(\widetilde{\frac{\partial \overline{u}_i}{\partial x_j}\frac{\partial \overline{u}_i}{\partial x_j}} - \frac{\widetilde{\partial \overline{u}_i}}{\partial x_j}\frac{\widetilde{\partial \overline{u}_i}}{\partial x_j}\right)}{\left(\frac{\overline{\Delta}}{\widetilde{\overline{\Delta}}}K^{3/2} - \widetilde{k_{sgs}^{3/2}}\right)} \tag{2.20}$$

Ghosal et al.[58] proposed a dynamic k_{sgs}-equation model that used the constrained localised dynamic procedure to calculate C_μ and an extended form of this procedure to compute C_1 and C_2 of Eq.2.13. The constrained localised form of the dynamic procedure differs from that described in section 1.3.7 in the final step of the computation of the model constant.

According to the Germano-Lilly approach [55, 101], the model constant is computed to fulfill Eq.1.61 using the least square approach. Ghosal et al. [58] proposed a formulation that employs a Fredholm's integral equation for this calculation, in order to avoid the mathematical inconsistency introduced by the least square approach. Unfortunately this method still raises some stability issues that require the value of C_μ to be always positive. Furthermore, the solution of Fredholm's integral equation increases the computational cost of the method.

Ghosal et al. [58] applied the model on an LES of decaying turbulence behind a grid, obtaining accurate results in terms of energy decay and energy density distribution.

Menon and Kim [120] applied a similar approach, where C_μ was given by:

$$C_\mu = \frac{\sigma_{ij} L_{ij}}{\sigma_{ij}\sigma_{ij}}, \text{ where } \sigma_{ij} = -\tilde{\overline{\Delta}} K^{1/2} \tilde{\overline{S}}_{ij} \tag{2.21}$$

and C_1 by:

$$\frac{C_1}{\tilde{\overline{\Delta}}} \simeq \frac{(\nu + \nu_t)\left(\widetilde{\frac{\partial \overline{u}_i}{\partial x_j}\frac{\partial \overline{u}_i}{\partial x_j}} - \widetilde{\frac{\partial \overline{u}_i}{\partial x_j}}\,\widetilde{\frac{\partial \overline{u}_i}{\partial x_j}}\right)}{K^{3/2}} \tag{2.22}$$

The model was used in high Reynolds number flows as well as in wall-bounded flows such as turbulent plane Couette flows, recirculating and separated flows, giving results in good agreement with experimental data [88].

Another implementation of the idea of a dynamic k_{sgs}-equation model was due to Davidson [26], who used the standard dynamic procedure for the calculation of C_μ and the assumption that the transport of k_{sgs} and K are the same, to obtain the following expression for C_1:

$$C_1^{n+1} = \left(Pr_K - \widetilde{Pr}_{k_{sgs}} + \frac{1}{\overline{\Delta}} \widetilde{C_1^n k_{sgs}^{3/2}}\right) \frac{\tilde{\overline{\Delta}}}{K^{1/2}\widetilde{k_{sgs}}} \tag{2.23}$$

where Pr_K is the production of K $(= -2C_1\tilde{\overline{\Delta}}K^{1/2}\widetilde{\overline{S_{ij}}})$ and $Pr_{k_{sgs}}$ is the production of k_{sgs}.

The interesting point in his implementation of the model was the use of C_μ. For the momentum equations, a constant value in space was employed, in order to achieve numerical stability. This value was computed by requiring that the SGS turbulence production would remain the same. In the k_{sgs} equation, however, the local value of C_μ calculated by the dynamic procedure, was used. Hence, all the local dynamic information was introduced in the system of equations through the production term of k_{sgs}.

The model was applied to a wall jet flow and it was soon realised that clipping of C_1 was necessary. This was due to the oscillatory behaviour of the coefficient, attributed to the formulation of Eq.2.23, which introduced positive feedback and hence unstable behaviour [26]. Therefore, Davidson proposed a modified expression for C_1:

$$C_1^{n+1} = \left(Pr_K - \widetilde{Pr}_{k_{sgs}} + \frac{1}{\Delta} \widetilde{C_1^n k_{sgs}^{3/2}} \right) \frac{\tilde{\bar{\Delta}}}{K^{3/2}} \tag{2.24}$$

This model was used successfully in a number of cases, such as flow around a surface mounted cube and a square cylinder by Krajnovic and Davidson [85, 86] and Sohankar et al. [166, 165].

When compared with the dynamic models proposed by Germano [55] and Ghosal [58], this formulation has the following advantages:

1) It is capable of predicting backscattering.

2) The local dynamic coefficients can be used. Note that in Germano model, the dynamic coefficients have to be clipped and/or averaged in homogeneous directions.

3) Dynamic k_{sgs}-equation models can be cheaper due to their numerical stability.

Krajnovic [88] used both the Menon and Kim model and the Davidson model in a recirculating flow around a surface mounted cube. The results indicated an improvement over the prediction with no SGS model and a higher sensitivity of the Menon and Kim model, to the grid refinement.

Finally, more recently, Krajnovic and Davidson [87], developed a mixed model based on the dynamic k_{sgs}-equation model of Davidson. The modelled equation of k_{sgs} was derived, taking into account the mixed model formulation, and the result was the presence of some additional scale-similarity terms. The model was applied to a fully developed channel flow and to a flow around a surface mounted cube, producing accurate results. In all the cases studied, it was observed that the scale similarity part of the SGS stress tensor was larger, limiting the adverse effects of any incorrect assumptions made during the formulation of the eddy viscosity part [87].

2.4 Near-wall treatment

The presence of a solid surface affects a LES of the flow of interest in two ways. Firstly, it raises the issue of grid refinement in the near-wall region, in order to capture all the flow mechanisms present in the region. Secondly, it introduces some further parameters to be considered, in relation with the SGS modelling adopted. The following overview aims to present the most widely used approaches to these issues, with particular interest to those used in the present study. For a more detail presentation, the reader can refer to [146, 155].

2.4.1 LES in near-wall region

LES of wall-bounded flows can be divided into two major groups [146]. If the grid employed is fine enough to be able to resolve the near-wall motions, then the result is LES with near-wall resolution, or LES-NWR. In boundary layer type flows, the near-wall region is of great importance as turbulence production, dissipation, kinetic energy and Reynolds stress anisotropies all achieve their peaks within 15 to 20 viscous length scales δ_ν off the wall. Comparing to the flow length scale δ, δ_ν is small and decreases approximately by $\frac{\delta_\nu}{\delta} \approx Re^{-0.88}$ [146].

In order to resolve the near-wall motions, LES-NWR has to employ grids with grid spacing of the order of δ_ν near the wall. In practice , this is achieved by placing the first cell in the zone $y^+ < 1.0$ [155]. There have been numerous studies on the resolution required for capturing the turbulence production mechanisms in the near-wall region. Schumann [159] has suggested a resolution that gives $\overline{\Delta}x^+ < 10, \overline{\Delta}y^+ < 2, \overline{\Delta}z^+ < 5$ while Zang [197] has proposed a more relaxed limits at $\overline{\Delta}x^+ < 80, \overline{\Delta}y^+ < 10, \overline{\Delta}z^+ < 30$. Although these are just some examples and much coarser grids have been occasionally used [138], it becomes clear that for high Re, LES-NWR requires very fine grids that increase significantly the computational cost, up to an extent that in some cases the calculation is practically infeasible.

Therefore, an alternative approach is to model the influence of the near-wall motions and use a grid which is coarse and cannot resolve properly these motions. The result is LES with near-wall modelling, or LES-NWM. In LES-NWM, the grid spacing scales with δ and hence is independent of Re [146]. However, since the near-wall motions are not resolved, they have to be modelled.

LES-NWM makes use of a model that represents the dynamics of the flow in this region. This is called the wall model. Since the first interior point is away from the wall, at a distance larger than the characteristic scales of the near-wall motions, the non-slip condition cannot be used. Instead, the boundary conditions required for the numerical solution of the filtered NS equations will be provided by the wall model. In practice, the wall model provides either the second order derivatives and the wall normal velocity component or a value for the wall shear stress, which will correspond to the instantaneous velocity at the node nearest to the wall. These parameters are then used as boundary condition along with the impermeability condition [174]. The first approach was proposed by Deardorff [28] but, in the form presented by this author, suffers from two defects; the formulation of the second derivatives is not a function of *Re* and it is assumed that the shear-stresses in the near-wall region are solely due to SGS scales [155].

As far as the second approach is concerned, it allows for a much coarser grid, comparing with LES-NWR requirements and it is the one that is most widely adopted. Two different methods have been presented in literature related to this wall model approach. Both methods assume that the instantaneous near-wall velocity is in phase with the instantaneous wall shear stress. In the first method developed by Schumann [158], the wall shear stress is proportional to the instantaneous near-wall velocity, with the constant of proportionality being equal to the ratio of the time-averaged values of the two. The main disadvantage of this method is the requirement of statistical data that has to be computed by the calculation itself. Grotzbach [61] proposed a method to alleviate this problem by applying the log-law, given by Eq.1.14, and spatial averaging over the plane parallel to the wall. Rajagopalan and Antonia [151] proposed a modified version of the Schumann model, based on shifted correlations. This concept was also used by Piomelli et al. [140] in their proposed model, in combination with the log-law, to estimate the shear stresses.

The second method proposes the use of a wall law to directly relate the instantaneous velocity of the first node at the interior of the flow field to the instantaneous shear stress. This is a preferred approach for LES due to the unsteady nature of the flow field considered.

A typical example of the second method is the wall model proposed by Werner and Wengle [186]. Werner-Wengle WW, wall model is based on the assumption that a $1/7^{th}$ power law holds for the region outside the viscous sub-layer, interfaced with a linear profile in the viscous sub-layer. Hence

$$u_P^+ = \begin{cases} y_P^+ \text{ for } y_P^+ \leq 11.8 \\ 8.3\left(y_P^+\right)^{1/7} \text{ for } y_P^+ > 11.8 \end{cases} \tag{2.25}$$

where all symbols have their usual meaning and the subscript P denotes the value at the first point next to the wall.

WW model has been employed by a number of researchers for a variety of cases, including flow around a cube in a plane channel [186] and the flow in a channel with periodic constrictions [174]. Despite the fact that the model was developed on the assumption of a canonical turbulent boundary layer, it has performed well even in separated flows [174, 186]. Therefore, it was employed for a number of test cases performed for the present study. Details regarding the implementation of the WW model are given in section 3.2.4.

2.4.2 SGS modelling in near-wall region

The description of the dynamic processes in section 1.1.3 showed that the turbulence production in the near-wall region is associated with a backwards energy cascade. With the exception of the models that adopt the dynamic procedure, the rest of the SGS models considered cannot capture this backscattering. Numerically, backscattering is introduced by the computation of negative values for the eddy viscosity. Despite the fact that dynamic models allow for this, it has been reported [55] that sustained negative ν_t over large regions of the flow domain can lead to numerical instability. As a result clipping or imposing some limitations to the range of ν_t is adopted.

Apart from the presence of backscattering, the near-wall region imposes some extra difficulties. The flow is highly anisotropic, in many cases under-resolved, due to the small scales of the flow structures close to the solid boundary, and in a state of energy disequilibrium [155]. Hence, the models based on hypotheses that are not in-line with these conditions are expected to give compromised results. The dynamic procedure can enhance the performance of such models but in a considerable computational cost and with some numerical issues that require ad hoc modifications in many cases.

For the models that do not use the dynamic-procedure, a number of techniques have been developed to compensate for these issues, forming three main categories: a) the use of structural sensors b) the accentuation technique and c) the damping functions for the near-wall region. The accentuation technique gives rise to the filtered form of the models considered, and it was described along with the structural sensor approach in section 2.2. The third technique introduces a damping function in the formulation of ν_t.

The first effort to use damping function was due to van Driest [181]. Van Driest developed a form of the law of the wall as a function of the mixing-length, l_m, for the buffering region of a canonical turbulent boundary layer:

$$u^+ = \int_0^{y^+} \frac{2}{1 + \left[1 + 4 l_m^+ \left(y'\right)^2\right]^{1/2}} dy' \tag{2.26}$$

In Eq.2.26, the use of $l_m^+ = \kappa_{vK} y^+$, which is the appropriate mixing-length for the log-law region, would result in the wrong variation of the implied turbulent stresses [181]. Therefore, van Driest realised that a sort of damping would be required, in order to correct this behaviour. Hence, a damping function was developed that reads:

$$l_m^+ = \kappa_{vK} y^+ \left[1 - \exp\left(-y^+/A^+\right)\right] \tag{2.27}$$

Eq.2.26 and Eq.2.27 provide a continuous profile that covers all the parts of the inner boundary layer and provide an accurate prediction of the mean velocity profiles [181].

The van Driest damping function was employed on a number of SGS models to allow for an improved presentation of the turbulence length scale in the near-wall region. The Smagorinsky model was widely used in combination with van Driest damping on plane channel flows [66, 196] giving good results. In the Smagorinsky model, it is used for the calculation of the model constant C_s, in the following form:

$$C_s = C_{so}\left(1 - \exp\left(-y^+/A^+\right)\right) \tag{2.28}$$

where y^+ is the distance from the wall in viscous wall units and A^+ is a constant, is taken to be 26 [181].

Although effective, van Driest damping does not give the correct near-wall behaviour for ν_t. Therefore, Piomelli [144] suggested a modification of the damping factor according to

$$C_s = C_{so}\left(1 - \exp\left(-y^+/A^+\right)^3\right)^{1/2} \tag{2.29}$$

The modification given by Eq.2.29 gives $\nu_t \propto y^3$, which is the desired behaviour.

Both van Driest damping and Piomelli's formulation require the calculation of y^+, which introduces two issues. The first is that y^+ is not solely based on flow parameters but rather, uses the wall-normal distance y. This does not correspond to the flow physics since, in reality, the flow does not behave according to this geometric parameter but rather, according to the conditions that are formed at any location given by this parameter. Secondly, the computation of y can be problematic. In complex flow geometries the calculation of y can be an issue. Even in simple geometries, such as a duct, the computation of y in the corner regions can introduce some difficulties.

Therefore, researchers have introduced other formulations for near-wall damping functions, based solely on flow variables. Yoshizawa et al. [196] developed a function like this, based on dimensional analysis of the eddy viscosity. The final form of the function reads:

$$F_{wY} = 1 - \exp\left(-\left(C_w \frac{u_s}{\overline{S}\,\overline{\Delta}}\right)^2\right) \tag{2.30}$$

where $C_w = 21.0$ and u_s is the turbulence intensity.

Yoshizawa et al. used Eq.2.30 in combination with the MS model and applied it in plane channel flow at $Re_\tau = 180$, 395 and 590. Smagorinsky model with van Driest damping was also used for the same test cases for comparison purposes. The results indicated that the new formulation gave predictions of the same or better quality than the Smagorinsky model, without using y.

More recently, Inagaki et al. [68], taking into consideration the different time scales present in different regions of the flow developed a SGS model of the following form:

$$\nu_t = C_{MTS} k_{sgs} T_S \tag{2.31}$$

where $C_{MTS} = 0.05$ and T_s is the representative time scale, given by:

$$T_s^{-1} = \left(\frac{\overline{\Delta}}{\sqrt{k_{sgs}}}\right)^{-1} + \left(\frac{C_T}{\overline{S}}\right)^{-1} \tag{2.32}$$

where $C_T = 10.0$, based on a priori test of the model on channel flow at $Re_\tau = 395$.

Eq.2.31 can be rewritten in the form:

$$\nu_t = F_{wI} C_{MTS} \sqrt{k_{sgs}}\,\overline{\Delta} \tag{2.33}$$

introducing the damping function:

$$F_{wI} = \frac{1}{1 + \dfrac{\overline{\Delta}\,\overline{S}}{C_T\sqrt{k_{sgs}}}} \tag{2.34}$$

Inagi et al. [68] estimated k_{sgs} using Eq.2.11. The formulation was applied to plane and rotating channel flow, backward facing step flow and the flow around the Ahmed [3] model, for a variety of Reynolds numbers. The model performed well in all test cases and in some cases better than the dynamic Smagorinsky model. Furthermore, it was superior to the latter regarding numerical stability issues.

From the above, it can be seen that both Yoshizawa and Inagi wall damping functions can be applied to complicated geometries and enhance the performance of the SGS model. Therefore, these functions were used extensively in this study. Van Driest and Piomelli's formulations were also employed for comparison purposes.

Chapter 3

Code Development

3.1 DELTA overview

In order to achieve the aims described in section 1.5, a computational fluid dynamics, CFD code had to be employed. The criteria set for the selection of this code were the following:

1. The code should be in a form that new features or modification of the existing ones could be implemented. In practice, this requires for the source code to be accessible. Although some commercial codes allow the introduction of new transport equations, still they do not provide enough flexibility to a developer. Hence, 'in-house codes' were favoured.

2. The code should have already been tested for a variety of flows, to confirm its accuracy and performance. This would ensure that the code and its subroutines are working properly and do not require further testing.

3. The code should handle complex geometries and anisotropic and, in some cases, non-orthogonal grids without introducing large numerical errors. This was due to the intention to assess the investigated SGS models on wall-bounded flows of a range of geometrical complexity.

4. The code should be accompanied by proper documentation.

Based on these four criteria, the code that was selected was an in-house code, called DELTA. DELTA has been developed in the Department of Aeronautical and Automotive Engineering of Loughborough University since 1994. In its original form, DELTA was an Euler code but later it was developed to compute RANS equations [133]. More recently, it was extended further to perform LES.

DELTA has been employed in the past, for the calculation of a wide range of flows, compressible [16] and incompressible [157], external [134] and internal [157], free [135] or wall-bounded [157]. In all cases it has performed reasonably well and therefore, it was considered to be the best choice available.

3.1.1 Technical characteristics of DELTA

DELTA is based on the finite volume approach for the solution of the governing equations of the flow. It uses collocated flow variables arrangement, on a curvilinear coordinate system, in combination with Rhie-Chow smoothing, to avoid pressure-velocity decoupling. DELTA adopts the SIMPLE pressure correction method, designed to handle both incompressible and compressible flow cases. In addition, laminar and Euler flow calculations are also available.

In a pressure correction method, the code initialises a flow field and then solves the momentum equations to obtain some intermediate flow variable values. Because these values will not necessarily satisfy the continuity equation, they are corrected by using a pressure correction, dP. dP is calculated by a pressure correction equation, which is derived by combination of the momentum and continuity equations. When the correct values for flow variables have been obtained, the procedure is repeated for the next timestep.

DELTA employs a central difference scheme for the calculation of the fluxes but it can also use an upwind scheme. In terms of time integration, DELTA can use either an Euler implicit or an explicit scheme. Finally, a Gauss-Seidel line solver [48] is used to solve the pressure correction equation.

DELTA can read a variety of grid file formats including PLOT3D files and mesh files produced by ICEM. Input grids have to be structured, single or multi-block. As far as the application of boundary conditions and the exchange of information between the blocks are concerned, DELTA uses two extra rows of hallo-cells, generated automatically along each face of every block. Boundary conditions are applied on the first row while the second is mainly used for the exchange of information in multi-block grids. Boundary conditions that are available in DELTA include, among others, fixed velocity inlet, inflow total, where total pressure and temperature are specified, Euler or viscous wall, symmetry, zero gradient or linear extrapolation outflow and free pressure, where free stream pressure based on static value can be specified. These can make the use of DELTA available on a very large variety of flow cases.

DELTA is written in FORTRAN 77 and it consists of 139 subroutines. The main flow of the program is prescribed by deltaFlow.f. This subroutine forms the back-bone of the code and it is the one that controls the order and the application of the various operations described by the rest of the subroutines. deltaFlow.f cooperates also with a number of subroutines written in C, which are capable of reading the three files that govern the simulation. These are:

1. the Resource file, where all the parameters that govern the numerical and modelling issues of the simulation are described,
2. the boundary condition file, where all the boundary conditions applied are described along with any initialisation values, whenever this is applicable and
3. the topology file that defines the grid topology and the connections between faces or blocks.

These three files are user defined and allow the specification of all the parameters that can affect the simulation. For the flow visualisation, DELTA uses VISUAL 3 graphics library [62], which allows the user to observe the flow field and the variables of interest. VISUAL 3 can generate iso-surfaces, cut-plane views and vector fields, providing a powerful tool. For further data post processing, DELTA can generate data files in PLOT3D and TECPLOT format.

3.1.2 The LES module of DELTA

An expansion of the simulation capabilities of DELTA was achieved by the addition of the LES module. The code was converted to run in LES mode essentially via four modifications:

(i) an explicit time stepping formulation was introduced employing a 3rd order accurate low storage Runge-Kutta method [187],

(ii) 2nd order central differencing was used for convection term discretisation rather than the MUSCL technique used previously,

(iii) correct scaling of the Rhie and Chow [152] smoothing terms was adopted to take account of the very small timesteps needed in LES calculations, combined with very significant variations in cell volume size across the solution domain,

(iv) a SGS model was introduced; namely the Smagorinsky model [163] with Piomelli's near-wall damping formulation [144].

The application of LES in DELTA employs the implicit filtering procedure which uses the grid as a spatial filter and hence avoids the requirement of an explicit filtering procedure.

The introduction of the LES module in DELTA highlighted the need for parallelisation as the computational requirements of LES are higher than the requirements imposed by RANS. Hence, the latest development of the code involved the generation of 'parallel' versions that make use of OpenMP or Message Passing Interface, MPI, libraries to enable parallel processing based on flow domain decomposition.

3.1.3 New features introduced

For the requirements of the present study, a number of new features were introduced to the code. These were related to the implementation of new SGS models, grid file formats and the Boundary Conditions BC. The introduction of the new SGS models to the code is described in section 3.2. As far as the grid file formats are concerned, a new format was introduced that would allow DELTA to work with grids generated by GridGen. GridGen is a commercial grid generation software, which can produce high quality structured or unstructured, single or multi-block meshes [145]. All the grids generated for this study were produced by GridGen and therefore the introduction of this format was necessary.

Regarding the boundary conditions, three new types were introduced; the fixed profile, the time-varying profile and the convective BC. The fixed profile type is usually applied for velocity components at inlet. Originally, DELTA could set a fixed variable value at the inlet boundary. However, for the purposes of the present study, this had to be extended to prespecified profiles. An algorithm had to be established, according to which DELTA would read an input file with all the required data, and impose appropriately the variable values on the boundary plane of interest.

The first problem that arises from this procedure is that there is no guarantee that the values given by the input file would coincide, in terms of coordinates, with the coordinates of the cell centres. Furthermore, the number of entries in the input file could be different from the number of cells on the boundary. Therefore, a form of interpolation had to be introduced that would generate the appropriate variable values for the cells coordinates. To simplify the problem, the algorithm developed was for one-dimensional 1D, profiles, i.e. for cases where the variable of interest varies only in one direction. Since the present study focuses on wall-bounded flows, this direction was the y direction.

In the first version of the algorithm developed, a cubic spline [148] was fit to the input data and used to generate a value for the variable of interest at each grid cell centre y coordinate. These values were then set as the boundary condition values, at each first hallo cell, in the state vector. Unfortunately, it was observed that in some cases, the generated cubic spline produced values that did not correspond to the input profile, leading to numerical instabilities.

Therefore, a linear interpolation was finally employed. The algorithm compares the y coordinate of each cell centre with the input profile and identifies the neighbour values. Then, it uses linear interpolation, given by Eq.3.1, to generated the appropriate value for the cell centre.

$$\phi_{int} = \frac{\vec{x}_R - \vec{x_{int}}}{\vec{x}_R - \vec{x}_L}\phi_L + \frac{\vec{x_{int}} - \vec{x}_L}{\vec{x}_R - \vec{x}_L}\phi_R \tag{3.1}$$

where ϕ is the variable of interest and subscript int indicates the interpolated value, L the left and R the right neighbour value respectively.

As long as the given profile is well described in terms of number and distribution of points, the linear interpolation can give an accurate representation of the specified profile, making sure that all interpolated values are arithmetically bounded by the two neighbour points of the input profile, as can be seen in Eq.3.1.

A fixed profile BC was coded to be applied only at the beginning of each timestep, prior to the solution to momentum equation, in order to reduce the iteration time. Since the variable profile was supposed to be fixed and the information related to the variable value at the first hallo cells was remaining unchanged between the Runge-Kutta sub-iterations, there was no reason to do otherwise.

When a fixed profile BC is employed, zero gradient is assumed at inlet for ρ, $\overline{P}$ and total enthalpy H. Hence, the values assigned on the hallo cells for these variables, are the same with the neighbour internal cells.

While velocity profiles can be easily found in published experimental data, k_{sgs} profiles are filter dependent. In the case of implicit filtering, k_{sgs} depends upon the grid used. There are two ways to obtain a profile for this variable. If there is experimental data for the velocity field, then k_{sgs} can be computed by subtracting the filtered kinetic energy from the total kinetic energy [58]. The total kinetic energy can be calculated directly from the velocity field data, while the filtered kinetic energy requires the experimental data to be filtered by the LES filter. If experimental data of the velocity field is not available, then k_{sgs} can be approximated based on Bardina's hypothesis of scale similarity [12], using the velocity profile and Eq.2.10.

This approximation of k_{sgs} requires a double filtering procedure, to obtain $\bar{\bar{u}}_i(\vec{x},t)$, which is required for Eq.2.11. $\bar{\bar{u}}$ field is obtained using a composition of a one-dimensional filter, given by Simpson's rule [128], Eq.3.3, applied in all three dimensions as follows:

$$\bar{\bar{\phi}} = \left(\left(\left(\bar{\bar{\phi}}_i\right)_x\right)_y\right)_z \tag{3.2}$$

$$\bar{\bar{\phi}}_i = \frac{1}{6}\left(\bar{\phi}_{i+1} + 4\bar{\phi}_i + \bar{\phi}_{i-1}\right) \tag{3.3}$$

After the computation of $\bar{\bar{u}}_i(\vec{x},t)$, Eq.2.10 can be used to obtain an approximation for k_{sgs} that will correspond to the velocity profile used and the grid filtering employed.

Ghosal [58] and Dejoan [31] proposed a method to obtain an initial value for k_{sgs} using the equilibrium hypothesis. The production Pr of k_{sgs} is given by:

$$Pr = 2\nu_t \overline{S}_{ij}\overline{S}_{ij} \tag{3.4}$$

Assuming that the turbulence is in equilibrium:

$$Pr = \varepsilon \tag{3.5}$$

and modelling ε using Term 3 of Eq.2.13, Eq.3.5 becomes:

$$2\nu_t \overline{S}_{ij}\overline{S}_{ij} = C_1 \frac{k_{sgs}^{3/2}}{\overline{\Delta}} \tag{3.6}$$

Substituting the k_{sgs}-equation model formulation for ν_t in Eq.3.6 and solving for k_{sgs} leads to:

$$k_{sgs} = 2\overline{S}_{ij}\overline{S}_{ij}\frac{C_\mu \overline{\Delta}^2}{C_1} \tag{3.7}$$

$\overline{S}_{ij}$ can be obtained by the velocity field profiles and $\overline{\Delta}$ is given by Eq.2.4.

The second type of inlet boundary condition introduced to the code was the time-varying profile, which was used to apply an unsteady velocity field at the boundary of interest. The unsteady velocity field was generated by a DFG, which is described in detail in section 6.1. The algorithm employed for the implementation of the time-varying profile BC was designed to read the input data, generated by the DFG, and then apply it to the first hallo cell. Note that the format of the generated data was such that it corresponded to the points of the grid used by the LES. Therefore, no interpolation as in the case of fixed profile type was required.

However, a linear interpolation method was adopted for the time marching. If the DFG algorithm generated velocity field realisations for a timestep larger than that used by the LES, for reasons that are explained in section 6.1, the linear interpolation method would identify the neighbour DFG data sets and it would apply linear interpolation to get the corresponding velocity field for the timestep of interest. Further details about this procedure are given in section 6.1. As in the case of fixed profile BC, when time-varying profile is used, zero gradient is assumed for ρ, $\overline{P}$ and H.

The third type of boundary condition introduced to the code was the convective outlet boundary condition. This boundary condition is widely used in the LES because it ensures the convection of the flow through the outlet plane, with a constant velocity U_B, without the generation of disturbance wave reflection [191]. According to the convective boundary condition, the velocity at the boundary of interest is defined as follows:

$$\frac{\partial \vec{u}}{\partial t} = -U_B \frac{\partial \vec{u}}{\partial \vec{x}} \tag{3.8}$$

where $\vec{u}$ denotes the velocity vector and $\vec{x}$ the spatial vector. U_B is the bulk velocity at the outlet plane, calculated by:

$$U_B = \frac{1}{A} \int_A \vec{u} \cdot \vec{n} dA \tag{3.9}$$

where A is the area of the boundary of interest, $\vec{n}$ is the unit vector normal to dA and dA is the surface element.

Regarding the convective boundary condition, U_B is firstly calculated by the numerical form of Eq.3.9, which for a Cartesian grid with BC applied on a plane in the x-direction, can be reduced to:

$$U_B = \frac{1}{A}\sum u_{in} dA \tag{3.10}$$

In Eq.3.10, u_{in} is the value of the velocity in the x-direction, at the internal cell, next to the outlet boundary. To calculate the value of u that should be applied on the first hallo cell as a boundary condition, the discretised form of Eq.3.8 was used, given by:

$$u_{out}^{n+1} = u_{in}^{n} - U_B \frac{u_{out}^{n} - u_{in}^{n}}{x_{out} - x_{in}} \Delta t \tag{3.11}$$

where n denotes the timestep, *in* the first internal cell next to the outlet boundary, and *out* the first hallo cell. x is the cell centre coordinate in the streamwise direction. As in the case of fixed profile at inlet, the implementation of convective BC assumes zero gradient for ρ, P and H at outlet.

Eq.3.11 is a valid discretised form of Eq.3.8 if the grid is Cartesian in the x-direction over the boundary plane of interest. If this is not the case, the calculation of $\frac{\partial \vec{u}}{\partial x}$ takes a more elaborate form that is described in detail in section 3.2.2. In all the cases studied, the grid was Cartesian at the outlet plane of the flow domain, where this BC was employed. Therefore, even the discretised form given by Eq.3.11 was adequate.

3.2 Numerical implementation of SGS models and near-wall treatment

For the purposes of this work, two SGS models were coded in DELTA. These were the k_{sgs}-equation model, given by Eq. 2.12 and the MS model, given by Eq. 2.8. The k_{sgs}-equation model would be used in combination with a number of near-wall functions, in order to investigate the potential of such formulation in LES of wall-bounded flows. The MS model was used to test and verify the implementation of some near-wall functions and illustrate an intermediate model, between zero equation and one equation models. Towards the end of the present study, a new SGS model was also developed and implemented in the code. It is based on a new approach to the calculation of ε and it is believed to be a good candidate for further development and testing.

3.2.1 Implementation of the MS model

According to the MS model formulation, ν_t is being given by Eq.2.8 with $F(\bar{u}_i(\vec{x},t)) = \overline{S}$. Hence, the magnitude of the strain rate tensor had to be calculated as well as an approximation of k_{sgs} using Eq.2.10 and 2.11. In order to compute $\overline{S}_{ij}$ and its magnitude, the derivatives of the velocity components had to be computed for all cell centres.

The derivative of the variable of interest ϕ can be expressed as

$$\frac{\partial \phi}{\partial x_j} = \frac{\partial \phi}{\partial \xi_k} \cdot \frac{\partial \xi_k}{\partial x_j} \tag{3.12}$$

where ξ_k are the computational space co-ordinates.

The calculation of $\frac{\partial \phi}{\partial \xi_k}$ is reduced to:

$$\frac{\partial \phi}{\partial \xi_k} = \frac{\phi_{i+1} - \phi_{i-1}}{\xi_{k,i+1} - \xi_{k,i-1}} = \frac{\phi_{i+1} - \phi_{i-1}}{2} \tag{3.13}$$

Note that the subscript i denotes the cell index. For the calculation of $\frac{\partial \xi_k}{\partial x_j}$ at the cell centre, the following, second order accurate formula [59] was employed:

$$\frac{\partial \xi_k}{\partial x_j} = \frac{A_{j,i} n_{j,i} + A_{j,i+1} n_{j,i+1}}{2V} \tag{3.14}$$

where A_j is the area of the face of interest, n_j is the unit vector in the direction of x_j and V is the cell volume. After the computation of the velocity derivatives at cell-centres, $\overline{S}$ was calculated using Eq.2.2.

Finally, the approximation of k_{sgs}, given by Eq.2.10, was computed as described in section 3.1.3. After the computation of k_{sgs} and $\overline{S}$, Eq.2.8 is used to calculate ν_t at the beginning of each timestep.

3.2.2 Implementation of the k_{sgs}-equation model

The implementation of the k_{sgs}-equation model was based on existing subroutines, coded for the RANS $k-\varepsilon$ model. The simplicity of the code, the minimum number of new subroutines and their compatibility with the initial version of the code, were the main reasons for this decision.

The calculation of ν_t was performed at the beginning of each timestep, using Eq.2.12, with $C_\mu = 0.05$ according to Horiuti [66] and $\overline{\Delta}$ given by Eq.2.4.

As discussed in earlier sections, the model required the solution of the transport equation of k_{sgs}, given by Eq.2.13. This involved the numerical solution of the equation at the beginning of each timestep. To achieve this in the framework of the finite volume approach, the whole expression of Eq.2.13, was integrated with respect to each cell control volume CV, leading to the following expression:

$$\int_{CV} \frac{\partial k_{sgs}}{\partial t} dV + \int_{CV} \frac{\partial \overline{u}_j k_{sgs}}{\partial x_j} dV = \int_{CV} \left(-\tau_{ij}\overline{S}_{ij}\right) dV + \int_{CV} \left(-C_1 \frac{k_{sgs}^{3/2}}{\overline{\Delta}}\right) dV$$

$$+ \int_{CV} C_2 \frac{\partial}{\partial x_j}\left(\overline{\Delta}\sqrt{k_{sgs}}\frac{\partial k_{sgs}}{\partial x_j}\right) dV + \int_{CV} \nu \frac{\partial^2 k_{sgs}}{\partial x_j \partial x_j} dV \tag{3.15}$$

where dV is the volume element.

Using Gauss divergence theorem, Eq.3.15 becomes:

$$\frac{\partial}{\partial t}\left(\int_{CV} k_{sgs} dV\right) + \int_A n_i \cdot \left(\overline{u}_i k_{sgs}\right) dA = \int_{CV} \left(-\tau_{ij}\overline{S}_{ij}\right) dV + \int_{CV} \left(-C_1 \frac{k_{sgs}^{3/2}}{\overline{\Delta}}\right) dV$$

$$+ \int_A n_i \cdot \left[\left(C_2 \overline{\Delta}\sqrt{k_{sgs}} + \nu\right) \frac{\partial k_{sgs}}{\partial x_i}\right] dA \tag{3.16}$$

Eq.3.16 has to be discretised, at each control volume, in order to form an algebraic expression of k_{sgs}, which can then be easily solved. Employing the backward Euler scheme [48] for the time-marching and assuming that the cell-centre values correspond to the mean values of the variables in each control volume, the transient term of Eq.3.16 can be written as:

$$\frac{\partial}{\partial t}\left(\int_{CV} k_{sgs} dV\right) = k_{sgs}^{n}\frac{V}{\Delta t} - k_{sgs}^{n-1}\frac{V}{\Delta t} \tag{3.17}$$

where V is the cell volume and the superscript n denotes the timestep. Note that according to this approach, all the rest of Eq.3.16 terms are in timestep level n, unless specified otherwise.

Using midpoint rule [48] for the area integral approximation, the convection and diffusion terms for $i = 1$ can be combined and integrated as follows:

$$\int_A n_x \cdot \left[\overline{u}k_{sgs} - \left(C_2\overline{\Delta}\sqrt{k_{sgs}} + \nu\right)\frac{\partial k_{sgs}}{\partial x}\right] dA =$$

$$A\left[n_x\overline{u}k_{sgs} - n_x\left(C_2\overline{\Delta}\sqrt{k_{sgs}} + \nu\right)\frac{\partial k_{sgs}}{\partial x}\right]_w^e \tag{3.18}$$

Similarly for $i = 2,\ 3$. Note that n_x is the component of n_i in the x-direction.

Using the same assumption regarding the volume integral, as in the transient term, the production and dissipation terms become:

$$\int_{CV} \left(-\tau_{ij}\overline{S}_{ij}\right) dV = -\tau_{ij}\overline{S}_{ij}V \tag{3.19}$$

$$\int_{CV} \left(-C_1\frac{k_{sgs}^{3/2}}{\overline{\Delta}}\right) dV = -C_1\frac{k_{sgs}^{3/2}}{\overline{\Delta}}V \tag{3.20}$$

Eq.3.18 requires the value and the first derivatives of variables involved at the control volume surfaces. On the contrary, Eq.3.19 and 3.20 require the cell-centre values. Since, DELTA uses a collocated grid arrangement, all variables are stored at the control volume centre and not at the surface. Therefore, in contrast with staggered grid arrangement where this information is readily available, some short of interpolation has to be performed.

The value of k_{sgs} and $\overline{u_i}$ at the control volume surface is calculated using linear interpolation between the neighbour cell-centre values, which, in finite differences, corresponds to central differencing scheme [48]. The interpolation scheme reads as:

$$\phi_{face} = \frac{\lambda_{i-1}}{\lambda_i + \lambda_{i-1}}\phi_i + \frac{\lambda_i}{\lambda_i + \lambda_{i-1}}\phi_{i-1} \tag{3.21}$$

where

$$\lambda_i = V_i\left(A_{i-1} + A_i\right) \text{ and } \lambda_{i-1} = V_{i-1}\left(A_i + A_{i+1}\right) \tag{3.22}$$

The calculation of the first derivative at the surface centre was computed according to Eq.3.12, with the metrics $\frac{\partial \xi_k}{\partial x_j}$ being calculated according to Gnoffo proposal [59] , which can be found in the Appendix. Gnoffo's formulation for the cell surface centre derivative is second order accurate. Finally, the first derivatives required for Eq.3.19 and 3.20 were computed as described in section 3.2.1.

Using the techniques described above and treating production and dissipation terms as source terms, Eq.3.16 was constructed in the following form:

$$a_P k_{sgs\ P} + a_E k_{sgs\ E} + a_W k_{sgs\ W} + a_N k_{sgs\ N} + a_S k_{sgs\ S} + a_T k_{sgs\ T} + a_B k_{sgs\ B} = S \tag{3.23}$$

where

$$a_P = \frac{V}{\Delta t} - \left(a_E + a_W + a_N + a_S + a_T + a_B\right) \tag{3.24}$$

with

$$a_E = A_x \left[n_x \overline{u_{face\,E}} - n_x \left(C_2 \overline{\Delta} \sqrt{k_{sgs}} + \nu \right) \frac{\partial}{\partial \xi} \frac{\partial \xi}{\partial x} \right] \tag{3.25}$$

and similarly for a_W, a_N, a_S, a_T and a_B,

$$\begin{aligned} S \ = \ & k_{sgs}^{n-1} \frac{V}{\Delta t} + \tau_{ij} \overline{S}_{ij} V + C_1 \frac{k_{sgs}^{3/2}}{\overline{\Delta}} V \\ & + A_x n_x \left(C_2 \overline{\Delta} \sqrt{k_{sgs}} + \nu \right) \left(\frac{\partial k_{sgs}}{\partial \eta} \frac{\partial \eta}{\partial x} + \frac{\partial k_{sgs}}{\partial \zeta} \frac{\partial \zeta}{\partial x} \right) \\ & + A_y n_y \left(C_2 \overline{\Delta} \sqrt{k_{sgs}} + \nu \right) \left(\frac{\partial k_{sgs}}{\partial \xi} \frac{\partial \xi}{\partial y} + \frac{\partial k_{sgs}}{\partial \zeta} \frac{\partial \zeta}{\partial y} \right) \\ & + A_z n_z \left(C_2 \overline{\Delta} \sqrt{k_{sgs}} + \nu \right) \left(\frac{\partial k_{sgs}}{\partial \xi} \frac{\partial \xi}{\partial z} + \frac{\partial k_{sgs}}{\partial \eta} \frac{\partial \eta}{\partial z} \right) \end{aligned} \tag{3.26}$$

Note that for the diffusion term of Eq.3.16, the coefficients were separated in two parts; the cross part and the normal part. This procedure was followed because the cross part is a result of the transformation of coordinates from Cartesian to curvilinear and it was treated as a source term, as it can be seen in Eq.3.26.

For the points along the flow domain boundaries, boundary conditions had to be applied for k_{sgs} and the production and the dissipation term of Eq.3.16. As far as k_{sgs} was concerned, Neumann or Dirichlet boundary conditions were used, depending upon the type of boundaries specified. Dirichlet type BC was employed for the k_{sgs}-equation when inlet profile or periodic BC was applied, and Neumann BC when zero gradient or viscous wall was used.

When a near-wall modelling simulation was performed, WW law, given by Eq.2.25, was used to provide values of the production and dissipation at the first internal cell. The boundary value of the production term was set according to y^+, as follows:

$$\tau_{ij}\overline{S}_{ij} = \begin{cases} 0 & \text{for } y^+ < 5.0 \\ \rho u_\tau^2 \frac{8.3}{7} \left[\frac{u_\tau^2}{\mu\left(y^+\right)^6}\right]^{1/7} & \text{otherwise} \end{cases} \tag{3.27}$$

Eq.3.27 is derived by the approximation of the production at the wall as $\tau_w \frac{\partial u}{\partial y}$. Note that $\overline{S}_{ij}$ is reduced to $\frac{\partial u_i}{\partial x_j}$ if the flow is incompressible. By definition, $\tau_w = \rho u_\tau^2$. Furthermore, $\frac{\partial u}{\partial y}$ is given by the differentiation of the WW velocity profile with respect to y. $\tau_{ij}\overline{S}_{ij}$ was set to zero within the viscous sublayer since no production of k_{sgs} takes place in this region.

Finally, using the equilibrium hypothesis, the value of ε at the first internal cell, was set equal to the production, by Eq.3.28, independently of the distance from the wall.

$$\varepsilon = \rho u_\tau^2 \frac{8.3}{7} \left[\frac{u_\tau^2}{\mu\left(y^+\right)^6}\right]^{1/7} \tag{3.28}$$

The calculation of u_τ and y^+ is described in section 3.2.4, along with the implementation of the WW law.

The discretisation of Eq.3.16 leads to the algebraic approximation given by Eq.3.23 at every point of the grid, forming a system of linear algebraic equations with as many unknowns, as the number of the equations in the system. All the equations could then be written in a matrix form as follows:

$$\left[\, a \,\right]\left[\, k_{sgs} \,\right] = \left[\, S \,\right] \tag{3.29}$$

$[a]$ is a square diagonal coefficients matrix, $\left[\, k_{sgs} \,\right]$ is the column matrix of the unknown variable and $\left[S \right]$ is the column source matrix. The system of Eq.3.29 was solved by a line Gauss-Seidel solver [48], providing the values of k_{sgs} at the new timestep.

3.2.3 Development of a new SGS model based on the energy spectrum dissipation

Using the experience gained from the study and the numerical implementation of the two models described above, a new SGS model was developed. As discussed in section 2.3.1, in the last decade, considerable work has been published, which combines a transport equation model with the dynamic procedure, in order to obtain these model coefficients dynamically as part of the flow simulation. Ghosal [58] used a constraint localised form of the dynamic procedure to obtain the coefficients in a $k_{sgs}-$equation model but presented only calculations for decaying turbulence behind a grid. Menon and Kim [120] used a similar formulation for high Reynolds number decaying and forced isotropic turbulence and a temporally evolving turbulent mixing layer to obtain results in good agreement with experimental and DNS data. More recently, Krajnovic [88] used both the Menon and Kim [120] model and a model proposed by Davidson [26] for a recirculating flow around a surface mounted cube, producing good results. However, during this study it was noted that for this complex recirculating flow, grid resolution influenced the effectiveness of the transport equation models and improved the accuracy of the flow prediction. Evidence from Krajnovic [88] implies that modelling improvements introduced so far by the combination of a one equation SGS model and the dynamic procedure are still not sufficient to cope with situations when an insufficiently resolved, coarse grid was used and therefore a significant fraction of the turbulence energy was contained in the subgrid scales of the flow.

In addition, particular implementations of the dynamic procedure have been reported to generate numerical instabilities [55], leading to the adoption of a 'clipping' approach, which, depending on numerical details, may be ad hoc or based on physical realisability considerations [55, 120]. This practice has a direct effect on the SGS stresses, potentially compromising the range of flow problems where the model can deliver good performance. Evidence to support this contention is that a homogeneous flow direction [138, 141] has normally been required for this clipping practice to achieve stability.

Considering the above, further improvement in the area of SGS modelling could either be achieved by the introduction of a second transport equation (as in RANS formulations) or by the improved formulation of one equation models. Following the second school of thought, the development of a new SGS model aims to introduce a new approach regarding the definition of the characteristic subgrid length scales used in the model via a careful consideration of the relevant flow physics. The increased use of flow physics in model formulation leads to a one equation model which does not suffer from some of the limitations discussed above. The new model retains the use of a transport equation for k_{sgs}, in the form proposed by Yoshizawa and Horiuti [195], but with the dissipation term, ε, in this equation calculated explicitly by integration of an assumed energy spectrum shape over the frequency range not resolved by the grid and hence captured in the subgrid scale region. In this way, the resulting behaviour of ε is more physically correct; the SGS model proposed here is hence termed as an energy spectrum dissipation model. Furthermore, the improved estimation of ε allows the model to produce a prediction of the local Kolmogorov length scale η and hence the maximum eddy wavenumber, κ_d. This enables an energy-weighted average wavenumber κ_{sgs} to be defined for the subgrid (non-resolved) scale motions as a more representative wavenumber from which the subgrid length scale can be extracted. This is necessary because in many cases, and particularly at high Re numbers, the non-resolved wave-numbers can still contain a considerable amount of energy and this should play an important role in the determination of both turbulence velocity and length scales used to evaluate ν_t. Such a role is not fulfilled by the classical, grid based, length scale used in the majority of subgrid scale models, but it is reflected in a transport equation based SGS model, supported by a length scale evaluated from the energy-weighted wavenumber κ_{sgs}, introducing a potentially more accurate representation of the whole range of non-resolved scales, in a manner more likely to be independent of the computational grid employed, and therefore successful for a wider range of levels of non-resolved SGS energy.

The Yoshizawa and Horiuti [195] one-equation SGS model is based on the transport equation for k_{sgs} and it has been used for wall-bounded flows giving good results [66]. This model was therefore used as the baseline for the development of the new model presented here. According to the Yoshizawa and Horiuti [195] model, ν_t is given by:

$$\nu_t = C_\mu \overline{\Delta}_G \sqrt{k_{sgs}} \tag{3.30}$$

In Eq.3.30, $C_\mu = 0.05$, $\overline{\Delta}_G = (\Delta x \Delta y \Delta z)^{1/3}$ (the subscript G indicates a grid-defined subgrid length scale) and k_{sgs} is derived from the solution of the following transport equation:

$$\frac{\partial k_{sgs}}{\partial t} + \frac{\partial \overline{u}_j k_{sgs}}{\partial x_j} = -C_1 \frac{k_{sgs}^{3/2}}{\overline{\Delta}_G} + C_2 \frac{\partial}{\partial x_j}\left(\overline{\Delta}_G \sqrt{k_{sgs}} \frac{\partial k_{sgs}}{\partial x_j}\right) + \nu \frac{\partial^2 k_{sgs}}{\partial x_j \partial x_j} - \tau_{ij}\overline{S}_{ij} \tag{3.31}$$

where $C_1 = 1.0$ and $C_2 = 0.1$.

The model proposed here uses the formulation presented above but introduces two new features: (i) an alternative approach to the calculation of the local subgrid length scale (used for ν_t and the k_{sgs} diffusion coefficient) based upon the energy content of all subgrid scales rather than the grid characteristics, and (ii) an improved representation of ε in Eq.3.31, replacing the $-C_1 \frac{k_{sgs}^{3/2}}{\overline{\Delta}_G}$ term.

In the majority of SGS models, the turbulence length scale in ν_t is specified purely via the local grid size, representing essentially the subgrid scales closest to the grid cutoff wavenumber $\kappa_c = \frac{2\pi}{2\overline{\Delta}_G}$, where, due to the Nyquist criterion, the smallest resolved length scale on a grid of cell size $\overline{\Delta}_G$ is $2\overline{\Delta}_G$. Although these are the most energetic of the subgrid scales, this does not necessarily mean that a length scale so derived represents the optimum approach to capture the effects of all subgrid scales on the resolved scale motions. This aspect will of course be particularly true when grid resolution is such that an appreciable level of energy is still present in the subgrid scales. This scenario will almost certainly occur in the near-wall region of LES simulations at high Re numbers.

An improved description of the subgrid scale length scale may be related to a representative SGS wavenumber. Figure 3.1 gives a graphical representation of this idea. In Figure 3.1, a typical energy spectrum $E(\kappa)$ is given, with the grid cutoff wavenumber κ_c lying in the inertial subregion and the dissipation wavenumber κ_d being the largest energy-containing eddy wavenumber, given by:

$$\kappa_d = \frac{2\pi}{\eta} \tag{3.32}$$

where η is the Kolmogorov length scale:

$$\eta = \left(\frac{\nu^3}{\varepsilon}\right)^{1/4} \tag{3.33}$$

The Kolmogorov scale is the smallest scale observed in the turbulent motions and its magnitude at high Re is dictated by the energy dissipation rate ε [146] and the fluid viscosity.

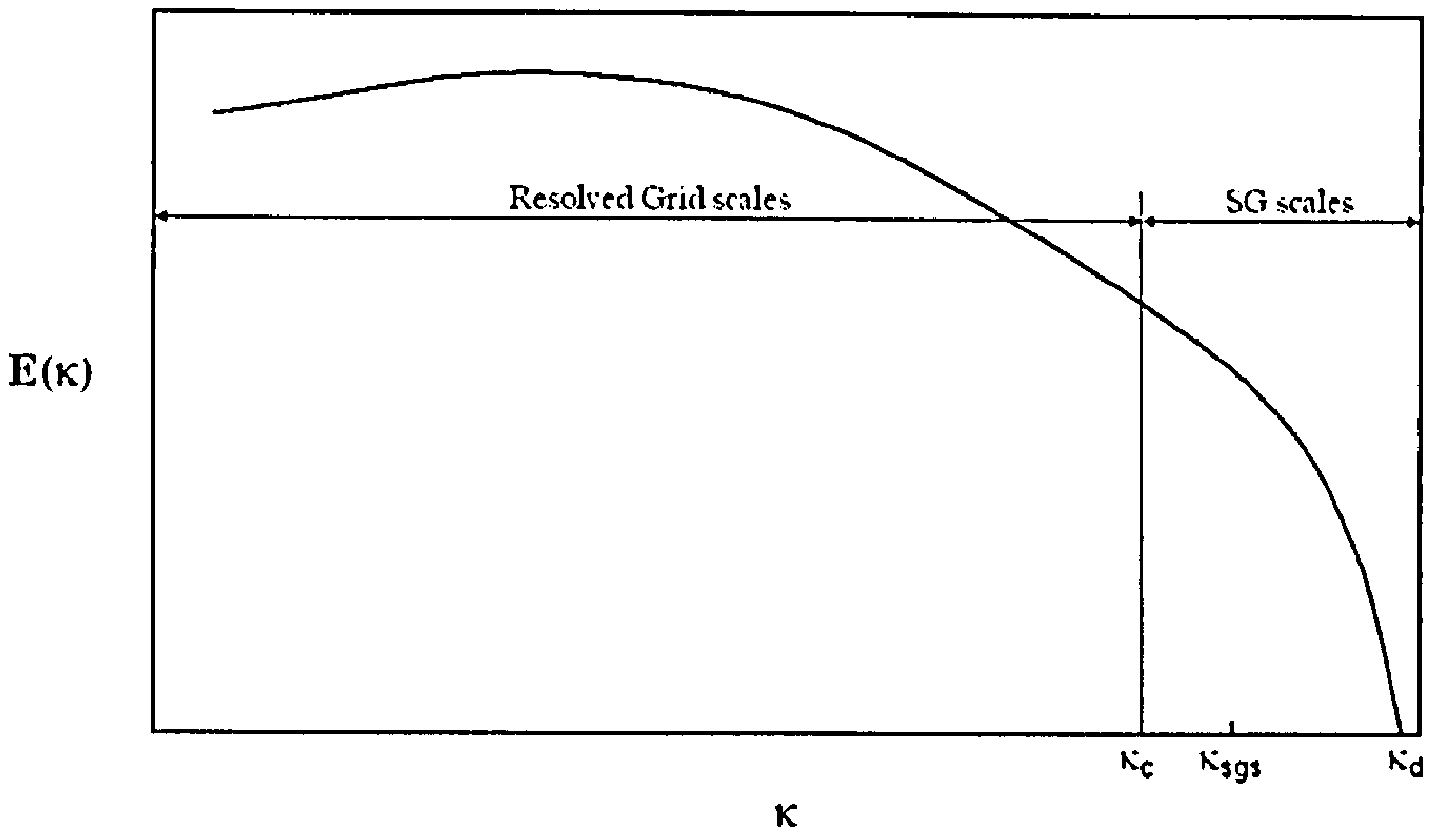

Figure 3.1: Schematic of energy spectrum

A representative wavenumber for the subgrid scales κ_{sgs}, may be defined via the convenient physical interpretation of an energy weighted average of all wave-numbers between κ_c and κ_d. Taking into account that:

$$k_{sgs} = \int_{\kappa_c}^{\kappa_d} E(\kappa)\, d\kappa \tag{3.34}$$

κ_{sgs} can be written as:

$$\kappa_{sgs} = \frac{1}{k_{sgs}} \int_{\kappa_c}^{\kappa_d} \kappa E(\kappa)\, d\kappa \tag{3.35}$$

The corresponding turbulence length scale can then be computed as:

$$\overline{\Delta}_{ES} = \frac{2\pi}{\kappa_{sgs}} \tag{3.36}$$

where the subscript ES indicates that the length scale is evaluated via the energy spectrum.

It is clear that the calculation of κ_{sgs} requires k_{sgs}, which may be obtained from solution of its modelled transport equation. Furthermore, it requires a function that describes accurately the energy spectrum $E(\kappa)$ in as wide range of flows as possible, also ensuring that the selected spectrum shape is consistent with the expected $\kappa^{-5/3}$ behaviour for the inertial subrange at high Re. In addition, the energy spectrum function is constrained by its relation to the dissipation rate at high Re [183]:

$$\varepsilon = 2\nu \int_0^\infty \kappa^2 E(\kappa)\, d\kappa \tag{3.37}$$

The Kolmogorov spectrum, given by Eq.3.38 below, is not a suitable candidate since, whilst it fits inertial subrange conditions well, it does not describe accurately the decrease of the energy content as κ_d is approached [183] and another form has to be employed.

$$E(\kappa) = K_o \varepsilon^{2/3} \kappa^{-5/3} \tag{3.38}$$

where $K_o = 1.4$.

Over the years, a number of researchers [? 83, 136, 177] have proposed a variety of energy spectra that obey Eq.3.37. Pope [146] proposed a general form for $E(\kappa)$, given by Eq.3.39, which demonstrates good correlation with experimental data obtained in a number of flows ranging from fully developed pipe and channel flows to grid turbulence and homogeneous shear flows, with wide Re number variation. This indicates that one real advantage of extracting information from the energy spectrum is that its form is, to a certain degree, flow type independent, giving a universal character to the information obtained.

$$E(\kappa) = C\varepsilon^{2/3}\kappa^{-5/3} f_L(\kappa L)\, f_\eta(\kappa\eta) \tag{3.39}$$

$f_L(\kappa L)$ and $f_\eta(\kappa\eta)$ are specified non-dimensional functions given by:

$$f_L(\kappa L) = \left(\frac{\kappa L}{\left[(\kappa L)^2 - c_L \right]^{1/2}} \right)^{11/3} \tag{3.40}$$

$$f_\eta(\kappa\eta) = \exp\left\{ -\beta \left\{ \left[(\kappa\eta)^4 + c_\eta^4 \right]^{1/4} - c_\eta \right\} \right\} \tag{3.41}$$

L is the length scale characterising the large eddies ($L \equiv \frac{k^{3/2}}{\varepsilon}$) and C, c_L, c_η and β are positive constants [146].

While Pope's spectrum is arguably a good candidate, its mathematical complexity could lead to numerical complexities and expense when used in full LES calculations. Therefore, at this stage of development and exploration of the model an alternative approach was selected namely the model spectrum proposed by Kovasznay [83], which was preferred due to its mathematical simplicity. The Kovasznay spectrum was developed based on locally isotropic turbulence:

$$E(\kappa) = K_o \varepsilon^{2/3} \kappa^{-5/3} \left[1 - \frac{K_o}{2} \left(\frac{\kappa}{\kappa_d} \right)^{4/3} \right]^2 \tag{3.42}$$

Eq.3.42 satisfies Eq.3.37 and reduces to the Kolmogorov spectrum for low values of κ . The spectrum vanishes at $\frac{\kappa}{\kappa_d} = \left(\frac{2}{K_o} \right)^{3/4}$ which fixes the value of K_o as 2 to match the Kolmogorov scale. However, it may be advantageous to retain K_o as a model parameter, to allow better description of the spectrum shape at wave-numbers containing most of the non-resolved energy, whilst departing strictly from the Kolmogorov constraint.

If the form of $E(\kappa)$ is assumed to be given by Eq.3.42, this equation can be substituted in Eq.3.34 and integrated, to give:

$$k_{sgs} = \kappa_d^{-2/3} \left(-\frac{3}{2}A - 3AB + \frac{AB^2}{2} \right) + 3AB\kappa_c^{2/3}\kappa_d - \frac{AB^2}{2}\kappa_c^2\kappa_d^{-8/3} + \frac{3}{2}A\kappa_c^{-2/3} \tag{3.43}$$

where $A = K_o\varepsilon^{2/3}$, $B = \frac{K_o}{2}$ and $\kappa_d = \frac{2\pi\varepsilon^{1/4}}{\nu^{3/4}}$.

The left hand side of Eq.3.43 can be assumed known from solution of the k_{sgs} transport equation. Hence, the only unknown in Eq.3.43 is ε. Rearranging Eq.3.43 in terms of ε gives:

$$\begin{aligned} k_{sgs} \quad = \quad & \varepsilon^{1/2} \left(B^3D^{2/3} - 6B^2D^{2/3} - 3BD^{2/3} \right) + \varepsilon^{1/3} \left(6B^2\kappa_c^{2/3}D^{4/3} \right) \\ & + \varepsilon^{2/3} \left(3B\kappa_c^{-2/3} \right) - B^3\kappa_c^2D^{8/3} \end{aligned} \tag{3.44}$$

where $D = \frac{\nu^{3/4}}{2\pi}$. Moving k_{sgs} to the RHS, Eq. 3.44 can be re-written as:

$$\begin{aligned} f(\varepsilon) = 0 = \; & \varepsilon^{1/2} \left(B^3D^{2/3} - 6B^2D^{2/3} - 3BD^{2/3} \right) + \varepsilon^{1/3} \left(6B^2\kappa_c^{2/3}D^{4/3} \right) \\ & + \varepsilon^{2/3} \left(3B\kappa_c^{-2/3} \right) - \left(B^3\kappa_c^2D^{8/3} + k_{sgs} \right) \end{aligned} \tag{3.45}$$

Eq.3.45 can be written as a fourth order polynomial in $\psi = \varepsilon^{1/6}$, in the following form:

$$g(\psi) = 0 = \psi^4\left(3B\kappa_c^{-2/3}\right) + \psi^3\left(B^3D^{2/3} - 6B^2D^{2/3} - 3BD^{2/3}\right)$$

$$+\psi^2\left(6B^2\kappa_c^{2/3}D^{4/3}\right) - \left(B^3\kappa_c^2D^{8/3} + k_{sgs}\right) \tag{3.46}$$

For the range of physically realisable values of all parameters involved in Eq.3.46 (i.e. $K_o \simeq 2.0$ and κ_c, k_{sgs}, $\nu \geq 0.0$), the terms $3B\kappa_c^{-2/3}(= C_{g1})$ and $6B^2\kappa_c^{2/3}D^{4/3}$ $(= C_{g3})$ are positive definite while the terms $B^3D^{2/3} - 6B^2D^{2/3} - 3BD^{2/3}$ $(= C_{g2})$ and $-\left(B^3\kappa_c^2D^{8/3} + k_{sgs}\right)$ $(= C_{g4})$ are negative definite. Using the Routh-Hurwitz criterion [24], it can be shown that Eq.3.46 has three roots with a positive real part. Factorisation of Eq.3.46 by ψ^2 leads to:

$$g(\psi) = 0 = \psi^2\left(\psi^2 + \frac{C_{g2}}{C_{g1}}\psi + \frac{C_{g3}}{C_{g1}}\right) + \frac{C_{g4}}{C_{g1}} \tag{3.47}$$

The quadratic expression in parentheses in Eq.3.47 has a pair of complex conjugate roots with positive real part due to the nature of the physically realisable values of the coefficients, leading to the conclusion that Eq.3.46 has only one positive real root. Due to the positive definite nature of ε, the only physically realisable root is that corresponding to this positive real root. This is confirmed by plotting $f(\varepsilon)$ against ε for two limiting cases of κ_{cmin} and κ_{cmax} (defined below) with $k_{sgs} = 0.0$. Note that for any isothermal incompressible flow, K_o and ν are considered to be constants and therefore the only variable parameters in a flow simulation will be κ_c (due to the use of a non-uniform grid) and k_{sgs}. κ_c will typically vary between κ_{cmax} (corresponding to the near-wall cells that are typically the smallest in the grid) and κ_{cmin} (corresponding to the largest cells in the grid, typically well away from any walls). Regarding k_{sgs}, the limiting case to consider is when it becomes zero, since then, for the same value of ε, $f(\varepsilon)$ is closest to the $f(\varepsilon) = 0$ axis, as can be seen from Eq.3.45.

Extracting κ_{cmin} and κ_{cmax} from a grid used below for a fully developed channel flow simulation at $Re_\tau = 180$, two plots were generated, presented in Figure 3.2 for κ_{cmax} and in Figure 3.3 κ_{cmin} , both with $k_{sgs} = 0.0$. The plots show that in this extreme case, $f(\varepsilon)$ crosses zero at only one point, corresponding to the single positive real root of $g(\psi)$. The second observation is that this root is larger in magnitude when closer to the wall, as shown in Figure 3.2, indicating a correct representation of the physical behaviour of ε. Finally, Figures 3.2 and 3.3 verify that the nature and the number of roots of $f(\varepsilon)$ does not vary with κ_c, as indicated previously by the mathematical analysis of $g(\psi)$.

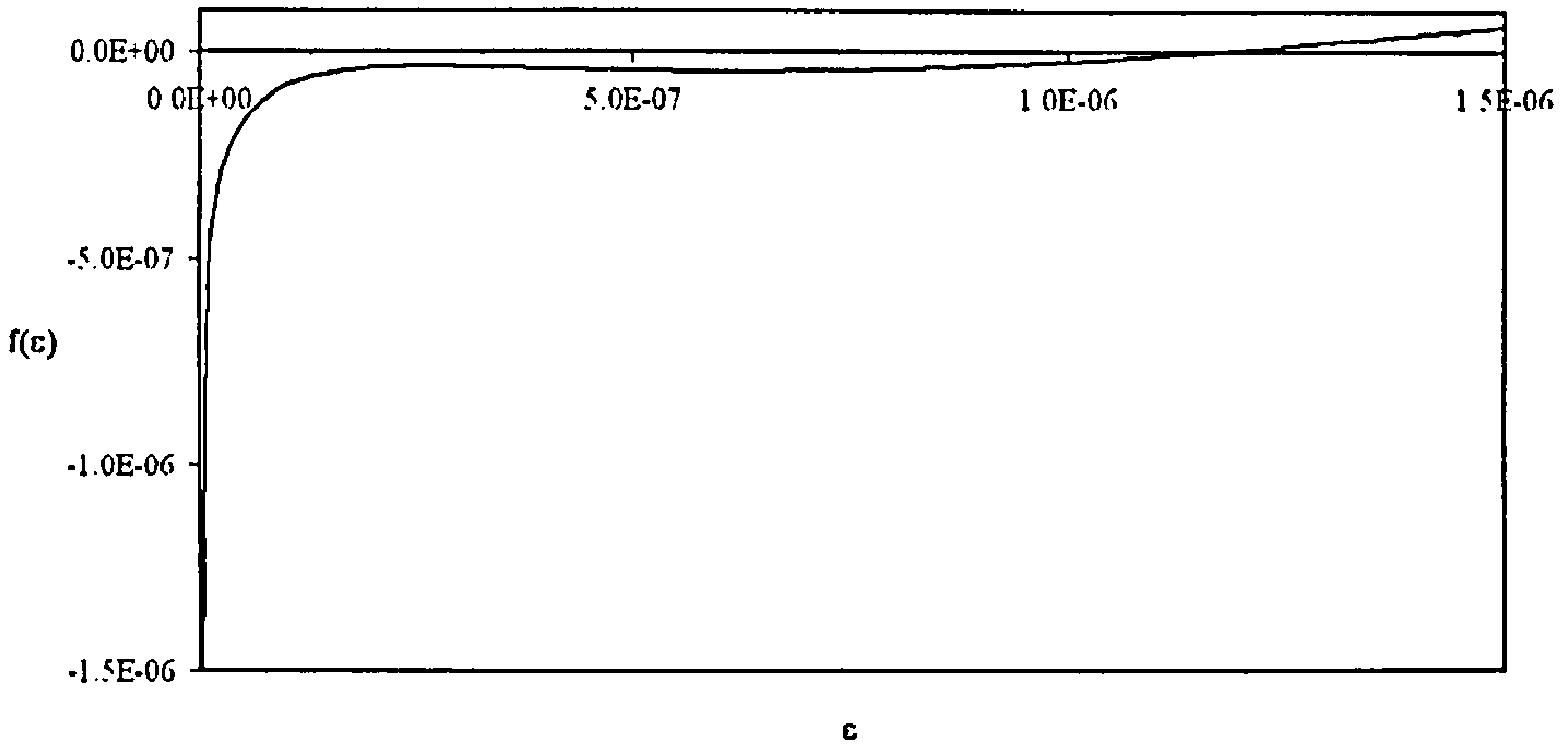

Figure 3.2: Variation of $f(\varepsilon)$ with ε for κ_{cmax}

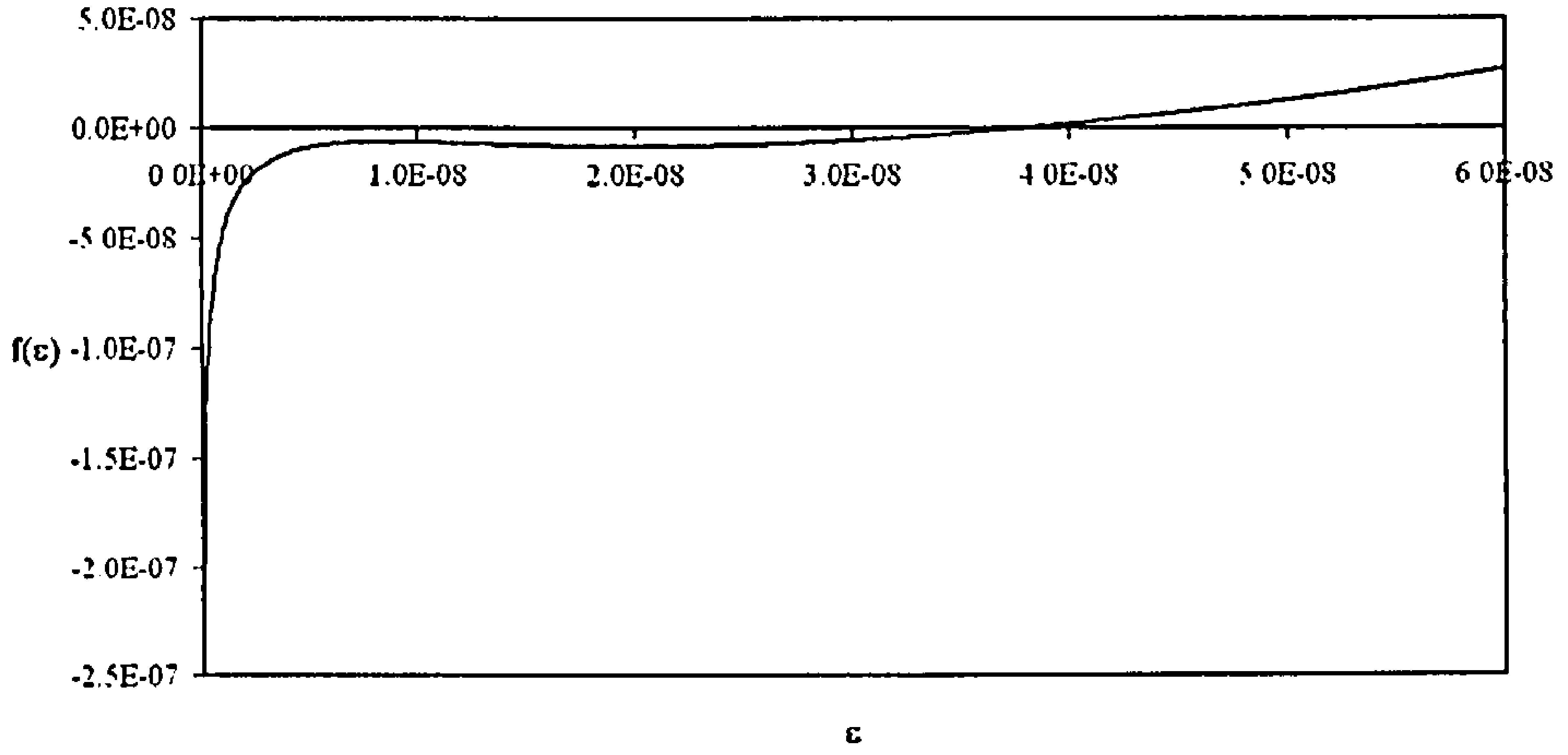

Figure 3.3: Variation of $f(\varepsilon)$ with ε for κ_{cmin}

From the above, it was concluded that solution of Eq.3.44 can return an accurate representation of ε. As soon as this value of ε is found, κ_d can be calculated and used in Eq.3.35 to calculate κ_{sgs} and hence, $\overline{\Delta}_{ES}$ from Eq.3.36.

In general, any root identification algorithm may be used to find the root of Eq.3.45. For the present study, a modified Newton-Raphson method [148] was employed, which uses the classic Newton-Raphson algorithm with an extra bisection step taken every time the algorithm begins to search outside a prespecified range of ε values or does not narrow down the field of possible roots in a steady manner [148]. The search range of ε for the identification of the Eq.3.45 root is user-defined and is based on a number of considerations. Since ε cannot be negative, the search range lower limit can be set to zero. The upper limit is set to a value ten times the value of ε from the previous timestep. The definition of the upper limit can be changed but it was found that this approach was adequate for all simulations performed and reported below.

The transport equation used for k_{sgs} is that given by Eq.3.31 with the only difference being that the SGS dissipation term is not the modelled form $-C_1\frac{k_{sgs}^{3/2}}{\overline{\Delta}_G}$ but rather ε calculated using the procedure described above; the subgrid length scale $\overline{\Delta}_{ES}$ is used to replace $\overline{\Delta}_G$ in both the ν_t definition (Eq.3.30 and the turbulent diffusion term in Eq.3.31.

The model proposed here is termed an Energy Spectrum Dissipation, ESD, model and involves the following steps:

1. Use the value of k_{sgs} from the previous timestep to calculate ε from Eq.3.44, using an enhanced Newton-Raphson method.
2. Use this value of ε to compute κ_d.
3. Use κ_d in Eq.3.35 to calculate κ_{sgs} and hence, $\overline{\Delta}_{ES}$.
4. Use $\overline{\Delta}_{ES}$ to compute ν_t.
5. Use ε for solution of the transport equation for k_{sgs}.

Hence, the new length scale $\overline{\Delta}_{ES}$ is also introduced into the production term of the k_{sgs} transport equation, through the formulation of $\nu_t = C_\mu \overline{\Delta}_{ES}\sqrt{k_{sgs}}$. At the beginning of the simulation, the initial value of k_{sgs} and ε are calculated as follows:

$$k_{sgs} = 2\overline{S}_{ij}\overline{S}_{ij}\frac{C_\mu \overline{\Delta}^2}{C_2} \tag{3.48}$$

$$\varepsilon = C_1\frac{k_{sgs}^{3/2}}{(\Delta x \Delta y \Delta z)^{1/3}} \tag{3.49}$$

Eq.3.48 was proposed by Ghosal [58] and Dejoan [31] and is based on an equilibrium assumption between k_{sgs} production and dissipation; $\overline{S}_{ij}$ is the resolved scale strain rate tensor and C_μ, C_1 and C_2 are the coefficients used in the model of Yoshizawa and Horiuti [195]. Finally, Eq.3.49 is the modelled form of ε, as used in the Yoshizawa and Horiuti model [195]. The transport equation of k_{sgs} given by Eq.3.31 was solved according to the procedure described in section 3.2.2.

3.2.4 Implementation of near-wall damping functions

Section 2.4 presented all the near-wall treatment methods that were employed in the present study, both in terms of LES and SGS modelling. Regarding LES, the WW near-wall model was employed, for the cases where the near-wall grid resolution was too coarse.

The WW model was present in the initial version of DELTA, where it had been implemented by previous workers. In this subroutine a critical tangential velocity U_{crit} is calculated as:

$$U_{crit} = \frac{\nu}{2\Delta y} 8.3^{\frac{2}{1-1/7}} \tag{3.50}$$

where Δy is the height of the first cell from the wall.

Eq.3.50 is derived by integrating the velocity profile given by WW model, see Eq.2.25, over the distance $0 < y \leq \frac{11.8\mu}{\rho u_\tau}$, and equating the result by the total flux through the first internal cell, in the direction parallel to the wall. If the tangential velocity at the first cell-centre is less than U_{crit}, then the value of the effective viscosity μ_e at the wall is equal to the absolute viscosity μ. Note that in general $\mu_e = \mu_t + \mu$. In this case τ_w is given by:

$$\tau_w = \mu_e \frac{\partial u}{\partial y} \simeq 2\mu \frac{U_t}{\Delta y} \tag{3.51}$$

and u_τ is given by Eq.1.5. Note that in Eq.3.51, U_t is the tangential velocity at the centre of the first internal cell.

If the tangential velocity is greater than U_{crit}, u_τ is calculated as follows:

$$u_\tau = \left[\frac{1-1/7}{2} 8.3^{\frac{1+1/7}{1-1/7}} \left(\frac{\nu}{\Delta y} \right)^{1+1/7} + \frac{1+1/7}{8.3} \left(\frac{\nu}{\Delta y} \right)^{1/7} U_t^{\frac{2}{1+1/7}} \right]^{\frac{1}{1+B}} \tag{3.52}$$

Eq.3.52 is derived by integration of the WW velocity profile, over the distance $0 < y \leq \Delta y$ and equating the result to the total flux through the first internal cell, in the direction parallel to the wall.

τ_w is then calculated using the definition of friction velocity, given by Eq.1.5, as follows:

$$\tau_w = \rho \left[\frac{6}{14} 8.3^{\frac{1+1/7}{1-1/7}} \left(\frac{\nu}{\Delta y} \right)^{1+1/7} + \frac{1+1/7}{8.3} \left(\frac{\nu}{\Delta y} \right)^{1/7} U_t^{\frac{2}{1+1/7}} \right]^{\frac{2}{1+B}} \tag{3.53}$$

and using $\tau_w = \mu_e \frac{\partial u}{\partial y}$, μ_e is approximated as:

$$\mu_e = \frac{\tau_w \Delta y}{2U_t} \tag{3.54}$$

Using this approach, u_τ can be calculated in any case, using only wall normal distance of the first cell-centre. Using the computed value of the friction velocity, y^+ can also be calculated using the definition, which is given by Eq.1.7.

Regarding the SGS modelling in the near-wall region, Piomelli's formulation for the near-wall damping function had been previously implemented and was modified to provide the option of the van Driest damping as well. Furthermore, two new functions were introduced; Yoshizawa and Inagi wall damping functions, both presented in section 2.4.2.

Yoshizawa function was developed to be used with all the models employed in the present study. In all forms $\overline{S}$ was computed in the same way described in section 3.2.1. The first form of the function was that proposed by Yoshizawa [196] and it was implemented with the same form of the MS model. This form, given by Eq.2.30, was also used by the k_{sgs}-equation model but with u_s term replaced by $\sqrt{2k_{sgs}}$. For the new SGS model, the same modification was adopted but, in addition, $\overline{\Delta}$ was given by Eq.3.36 and not by Eq.2.4 as in the other models.

Chapter 4

Application of SGS Models on the Channel Flow

Prior to the application of the implemented SGS models to complicated flow cases, it was considered appropriate to perform a series of test cases. The main objectives of these simulations were to identify any problems related to the implementation of the models in terms of coding, and to form a first stage of their assessment. Furthermore, these initial test cases could be used for the verification of two visualisation techniques that could be later used to investigate more complicated flows.

The flow case that was selected for the purposes described above, was the plane channel flow. This type of flow, although simple, incorporates all the main features of wall-bounded flows. It is easy to setup computationally in terms of grid and boundary conditions and it provides a good first case for testing SGS models due to the variation of scales involved in the flow and the sensitivity to correct SGS modelling. Furthermore it is well documented in literature and there is a large amount of both numerical data, in the form of DNS results [69, 78, 126], and experimental data [27, 185] that can provide reference values to be used for comparison purposes.

4.1 Description of the flow case and preliminary simulations

The flow cases considered for the purposes of the present study varied in terms of Re_τ, based on u_τ and the channel half-height δ, and grid resolution. Hence, the SGS models of interest could be assessed on a range of flow velocities and grid refinements. This resulted in test cases of increasingly larger role of the SGS model, due to the coarser grids used, in terms of Δx^+, Δy^+ and Δz^+ , as the flow bulk velocity was increasing. Four flow cases were studied with $Re_\tau = 180$, 395, 640and 1800.

In all cases, the geometry involved two parallel walls, normal to the y direction. The bulk flow was moving in the positive x direction, parallel to the wall surfaces. Figure 4.1 presents the geometry and the bulk flow direction. The extent of the flow domain in the wall-normal direction was set to $2m$. The streamwise and spanwise extent differed from case to case, to match reference DNS calculations that would be used for comparison purposes. The extents of the flow domain, Re_τ and Re_B, based on the flow bulk velocity and channel half-height, the number of grid points in each direction and Δx^+, Δy^+ and Δz^+ are presented in Table 4.1. Note that the values of Δx^+, Δy^+ and Δz^+ have been calculated using the grid resolution and the target friction velocity.

The grids employed had constant spacing in streamwise and spanwise direction. Hyperbolic tangent stretching was used for the wall-normal direction, resulting in finer grid resolution closer to the walls and coarser towards the channel centre-line.

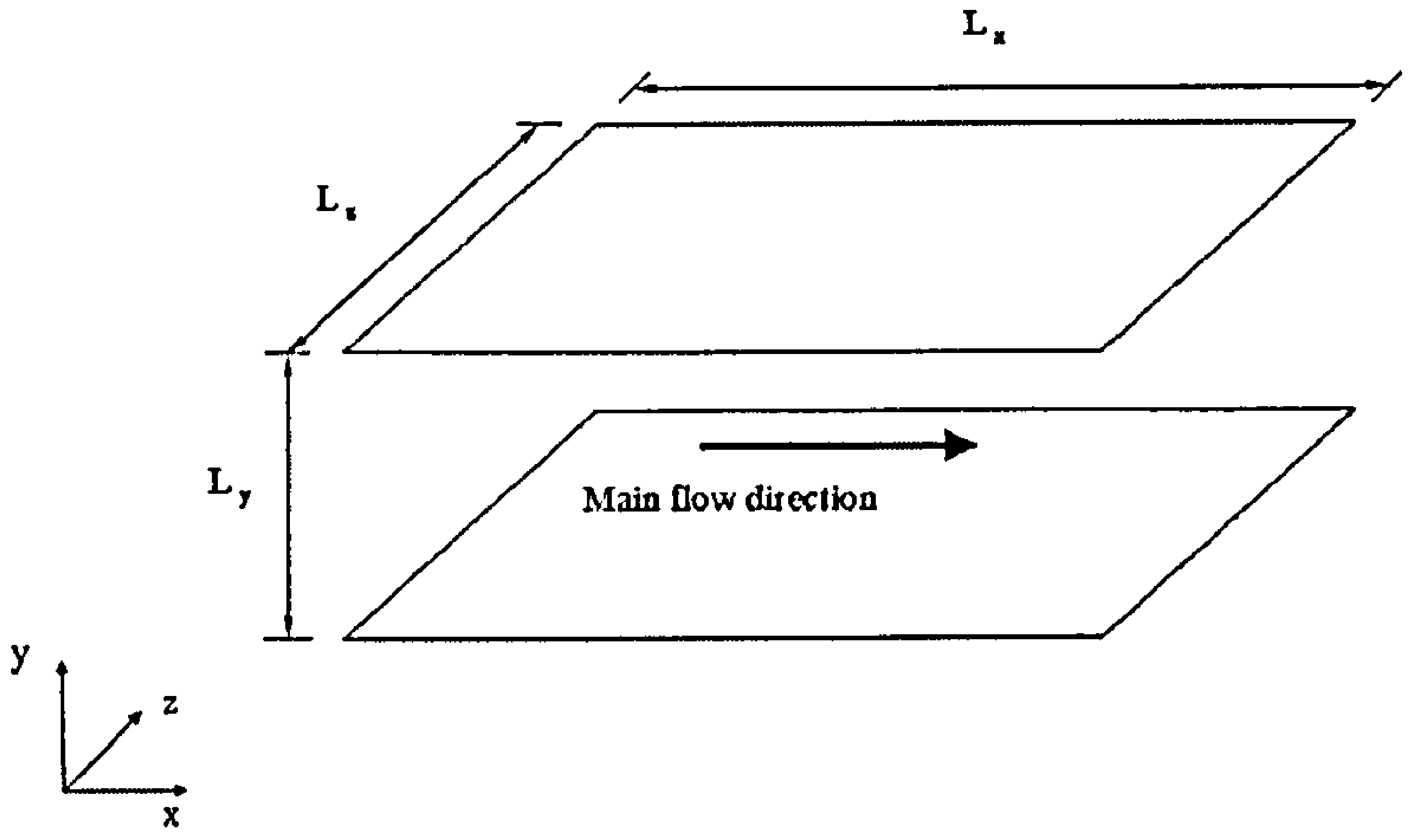

Figure 4.1: Channel geometry and bulk flow direction

Reference data used below for the first and second cases were provided by DNS calculations performed by Kim et al. [78] and Moser et al. [126]. For the $Re_\tau = 180$ simulation, Kim et al. used a $192 \times 129 \times 160$ grid to resolve the turbulent flow through a channel of dimensions

Table 4.1: Description of test cases

Case Name	Re_B	Re_τ	$L_x \times L_y \times L_z$	$N_x \times N_y \times N_z$	Δx^+	Δy^+	Δz^+
1	3000	180	$12\delta \times 2\delta \times 2\delta$	$70 \times 56 \times 38$	34	1.16-15	10
2	6960	395	$2.5\pi\delta \times 2\delta \times \pi\delta$	$64 \times 64 \times 64$	50	0.18-39	20
3	12155	640	$2.5\pi\delta \times 2\delta \times \pi\delta$	$64 \times 64 \times 64$	81	0.30-63	32
4	38000	1800	$2.5\pi\delta \times 2\delta \times \frac{\pi\delta}{2}$	$64 \times 80 \times 80$	218	0.66-136	35

$4\pi\delta \times 2\delta \times 2\pi\delta$. The resulting cell dimensions in wall units were $\Delta x^+ \simeq 12$, $0.05 < \Delta y^+ < 4.4$ and $\Delta z^+ \simeq 7$. For the $Re_\tau = 395$ simulation, Moser et al. used a $256 \times 193 \times 192$ grid, to resolve the turbulent flow through a channel of dimensions $2\pi\delta \times 2\delta \times 2\pi\delta$. Their resulting resolution in terms of wall units was $\Delta x^+ \simeq 10$, $0.05 < \Delta y^+ < 6.5$ and $\Delta z^+ \simeq 6.5$. For the third case, where $Re_\tau = 640$, reference DNS data were provided by the calculation performed by Iwamoto et al. [69]. The extent of the flow domain in that calculation was $2.5\pi\delta \times 2\delta \times \pi\delta$ and the number of points used was $288 \times 384 \times 257$ in the x, y and z direction respectively. This resulted in $\Delta x^+ = 17.7$, $0.049 < \Delta y^+ < 7.98$ and $\Delta z^+ = 5.32$. In the fourth case, the bulk Reynolds number was significantly higher, at $Re_B = 38,000$. This test case was originally presented by Piomelli [138], who used a dynamic SGS model to obtain good results. Shah and Ferziger [161] have also predicted this flow, employing a non-eddy viscosity based SGS model. Experimental results for this flow are available from the study of Wei and Willmarth [185], using a water-tunnel and Laser Doppler Anemometry, LDA, instrumentation. In the computations performed for the present study, the flow domain size and the grid resolution used matched those employed by Piomelli [138] and Shah and Fersiger [161] as given in Table 4.1.

The simulations performed can be divided into three groups. The first group consists of a series of preliminary simulations that were performed to investigate the effect of a number of computational and physical parameters on the simulation result and hence, identify the best computational setup. These simulations were performed on case 4, using the Smagorinsky model in combination with Piomelli's near-wall damping function [138] and can be seen in Table 4.2. The second group involved a second series of preliminary simulations which were performed to assess the near-wall damping function effect. These can be seen in Table 4.3. Finally, using the experience from the preliminary simulations, a final series of simulations were performed in order to assess the SGS models performance. These can be seen in Table 4.4.

In all simulations described in this Chapter, a mass scaling algorithm was used to ensure constant mass flow rate. Therefore, an accurate match of Re_B was achieved for all cases but some discrepancies were observed regarding the resulting Re_τ of the flow. Furthermore, periodic boundary conditions were used for the spanwise direction in combination with no-slip condition for the wall surfaces.

Finally all simulations presented in this Chapter run for 10 Flow Through Times, FTT, in order for the flow to develop and for another 10 FTT in order to obtain the flow statistics. Note that Reynolds stresses were obtained over the last 5 FTT since their calculation required a set of first order statistics. All case 4 preliminary simulations performed used a timestep of 0.01sec unless stated otherwise.

4.1.1 Investigation of computational setups

The most challenging of the channel flows selected to be simulated was that of $Re_\tau = 1,800$. The first preliminary simulation indicated a large over-prediction of the time-averaged non-dimensional velocity profile, over the log-law region. This was caused by an under-prediction of the shear stresses at the wall and hence, the friction velocity, which resulted in a shift of the whole distribution towards higher U^+ values. Hence, a number of simulations were performed in order to investigate the possibility of improving the prediction by the use of a better computational setup. The simulations and the parameters involved in this investigation can be seen in Table 4.2, where 'Per. In.' stands for periodic inlet, 'Fully Periodic' for periodic inlet and outlet, 'Conv. Out.' for convective outlet and 'Z/G Out.' for zero gradient outlet.

The parameters that were investigated were grid refinement, the accuracy of the pressure correction equation and the time marching scheme. Grid refinement would enlarge the range of scales captured by the grid resolution and hence could improve the solution. Furthermore it would decrease the discretisation errors. Improvement of the accuracy of the pressure correction equation and the time marching scheme could decrease the numerical error and hence provide more accurate flow solution. In addition, different values of the Smagorinsky constant were employed as well as different boundary conditions. The variation of C_s would affect the dissipation introduced by the SGS model and hence it could potentially have an impact on the resolved field. Finally, the boundary conditions also have an effect on the final solution.

Although, for comparison reasons presented in the previous section, the number of grid points was to remain the same as in the reference simulations, a grid study was performed

Table 4.2: Simulations for identification of optimum setup for $Re_\tau = 1800$ case

C_s	Poisson Iterations	Time March. Scheme	Grid	Δt	Boundary Conditions	C_f	error (%)
0.065	20	Euler Implicit	128 × 80 × 80	0.01	Per. In. - Conv. Out.	0.002805	-36.2
0.065	20	Euler Implicit	64 × 80 × 160	0.01	Per. In. - Conv. Out.	0.003003	-31.70
0.065	20	Euler Implicit	64 × 80 × 80	0.01	Per. In. - Conv. Out.	0.003127	-28.89
0.065	20	Euler Implicit	64 × 100 × 80	0.01	Per. In. - Conv. Out.	0.003025	-31.20
0.065	20	Euler Implicit	64 × 120 × 80	0.01	Per. In. - Conv. Out.	0.003059	-30.42
0.065	20	Euler Implicit	64 × 160 × 80	0.01	Per. In. - Conv. Out.	0.002995	-31.87
0.065	12	Euler Implicit	64 × 80 × 80	0.01	Fully Periodic	0.002795	-36.43
0.065	20	Euler Implicit	64 × 80 × 80	0.01	Fully Periodic	0.002963	-32.61
0.065	20	Euler Implicit	64 × 80 × 80	0.0025	Fully Periodic	0.003363	-23.52
0.065	20	Runge-Kutta	64 × 80 × 80	0.0025	Fully Periodic	0.003478	-20.90
0.1	20	Euler Implicit	64 × 80 × 80	0.01	Fully Periodic	0.002988	-32.05
0.065	20	Euler Implicit	64 × 80 × 80	0.01	Per. In. - Z/G Out.	0.002806	-36.18

to identify the importance of the grid resolution in the final prediction of the computed flow field. Towards this intention, six simulations were performed using the Smagorinsky model in combination with Piomelli's near-wall damping function. The grid resolutions used are summarised in Table 4.2. The first three had double the number of points in each direction at a time. The predicted wall-normal U^+ distribution is presented in Figure 4.2. The rest had increased number of points only in y direction and their U^+ prediction can be seen in Figure 4.3, where "y refinement 1" represents the baseline grid of 64 × 80 × 80, "y refinement 2" represents the refined grid of 64 × 100 × 80, "y refinement 3" represents the refined grid of 64 × 120 × 80 and "y refinement 4" represents the refined grid of 64 × 160 × 80. As can be seen from Figure 4.3, y refinement did not make any significant difference at all.

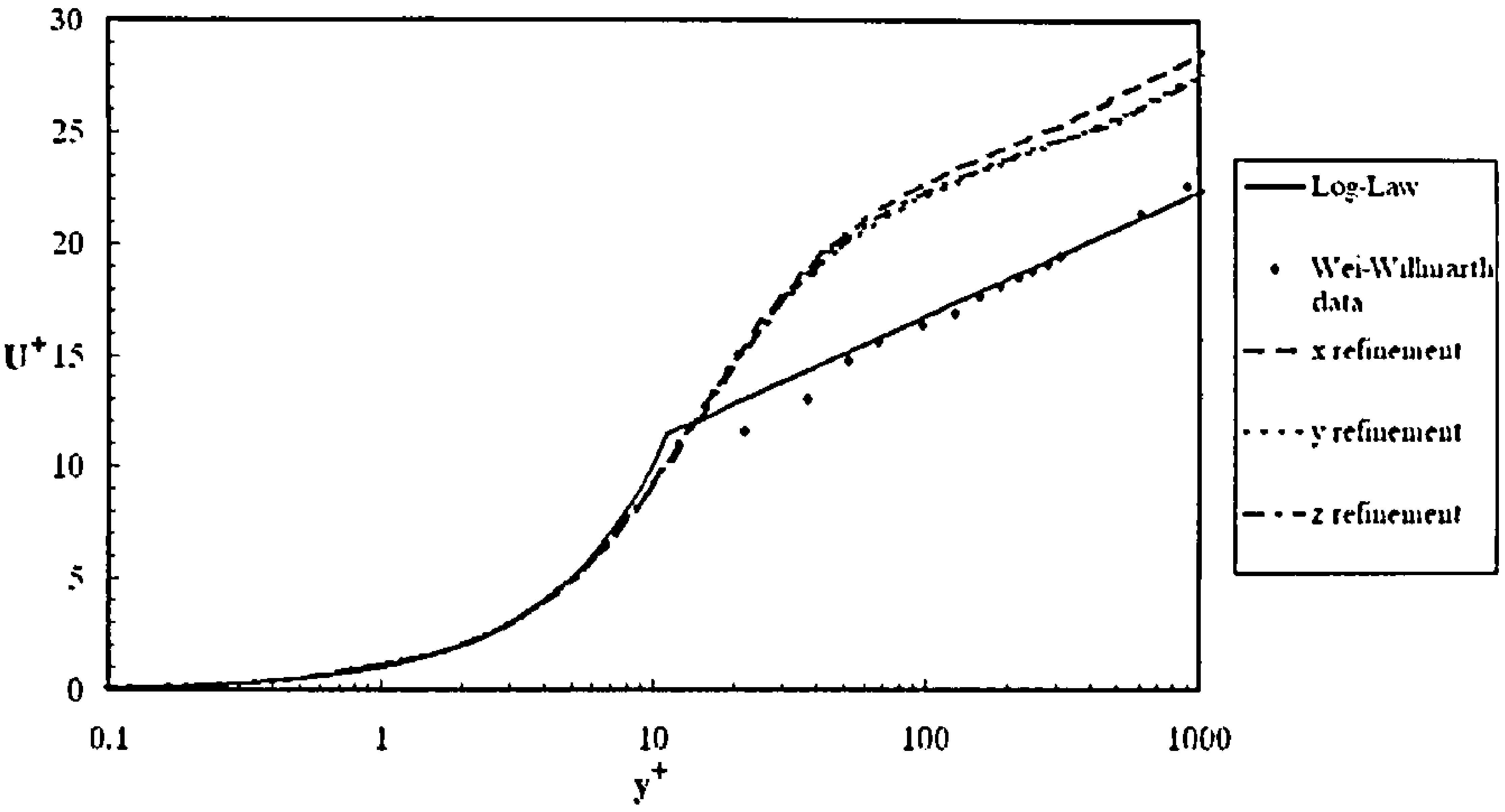

Figure 4.2: Effect of grid refinement on wall-normal U^+ distribution

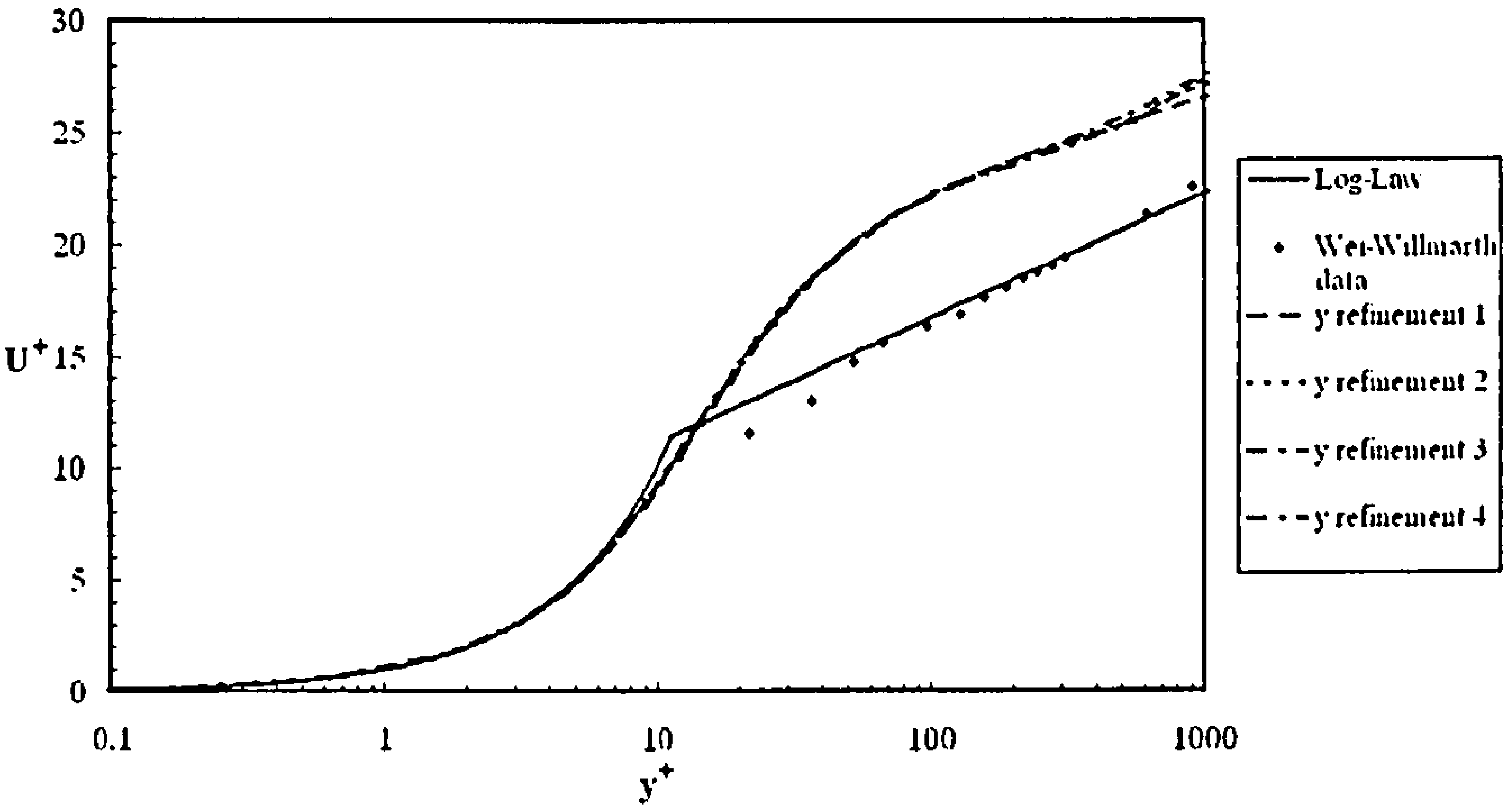

Figure 4.3: Effect of grid refinement in y direction, on wall-normal U^+ distribution

The error in the predicted skin friction coefficient C_f for each simulation can be seen in Table 4.2. For the calculation of the error, the empirical formula proposed by Dean [27] was used, according to which, C_f is given as:

$$C_{f\,Dean} = 0.073 \left(\frac{2U_B}{\nu}\right)^{-1/4} \tag{4.1}$$

The error in the C_f prediction was then calculated according to Shah and Ferziger [161] as:

$$e_{C_f} = \frac{C_f - C_{f\,Dean}}{C_{f\,Dean}} \tag{4.2}$$

The predicted values show that grid refinement in each direction separately had little effect on the computed C_f. In all cases the under-prediction error was similar, resulting in an over-prediction of the velocity profile, over the log-law region. This can be seen in both Figures 4.2 and 4.3. However, increasing the number of points in x and y direction by a factor of two, showed an improvement in the prediction of the log-law region slope. This was an indication that the spanwise resolution was adequate, while there was some space for improvement in the other two directions, at a corresponding computational cost.

The limited improvement can be explained, if Eq.2.4, which was employed to provide the length scale used by the Smagorinsky model, is taken under consideration. By performing grid refinement in one direction at a time, it would require 8 times more grid points in the direction of grid refinement, only to reduce the length scale employed by half, due to the presence of the cubic root in Eq.2.4. Hence, by increasing the grid resolution in each direction separately, by a factor of two, the resulted reduction of the effective length scale is only 20%. However, the results indicated that this was not adequate for a significant improvement. Therefore, it was decided to use the initial grid of the $64 \times 80 \times 80$ nodes, which could also provide a direct comparison with other published results on the same case [161, 172].

The second parameter that was investigated was the number of iterations required for the accurate solution of the Poisson type equation, responsible for the calculation of the pressure correction. Two simulations were performed with the same computational setup but different number of iterations; in the first 12 iterations were used while in the second 20. The results can be seen in Figure 4.4. As expected, the more iterations performed, the more accurate the solution and hence the prediction of the time-averaged flow field. Therefore, in all simulations performed the number of iterations required for the solution of Poisson equation was set to 20.

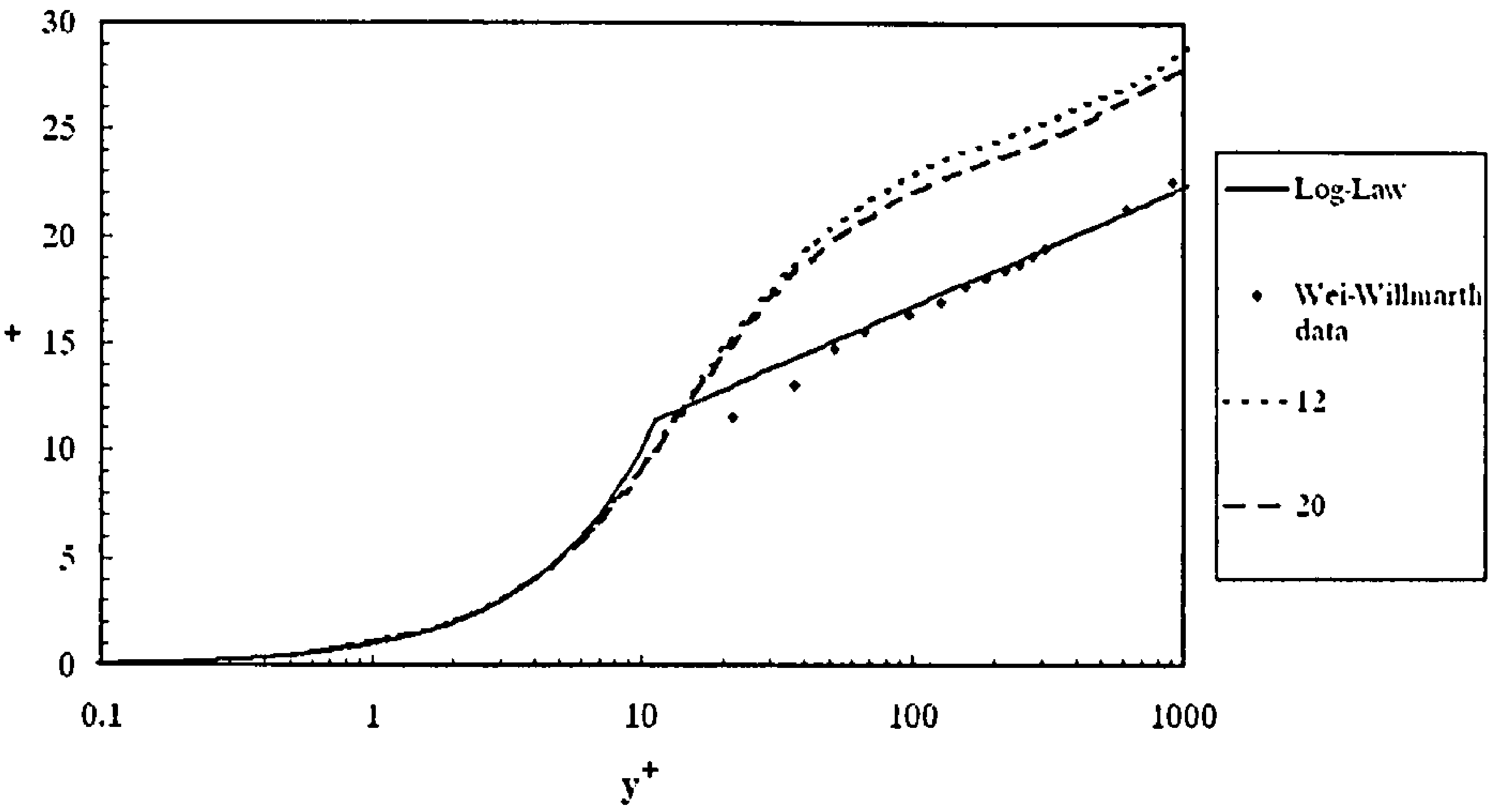

Figure 4.4: Effect of number of iterations of Poisson equation on wall-normal U^+ distribution

The next computational parameter that was investigated was the time marching scheme. In DELTA there were two schemes available; Euler implicit of 1^{st} order and the 3-stage Runge-Kutta explicit scheme of 3^{rd} order of accuracy. Both were tested and the results can be seen in Figure 4.5 and in Table 4.2.

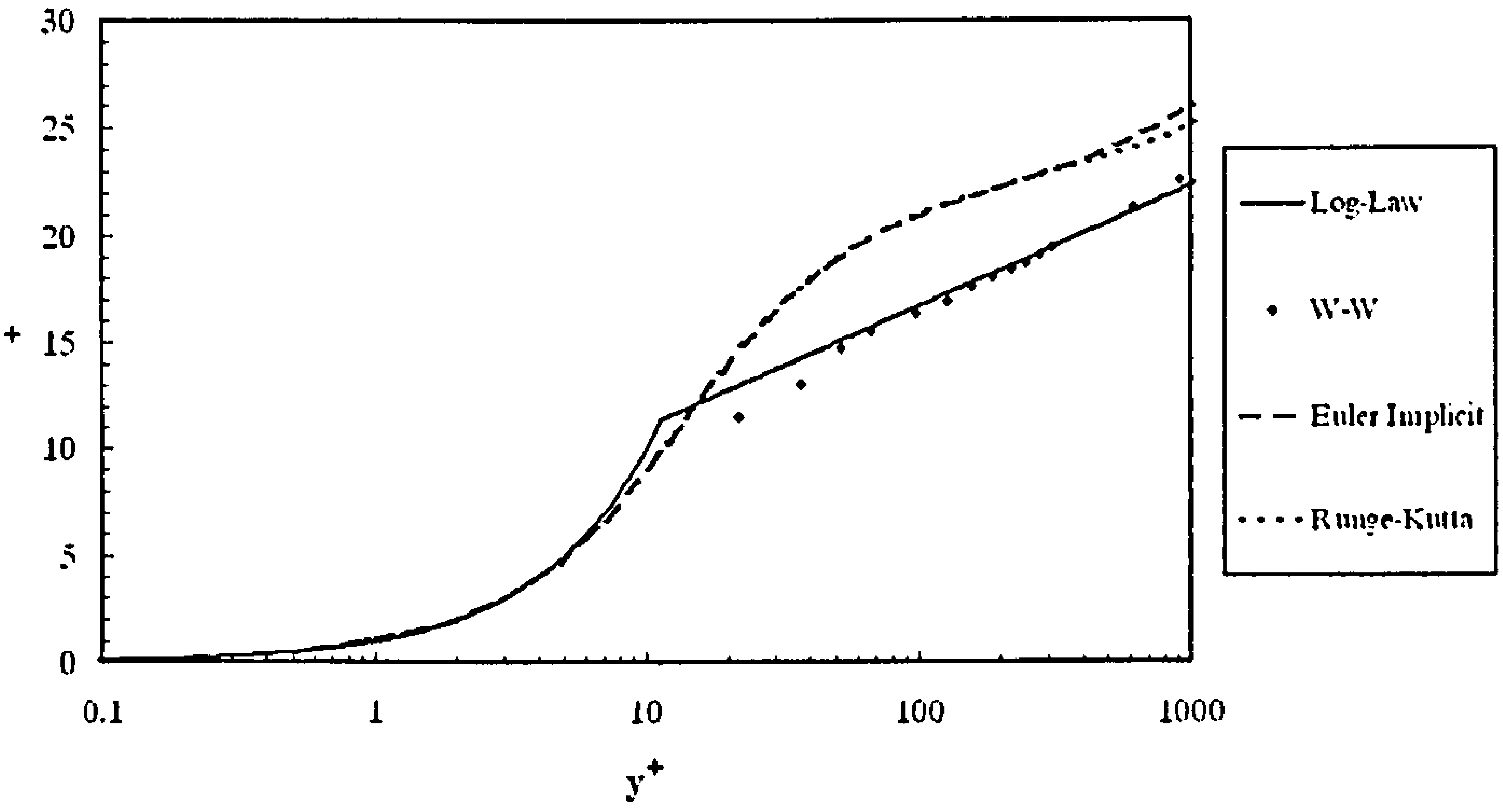

Figure 4.5: Effect of time marching scheme on wall-normal U^+ distribution

It should be noted that these two simulations were performed with a timestep which was a quarter of that used for the rest of the preliminary simulations, corresponding to a Courant Friedrichs Levy, CFL, number of 0.3. This was required in order to achieve a CFL number less than 1.0 and hence avoid any stability problems when using the Runge-Kutta scheme. As can be seen, with the fine timestep, the two schemes, although of different accuracy, gave similar results. Considering the significantly larger cost of the Runge-Kutta method, it can be seen that in cases of fine timestep, the savings in computational time can outweigh the small difference in the accuracy.

A further comment related to the timestep is that it affected significantly the flow resolution and hence the prediction of the near-wall stresses. Comparing the error in C_f between simulations that employed the same time marching scheme but different timestep, it can be seen that a decrease of about 10% was achieved by the finer timestep simulation. This observation was in accordance to the general conclusions made by Choi and Moin [18], who pointed out that even for CFL numbers of 0.5, the time filtering effects on a plane channel were significant, due to the inability of turbulence to be maintained numerically if the timestep is larger than the characteristic time associated with the smallest scales in the flow [155].

It should be noticed at this point that the majority of the preliminary simulations were performed using large timestep and Euler implicit scheme in order to decrease the computational time required. This was considered to be acceptable for these simulations since the objective was to investigate qualitatively the effect of the various parameters rather than obtaining quantitatively accurate results.

In the enlightenment of the observations related to the timestep, another further suggestion can also be made, related to the grid refinement investigated previously. A possible reason for the limited improvement might well be the fact that, despite the improved spatial resolution introduced, the use of large timestep implied the application of coarse time filtering that affected a considerable portion of the small scales structures that could have been spatially resolved. As a result, these scales were not resolved properly, limiting the expected improvement of the final results.

The fourth factor that was examined was the value of C_s. Although this was applicable only to Smagorinsky model, it could provide an indication of the degree of sensitivity of the flow to the action of the SGS model. Two simulations were performed with $C_s = 0.065$ and $C_s = 0.1$, which are both values suggested in literature for plane channel flows [48, 28]. Figure 4.6 shows the results in terms of wall-normal distribution of U^+. As it can be seen, the difference was very small, with the simulation using $C_s = 0.065$ giving a slightly better behaviour in terms of the mean slope of the log-law region. The small variation between the two simulations was also reflected in the prediction of C_f as can be seen from Table 4.2. Considering both the predicted wall-normal U^+ distribution and the C_f value, it was decided to use $C_s = 0.065$ for case 4 simulations.

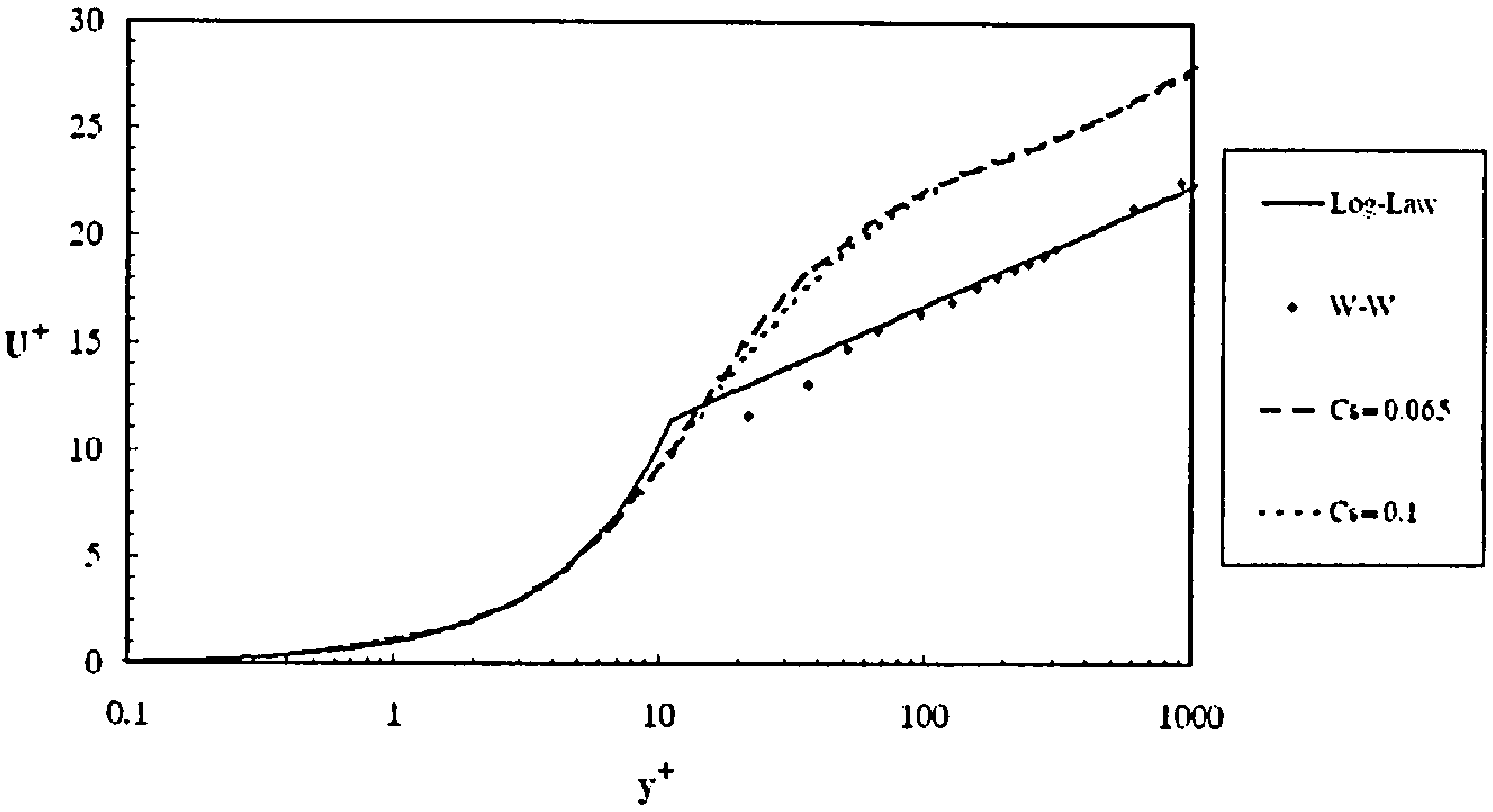

Figure 4.6: Effect of C_s on wall-normal U^+ distribution

Finally, the boundary conditions were investigated with the data gathered from three simulations; the first with periodic boundary conditions on both inlet and outlet, the second with periodic condition on the inlet and convective on the outlet and the third with periodic conditions at the inlet and zero gradient (Z/G) at the outlet. The results can be seen in Figure 4.7 in terms of U^+ distribution and in Table 4.2 in terms of the predicted skin friction coefficient and the corresponding error relative to Dean's prediction.

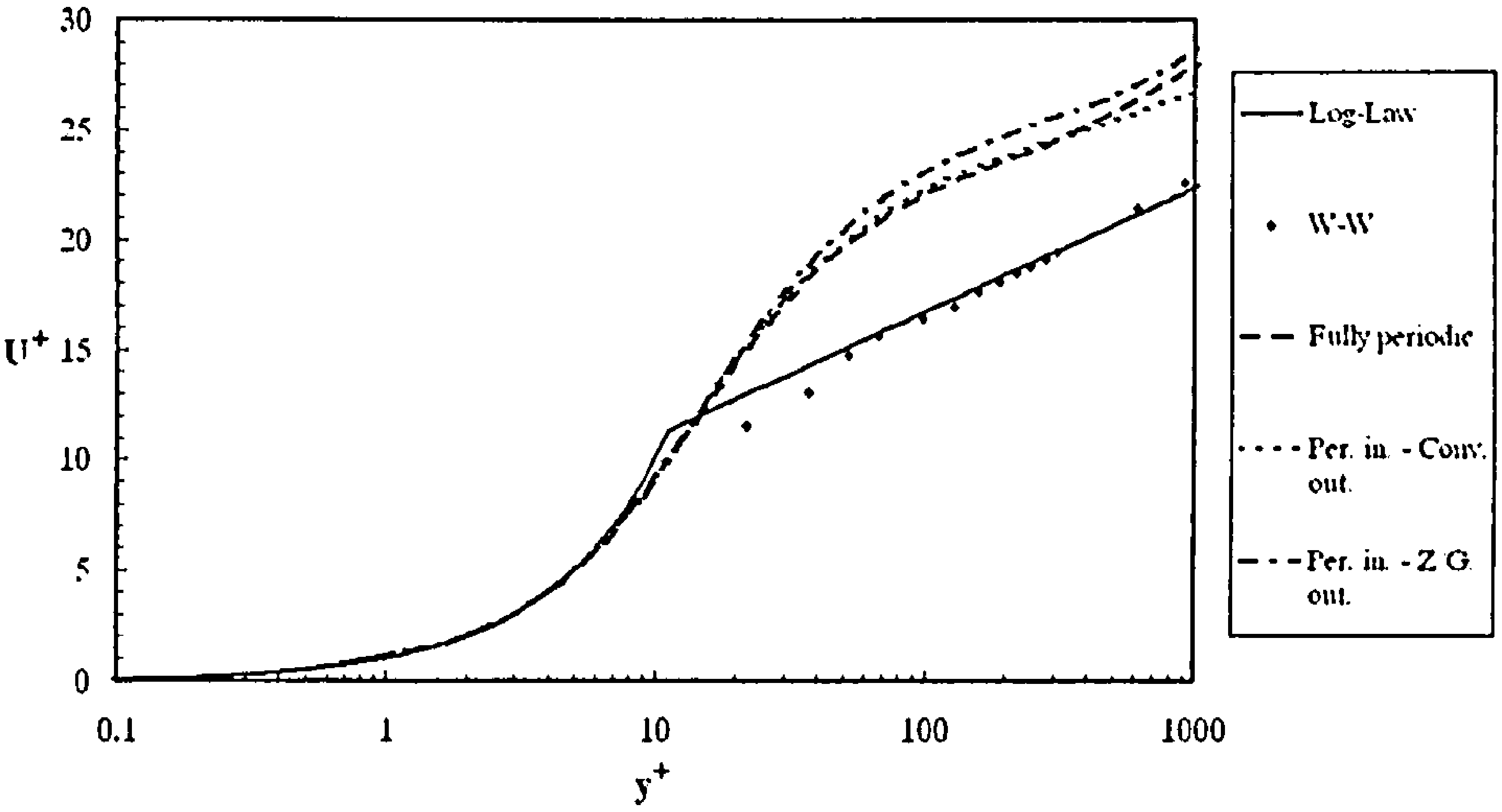

Figure 4.7: Effect of boundary conditions on wall-normal U^+ distribution

The use of different boundary conditions had an impact on the predicted flow field. The effects were more pronounced in the near-wall region and in the wake region. This can be seen in the variation of the C_f prediction and in Figure 4.7, which shows that in the wake region, the predicted mean flow field was different for each simulation.

The least accurate boundary condition from all three combinations tested was that of periodic inlet and zero gradient outlet. In principle, such a condition for the outlet plane of a fully developed turbulent unsteady flow is not correct since the instantaneous velocity spatial gradients in the streamwise direction cannot be zero throughout the duration of the simulated time. This is even more pronounced if there is coarse grid resolution in this direction, as in the case of the grid used, where $\Delta x^+ = 218$.

Regarding the other two combinations investigated, both have been used for this case in the past with good results [138, 172]. Both can successively reproduce the unsteadiness of the turbulent flow field and hence give accurate predictions. This was also reflected in the results obtained in the present study that showed a close similarity, in the C_f prediction and the slope of the log-law region. In terms of C_f, the most accurate prediction was given by the simulation employing periodic inlet and convective outlet conditions. However, this simulation did not reproduce correctly the mean log-law region slope, which was represented more accurately by the use of fully periodic conditions. Taking into account the small variation in C_f and the improved behaviour over the log-law region, it was decided that fully periodic boundary conditions should be employed for the rest of the simulations.

4.1.2 A note on the role of variable arrangement

As it was described in section 4.1.1, a number of parameters were investigated in order to improve the results obtained in case 4. From the study performed, it was realised that the largest improvement was achieved by the use of a finer timestep. Still, the error in the prediction of C_f was not insignificant, comparing to the results obtained by other studies of the same case [161]. One possible reason for this discrepancy could be related to the energy non-conservation properties of the collocated variable arrangement.

Previous studies on case 4 [161, 138, 172] that made use of Smagorinsky model, presented improved results in terms of C_f, comparing to those obtained by the present study. The main difference between those studies and the present was the use of staggered variable arrangement codes, in contrast to the collocated variable arrangement used by the code employed here. Other published results on this case [53], which also made use of the collocated arrangement showed similar accuracy levels to those of the present study. Despite the possible differences among the codes used, in terms of the implementation of discretisation and time marching schemes, this observation could suggest that staggered grid codes may be less sensitive to grid resolution due to their energy conservation properties, compared to collocated variable arrangement codes. This observation is in accordance to Morinishi study, which indicated that the numerical error generated by collocated variable arrangement was larger than that produced by a staggered arrangement, for the same discretisation schemes [125].

This effect becomes more important with the *Re* number of the flow tested [125] as well as the grid resolution used. This can be seen by comparing the results obtained for case 1 and 4, using DELTA and LU-LES. The latter is a finite volume code that solves the filtered Navier-Stokes equations in conserved form, using staggered variable arrangement, Adams-Bashforth scheme for time stepping and multi-grid method for the solution of Poisson equation of pressure[172, 198].

Case 1 and 4 were tested using the same computational setup. The results of LU-LES were courtesy of Dr. M. Dianat and Dr. G. Tang. The resulted wall-normal U^+ distributions can be seen in Figure 4.8. Both codes gave almost identical results for case 1, where *Re* was low and the grid resolution relatively fine. However, in case 4, the staggered code outperformed the collocated one, giving significantly more accurate predictions.

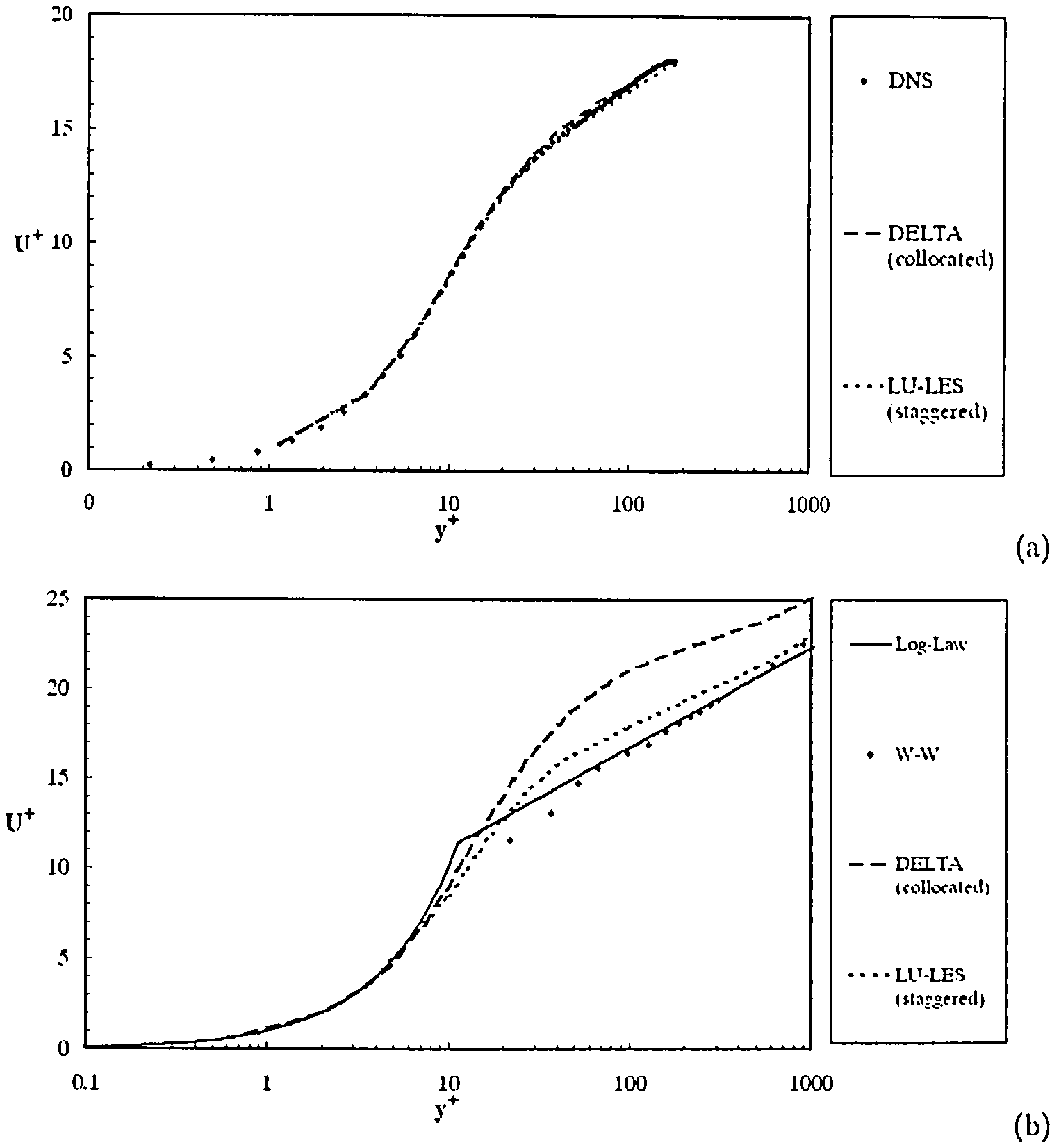

Figure 4.8: Comparison of staggered and collocated variable arrangement for case 1 (a) and 4 (b)
(LU-LES case 1 results courtesy of Dr. M. Dianat, LU-LES case 4 results courtesy of Dr. G. Tang)

4.1.3 Investigation of near-wall effects

The second group of preliminary simulations was concerned with the investigation of the effect of the near-wall damping function on the final predicted flow field. Due to the variation of eddy viscosity levels introduced by each SGS model, different levels of damping are required for each model to achieve the best possible results. In that respect the same near-wall damping function may give accurate results when used in combination with one SGS model but perform purely when used with another. Therefore, a study was performed to identify the best combination of SGS model and near-wall damping function for all models of interest.

Towards this objective, six simulations were performed, as listed in Table 4.3. Three of them were concerned with the Smagorinsky model and three with the k_{sgs}-equation model. The MS model was not tested with other than the Yoshizawa near-wall damping function [196]. This model was coded in order to assess the implementation of the Yoshizawa near-wall damping function [196] and therefore it was not considered for the investigation of any other near-wall damping function. Finally, the ESD model was initially tested in combination with the Yoshizawa function but, the resulted dissipation levels led to extensive damping of turbulent activity throughout the flow field. Therefore, the ESD model was only used in combination with the function proposed by Inagi [68].

It should be noted at this point that these simulations were performed to assist a quantitative comparison of the near-wall functions. Therefore, as in the previous simulations, Euler implicit time marching scheme was used in combination with a coarse timestep, in order to decrease the computational time. This was the main reason for the large discrepancies between the calculated C_f values and those predicted by Dean's formula. As can be seen in the following sections, these predictions were significantly improved when a finer timestep was employed.

Table 4.3: Simulations for the assessment of near-wall functions on the Smagorinsky and k_{sgsg}-equation model

Case Name	Model	NW Treatment	C_f	error (%)	U_C/U_B	error (%)
3	Smag	van Driest	0.004701	-19.68	1.124	-1.26
3	Smag	Piomelli	0.004644	-20.64	1.118	-1.79
3	Smag	Yoshizawa	0.004176	-28.64	1.132	-0.58
4	k_{sgs}-eqn	van Driest	0.002939	-33.17	1.098	-2.25
4	k_{sgs}-eqn	Piomelli	0.002737	-37.74	1.088	-3.19
4	k_{sgs}-eqn	Yoshizawa	0.002980	-32.23	1.108	-1.42

The wall-normal variation of U^+ obtained by the simulations presented in Table 4.2 can be seen in Figure 4.9 for $Re_\tau = 640$, and in Figure 4.10 for $Re_\tau = 1800$. The corresponding normal stresses can be seen in Figures 4.11 and 4.12 respectively.

As can be seen from Figures 4.9 and 4.10, near-wall damping functions can affect the predicted flow field to a significant degree. Mainly due to the suppression of the dissipative action of the SGS model in the near-wall region, near-wall damping functions can play an important role in the accuracy of the stresses prediction at the wall and hence the friction velocity. Therefore, they can affect the whole wall-normal U^+ distribution.

Van Driest [181] and Piomelli [138] used the non-dimensional wall-normal distance in combination with the exponential function in order to produce a damping that was quite intense in the viscous sublayer and lower buffer layer, but recovering quickly to one in the rest of the boundary layer.

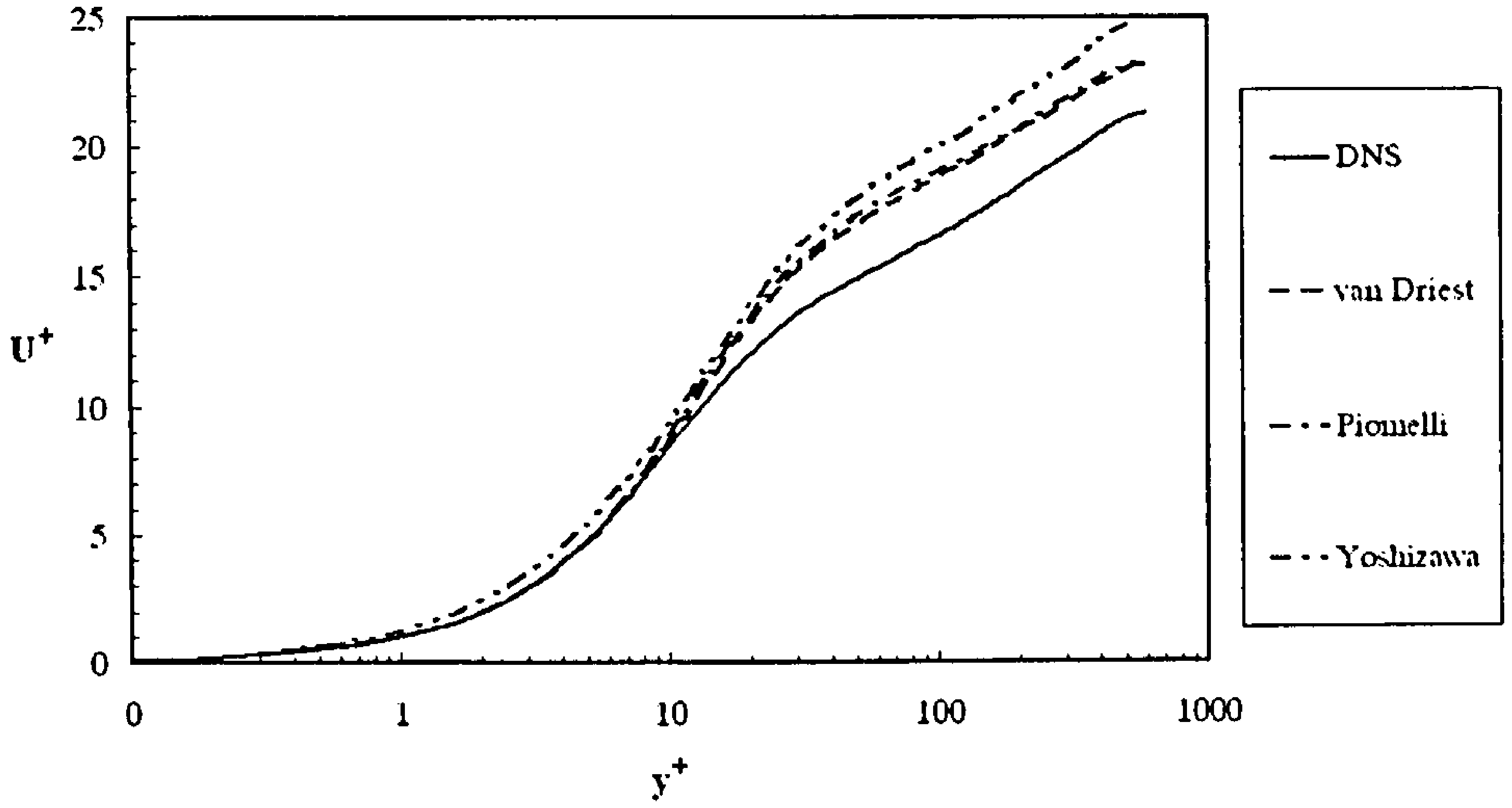

Figure 4.9: U^+ vs. y^+ using different near-wall functions for $Re_\tau = 640$ (Smagorinsky model)

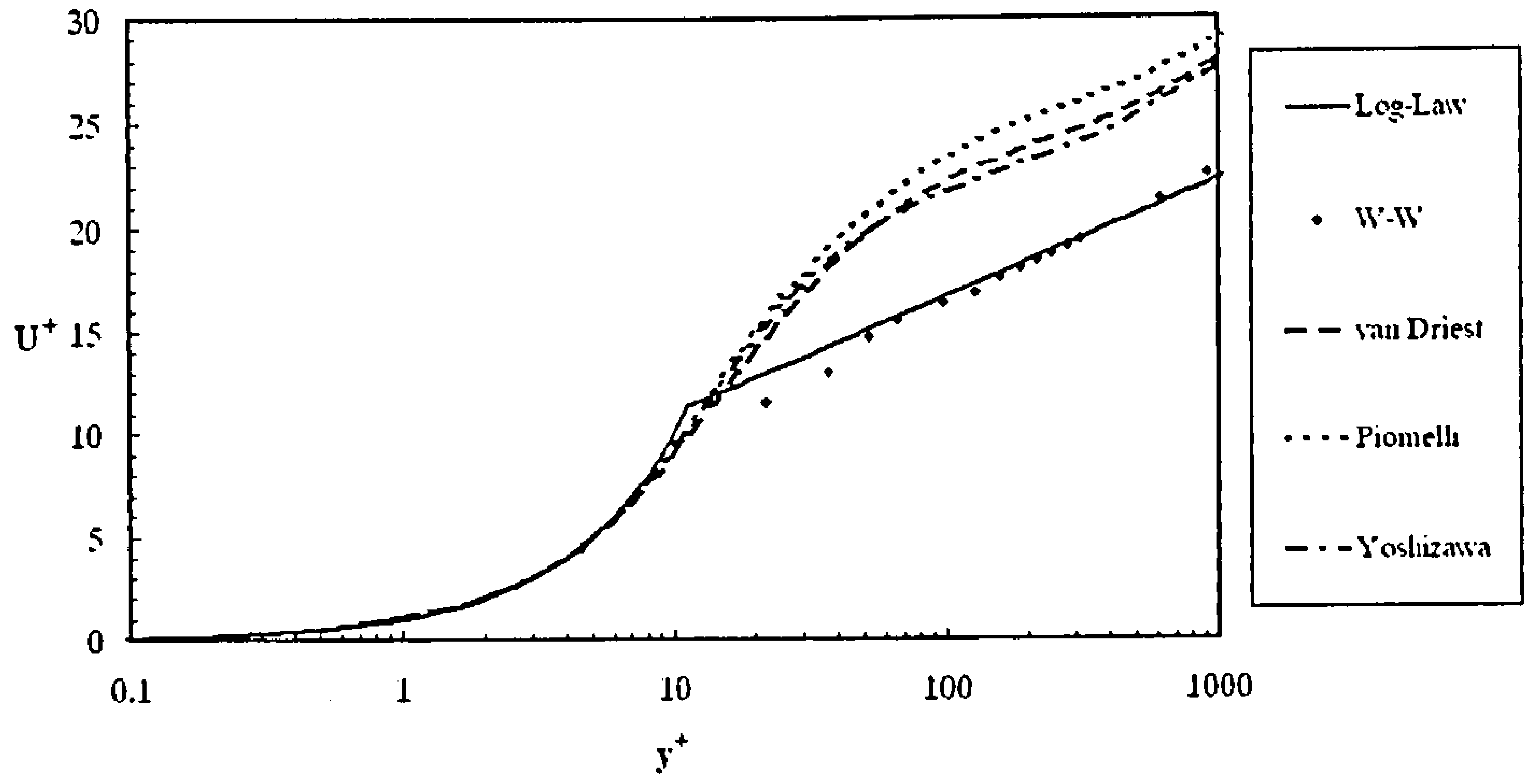

Figure 4.10: U^+ vs. y^+ using different near-wall functions for $Re_\tau = 1800$ (k_{sgs}-equation model)

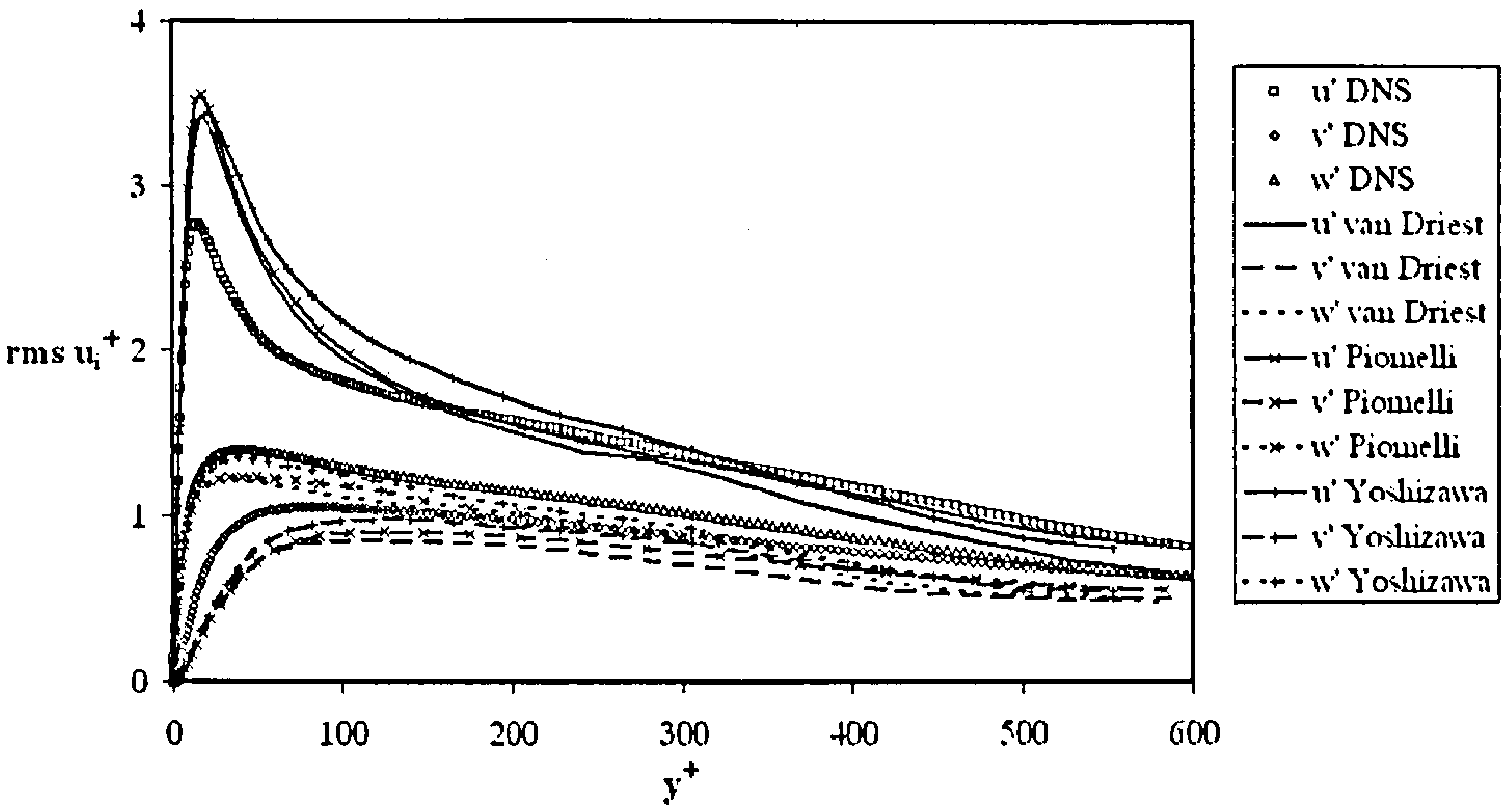

Figure 4.11: Rms values of $\overline{u'}^+$, $\overline{v'}^+$ and $\overline{w'}^+$ vs. y^+ using different near-wall functions for $Re_\tau = 640$ (Smagorinsky model)

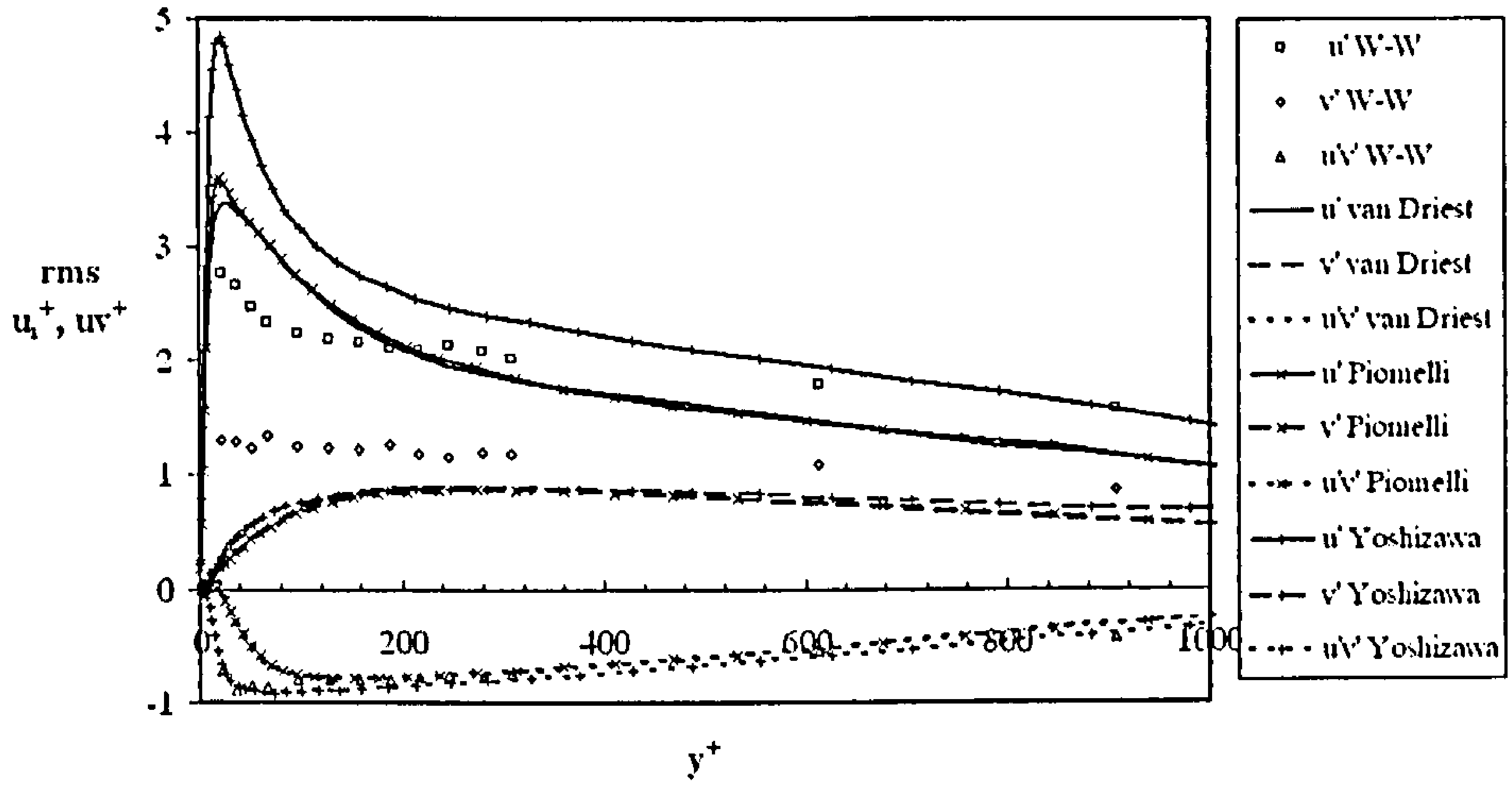

Figure 4.12: Rms values of $\overline{u'}^+$, $\overline{v'}^+$ and $\overline{u'v'}^+$ vs. y^+ using different near-wall functions for $Re_\tau = 1800$ (k_{sgs}-equation model)

Yoshizawa employed a different approach in an effort to avoid the use of wall-normal distance, which can be difficult to compute in some, even simple, geometries. Instead of y^+, Yoshizawa et al. [196] used $\frac{\overline{\Delta}\,\overline{S}}{\sqrt{2k_{sgs}}}$, which can be interpreted as the ratio of the resolved velocity scale U_{RG}, to the subgrid velocity scale U_{SG}. The fundamental idea behind this formulation is that in the vicinity of the solid wall, k_{sgs} decreases while $\overline{S}$ remains non-vanishing. With increasing distance from the wall, k_{sgs} increases and $\overline{S}$ decreases rapidly in general [196]. As a result, the exponential term of the near-wall function decreases and therefore the function goes to one as we move away from the wall. Hence, using physical parameters only, a function can be obtained with correct behaviour in both viscous regions and fully resolved regions.

As far as the Smagorinsky model was concerned, the van Driest and Piomelli functions resulted in the most accurate U^+ distributions, with the Piomelli function giving a slightly more pronounced overshooting over the buffer region. The Yoshizawa function resulted in the largest overshooting of the log-law region and therefore the least accurate results. This can be seen in Figure 4.9.

In terms of Reynolds stresses, both the van Driest and the Piomelli function gave the most accurate $\overline{u'}^+$distributions, with Piomelli giving slightly better results except for the $\overline{u'}^+$ prediction in the near-wall region, which indicated higher overshooting relative to the other two functions. This can be seen in Figure 4.11.

In the same Figure, it can be seen that Yoshizawa function gave the most accurate $\overline{v'}^+$ and $\overline{w'}^+$distributions, while it resulted in a considerable over-prediction of $\overline{u'}^+$ in the region of $70 < y^+ < 280$. It seems that the use of the $-\left(C_w\frac{\sqrt{2k_{sgs}}}{S\Delta}\right)^2$ term in the exponential function, introduces higher damping to the eddy viscosity in the near-wall region than the $-\left(\frac{y^+}{A^+}\right)$ term and this results in less diffusion introduced by the SGS model. Therefore, the use of $-\left(C_w\frac{\sqrt{2k_{sgs}}}{S\Delta}\right)^2$ leads to increased levels of near-wall turbulence activity. As a result, the accuracy of $\overline{v'}^+$ and $\overline{w'}^+$that are usually under-predicted by the SGS model, has been improved while the $\overline{u'}^+$ overshooting which is usually observed is even more pronounced.

Based on the performance of the tested functions on both U^+ and Reynolds stresses distributions, it was decided that the Smagorinsky model would be used in combination with the Piomelli function.

Case 4 was used to assess the use of the van Driest, Piomelli and Yoshizawa functions with the k_{sgs}-equation model. As it can be seen from Figure 4.10, Yoshizawa gave the best overall distribution and Van Driest the worst. This was also reflected in the prediction of C_f, as can be seen in Table 4.3.

Similar behaviour can also be seen in terms of the predicted stresses in Figure 4.12. For the reasons explained earlier Yoshizawa function provided accurate predictions for $\overline{v'}^+$ and $\overline{u'v'}^+$ but it highly over-shooted for $\overline{u'}^+$.

Based on the overall behaviour observed, the k_{sgs}-equation model would be used in combination with the Yoshizawa near-wall damping function in all subsequent simulations.

4.2 Results and discussion on channel flow

The preliminary simulations described in the previous sections served the purpose of identification of the optimum computational setup and the effect of different near-wall functions on the accuracy of the predicted flow field. Taking into consideration the results of these computations, a final series of simulations was performed. In these simulations, the Smagorinsky model was used in combination with Piomelli's near-wall function [138], MS and k_{sgs}-equation model in combination with Yoshizawa function [196] and ESD model in combination with Inagi function [68]. The cases tested as well as the results in terms of C_f and U_C/U_B can be seen in Table 4.4.

Table 4.4: Simulations for the assessment of SGS models

Case Name	Model	C_f	error (%)	U_C/U_B	error (%)
1	Smag	0.008351	0.66	1.145	-1.04
2	Smag	0.005665	-15.71	1.140	-0.52
3	Smag	0.004428	-24.27	1.135	-0.35
4	Smag	0.003478	-20.90	1.079	-4.00
1	MS	0.008459	1.96	1.146	-0.95
2	MS	0.006180	-8.04	1.138	-0.70
1	k_{sgs}-eqn	0.008427	1.58	1.147	-0.86
2	k_{sgs}-eqn	0.006282	-6.51	1.150	0.35
3	k_{sgs}-eqn	0.004874	-16.63	1.140	0.09
4	k_{sgs}-eqn	0.003707	-15.67	1.074	-4.45
1	ESD	0.008731	5.25	1.150	-0.61
2	ESD	0.006701	-0.30	1.157	0.96
3	ESD	0.005694	-2.60	1.147	0.70
4	ESD	0.004611	4.89	1.096	-2.49

The results of the channel flows simulated were divided into four groups. The first group was related to the mean flow properties of the computed flow fields, while the other three groups were related to information of turbulence related quantities. Hence, the second group of the results presented the distribution of turbulent stresses, the third group presented the coherent structures observed in the instantaneous flow field and finally the fourth group presented the distribution of the second and third invariants of the anisotropic stress tensor to verify the realisability of the results.

The time-averaged statistics used for the analysis of the results were obtained using instantaneous data gathered over twelve flow-through times, in order to ensure fully converged statistical properties.

4.2.1 Mean flow field characteristics

The first flow variable that was investigated was the time-averaged, streamwise velocity component $\langle \overline{u} \rangle$. Due to the periodicity of the test case in the streamwise and spanwise direction, the distributions that were generated were referring only to the wall-normal variation of this variable. Note that for all flow conditions tested, the description and theoretical analysis given in section 1.1.1 and 1.1.2 do apply. Therefore, apart from available DNS or experimental data, the non-dimensional velocity profile given by the log-law was also used as a reference data.

Figures 4.13, 4.14, 4.15 and 4.16 show the results of the mean flow field, in terms of the U^+ distribution, for Re_τ = 180, 395, 640 and 1800 respectively. In all figures presented, the Smagorinsky model's results were labelled as '*Smag.*', the Mixed Scale model's as '*MS*', the new model's as '*ESD*', Yoshizawa and Horiuti model's [195] as '$ksgs - eqn$' and DNS data [78, 69] as '*DNS*'. In case 4, the reference data used was provided by the experiments of Wei and Willmarth [185], labelled as '*W-W*'.

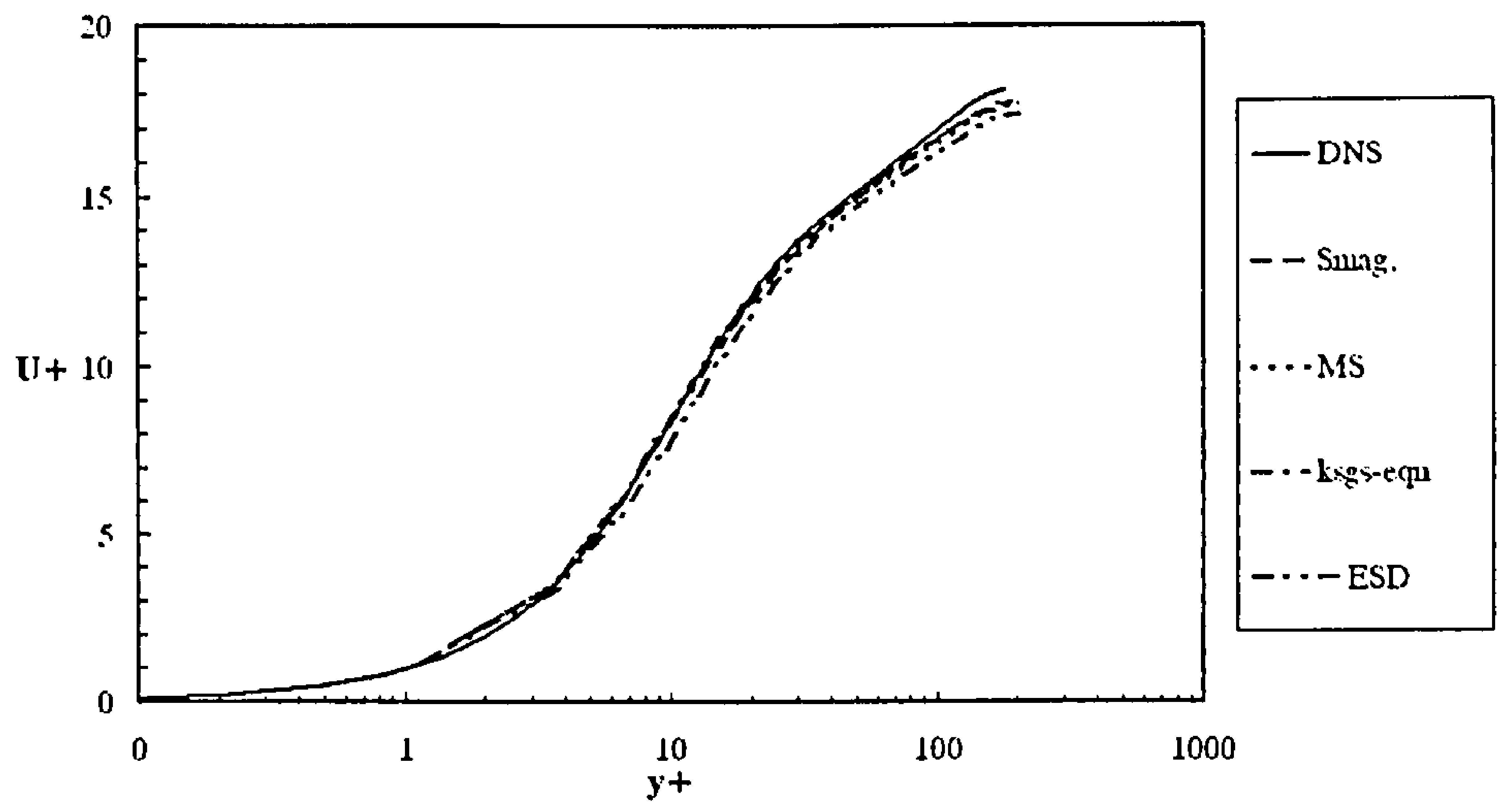

Figure 4.13: $U^+ vs. y^+$ for $Re_\tau = 180$

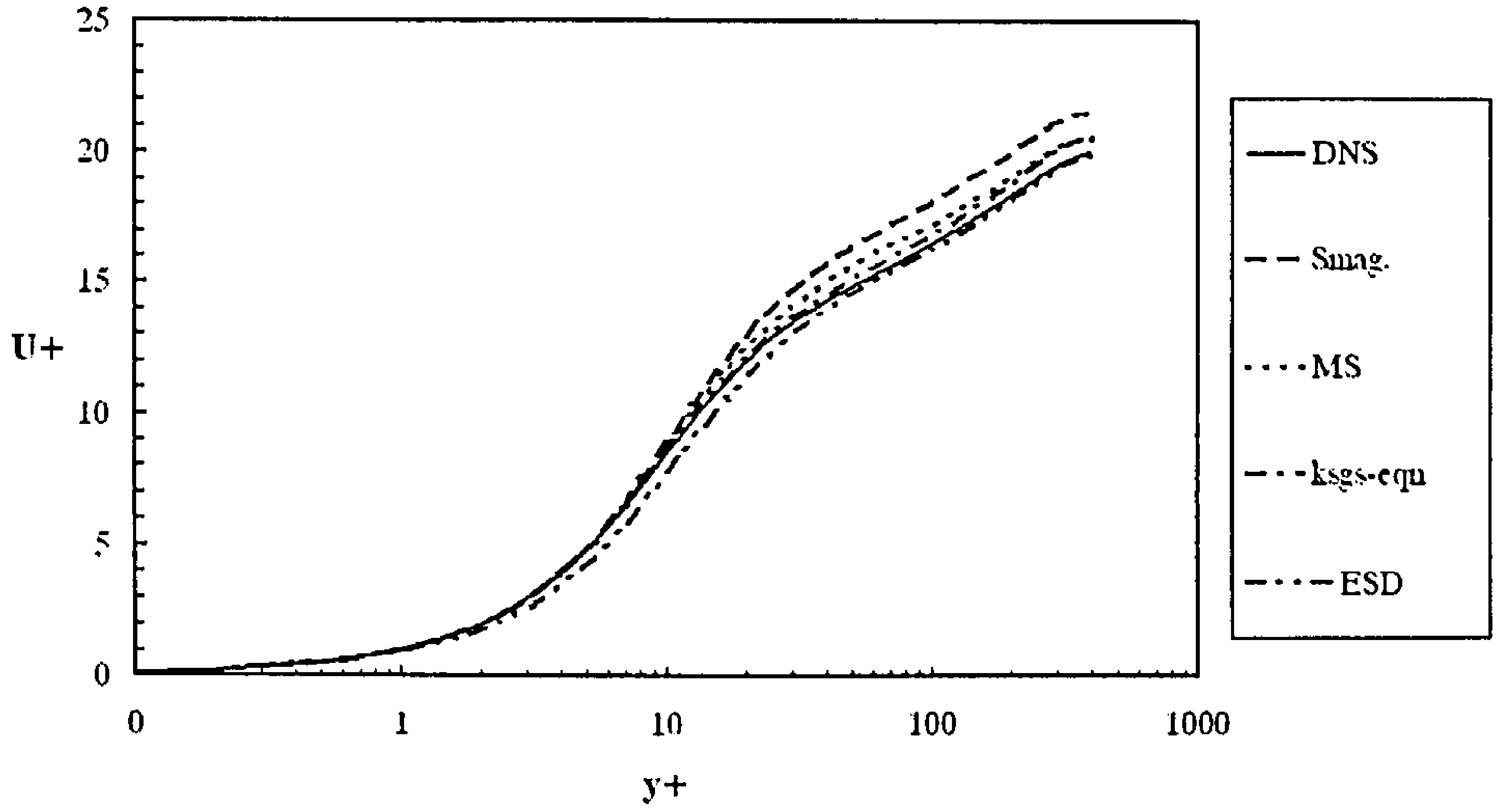

Figure 4.14: $U^+ \, vs. \, y^+$ for $Re_\tau = 395$

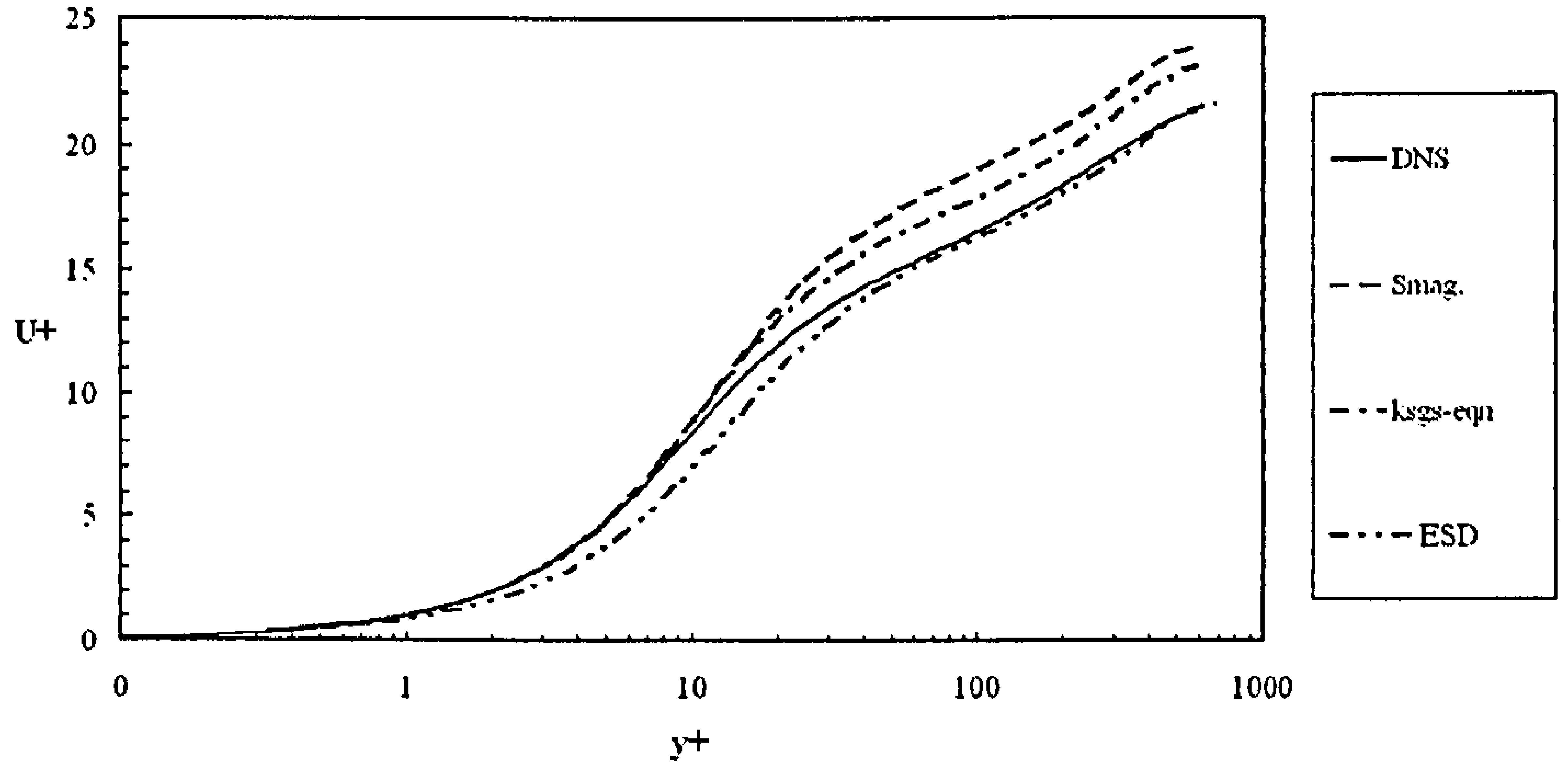

Figure 4.15: $U^+ \, vs. \, y^+$ for $Re_\tau = 640$

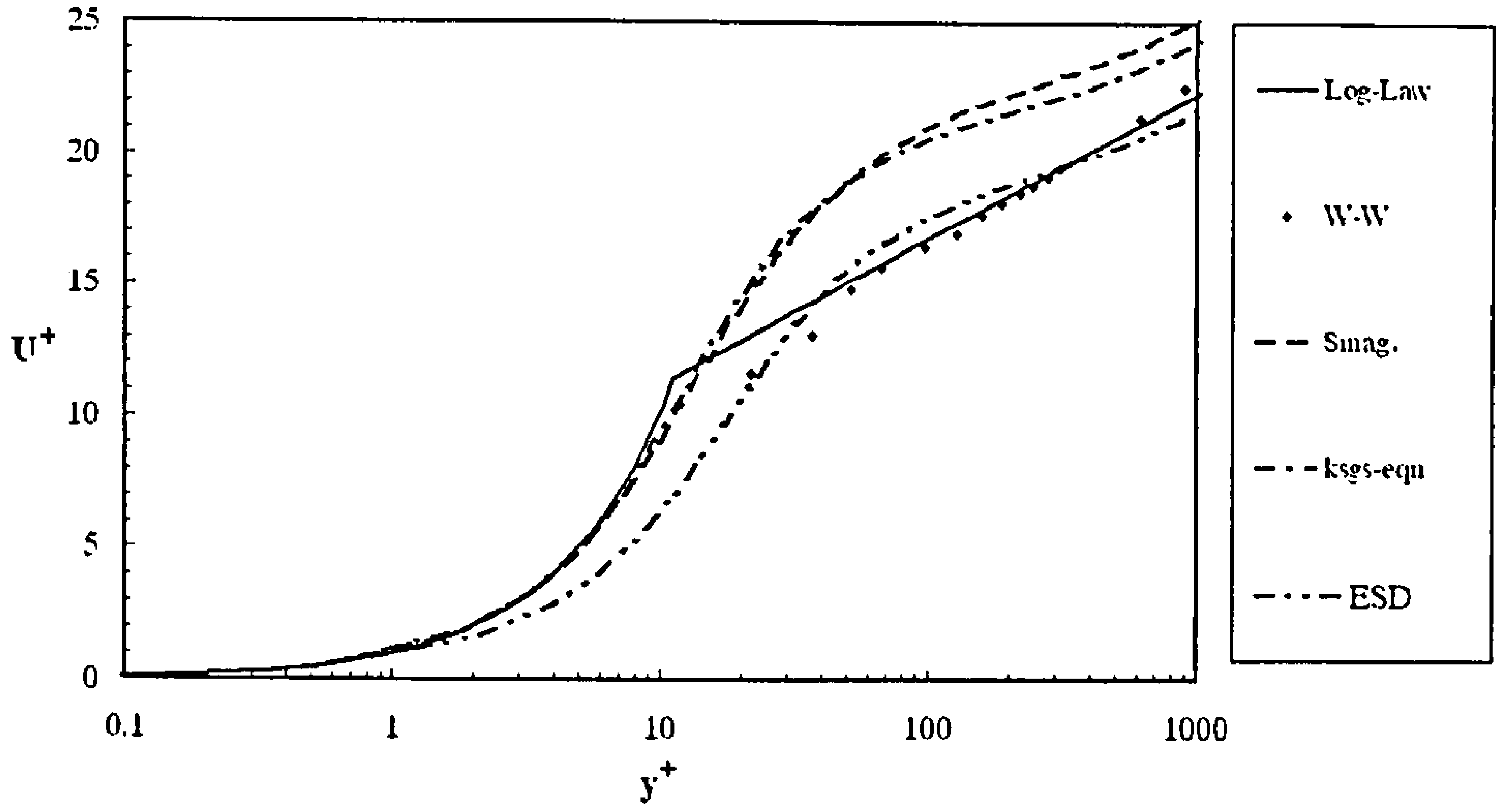

Figure 4.16: $U^+ vs. y^+$ for $Re_\tau = 1800$

4.2.2 Reynolds stresses distributions

The investigation of time-averaged normal and shear stresses is a significant part of the assessment of the predicted turbulent field. Based on the DNS and experimental data available, case 1, 2 and 3 were investigated in terms of the variation of the normal stresses while case 4 in terms of $\overline{u'}^+$, $\overline{v'}^+$ and $\overline{u'v'}^+$.

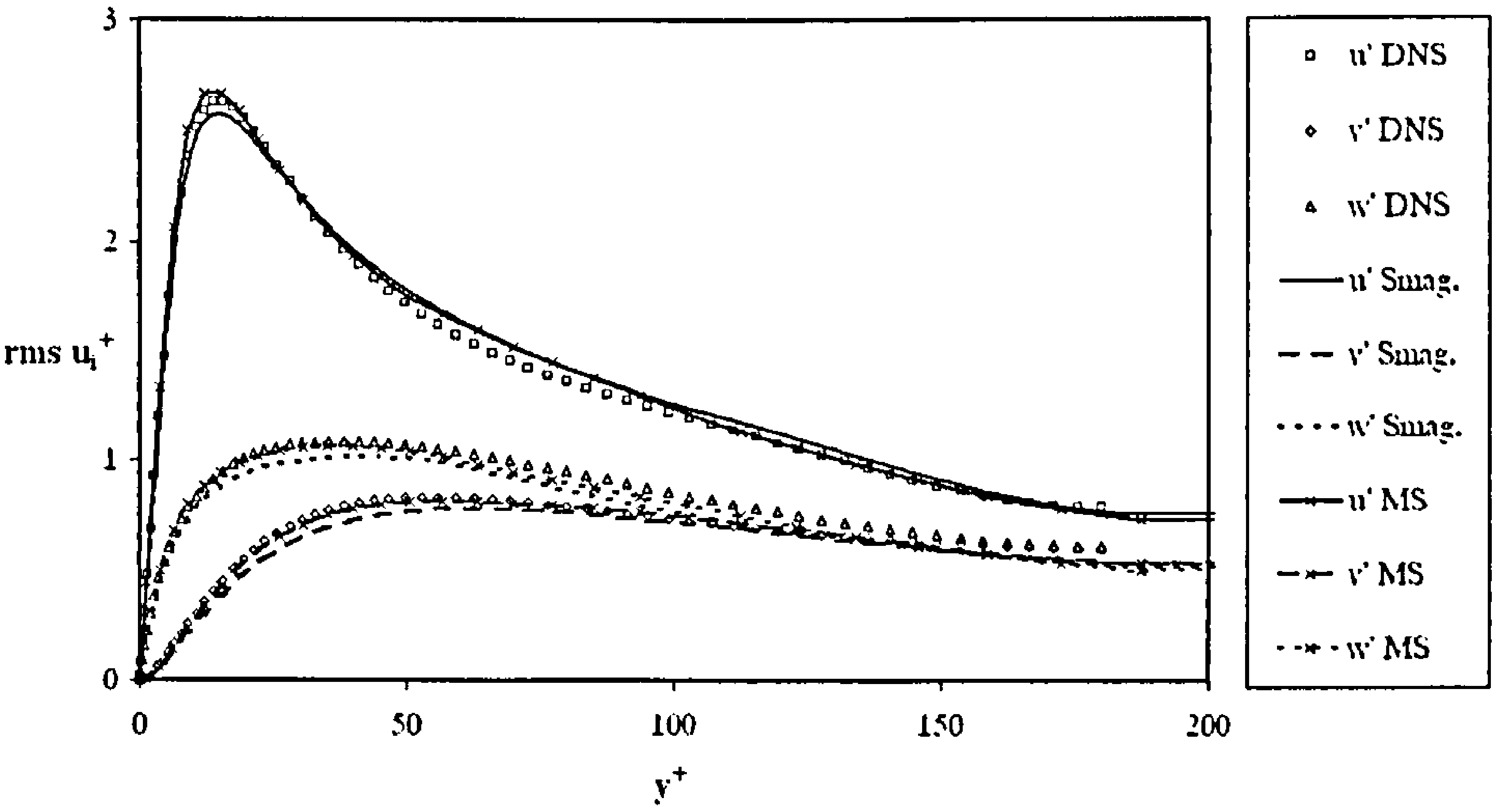

Figure 4.17: Rms values of $\overline{u'}^+$, $\overline{v'}^+$ and $\overline{w'}^+$ vs. y^+ for $Re_\tau = 180$ (Smagorinsky and MS model)

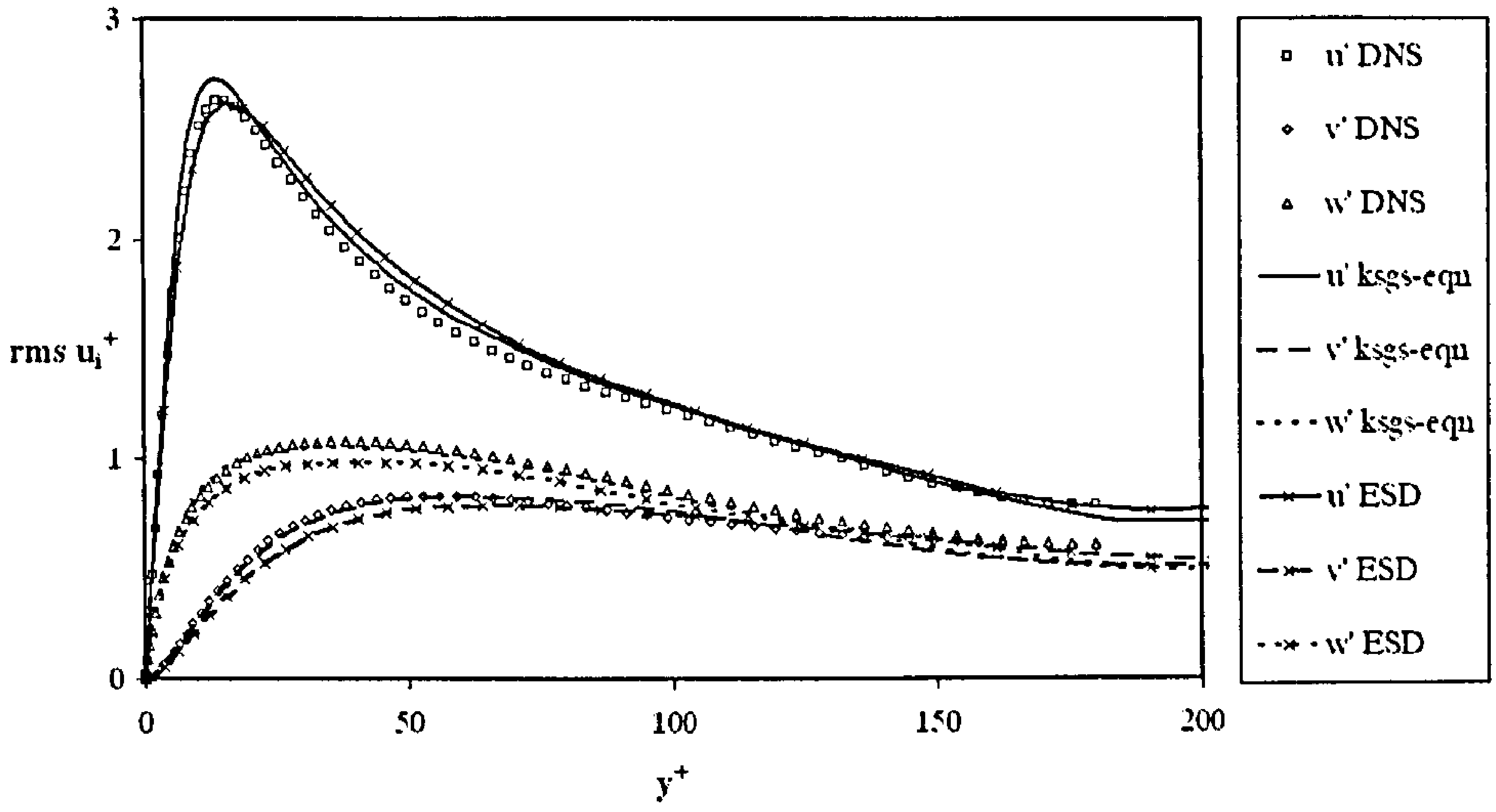

Figure 4.18: Rms values of $\overline{u'}^+$, $\overline{v'}^+$ and $\overline{w'}^+$ vs. y^+ for $Re_\tau = 180$ (k_{sgs}-equation and ESD model)

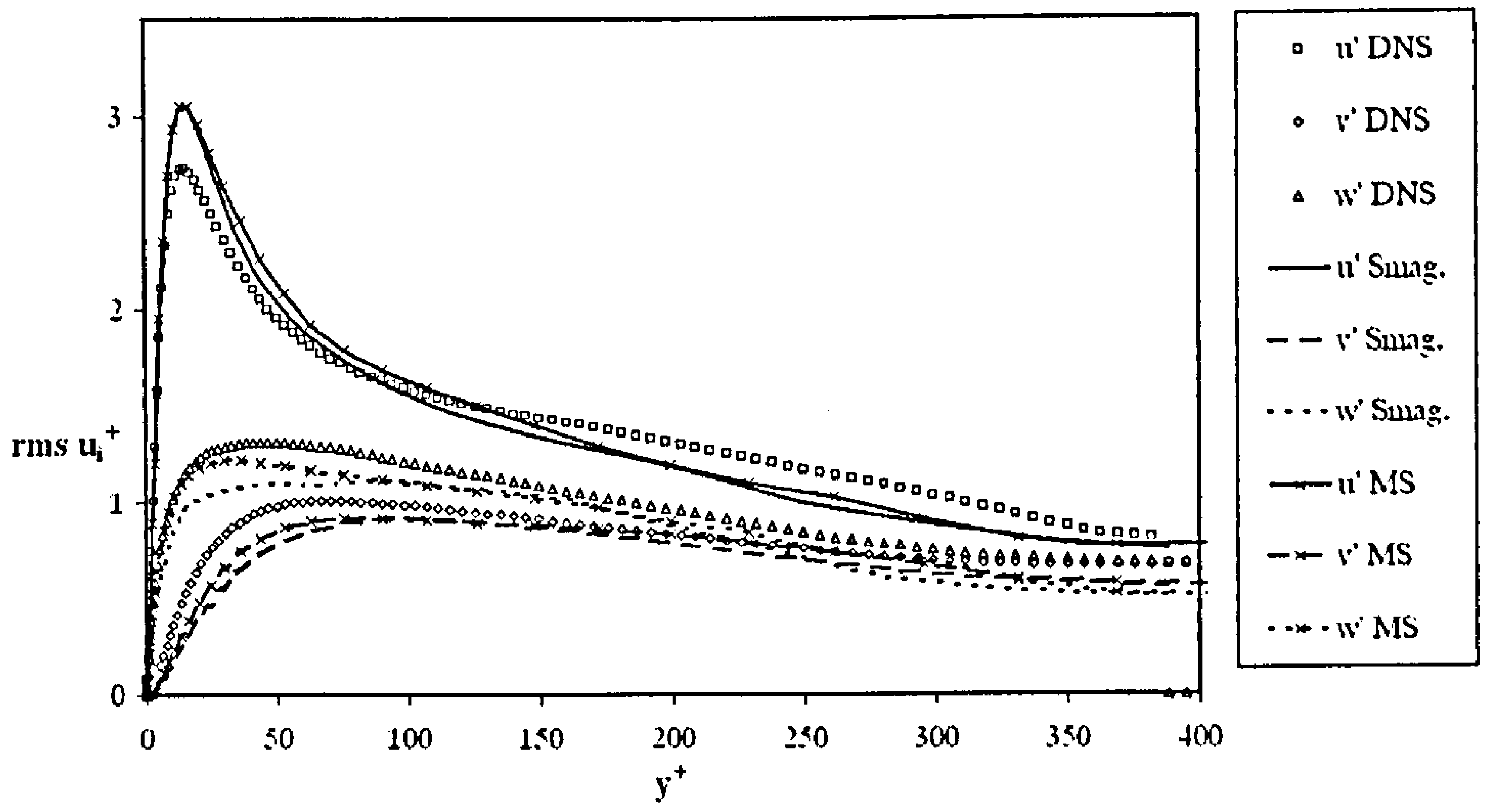

Figure 4.19: Rms values of $\overline{u'}^+$, $\overline{v'}^+$ and $\overline{w'}^+$ vs. y^+ for $Re_\tau = 395$ (Smagorinsky and MS model)

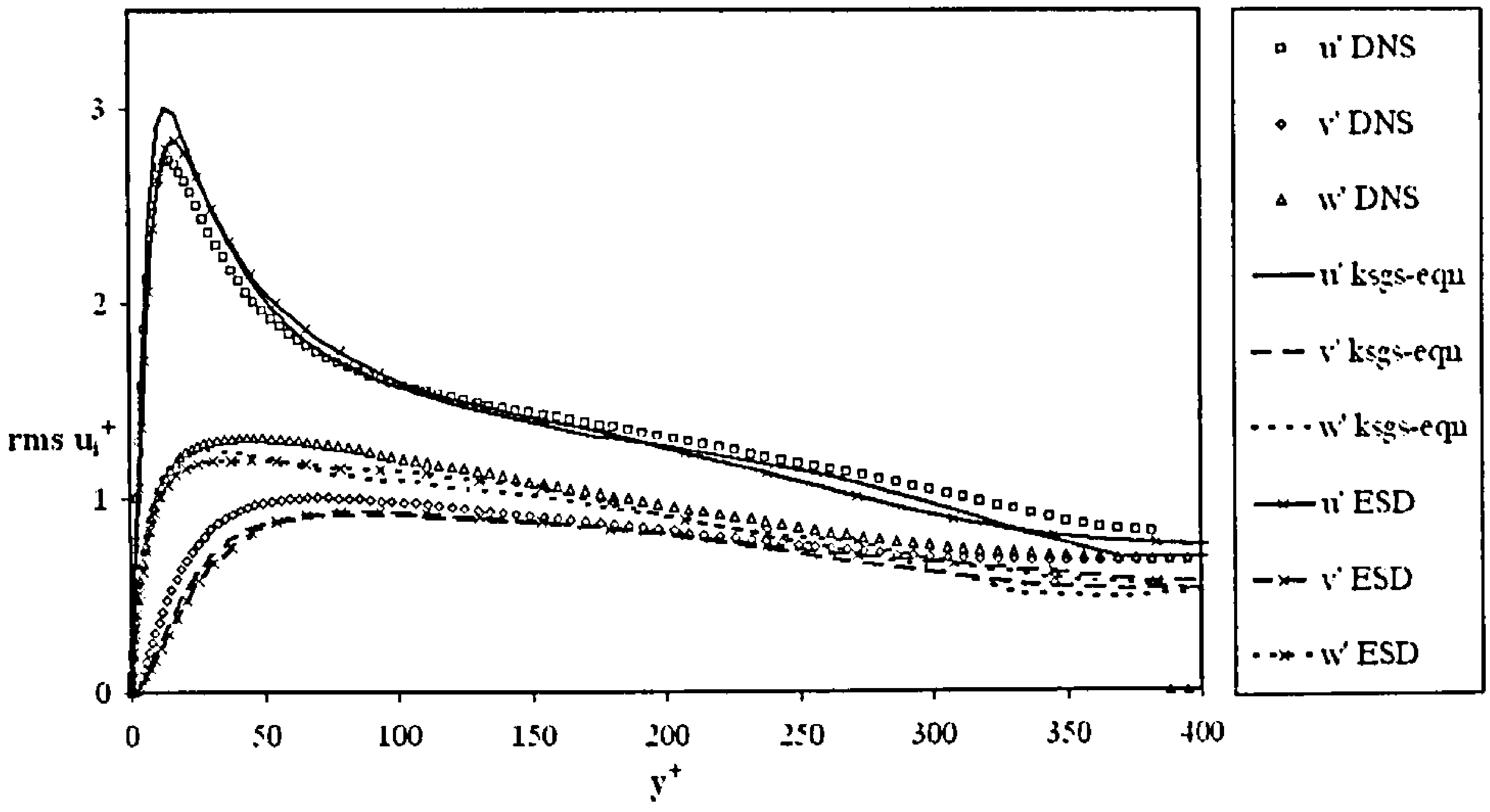

Figure 4.20: Rms values of $\overline{u'}^+$, $\overline{v'}^+$ and $\overline{w'}^+$ vs. y^+ for $Re_\tau = 395$ (k_{sgs}-equation and ESD model)

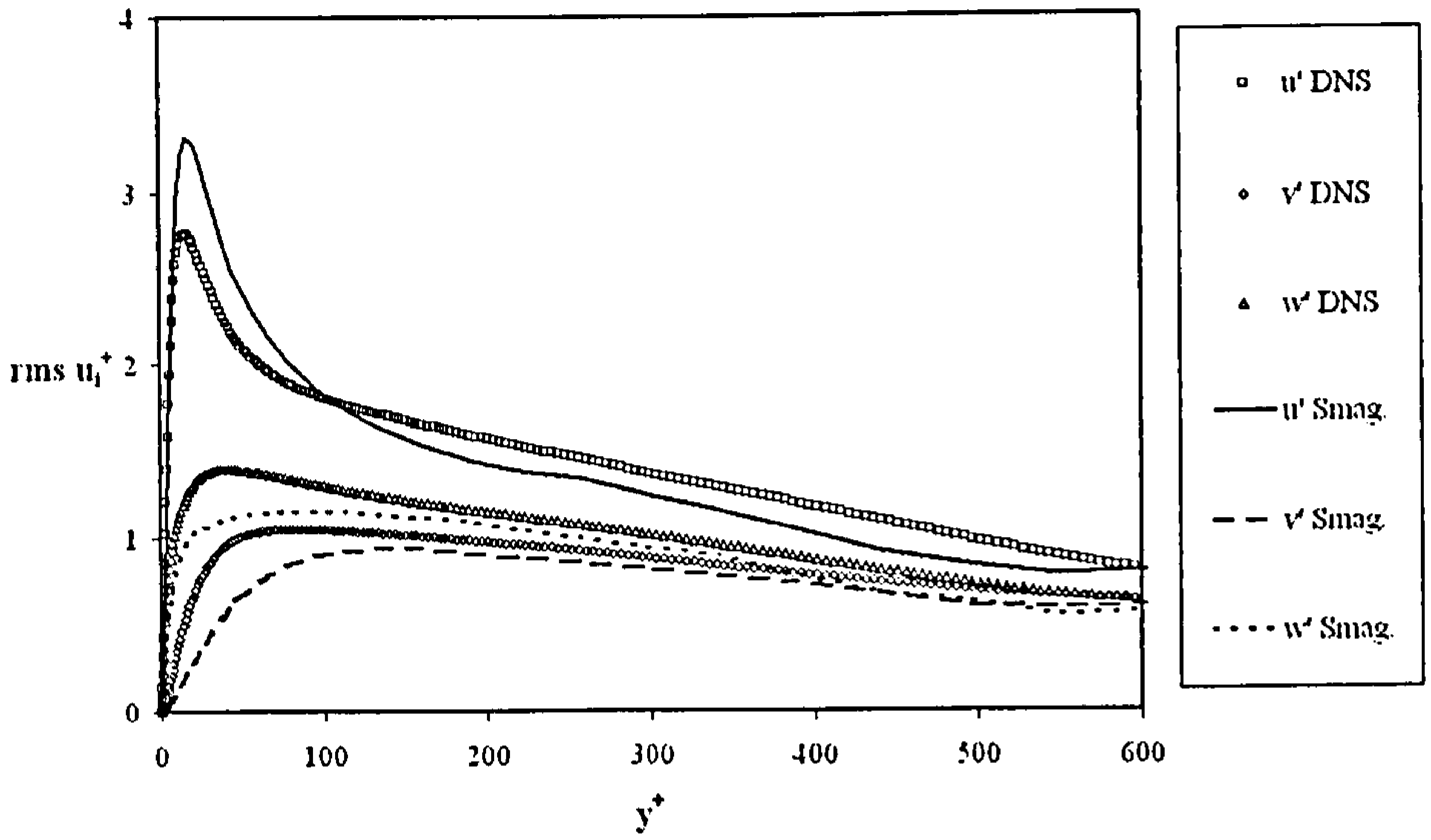

Figure 4.21: Rms values of $\overline{u'}^+$, $\overline{v'}^+$ and $\overline{w'}^+$ vs. y^+ for $Re_\tau = 640$ (Smagorinsky model)

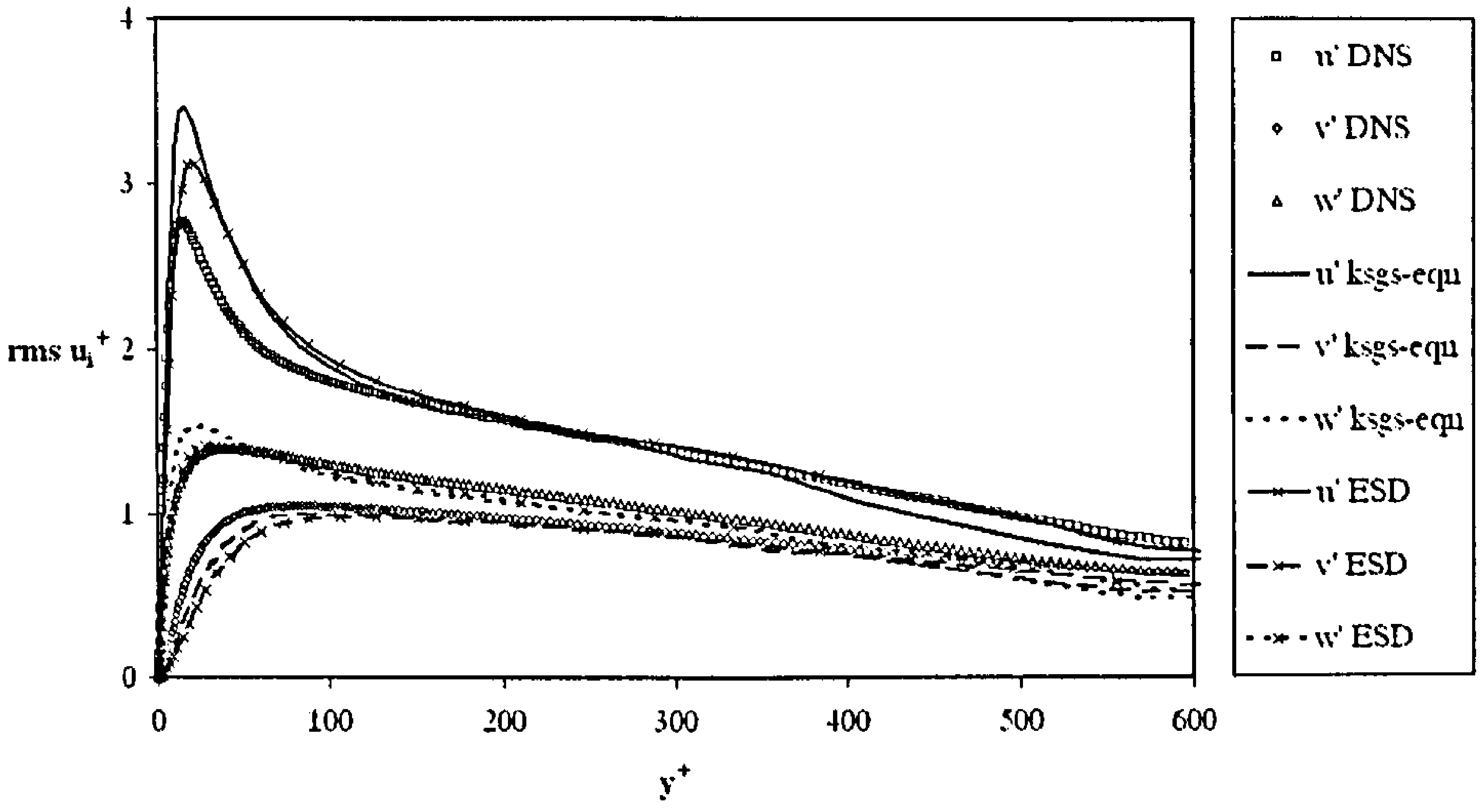

Figure 4.22: Rms values of $\overline{u'}^+$, $\overline{v'}^+$ and $\overline{w'}^+$ vs. y^+ for $Re_\tau = 640$ (k_{sgs}-equation and ESD model)

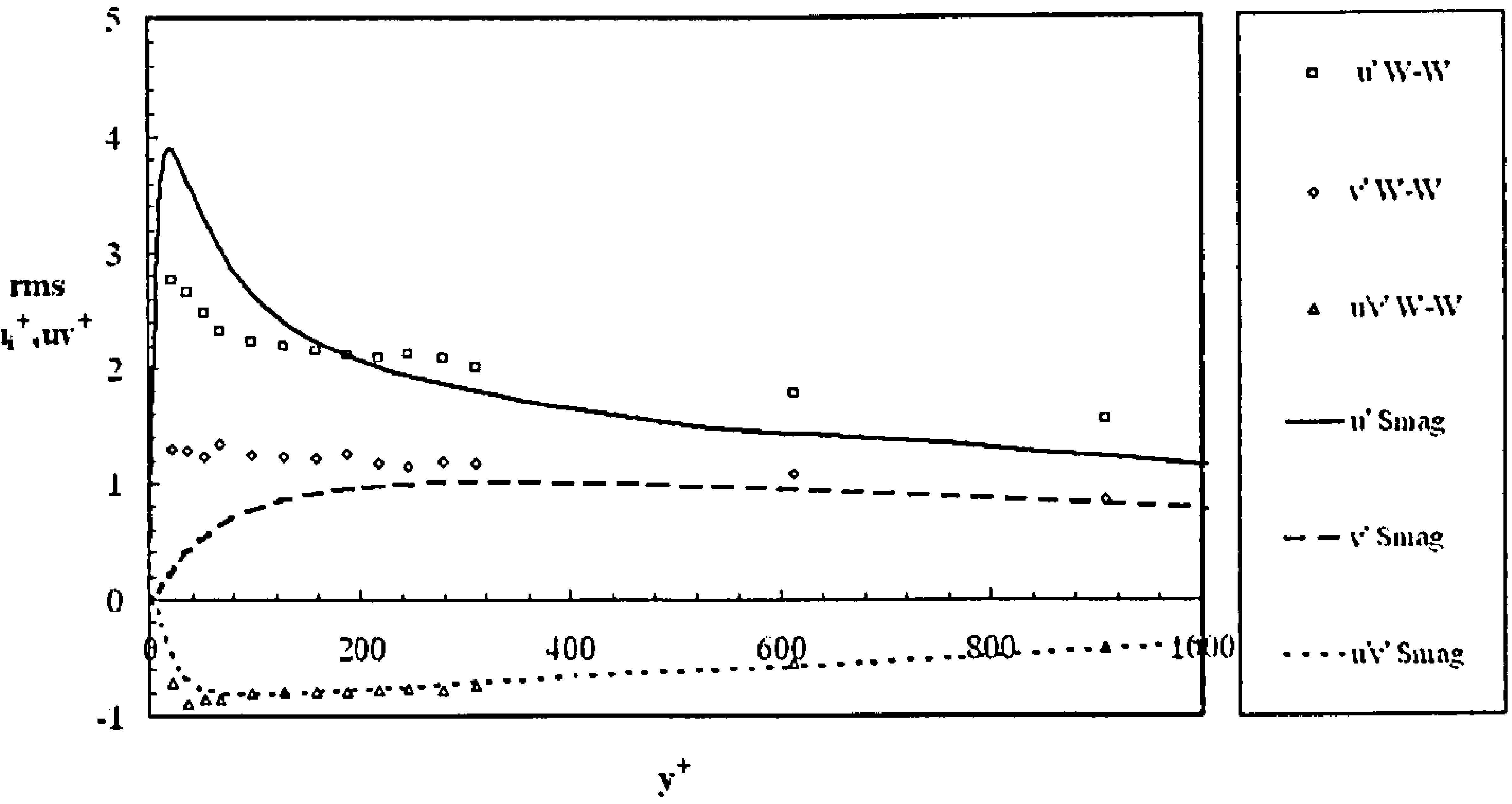

Figure 4.23: Rms values of $\overline{u'}^+$, $\overline{v'}^+$ and $\overline{u'v'}^+$ vs. y^+ for $Re_\tau = 1800$ (Smagorinsky model)

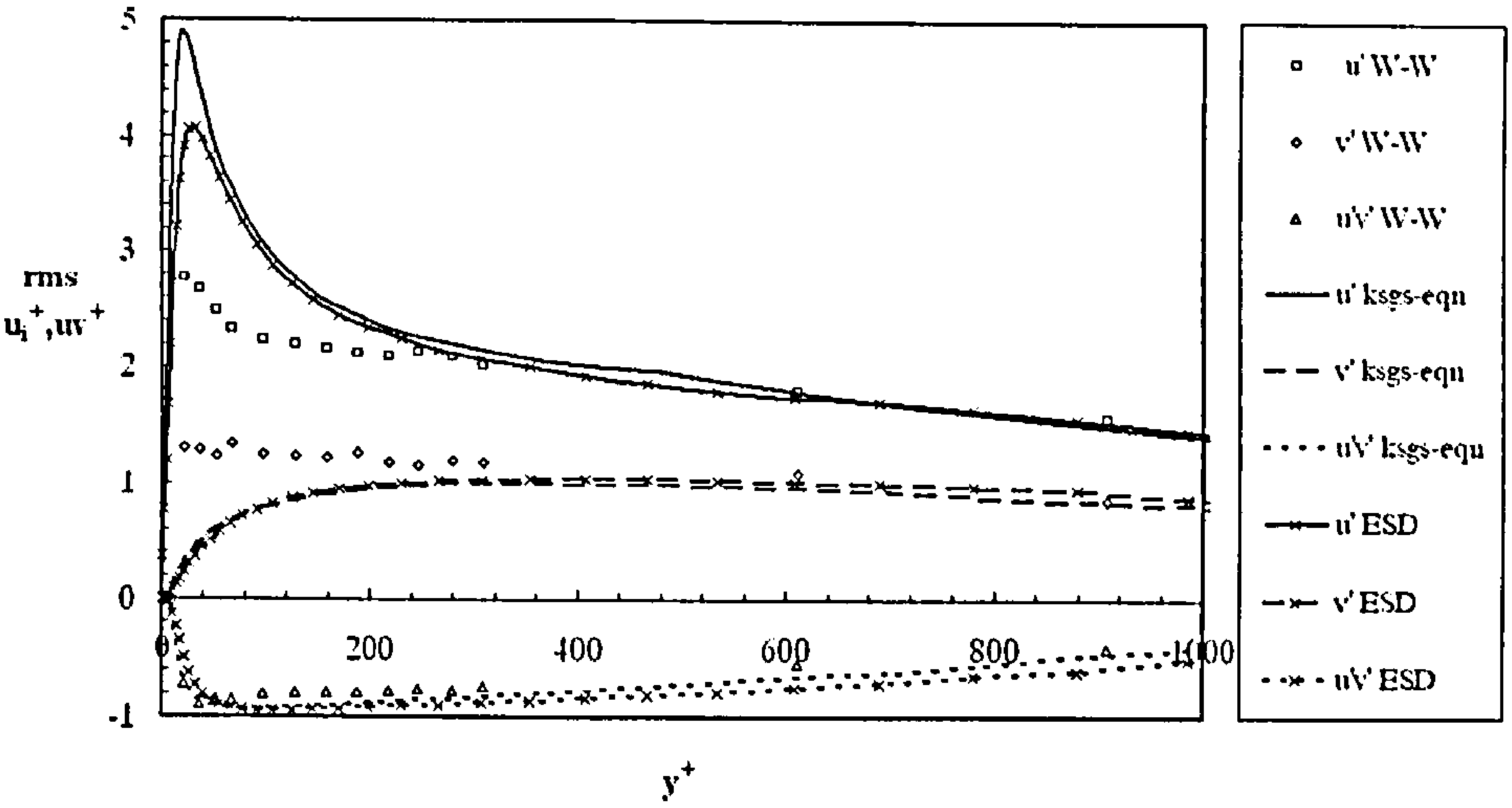

Figure 4.24: Rms values of $\overline{u'}^+$, $\overline{v'}^+$ and $\overline{u'v'}^+$ vs. y^+ for $Re_\tau = 1800$ (k_{sgs}-equation and ESD model)

4.2.3 Coherent structures

Apart from the mean flow characteristics and the stresses distribution, coherent structures were also studied in order to investigate further the effect of the SGS models in the prediction of the turbulent flow field. Coherent structures are organised structures of a fluid in turbulent state, characterised by repeating patterns of flow coherent motion. It is believed that their role on the maintenance of turbulence is of great importance and therefore, a number of studies [105, 177, 178] have been performed over the years, the first of which can be traced back to the work of Townsend [177, 178].

The most widely used method to visualise these structures and hence study them, involves the generation of iso-surface plots, of certain instantaneous flow field parameters. It has been observed that coherent structures are related with vortex cores and therefore a first approach would be to consider the regions over which pressure minima occur. Another very commonly used approach is to use the modulus of vorticity, given by $\omega = \nabla \times u$, or regions of high ω_x, ω_y or ω_z. However, the use of vorticity can give misleading results in regions of high shear, predicting the presence of vortices that do not exist [70].

For the purposes of the present study, two visualisation techniques were employed. The first had been proposed and developed by Chong et al. [20] and the second by Hunt et al. [67]. Chong et al.[20] suggested that a vortex core is a region where the eigenvalues of the velocity-gradient tensor $A_{ij} = \frac{\partial u_i}{\partial x_j}$ are complex, which implies that the local streamlines are closed. The characteristic equation of A_{ij} is given by:

$$\lambda^3 + P\lambda^2 + Q\lambda + R = 0 \tag{4.3}$$

where P, Q and R is the first, second and third tensor invariant given by:

$$P = -tr\left(A_{ij}\right) \;\; Q = \frac{1}{2}\left(P^2 - tr\left(A_{ij}A_{ij}\right)\right) \;\; R = -det\left(A_{ij}\right)$$

where $tr\,()$ denotes the trace and $det\,()$ the determinant of the tensor of interest. Because for incompressible flow P is zero, Eq.4.3 reduces to:

$$\lambda^3 + Q\lambda + R = 0 \tag{4.4}$$

and therefore, the discriminant of A_{ij} D is given by:

$$D = \frac{Q^3}{27} + \frac{R^2}{4} \tag{4.5}$$

Chong et al. [20] showed that the eigenvalues of A_{ij} will be complex if $D > 0$. Hence iso-surfaces of these regions were plotted using instantaneous data of the fully developed flows. These can be seen in Figure 4.25 (c) for the flow of $Re_\tau = 395$, using the ESD model.

Hunt et al. [67] proposed another criterion for the presence of the vortex core, based on the second invariant. According to their proposal, in the vortex core region the second invariant Q is positive and the local pressure has a lower value than the ambient. Based on this approach, two figures were produced; the first presents iso-surfaces of regions where the local pressure was lower than ambient and the second presents positive Q regions . These can be seen in Figure 4.25 (a) and (b) respectively, for $Re_\tau = 395$ case using the ESD model. Comparing to the first method presented, the main disadvantage of Hunt's method is the requirement of a combination of two iso-surface plots in order to extract the information required.

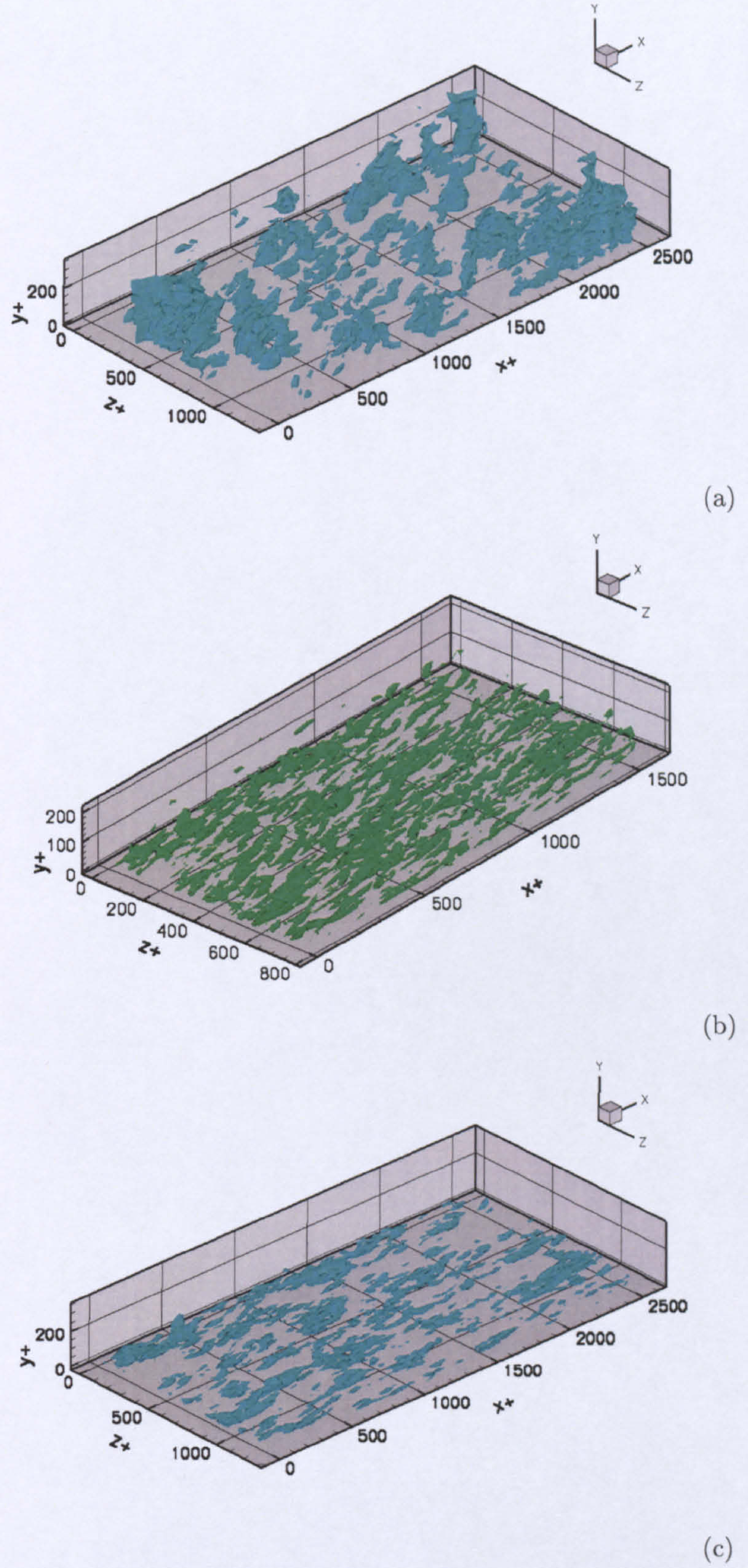

Figure 4.25: Comparison of the visualisation methods for $Re_\tau = 395$, using the ESD model (a: Pressure iso-surfaces, b: Q iso-surfaces, c: D iso-surfaces)

A comparison of Figure 4.25 (a) and (b) with (c) indicates that both methods showed similar, streak-like structures in the near-wall region. Pressure iso-surface plot produced fewer and larger shapes, in agreement with observations made by other researchers [99].

The structures shown in these figures are aligned with the streamwise direction and inclined to the wall surface at an angle of 30° – 45°. Their average length in wall units is 200 – 300 and their width approximately 100. The inclination and the length of these structures can also be seen by the instantaneous velocity contours. Figure 4.26 shows contours of u'/U_B at $y^+ = 6.8$ and it can be seen the shape of the near-wall structures as well as the associated length.

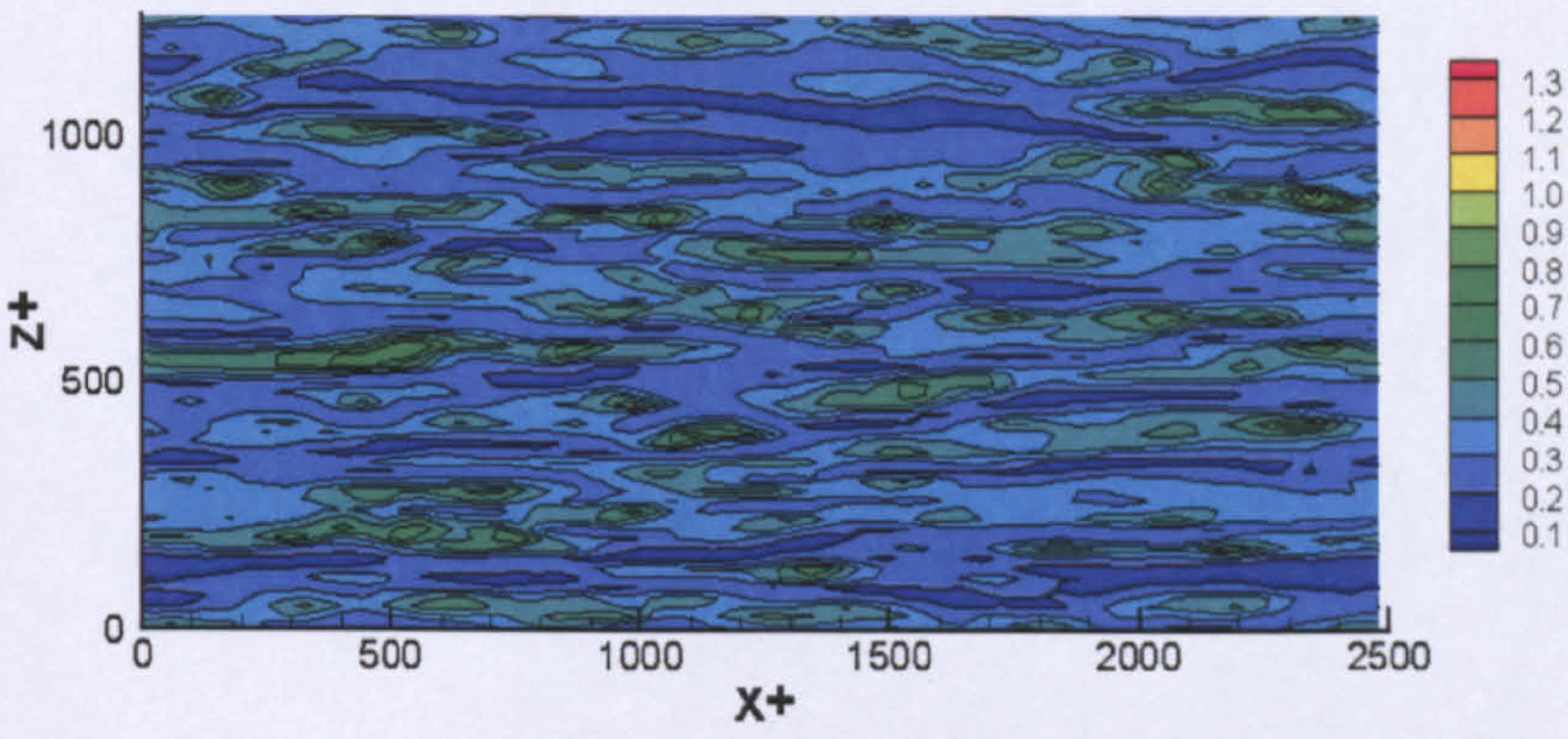

Figure 4.26: u'/U_B contours for $Re_\tau = 395$,
using the ESD model

Figure 4.27 shows contours of w'/U_B across the mid-span plane of the channel. The characteristic inclination present in the flow close to the wall is a consequence of the action of the mean shear on the outer layer fluid elements that are moving towards the wall [1]. The observations regarding the length and the inclination of the coherent structures present in the near-wall region were in good agreement with the description of coherent structures of a channel flow given by Sagaut [155].

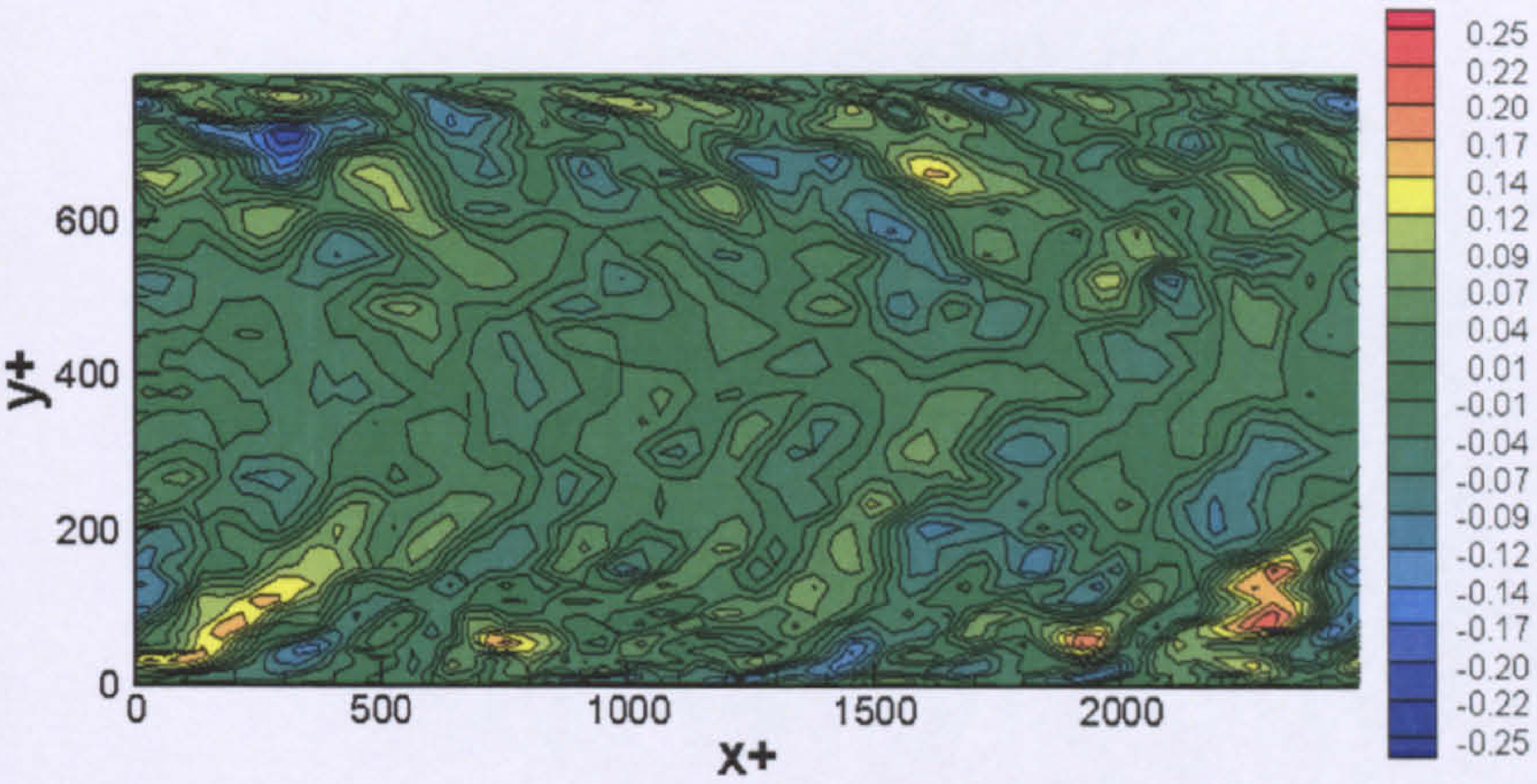

Figure 4.27: w'/U_B contours for $Re_\tau = 395$, using the ESD model

Figures 4.28 (a), (b) and (c) show the coherent structures in the near-wall region, using Chong et al. [20] method, as these were obtained for the $Re_\tau = 395$ flow case, predicted with Smagorinsky, MS and k_{sgs}-equation model respectively. These Figures in combination with Figure 4.25 (c) show the effect of SGS models on the fluid formations. This effect is discussed in detail in section 4.2.5.

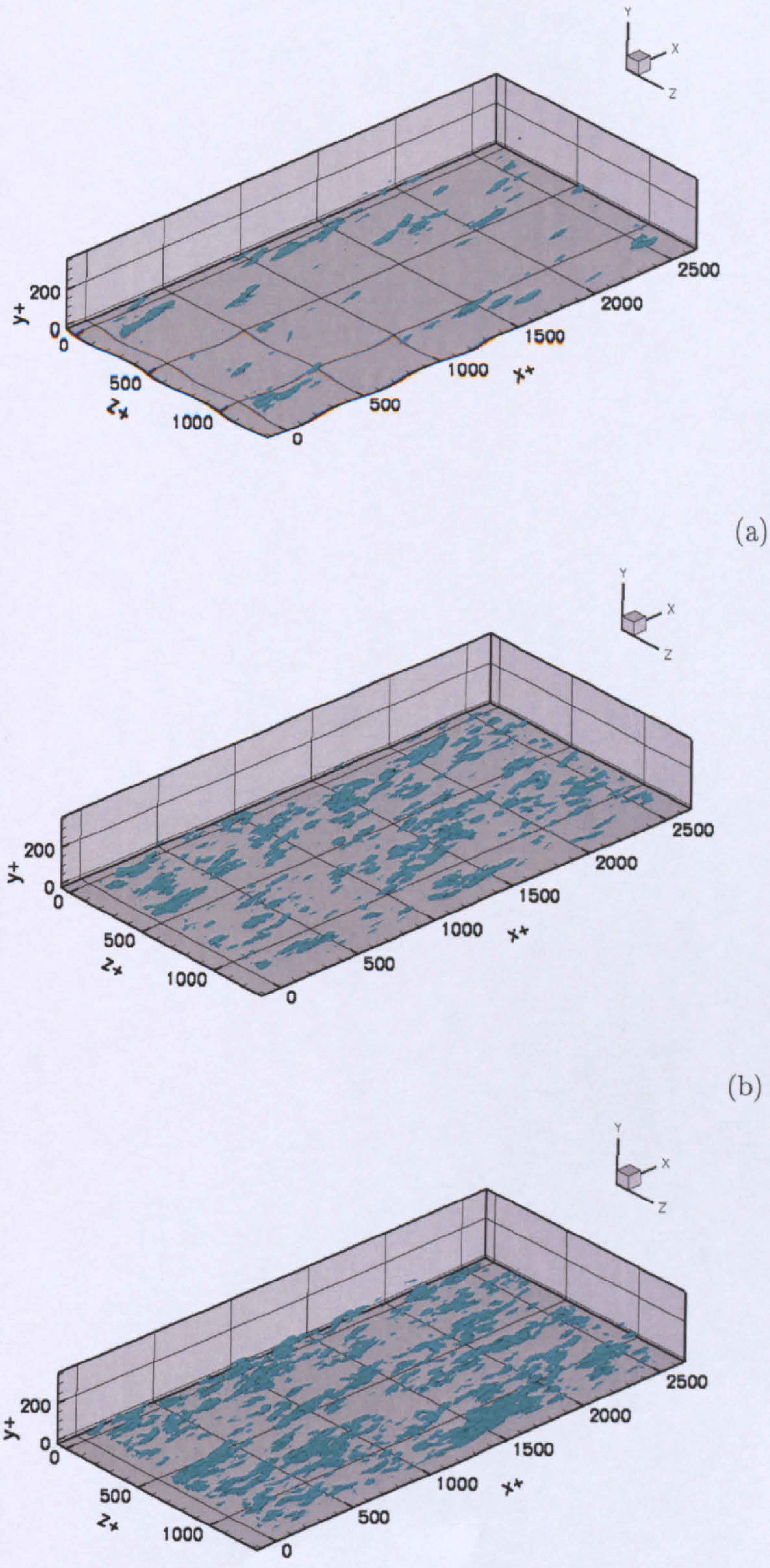

Figure 4.28: Comparison of SGS model effect on coherent structures for $Re_\tau = 395$, using $D = 3.0 \times 10^{-5}$ iso-surfaces (a: Smagorinsky, b: MS, c: k_{sgs}-equation model)

4.2.4 Anisotropic stress tensor invariants and realisability of the results

Back in 1978 Lumley [104] developed a method, which can be used to check the physical realisability of the predicted turbulent stresses. The method was based on the tensorial properties of the non-dimensional form of the anisotropic part of the stress tensor, given as:

$$b_{ij} = \frac{\overline{u_i'u_j'}}{\overline{u_k'u_k'}} - \frac{1}{3}\delta_{ij} \tag{4.6}$$

The fact that b_{ij} is traceless reduces the non-zero invariants to two; namely the second, given by $II = -\frac{b_{ij}b_{ji}}{2}$, and the third, given by $III = \frac{b_{ij}b_{jk}b_{ki}}{3}$. Furthermore, the sum of its eigenvalues λ_1, λ_2 and λ_3 is zero, which results in $-1/3 \leq \lambda \leq 2/3$. Hence, every physically realisable turbulent state should produce eigenvalues that lie between these extrema or the corresponding invariant values. Lumley [104] plotted the limiting variation of II against III, producing the *Lumley triangle* or *anisotropy invariant map*, which can be seen in Figure 4.29. Figure 4.29 shows that each side of the Lumley triangle corresponds to a different state of turbulence. For the analytical derivation, the reader should refer to Pope [146] and Jovanovic [74]. Any turbulent flow should generate values for II and III that will lie within the boundaries of the Lumley triangle. Otherwise, the flow cannot be physically realisable. Therefore, the anisotropy invariant map can be used to check the realisability of the predicted flow. Figures 4.30 and 4.31 show the resultant maps for case 1 and 4, for all models tested.

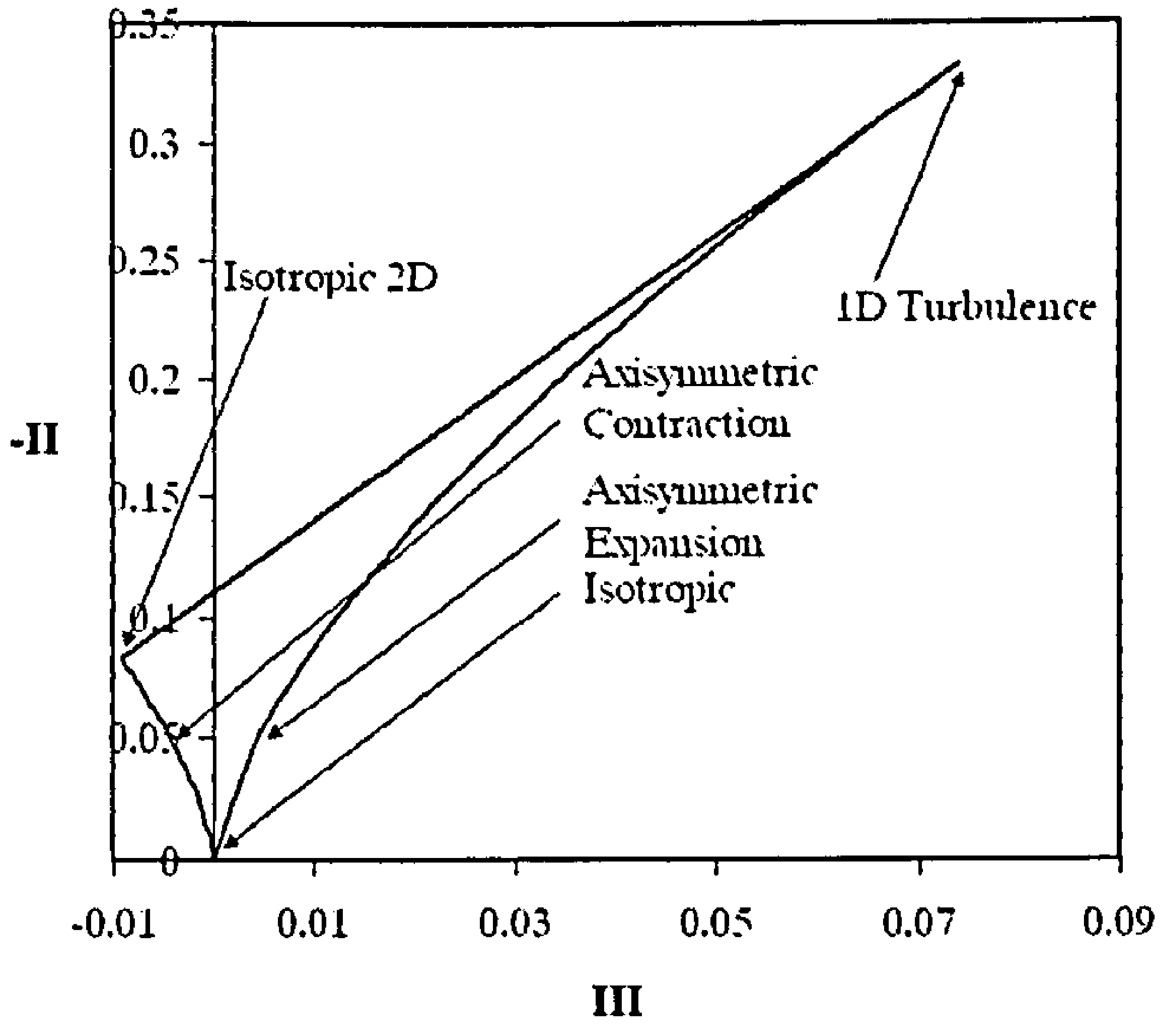

Figure 4.29: Lumley triangle

Both Figures indicate that the models tested produced physically realisable stresses since all points of the second and third invariants were laying within Lumley's triangle. In accordance to DNS data [78], the turbulent state varied from two-dimensional in the near-wall region to almost isotropic along the channel centre-line. Figure 4.30 shows that turbulence was in a 2D isotropic state in the near-wall region. This was expected as in this region the wall-normal velocity component is damped due to the presence of the wall, resulting in a 2D like turbulence state. Moving away from the wall turbulence tends to the 1D state due to the increased anisotropy present in the flow. This behaviour extends up to $y^+ \simeq 9$, where the increase of the wall-normal component changes the behaviour of turbulence, which now starts undergoing an axi-symmetric expansion state. This behaviour extends through the upper buffer region and the log-law region to lead monotonically towards an almost isotropic state in the wake region, located in the channel mid-height area.

Similar behaviour can be seen in Figure 4.31, corresponding to case 4, where $Re_\tau = 1800$. However, the distribution in this case differentiated from the previous as follows; the first point of the anisotropy invariant maps indicated that the state of turbulence was still 2D isotropic but closer to 1D turbulence. This was an indication that the ratio of streamwise to spanwise stresses was larger than in case 1, resulting in higher levels of anisotropy.

The turning point, where turbulence enters the axi-symmetric expansion state varied from $y^+ \simeq 9$ for Smagorinsky model, to $y^+ \simeq 14$ for the ESD model. The turning point for k_{sgs}-equation model was at $y^+ \simeq 12.5$. Finally, moving away from the wall, the state of turbulence did not approach the isotropic state monotonically but a small 'kink' was present, in all three cases investigated, in the region of $600 < y^+ < 1170$ for the Smagorinsky, $700 < y^+ < 985$ for the k_{sgs}-equation and $985 < y^+ < 1100$ for the ESD model.

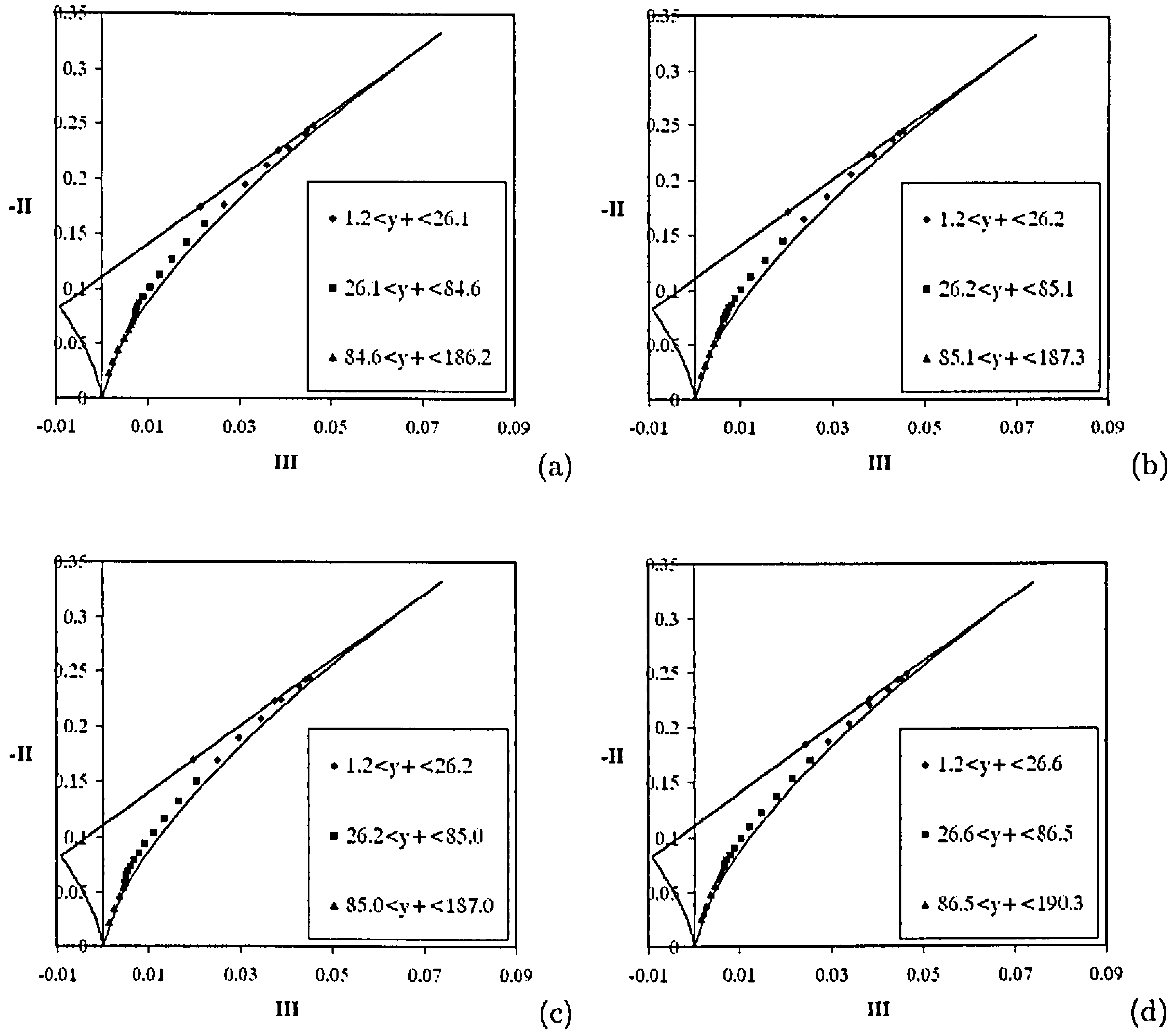

Figure 4.30: Lumley triangles for $Re_\tau = 180$
(a: Smagorinsky, b: MS, c: k_{sgs}-equation, d: ESD model)

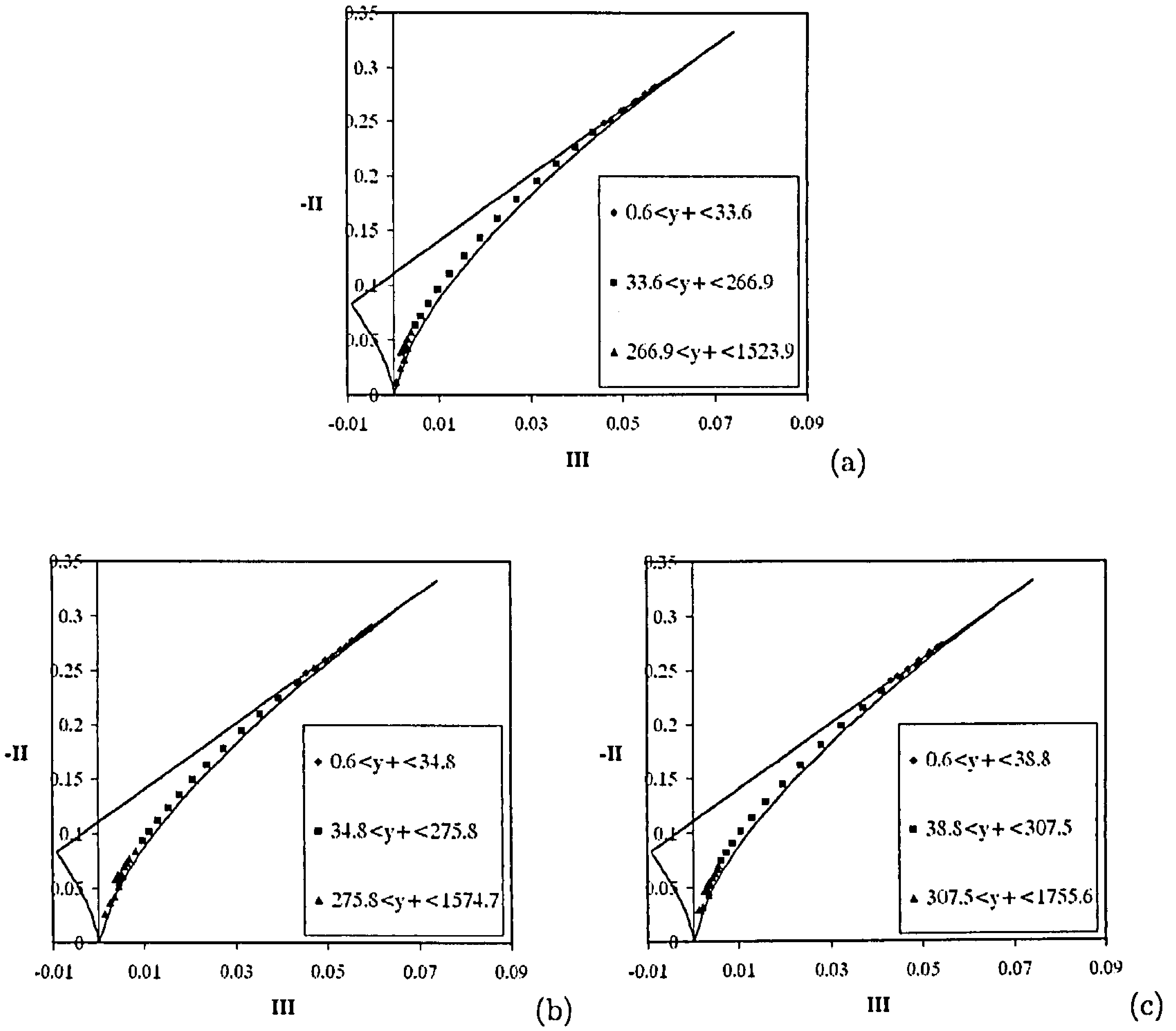

Figure 4.31: Lumley triangles for $Re_\tau = 1800$
(a: Smagorinsky, b: k_{sgs}-equation, c: ESD model)

4.2.5 Discussion on SGS modelling

In case 1, the influence of the subgrid scale models was insignificant due to the low Re_τ, and the overall good grid resolution. All the models appeared to behave in the same manner with ESD being slightly less dissipative than the others. The new model gave the largest error in the prediction of the skin friction coefficient C_f (but still only 5%) but the smallest error in the prediction of the centre-line to bulk velocity ratio U_C/U_B as can be seen in Table 4.4. The fact that the grid was not particularly fine in the region next to the wall (note $y^+ = 1.16$) is believed to have played a role to the error of the C_f prediction. In the same Table, the predicted values of U_C/U_B and C_f are compared with the expected values, calculated from the empirical formula proposed by Dean [27] with corresponding percentage errors. Note that according to Dean's proposal, U_C/U_B is given by:

$$U_C/U_B = 1.28\left(\frac{2U_B}{\nu}\right)^{0.0116} \tag{4.7}$$

As Re increases, without corresponding grid refinement, the role of the subgrid scale model in the calculation of the flow becomes increasingly important and the physical realism of the model is more closely reflected in the results. Hence, it can be seen that in the rest of the flow cases considered, the models give clearly distinguishable predictions. In case 2, the Smagorinsky model over-predicted the log-law region due to a 16% under-prediction of C_f that feeds through to the skin friction velocity and hence to the non-dimensionalisation of U. This however did not affect the slope of the log-law region which was captured accurately. This feature of the U^+ distribution was captured by all models tested.

The MS model predicted C_f more accurately than the Smagorinsky model, as can be seen in Table 4.4, resulting in a better wall-normal U^+ distribution, with reduced overshooting of the log-law region, whose slope was also captured better. It is important to note at this point that this result compared very well with that obtained by Yoshizawa et al. [196] indicating a correct implementation of the model and the near-wall damping function.

The k_{sgs}-equation model gave the most accurate overall distribution of U^+ for case 2, with 6.51% error in C_f. The capture of the overall streamwise velocity profile was also accurate, as indicated by the small error in U_C/U_B. A factor that contributed to this level of accuracy was the near-wall damping function used, which had been 'calibrated' by Yoshizawa [196] for this specific case.

The ESD model captured the log-law region very well for all cases and managed to give the most accurate prediction for C_f overall. However, the model did not reproduce properly the upper part of the linear sublayer and the buffer layer. This behaviour was repeated, more pronounced, in cases 3 and 4. At $Re_\tau = 640$, the ESD model indicated a poor prediction in these two regions, despite providing accurate prediction of C_f and the best representation of the log-law region. As in case 2, the error in U_C/U_B was the largest of all models but still less than 1.0%.

There are two factors that it are believed to have contributed to the under-prediction of U^+ in the linear-sublayer and buffer layer regions, namely the model energy spectrum shape and the near-wall damping function employed. The Kovasznay spectrum has been developed on the assumption of equilibrium between turbulent energy production and dissipation. However, in the regions of interest this assumption is not valid and as a result, the model spectrum is not representative of the energy distribution. As a result, the computed length scale may not reflect the characteristic scales of the SGS structures, producing excessive dissipation. Therefore, the use of a more accurate model spectrum, such as Pope's [146] could be beneficial.

As far as the near-wall damping function is concerned, Inagi et al. had calibrated the function for $Re_\tau = 395$ [68]. This could have an adverse effect on the use of the function for other Re numbers. This was confirmed by a test simulation performed using $C_T = 5.0$, for $Re_\tau = 180$. The results in terms of wall-normal U^+ distribution show a considerable improvement over the whole distribution, as can be seen in Figure 4.32. The improvement extends to the C_f prediction error which was reduced from 5.25% to 1.11%.

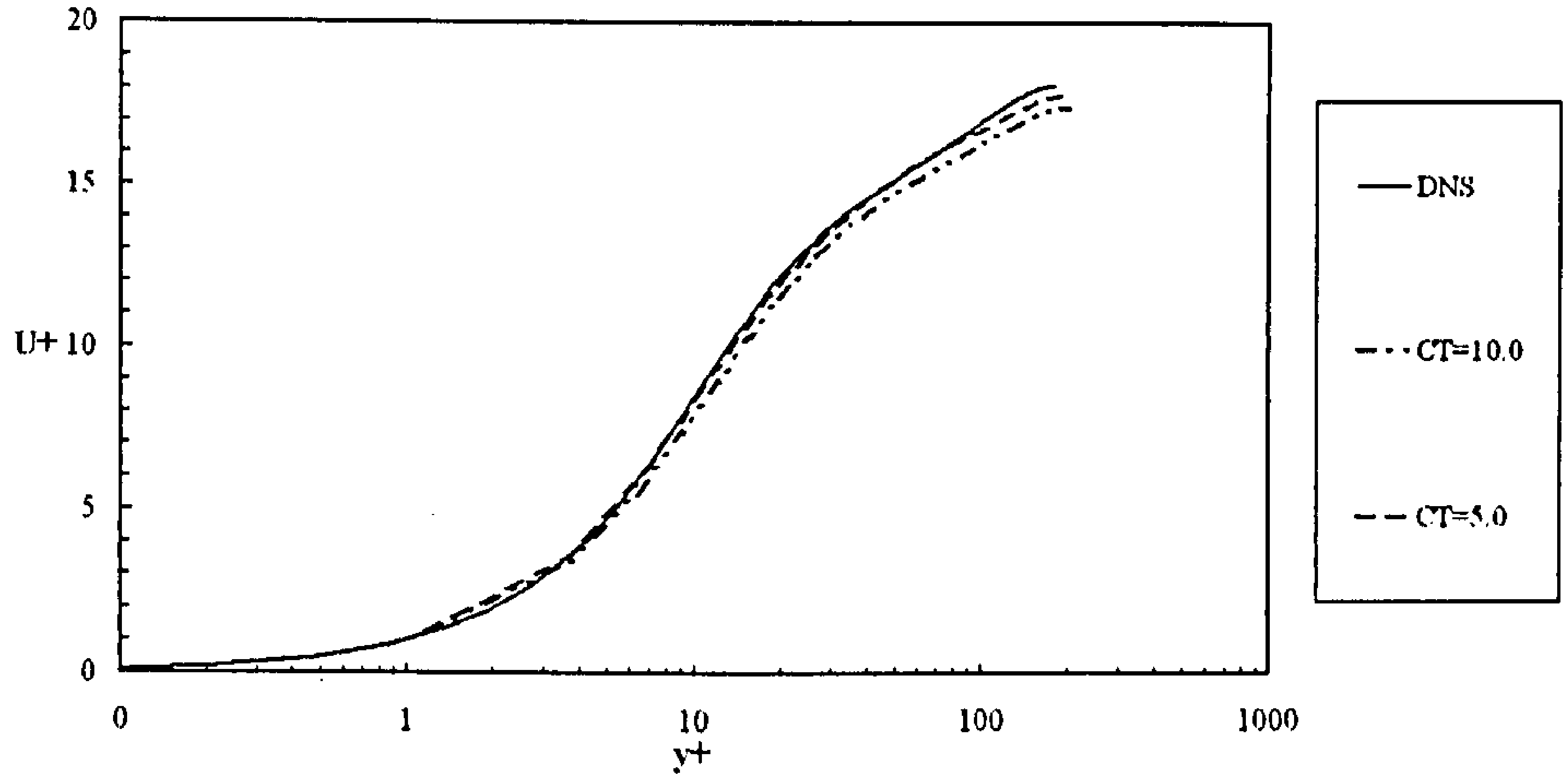

Figure 4.32: U^+vs. y^+ for $Re_\tau = 180$ using ESD model and Inagi et al.[68] function with $C_T = 5.0$ and 10.0

The marginally more accurate prediction of U_C/U_B by the other models did not counteract their larger error in C_f, resulting in over-prediction of the log-law region, with the worst case being that of Smagorinsky model. This same pattern can also be seen in the final flow case. In case 4, the Smagorinsky and k_{sgs}-equation model produced similar flow behaviour in the linear sublayer and buffer regions with some differences at the end of the latter, mainly due to the better prediction of the skin friction by the transport equation model. The ESD model clearly gave an improved overall prediction although with some deviations, as noted above, up to $y^+ \simeq 30$. The slight overshoot at the end of the buffer layer is typical for linear eddy viscosity based models and has been reported by a number of researchers [161, 53].

From the observations made it becomes clear that as Re_τ was increased and the energy in the subgrid scales was larger due to the lack of corresponding grid refinement, the error in the prediction of C_f increased as well for Smagorinsky and standard one equation models.

However, the behaviour of the ESD model indicates a robust independence on Re number with predictive accuracy for a number of parameters such as C_f and Reynolds averaged velocity distributions remaining essentially constant over all test cases, compared to the other SGS models. This confirms the idea that information extracted from the energy spectrum, even if this adopts an approximate, modelled form, can be used for a variety of flow conditions giving satisfactory results.

In order to investigate further the possible causes of this observation, the distribution of the Reynolds stresses had to be taken into account. Figures 4.17 to 4.24 show that the main difference in the predicted stresses were concentrated in the near-wall region, while in general, further away and in the flow core, all models gave the same level of accuracy and were in good agreement with the reference data.

The general trend was an overestimation of $\overline{u'}^+$ and an underestimation of $\overline{v'}^+$ and $\overline{w'}^+$, with the worst case being at $Re_\tau = 1800$ and the best at $Re_\tau = 180$ and $Re_\tau = 395$. In case 1, MS and k_{sgs}-equation model gave very similar predictions for $\overline{v'}^+$ and $\overline{w'}^+$, both showing very good agreement with the DNS data. Smagorinsky and ESD model predictions were very similar but less accurate. In terms of the streamwise normal stresses, MS gave the most accurate prediction and Smagorinsky the worst. Hence, at such low Re_τ , and the flow being relatively well resolved, there was no clear advantage of the models based on information from the subgrid scales.

However, this behaviour changed with increasing Re_τ. In case 2 both ESD and k_{sgs}-equation model gave more accurate normal stresses than Smagorinsky and MS model, with ESD model producing the best results and Smagorinsky the worst. This was an indication that as the role of SGS models was becoming increasingly important, the models based on the resolved scales could not perform as well as those based on the subgrid scales.

In case 3 k_{sgs}-equation model gave a considerable over-prediction of the streamwise stresses, comparing to ESD model, but still, the prediction for the rest of the stresses was at the same levels as that given by the other models. Finally, in case 4, ESD and Smagorinsky model gave the most accurate $\overline{u'}^+$ distribution while again, k_{sgs}-equation model over-predicted the streamwise normal stresses. All models captured $\overline{v'}^+$and $\overline{u'v'}^+$ with the same level of accuracy.

Regarding case 3 and 4, a possible reason of the general trend described in the previous paragraphs was believed to be related to the grid resolution. Coarse grid resolution could result in poor resolution of the near-wall structures and hence reduced effective shear stress at the wall [109]. This, in combination with any difficulty of the subgrid scale model to reproduce the effects of the subgrid scales accurately, caused an under-prediction of C_f and $\overline{v'}^+$. The latter caused less momentum to be transfered from the energetic flow core to the lower energy flow near the wall, resulting in increasing streamwise stresses. It should be noted at this point, that in this respect, ESD model gave the most desired behaviour since it could provide a very good prediction of C_f, even when the grid resolution was not adequate.

A final comment regarding the predicted stresses for case 4 was related to the shear stress, which was captured very well by all three models. It is believed that the over-prediction of $\overline{u'}^+$and the under-prediction of $\overline{v'}^+$ counteracted each other, resulting in an accurate prediction for $\overline{u'v'}^+$.

The effect of the subgrid scale modelling on the development of the turbulent flow field can also be seen through visualisation of the coherent structures present in the flow. Using Chong et al. proposal [20], the core of such structures could be unveiled using iso-surfaces of regions where the discriminant D of the characteristic equation of the velocity-gradient tensor is positive. Figures 4.28 (a), (b) and (c) and Figure 4.25 (c) show coherent structures, using this technique, in $Re_\tau = 395$ flow case.

It is clear that the coherent structures predicted using the Smagorinsky model were significantly fewer than in the other two cases. This was an indication that the dissipative character of the Smagorinsky model resulted in a flow field with lower turbulence levels, compared to the other two models. ESD and k_{sgs}-equation model predicted similar number of coherent structures with ESD model producing slightly wider fluid formations. Considering the degree of sensitivity of C_f to the near-wall fluid structures activity, it can be suggested that there is a link between the predicted C_f and the coherent structures present in the flow. More coherent structures in the near-wall region contribute to higher turbulent activity which can lead to higher wall shear stresses and hence larger C_f values. This is in accordance to the results of the present study that show that when there are fewer coherent structures, as in the case of Smagorinsky model, the predicted C_f is decreased.

The variation in the behaviour of the predicted flow fields in the near-wall region can also be seen from the contour plots of u'/U_B presented in Figures 4.33 (a) to (d). The elongated regions of high u'/U_B correspond to the experimentally observed streaks [66]. The dissipative nature of the Smagorinsky model, as already reported in literature by Moin and Kim [123], resulted in a mean spacing of these streaks of about 200-300 wall units, instead of the generally accepted value of 100, which was given by the rest of the models. This behaviour was in accordance with observations made by Horiuti [66] and it affected the formation of coherent structures in the near-wall region. The rest of the models tested gave similar patterns, which were in accordance to observations made in experiments.

Finally, during the calculations presented, it was found that the ESD model was approximately 50% more expensive than the k_{sgs}-model, due to the root search algorithm required. This was an indication that future implementations should either involve a quicker algorithm or adopt an analytical solution of the polynomial equation for ε whenever this is possible. However, even this increase in computational cost was less than the increase that would result from the introduction of a further transport equation for ε, offering a more realistic behaviour for ε compared to the traditional modelling of the term adopted by the Yoshizawa and Horiuti k_{sgs}-equation model.

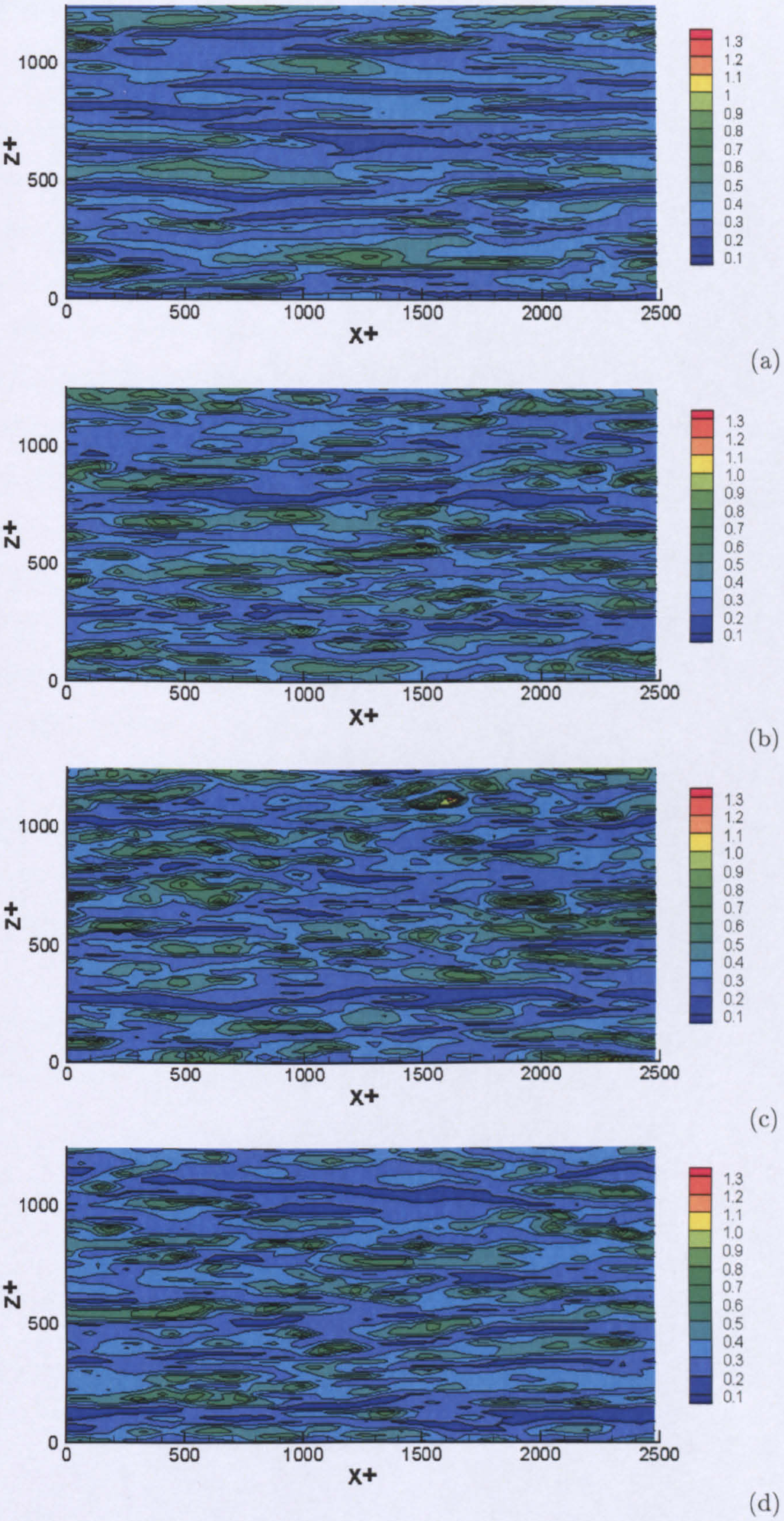

Figure 4.33: u'/U_B contours for $Re_\tau = 395$
(a: Smagorinsky, b: MS, c: k_{sgs}-equation and d: ESD model)

4.3 Channel flow simulation conclusions

The objective of the channel flow simulations was to test the implementation of the new SGS models introduced to the code and investigate their ability to provide accurate results of this basic flow case. Overall, the code performed well and the implementation of the new SGS models did not give rise to any problems during any of the computations.

The SGS models worked well with the near-wall damping functions and especially the ESD and k_{sgs}-equation model indicated that they could be used successively in combination with damping functions that did not make any use of y^+ in their formulation.

Regarding the simulations performed, the general trend was an increase of C_f error with Re_τ for all models. None of the models was totally accurate throughout the simulations but the models based on subgrid scales did manage to give more accurate predictions in all cases. This confirmed the validity of the idea presented in section 1.3.3. The new model proposed in the present study, although not without its shortcomings, indicated in general good behaviour and promising results for future implementations.

The most challenging of all cases presented in this Chapter was case 4. Although considerable improvement was made regarding the accuracy of the simulation, still the error in the predicted values of C_f and the wall-normal U^+ distribution was considerable. This case pointed out a number of issues, with most pronounced that of filtering introduced by large timestep and the the energy conservation properties of different variable arrangement schemes.

Finally, the use of different visualisation techniques provided useful experience for later implementation on more complex flow cases.

Chapter 5

Application of SGS Models to the Wing-Body Junction Flow

The use of the Smagorinsky and the k_{sgs}- equation models for the LES of a series of channel flows indicated that the one-equation model could provide more accurate results for a wide range of Re numbers. The next step in the study of the behaviour of a model of this type should involve a number of new features that would comprise a more demanding test case. Since the first test case was related to statistically stationary flow, the models should be tested on a case that would involve more unsteady flow behaviour. Furthermore, the flow case should involve a number of flow phenomena that did not appear in the first test case. Preferably, these phenomena should be related to those observed in common engineering applications, such as flow separation and reattachment, three-dimensional boundary layers and vortical structures. These features would then impose a challenging test with the potential to show the advantages and disadvantages of the k_{sgs}-equation model in comparison with the classical Smagorinsky model formulation.

Along with the k_{sgs}-equation model, the application of the ESD model to the wing-body junction would also be of great interest and a logical next step to its assessment. Unfortunately the ESD model was developed at the very last stage of the present study and therefore the time limitations did not allow for this second stage of testing to take place.

5.1 Description of the wing-body junction test case

Considering all the factors that were mentioned above, the second test case that was selected for the k_{sgs}- equation model was a wing-body junction flow. The wing-body junction geometry used in the present study was first introduced in 1986 by Dickinson [41]. The geometry consists of a wing that is standing perpendicular to a horizontal plane. The cross section of the wing is a NACA 0020 profile with the leading tip modified to form the contour of an ellipse of an axes ratio of 3:2.

The flow is assumed to be incompressible and the Reynolds number based on the mean inflow velocity and the wing chord is around 5×10^5. A schematic of the main flow features is given in Figure 5.1.The flow is coming from a plane upstream, passes around the wing and is convected through the exit plane. A two dimensional boundary layer is formed upstream of the wing section, that becomes three dimensional as the flow approaches and passes around the wing. This is because close to the wall, in the wing region, part of the flow separates due to an adverse pressure gradient present in the area and, in addition, the transverse vorticity, ω_z , present in the incoming turbulent boundary layer is stretched, skewed and realigned along the streamwise direction. It is the combination of these phenomena that generates a horse shoe vortex [49] that extends all around the wing and interacts with the boundary layer of the horizontal plane and the wing and with the wake formed downstream of the wing.

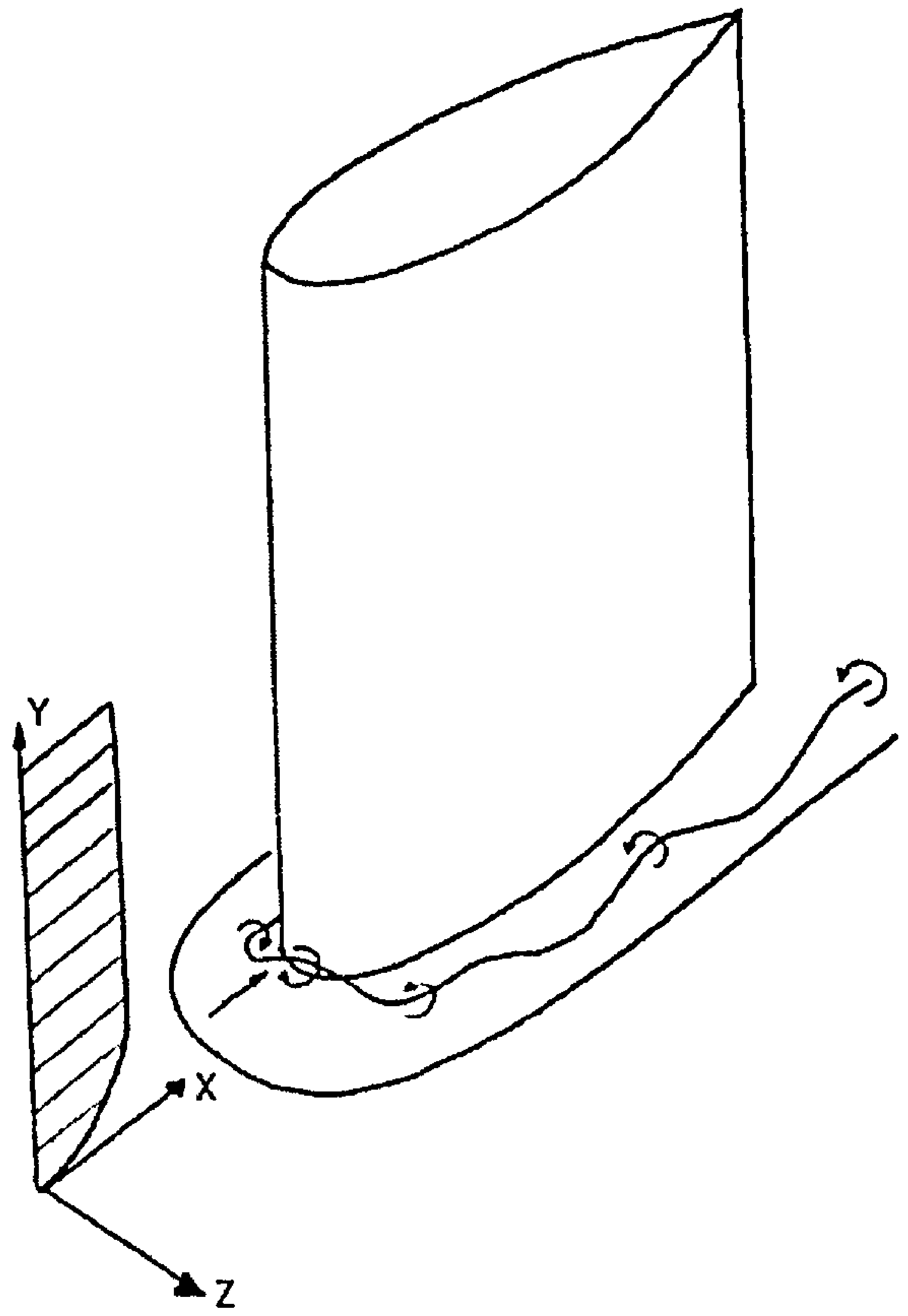

Figure 5.1: Schematic representation of the flow pattern observed in the wing-body junction flow

The horse shoe vortex itself has been observed to contain several weak, unsteady bimodal secondary eddies [38] which are responsible for high surface pressure fluctuations and heat transfer in this region [162]. Devenport and Simpson [34, 36, 35, 38] showed that the flow in this region switches aperiodically from one mode to the other in a self-induced chaotic manner. As a result, turbulence energy production and turbulence stresses were found to be of an order of magnitude larger than in the upstream boundary layer. It is worth noting that the incoming flow Reynolds number is not the dominant factor for the existence of the bimodal behaviour but rather, it is the wing shape because this is the factor that largely determines the pressure gradients around the wing, which by turn govern the horse show vortex stretching [162].

In the region upstream of the wing leading edge, a strong circulation about the z-axis is set up in the junction, which induces strong skewness in the boundary layer and makes the flow highly three-dimensional. One of the important consequences of the secondary motion is the transverse convection of streamwise momentum which energises the low-momentum flow in the corner of the junction, counteracting any tendency towards separation that might arise from the adverse pressure gradient [6].

The presence of the horse shoe vortex makes this type of flow of particular interest to the evaluation of an SGS model as it involves most of the vortical structures that can be accounted for in common engineering application flows such as flow at aircraft wing root, turbomachinery, submarine appendage-hull junctions and bases of bridge supports.

5.2 Experimental and numerical studies

Experimental data for the flow case described above was generated by a number of researchers. Dickinson [41] used X-configuration hot films and made measurements of all Reynold stresses but $-\overline{vw}$ at seven streamwise planes. Merati, McMahon & Yoo [121] used two hot-wire probes to measure all Reynold stresses at five streamwise planes. Fleming et al. [49] generated single hot-wire data close to the wing but reported interference with the flow when near the wall. The same issue was reported by Dickinson [41] and Merati et al. [121]. Devenport and Simpson [38, 37, 39] presented LDA data close to the wing, without reporting any flow interference problems. Finally, Olcmen and Simpson [131] made velocity and Reynold stress measurements by using both laser-Doppler velocimetry and hot-wire anemometry to confirm the reliability of the data obtained at seven locations in the nose region. A collection of these data sets was later gathered by ERCOFTAC web site at http://cfd.me.umist.ac.uk/ercoftac/ [52], to form an experimental database for this test case. This collection was used by the present study to comment on the accuracy of the results obtained by the simulations performed.

From the numerical simulation point of view, throughout the years a number of researchers used this case as a part of the validation process of turbulence models for RANS calculations. Leschziner and Apsley presented a summary of the results obtained by a number of European companies and universities [97, 6]. It was among the main conclusions of this study that only the second moment closure performed well and presented a supremacy over the rest of the models. Only the Shear Stress Transport, SST, model managed to follow the accuracy of second moment closure but with a formulation particularly sensitive to adverse pressure gradient provoking separation. On the other hand, non-linear, cubic eddy viscosity models did not present any clear advantage over their linear counterparts, in contrast to observation that had been made previously on 2D separated flows [97].

More recently, Paciorri et al. [132] presented a study of this flow, employing the one equation Spalart -Allmaras model [168] and the two equation $k-\varepsilon$ model proposed by Lam and Bremhorst [89]. In their conclusion they mentioned an under prediction of the horse shoe vortex presence, due to the excessive eddy viscosity production inside the vortex region. However, reasonable predictions were made by both models for time-averaged quantities, with the Spalart -Allmaras model showing a slightly better performance.

From the studies performed so far on the particular case, it has been shown that RANS cannot capture satisfactorily the flow features. However, good results have been obtained by one equation models. Our calculation was the first attempt of LES on this flow at the time of the present study. The higher accuracy provided by the combination of the LES technique and an SGS model that calculates eddy viscosity directly from SGS quantities rather than the resolved ones, could potentially lead to better results.

5.3 Description of grid

The flow domain geometry employed for the simulations of the present study was based on the one proposed by ERCOFTAC Classic database [52] case 63. The wing maximum thickness T was $0.0717m$ and the chord was $c = 4.254T$. The wing leading edge was located $18.24T$ downstream of the inlet plane, providing enough space for the boundary layer to develop. The flow domain outlet plane was located $10T$ aft the leading edge, resulting in a total streamwise (x) extent of $28.24T$. The spanwise (z) extent of the domain was $19T$, with the wing located in the middle. Finally, the flow domain extent in the wall normal direction (y) was $3T$. The flow domain geometry can be seen in Figure 5.2.

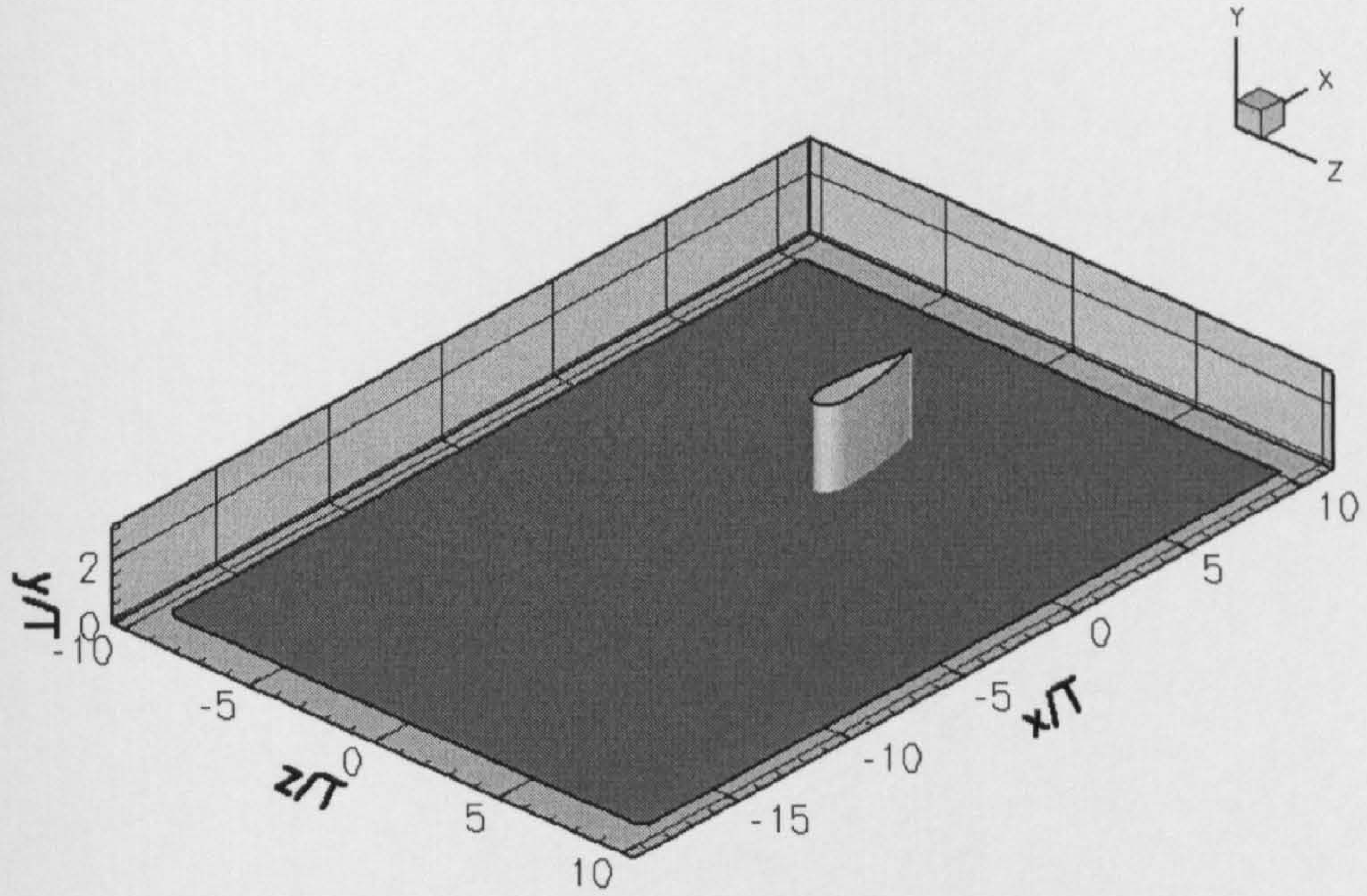

Figure 5.2: Wing-body junction flow domain geometry

Although a grid is provided by ERCOFTAC [52], it was decided that a new one had to be generated, in order to be more appropriate for the LES calculation. The new grid had 312 × 60 × 84 cells, forming four blocks in the wall normal direction. Each block had 15 cells in the y direction to maximise the performance of the parallel implementation of the code. Particular attention was given to the grid quality. Hence, the average cell aspect ratio was 15 and the average cell skewness was 81°. In terms of grid resolution, the points were distributed in such manner that the grid was denser closer to the leading and trailing edge as well as in the near-wall regions to allow for better resolution of the flow features present in these areas. This distribution resulted in $\Delta x = 0.007T$, $\Delta y = 0.0035T$ and $\Delta z = 0.0042T$ in the near-wall regions, which corresponded to $y^+, x^+ \simeq 3.0$. Although beneficial in terms of simulation accuracy, the use of a finer grid would increase even further the computational cost and the time required to finish the simulation. Furthermore, the assessment of the two SGS models on a relatively coarse grid was one of the objectives of the study since it would indicate the importance of the grid resolution for such complicated flow case and the ability of the model to compensate in a case where large part of the turbulence energy is in the subgrid scales. A plan view of the grid can be seen in Figure 5.3.

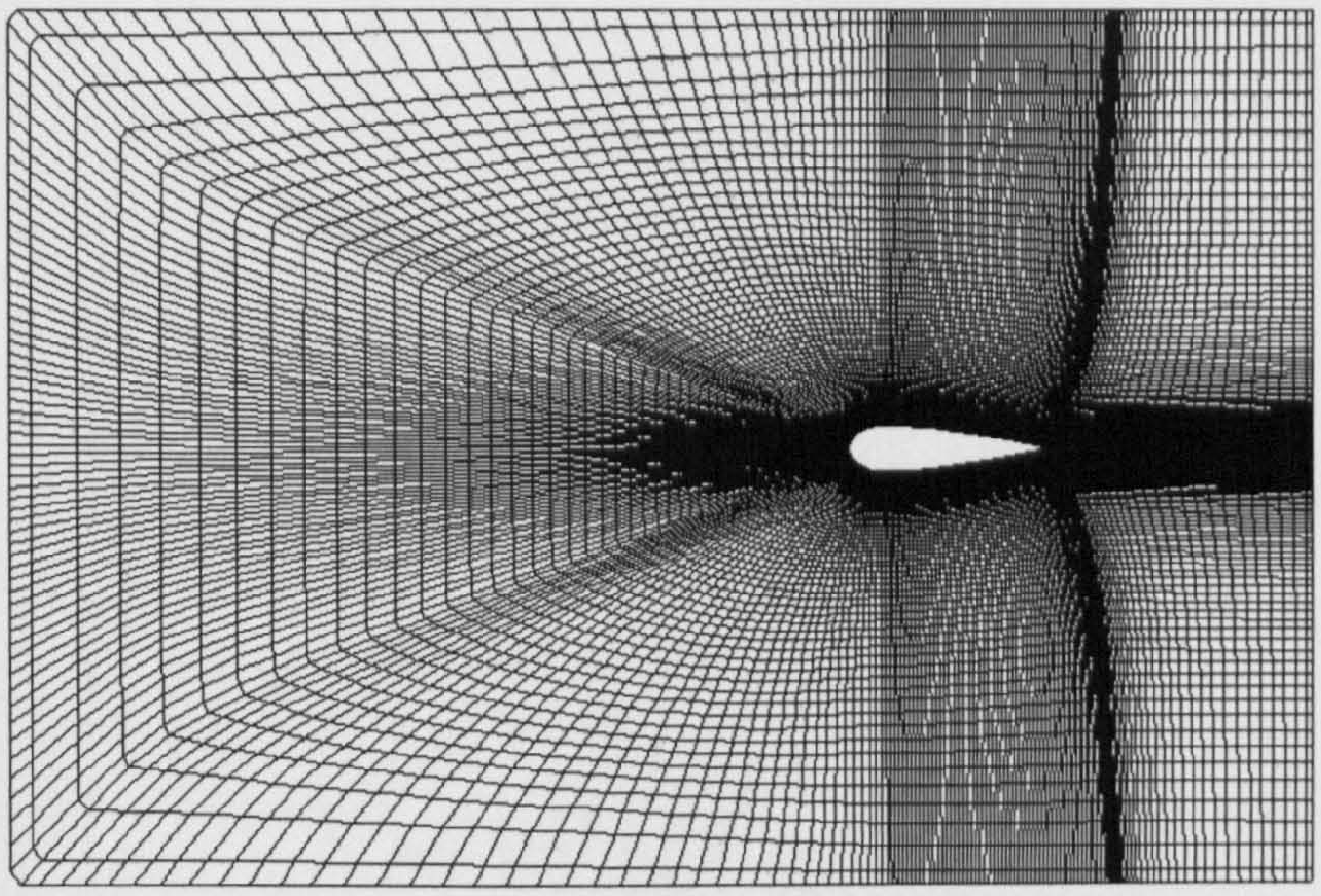

Figure 5.3: Plan view of wing-body junction grid

5.4 Description of general boundary conditions

In terms of boundary conditions, at the inlet plane of the flow domain, a wall-normal profile of u was imposed, constant along the span of the domain under the assumption of parallel flow.

Olcmen and Simpson [131] reported a negligible blockage effect due to the presence of the sidewalls. Furthermore, a $37mm$ gap had been left between the upper wall of the wind tunnel and the wing, in order to avoid the interaction of the roof boundary layer and the model [131]. Therefore, side and top flow domain boundaries were treated as non-viscous walls. The lower wall and the wing surface were treated as viscous walls. Finally, convective boundary condition was presented to the flow outlet plane.

5.5 RANS calculation

The first simulation performed for the wing-body junction flow was a RANS calculation. The objectives of this calculation were to establish the validity of the code with the new modifications and to generate an initial flow field for the LES calculations that would follow.

5.5.1 Numerical procedure and specific boundary conditions

In RANS mode, DELTA used a 2^{nd} order upwind scheme [189] for the discretisation of convective fluxes of momentum and $k-\varepsilon$ equations and the Rhie-Chow algorithm [152] for the prevention of checkerboard oscillations in the pressure field. Furthermore, 1^{st} order backward Euler implicit method was employed for time marching, using $\Delta t = 1.8e-5$ that corresponded to a CFL number of 0.89.

During this calculation, the standard $k-\varepsilon$ model [92] was employed in combination with the log-law, given by Eq.1.14. The grid and the boundary conditions described in the previous subsection, were used with an additional profile for k and ε specified at the inlet plane. The profile for k was calculated from the normal stresses as

$$k = \frac{1}{2}\left(u_i' u_i'\right) \tag{5.1}$$

where $u_i' u_i'$ were obtained by the Reynolds averaged experimental data of Olcmen and Simpson [131]. Note that only experimental data for $\overline{uu}$ and $\overline{ww}$ was available and therefore $\overline{vv}$ was approximated as $\overline{vv} = 0.4\overline{uu}$ according to ERCOFTAC [52] instructions.

ε was calculated using the Norris and Reynolds algebraic model [130] as:

$$\varepsilon = \frac{C_\mu^{3/4} k^{3/2}}{l_{Diss}} \tag{5.2}$$

where

$$l_{Diss} = \frac{\kappa_v K\, y\, y^*}{y^* + 2\frac{\kappa_v K}{C_\mu^{3/4}}} \tag{5.3}$$

In Eq. 5.3, $y^* = \frac{y k^{1/2}}{\nu}$. As in the case of k profile, the formulation presented above was in accordance to the ERCOFTAC recommendation [52] for the numerical simulation of the flow.

RANS simulation performed 7000 timesteps corresponding to 15 flow through times, ensuring that the flow had been fully developed and that the obtained results were statistically stationary.

5.5.2 RANS results and discussion

The flow field predicted by the RANS simulation described above was assessed through a number of contours of Reynolds averaged streamwise velocity and stresses, and compared against experimental data by Olcmen and Simpson [131]. Pressure coefficient C_P distributions were also examined along the wing and the bottom wall. Furthermore, boundary layer profiles were assessed in the upstream symmetry plane. Figure 5.4 shows $\frac{U}{U_B}$ contours over the mid-plane, upstream of the wing leading edge.

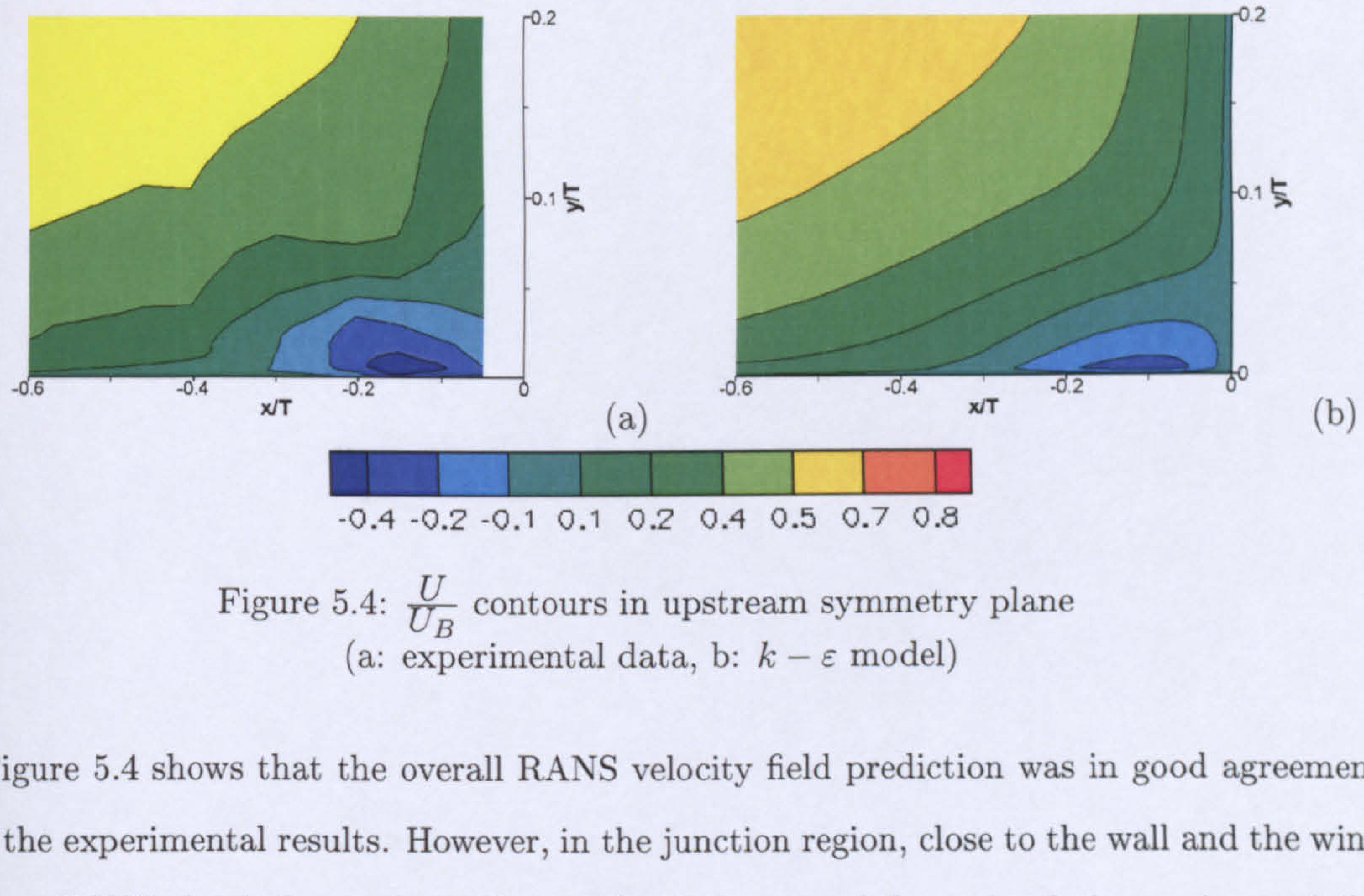

(a) (b)

Figure 5.4: $\frac{U}{U_B}$ contours in upstream symmetry plane
(a: experimental data, b: $k-\varepsilon$ model)

Figure 5.4 shows that the overall RANS velocity field prediction was in good agreement with the experimental results. However, in the junction region, close to the wall and the wing surface, RANS simulation under-estimated both the size of the recirculation region and the magnitude of the negative velocities which were predicted to be concentrated mainly closer to the lower wall.

The characteristics of the flow in this region can be seen more clearly in Figure 5.5, where the velocity vectors on the same plane are shown. Figure 5.5 (a) shows that according to the time-averaged experimental results the flow separates at $x \simeq -0.375T$, forming a recirculation region, whose centre is located at $x \simeq -0.175T$ and $y \simeq 0.05T$. Figure 5.5 (b) shows that RANS simulation predicted a flow separation at $x \simeq -0.3T$ and a recirculation region with a centre located at $x \simeq -0.175T$ and $y \simeq 0.038T$. Hence, while the streamwise location of the recirculation centre was accurate, the wall-normal location as well as the streamwise extent of the recirculated flow region was under-estimated.

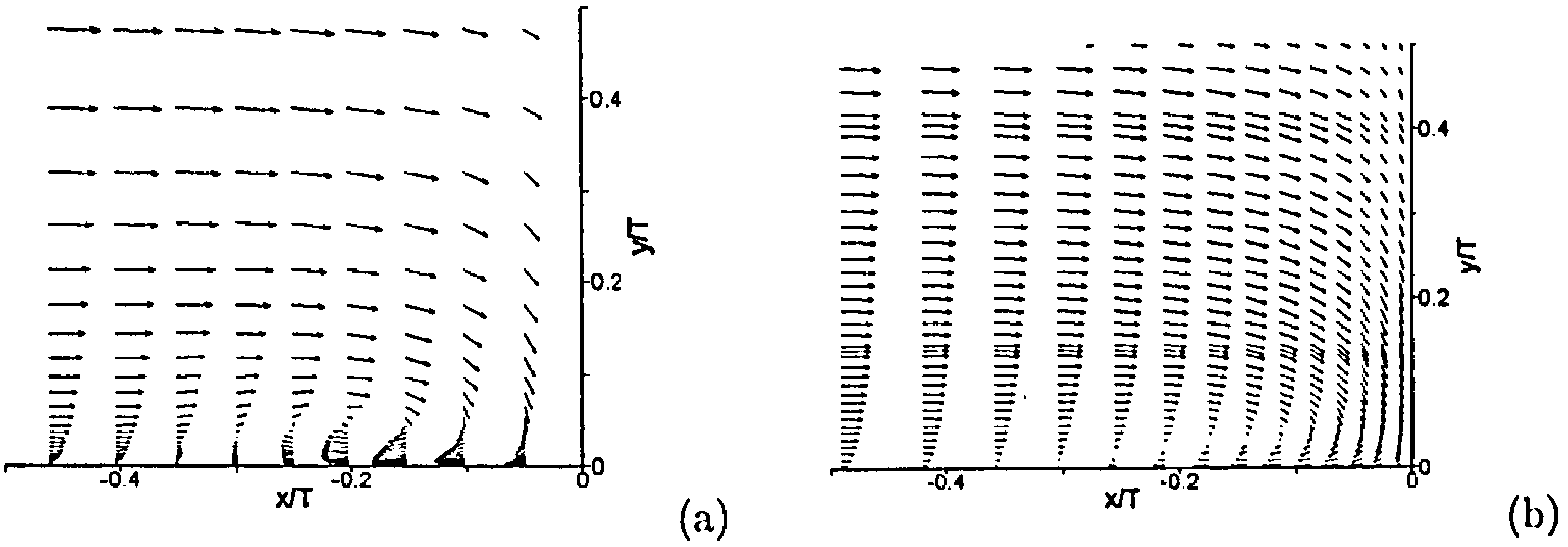

Figure 5.5: Velocity vectors in upstream symmetry plane
(a: experimental data, b: $k-\varepsilon$ model)

Possible reason for this feature could be the state of the boundary layer upstream of the junction region. Belik [15] and Baker [9, 10] had performed parametric studies on appendage-body junction flows and found that the separation point was weakly dependent on the ratio of the boundary layer displacement thickness δ^* to the appendage thickness, and proportional to the Reynolds number based on δ^*, Re_{δ^*}. A fuller turbulent boundary layer profile with smaller displacement thickness could result in higher momentum fluid in the near-wall region, leading to a delay of the flow separation and a consequent alteration of the recirculating region characteristics. This is confirmed by Figure 5.6, which shows boundary layer profiles on ten streamwise stations upstream of the junction, over the flow field mid-plane. Close inspection of Figure 5.6 indicates that the upstream boundary layer predicted by the RANS simulation was slightly more turbulent close to the lower wall in comparison with that observed in the experiments. This alteration of the upstream boundary layer characteristics can be attributed to the inlet boundary conditions as well as the grid resolution in the area.

Apart from the state of the boundary layer, another reason for the resulted characteristics of the recirculation region could be related to the prediction of stresses in the region and of their effect on the generated vortex. Contours of the streamwise normal stresses as well as shear stresses over the upstream symmetry plane can be seen in Figures 5.7 and 5.8. These contours are highly sensitive indicators of the upstream vortex structure and they can provide a mean of identification of the vortex strength in terms of the turbulence-generating strain

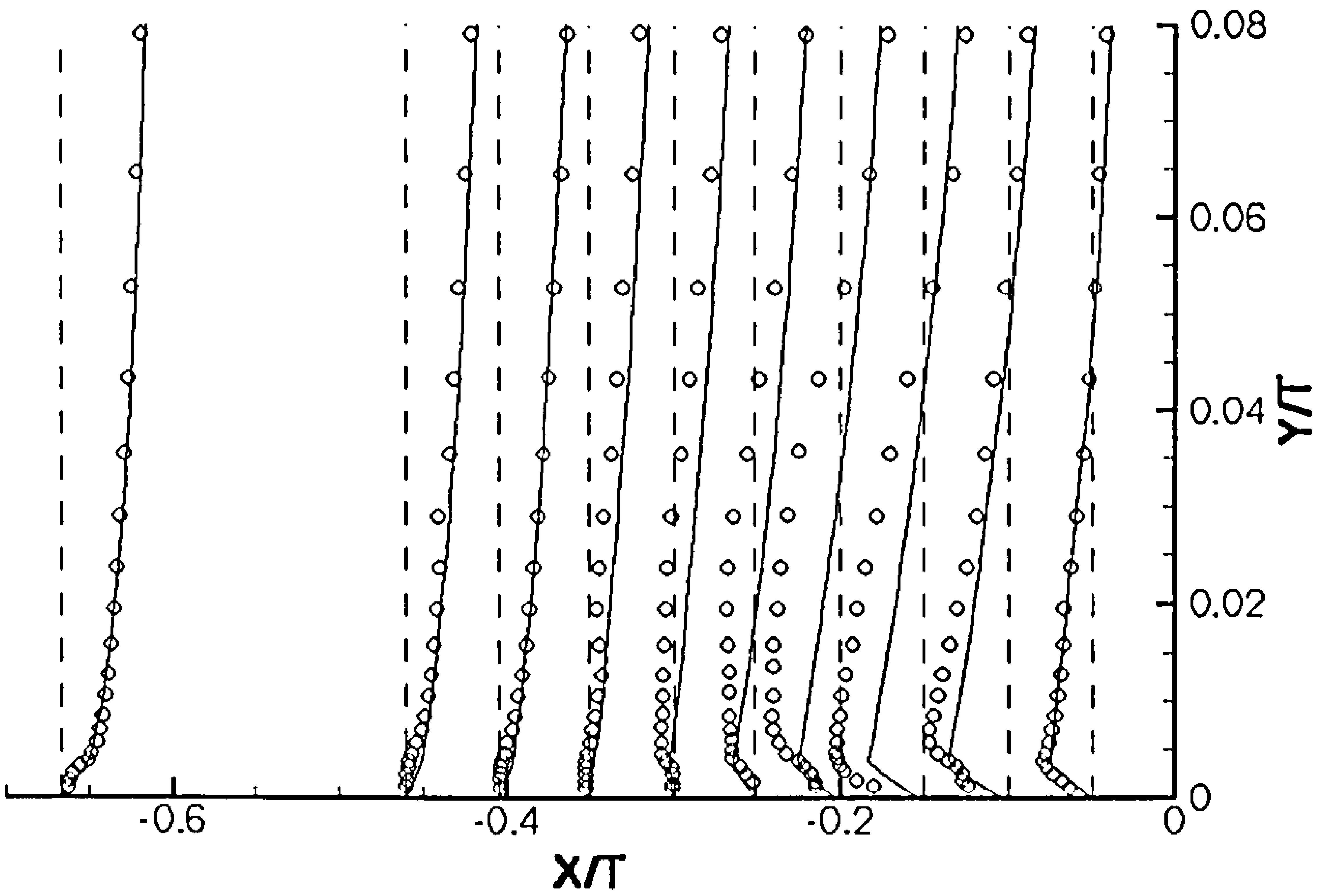

Figure 5.6: Boundary layer profiles in upstream symmetry plane (circles: experimental data, solid line: $k-\varepsilon$ model data, dashed line: streamwise station location)

within it [97]. The experimental data, shown in Figures 5.7 (a) and 5.8 (a), presents an increase of the streamwise normal stresses close to the highly sheared region of the vortex central area. Apsley and Leschziner [6] suggest that this is an indication that shear feeds, preferentially, the streamwise normal stresses through generation, while this generation is reduced in other areas where either shear-straining is low or normal straining is dominant.

The inability of the $k-\varepsilon$ model to reproduce this anisotropic behaviour and its interaction with the stress generation mechanism resulted in RANS simulation failing to predict accurately the normal stresses distribution. Figure 5.7 (b) shows that excessive levels were predicted along the stagnation region at the leading edge of the wing, underestimating the level of normal stresses in the vortex itself.

The prediction of the normal stresses had an effect on shear stresses, where RANS simulation failed to predict the high levels in the vortex central region but the locations of low shear-stresses were predicted slightly more accurately. Despite the discrepancies from the experimental data, the results obtained here were comparable with published results [6], obtained using Launder and Sharma $k-\varepsilon$ model [91].

The accuracy of the prediction of the vortex structure present upstream of the leading edge should have a result on the flow structures forming the vortices evolving around the

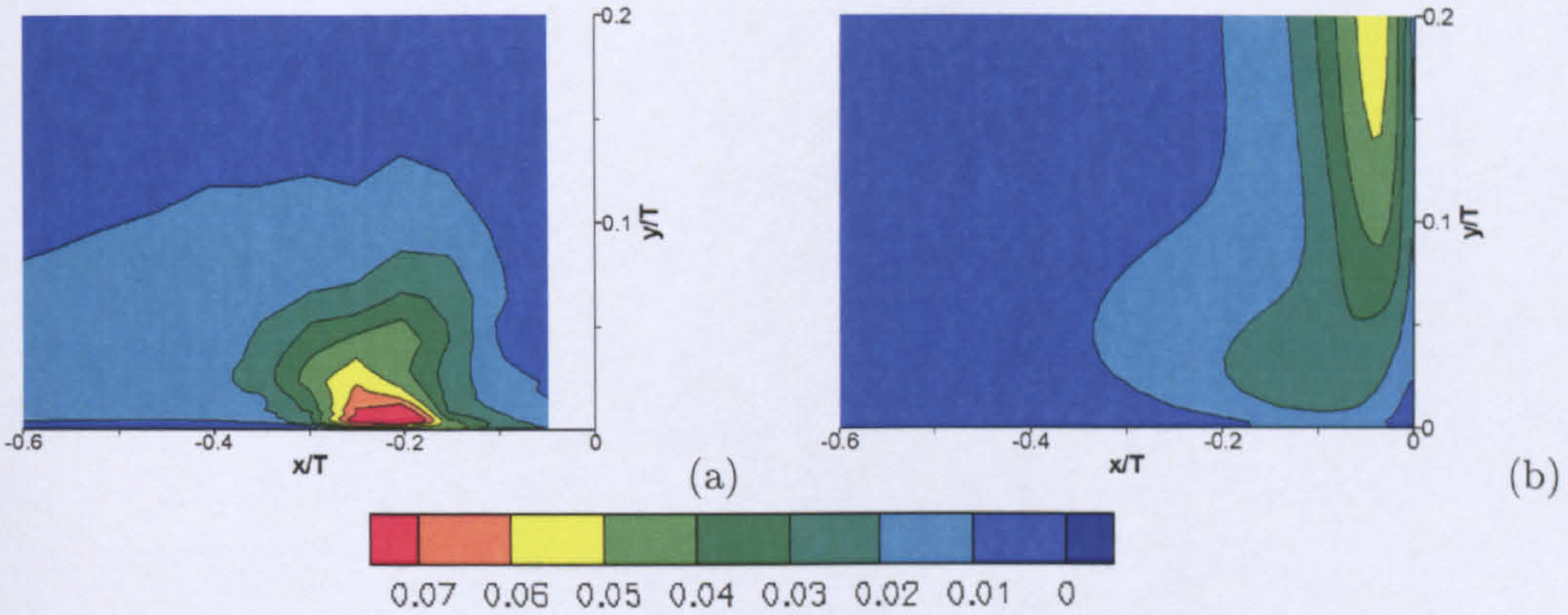

Figure 5.7: $\frac{\overline{u'u'}}{U_B^2}$ contours in upstream symmetry plane
(a: experimental data, b: $k - \varepsilon$ model)

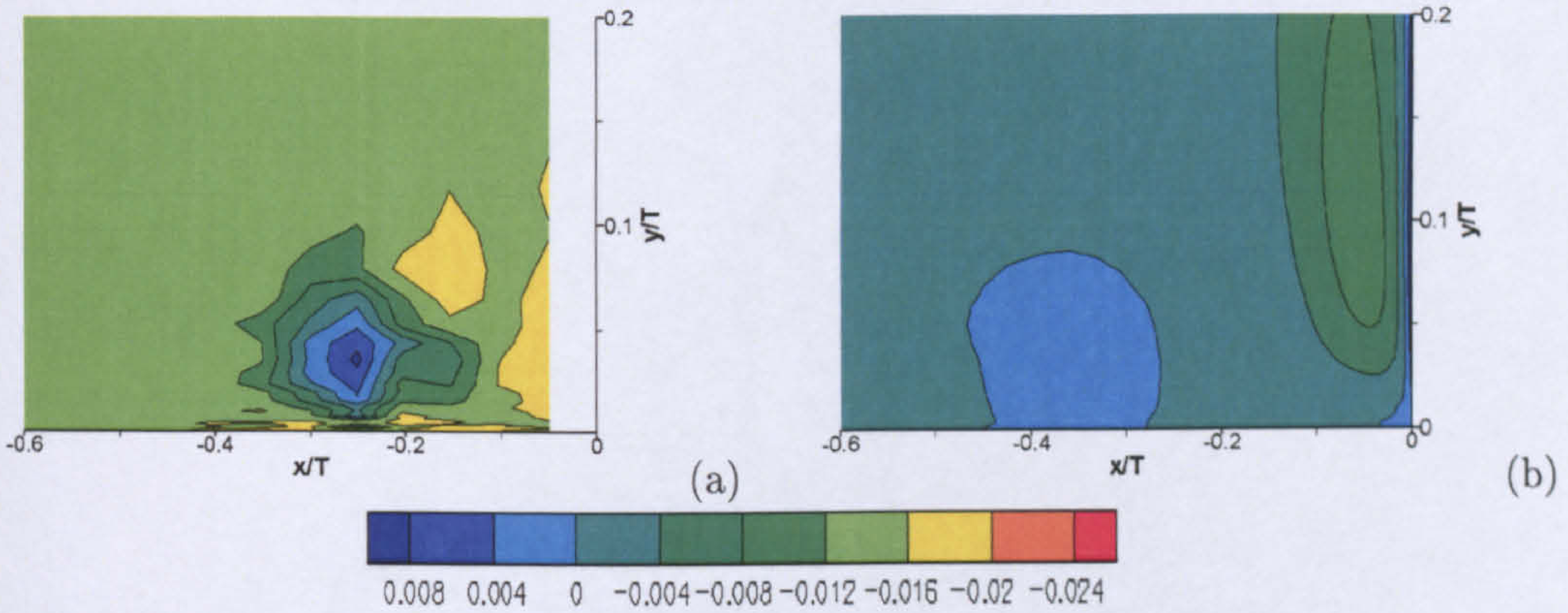

Figure 5.8: $\frac{\overline{u'v'}}{U_B^2}$ contours in upstream symmetry plane
(a: experimental data, b: $k - \varepsilon$ model)

wing-wall junction further downstream of the leading edge. This is reflected on the contours of streamwise velocity, as can be seen in Figures 5.9 to 5.11.

When the flow passes the maximum thickness point, located at $x = 0.75T$, the boundary layer over the wing surface is fairly thin, increasing in the junction region due to the interaction with the boundary layer developed over the lower wall. The latter results in a region of low momentum fluid close to the wall, comparing to the experimental data, adopting velocity at higher rates as we move further away from the wall. Further downstream, the streamwise vortical structure (ω_x) forming the bound vortex entrains fluid from the lower levels of the plate boundary layer, as can be seen in Figure 5.10. RANS simulation under-predicted the extent of the fluid entrainment, indicating a reduced vortex structure, located closer to the wing surface, as can be seen in Figure 5.10 (b), comparing with the experimental data, presented in Figure 5.10 (a).

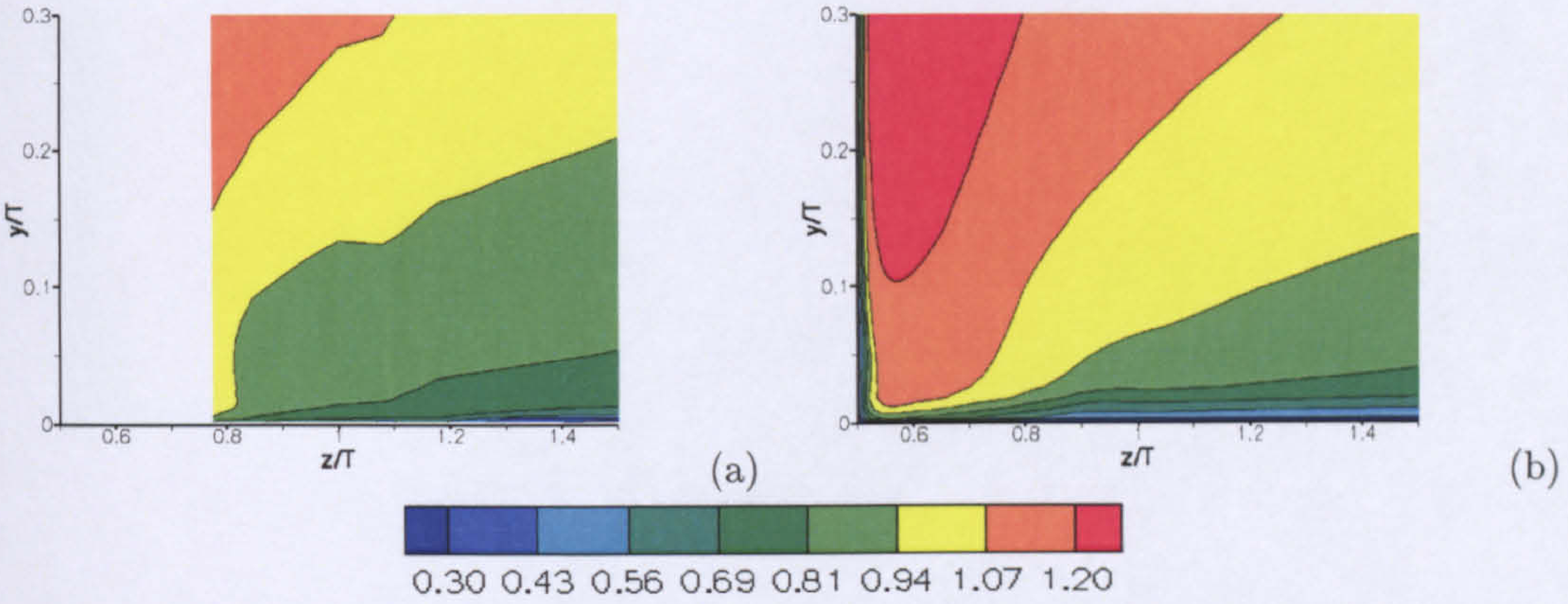

Figure 5.9: $\frac{U}{U_B}$ contours at $x = 0.76T$
(a: experimental data, b: $k - \varepsilon$ model)

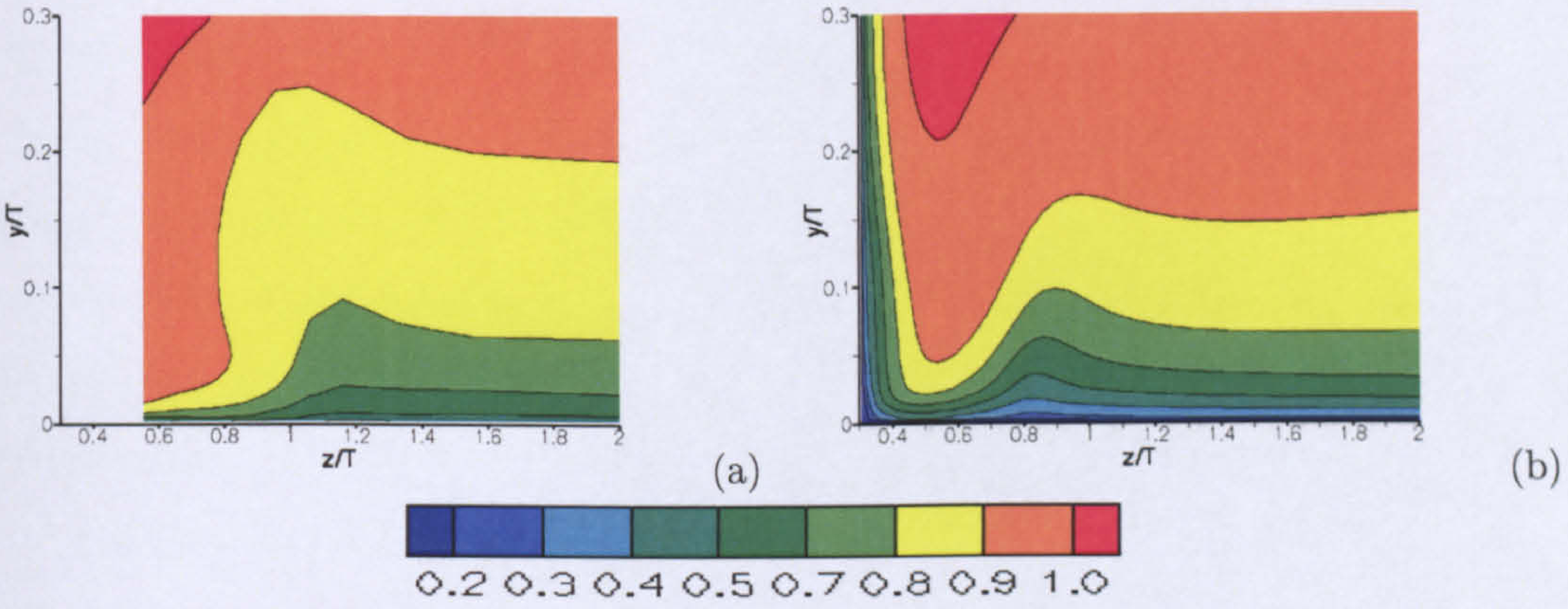

Figure 5.10: $\frac{U}{U_B}$ contours at $x = 2.72T$
(a: experimental data, b: $k - \varepsilon$ model)

Close to the trailing, at $x = 4.46T$, the streamwise velocity contours form a structure that can be seen in Figure 5.11. The boundary layer on the wing surface is fairly thick, due to the presence of adverse pressure gradient along the rear half of the wing. On the contrary, the boundary layer formed over the lower wall is thin and appears to thicken only in the junction region and the area where the streamwise vortex is present, due to the transfer of low momentum fluid from the wall to regions higher above, by the streamwise vortex itself. This characteristic has only loosely been captured by the RANS simulation, which has predicted that the location of the vortex is closer to the wing. Furthermore, RANS simulation has shown higher interaction between the wing and the lower wall boundary layer in the junction region, resulting in a distribution different from that shown by the experimental data.

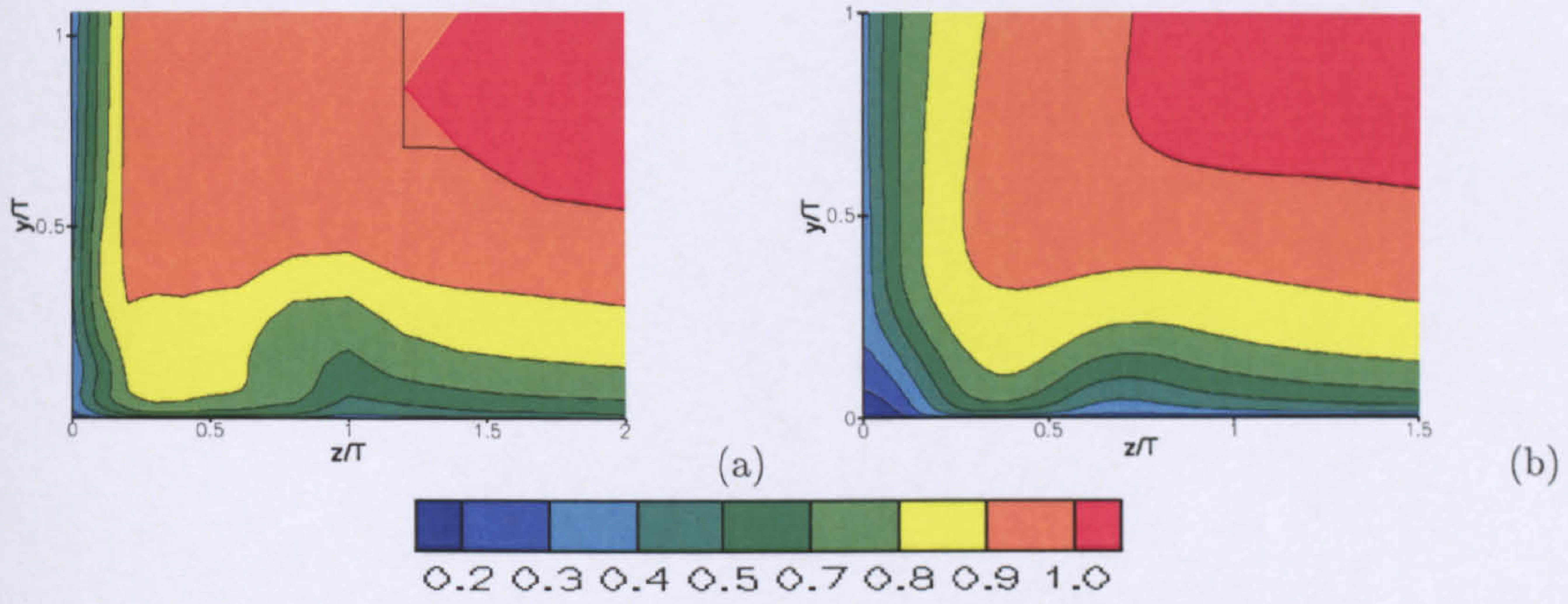

Figure 5.11: $\frac{U}{U_B}$ contours at $x = 4.46T$
(a: experimental data, b: $k - \varepsilon$ model)

The difference of the flow structures location between the experimental and numerical data had an impact on the prediction of $\frac{\overline{u'u'}}{U_B^2}$ contours, as can be seen in Figure 5.12. RANS simulation over-predicted the high normal stresses area in the junction region, while the normal stresses present in the streamwise vortex, shown to be well away from the wing surface, are closer to the junction region, due to the location of the streamwise vortex. Furthermore, RANS simulation over-predicted the normal stresses in the near wing surface region, away from the lower wall. As in the case of the results for the upstream mid-plane, the results shown here compared well with results obtained by using Launder and Sharma $k - \varepsilon$ model [91].

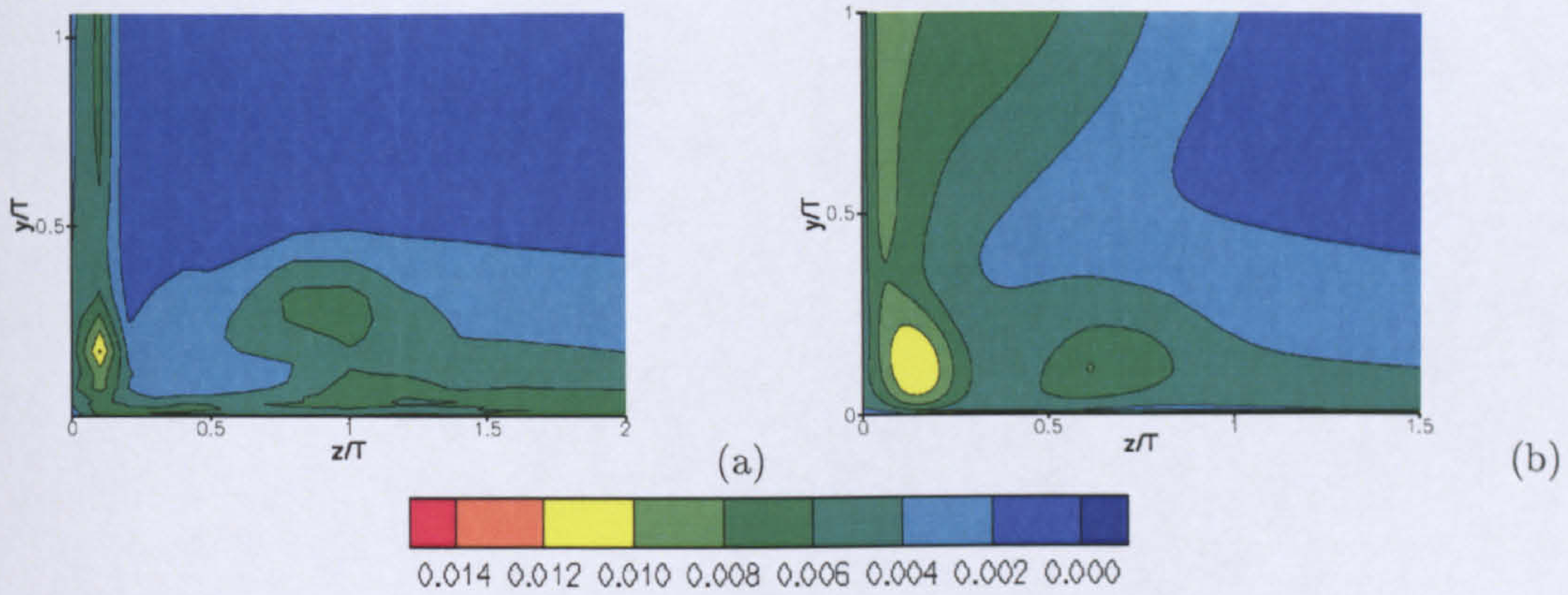

Figure 5.12: $\frac{\overline{u'u'}}{U_B^2}$ contours at $x = 4.46T$
(a: experimental data, b: $k - \varepsilon$ model)

In terms of C_P distribution along the wing, RANS simulation captured the pressure suction region fairly well close to the wall and the bound vortex region, although the pressure recovery was slightly under-predicted as can be seen in Figure 5.13 (a). The maximum positive C_P value as well as the negative suction peak indicate a slow moving boundary layer. Further downstream, the under-predicted pressure recovery shows higher velocity fluid close to the wall, possibly due to the interaction with the streamwise vortical structures described above, whose location was predicted to be closer to the wing than the location given by the experimental data. Finally, a comparison of the highest positive C_P value between Figure 5.13 (a) and (b) indicates a considerable wall-normal pressure gradient.

In wall-normal stations further away from the lower wall, shown in Figures 5.13 (c) and (d), the maximum pressure suction was under-predicted as well as the levels of the pressure recovering further downstream. Grid resolution was ruled out as a possible cause due to comparison with published results on coarser grids [6]. Hence, the most likely cause was considered to be the discrepancy between the experimental and numerical flow condition prescribed for the upper boundary of the flow domain. While in the experimental setup there was a gap between the end of the wall and the upper wall of the wind tunnel, a non-viscous wall was used as an upper boundary condition at $y/T = 3.0$ during the RANS simulation. This boundary condition was considered sufficient for the simulation purposes and it was believed that its location would not affect adversely the flow prediction in the junction region. However the location of C_P distributions presented in Figures 5.13 (c) and (d) were relatively close to the upper boundary, and hence affected to a greater extent than if they were further away, closer to the lower wall.

The predicted flow field described above presented some differences from the experimental data, which were attributed to the limitations of the turbulence model used and the computational setup. Although not all the variables of interest were accurately predicted, still, the results were in good agreement with published data obtained using similar simulation approaches. This was an indication that the code performed well using the new additions in terms of boundary conditions and could provide a flow field that was adequately accurate to be used as an initial field for the LES calculations to follow.

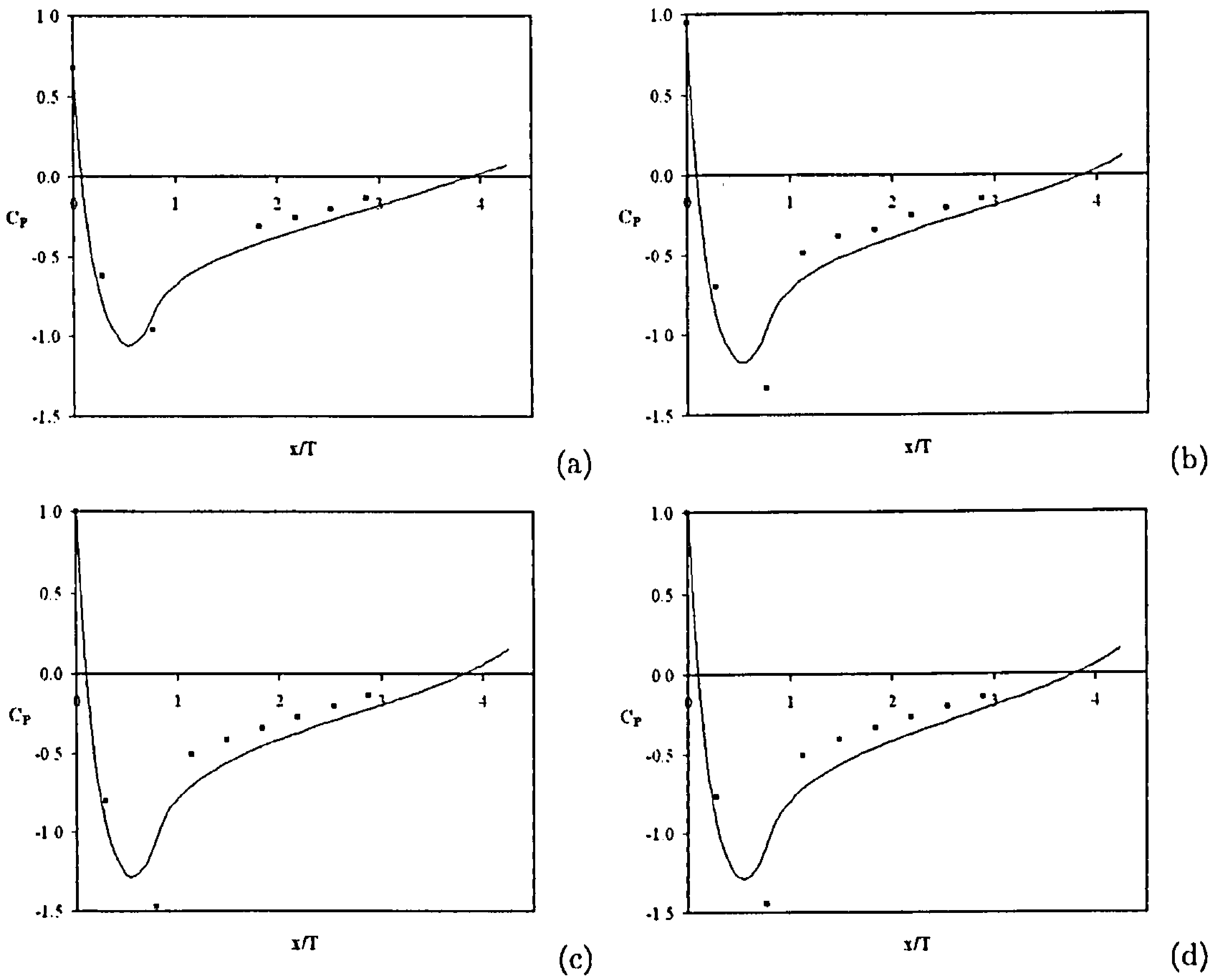

Figure 5.13: C_P distributions along wing surface: solid line $k-\varepsilon$, squares experimental data [131, 49]
(a: at $y = 0.13279T$, b: at $y = 0.39837T$, c: at $y = 1.4607T$ and d: at $y = 1.7263T$)

5.6 LES calculation

Two LES calculations of the wing-body junction test case were performed to further assess the performance and behaviour of two types of SGS models. Both employed the grid described in section 5.3 and they were initialised using the flow field produced by the RANS simulation. The numerical setup used was common for both calculations as well as the simulation strategy that was followed as described in section 5.6.2. This approach aimed to assist the author to a direct comparison of the results obtained from the two models, eliminating any other sources of discrepancies.

5.6.1 SGS modelling and specific boundary conditions

The first LES calculation of the wing-body junction case employed the Smagorinsky model [163], as described in section 2.1, in combination with Piomelli's near-wall damping function, given by Eq.2.29. The general boundary conditions, already described in section 5.4, were applied. In addition, on the walls, the Werner-Wengle near-wall model [186] was applied to allow for unresolved areas of the flow.

The second LES of the wing-body junction flow made use of the k_{sgs}-equation model, in combination with the Yoshizawa et al. [196] near-wall damping function, given by Eq.2.30. In terms of boundary conditions, the general boundary conditions were applied, as described in section 5.4 but an additional condition was required for k_{sgs} at the inlet. Therefore, similar to the case of k, a spanwise-constant, wall-normal profile for k_{sgs} was imposed, calculated by the method described in section 3.1.3. Finally, as in the case of the first simulation, the Werner-Wengle near-wall model was applied.

In contrast to RANS simulations, LES requires a form of unsteady inlet boundary conditions in order to explore the full potential of the method. Unfortunately, from the experimental data available there was no time history provided or any information that could be used to generate a 'quasi-realistic' unsteady signal. Therefore, it was decided to use a 10% random disturbance zero mean signal, superimposed to the time-averaged velocity profile, in order to introduce some disturbance to the flow. Although the lack of any phase information in this signal was expected to lead to a relatively rapid decay of the disturbance, it was thought that the extent of the flow domain upstream of the wing leading edge could provide enough space to allow the flow to be fully developed before reaching the main region of interest. RANS simulation produced velocity profiles in good agreement with the experimental data, upstream of the junction area, as can be seen in Figure 5.6, indicating the feasibility of the approach. It is worth to note at this point that in the experiments of Olcmen and Simpson [131] the inlet turbulence intensity was only 0.1%. Therefore, the combination of the time-averaged profile with the superposition of low magnitude random disturbance was considered adequate.

5.6.2 Numerical procedure

The LES calculations started with the initialization of the flow field using the RANS solution described in section 5.5.2. At the beginning of the simulation, a first order Euler implicit time marching was employed with a large timestep in order for the flow to develop quickly. The timestep used was 0.000018 seconds, corresponding to 0.000243 FTT, and to a maximum CFL number of 0.74. This time marching scheme was employed for the first 10 FTT. During that period, weighted central differencing scheme, CDS, was used for the convective fluxes, resulting in a 2nd order accuracy.

When the flow became fully unsteady, a third order accurate Runge-Kutta scheme [187], RK, was employed in combination with a smaller timestep in order to limit the maximum CFL number to 0.18. However, the use of second order CDS for the spatial discretisation of fluxes gave rise to high dispersion errors, in form of wiggles. The result was the contamination of a large part of the flow field with non-physical oscillations. These oscillations were amplified with time causing eventually the calculation to stop.

Similar problems have been reported in literature in a number of studies related to LES of high Reynold number flows with the use of CDS for the convective fluxes [76]. For the LESFoil project [117], a number of researchers faced these issues when the grid was not fine enough, causing the cell Peclet number to reach very large values. Two remedies were suggested. According to the first approach, the flow field was divided into two zones. The first zone was extending over a part of the Aerospatiale A-airfoil, where from experiments it was known that the boundary layer was turbulent. In this zone, CDS was used. The second zone was covering the rest of the flow field and a higher order upwind differencing scheme, UDS, was employed. The dissipation provided by the UDS was enough to suppress the formation of the wiggles. Although requiring some previous knowledge of the transition point location and the extent of the turbulent boundary layer, this method did avoid the formation of wiggles and provided a numerical mechanism for the flow transition.

The second approach employed a higher order UDS throughout the flow field that resulted in the suppression of any non-physical oscillations. In the LESFOIL project [117], ONERA employed a second order upwind scheme [117] obtaining good results. Tenaud and Phuoc [175] employed a second order upwind Total Variation Diminishing, TVD, scheme for the

LES of separated flow around a NACA 0012 airfoil without showing any excessive levels of numerical dissipation. In other type of flows, such as turbulent free jets [189] and nozzle jet configuration [5], third or higher order upwind schemes have been used successively, leading to the conclusion that although UDS can introduce more dissipation than a CDS would, it is still a viable option to avoid wiggles as soon as the scheme employed is of adequate accuracy.

For the present study it was decided that a hybrid method should be used, switching from UDS to CDS when the Peclet number was lower than two. However, the implementation of the method showed that in practice the CDS was not employed since the Peclet number was always above the limiting value. Therefore it was decided that the best next option would be to employ a third order UDS [189] which could avoid the generation of any unphysical oscillations. At the same time the order of accuracy was considered adequate to avoid the introduction of any excessive dissipation in the flow.

In order to assess the effect of the third order upwind scheme on the turbulence development, two test simulations were performed on a periodic hill channel flow [174]. Detail description of this test case is given in section 6.3.1. The first simulation made use of a second order CDS for the discretisation of the convective terms of the equations. In the second simulation, the third order upwind scheme was employed. Both simulations made use of the Smagorinsky model and Piomelli's near-wall function. Prescribed unsteady inlet velocity data was imposed at the inlet and convective boundary conditions were applied on the outlet. The upper and lower walls were treated as viscous and the sides as periodic boundaries. The results of these two calculations can be seen in Figures 5.14, 5.15 and 5.16, where contours of $\frac{U}{U_B}$, $\frac{\overline{u'u'}}{U_B^2}$ and $\frac{\overline{u'v'}}{U_B^2}$ are presented. These are time-averaged results over a period of 10 FTT. As can be seen, in terms of the mean velocity, the agreement of the two calculations is satisfactory. The separation points and reattachment points difference is 1.1% and 1.7% respectively and the geometry of the separation bubble has been captured in the same manner by both calculations. In terms of the Reynolds stresses, the use of the third order upwind scheme results in enlarged areas of peak stress values but there is no indication that it produces excessive dissipation that can result in a suppression of the turbulence activity. Hence, the results obtained from this test case indicated that the use of the third order upwind scheme should not act in an adverse manner regarding the development of turbulence in the flow field of interest.

Both LES calculations of the wing-body junction test case continued with the RK and the

3^{rd} order UPS for 10 FTT. After this period, first and second order moment statistics were collected over a period of 15 and 10 FTT respectively.

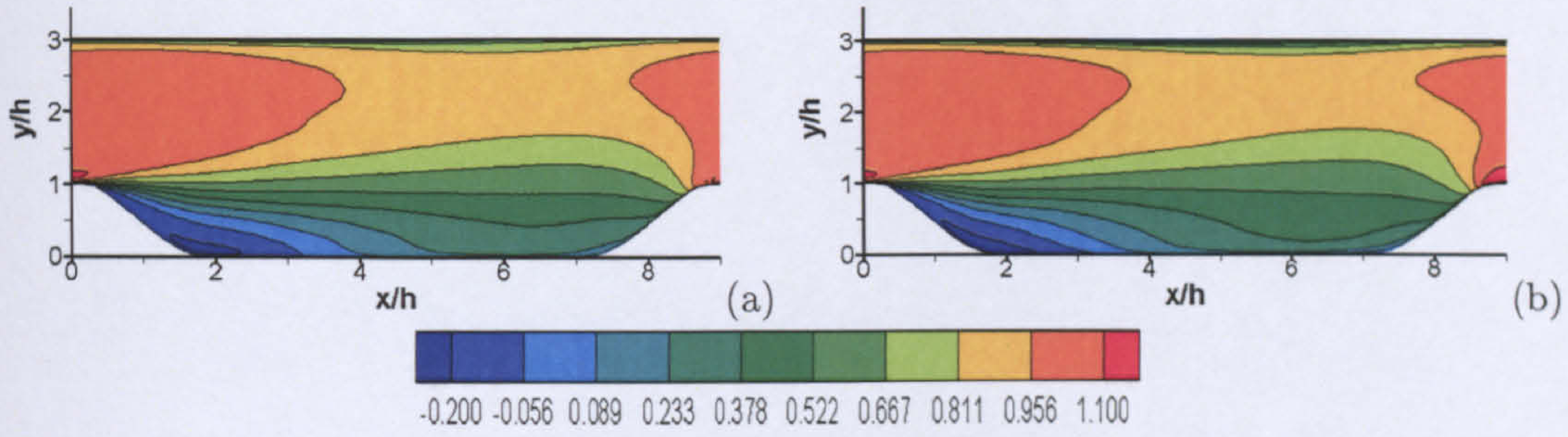

Figure 5.14: Contours of $\frac{U}{U_B}$ (a: 2^{nd} order CDS, b: 3^{rd} order UPS)

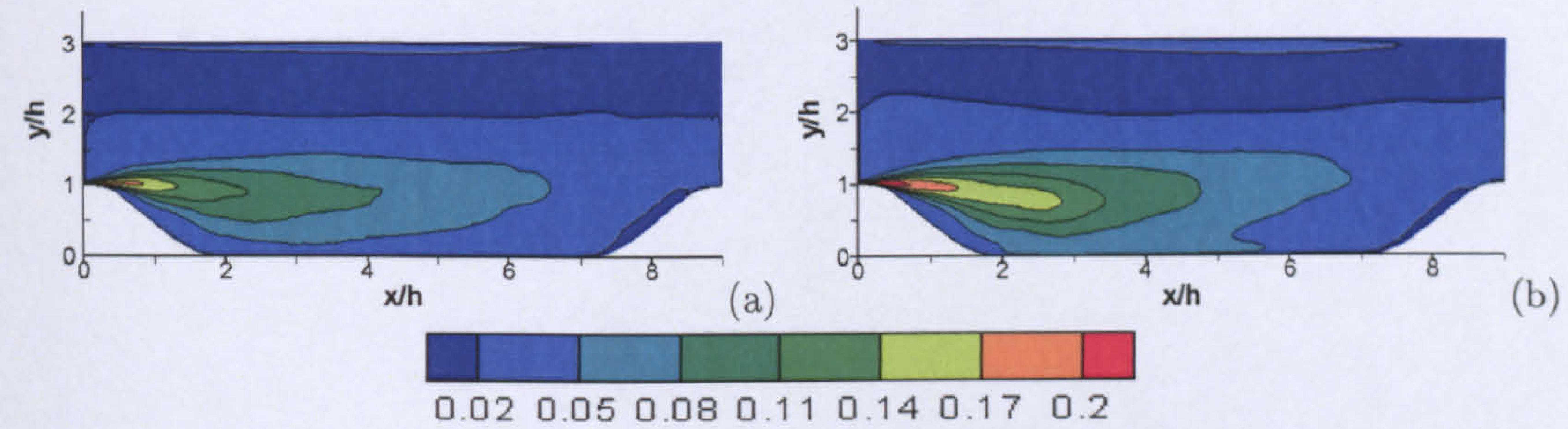

Figure 5.15: Contours of $\frac{\overline{u'u'}}{U_B^2}$ (a: 2^{nd} order CDS, b: 3^{rd} order UPS)

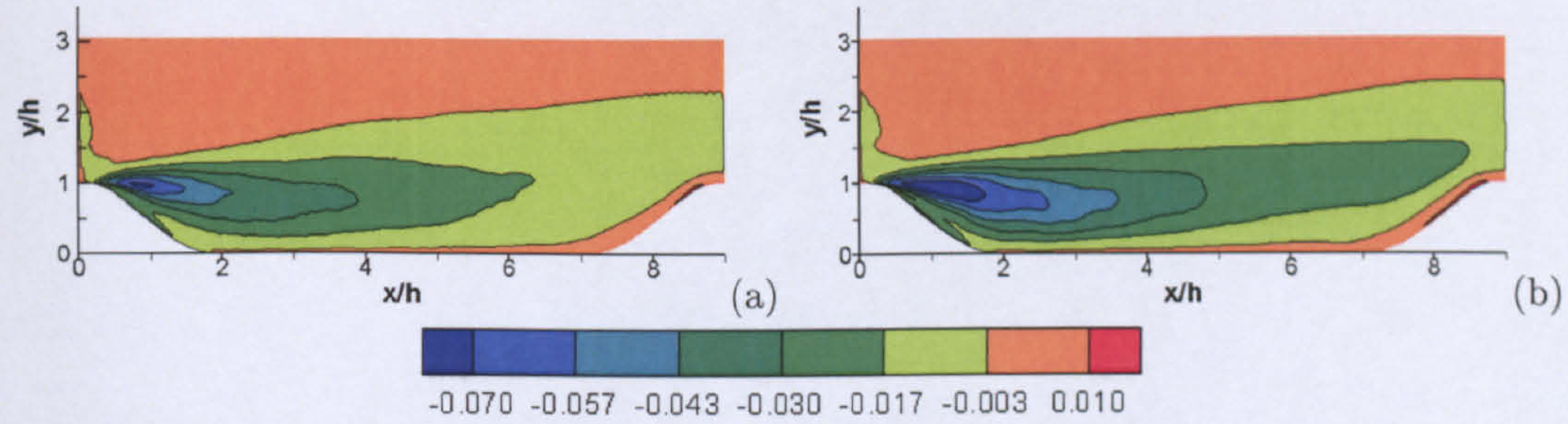

Figure 5.16: Contours of $\frac{\overline{u'v'}}{U_B^2}$ (a: 2^{nd} order CDS, b: 3^{rd} order UPS)

5.6.3 LES results and discussion

The flow field obtained by the two LES calculations can be seen in Figures 5.17 (a) and (b) where contours of the non-dimensional streamwise velocity component are presented at $y = 0.02T$. These figures show that the predominant characteristic of the flow field predicted by the LES calculations was an enlarged recirculation region, upstream of the wing-body junction region, which was particularly pronounced in the case of the Smagorinsky model.

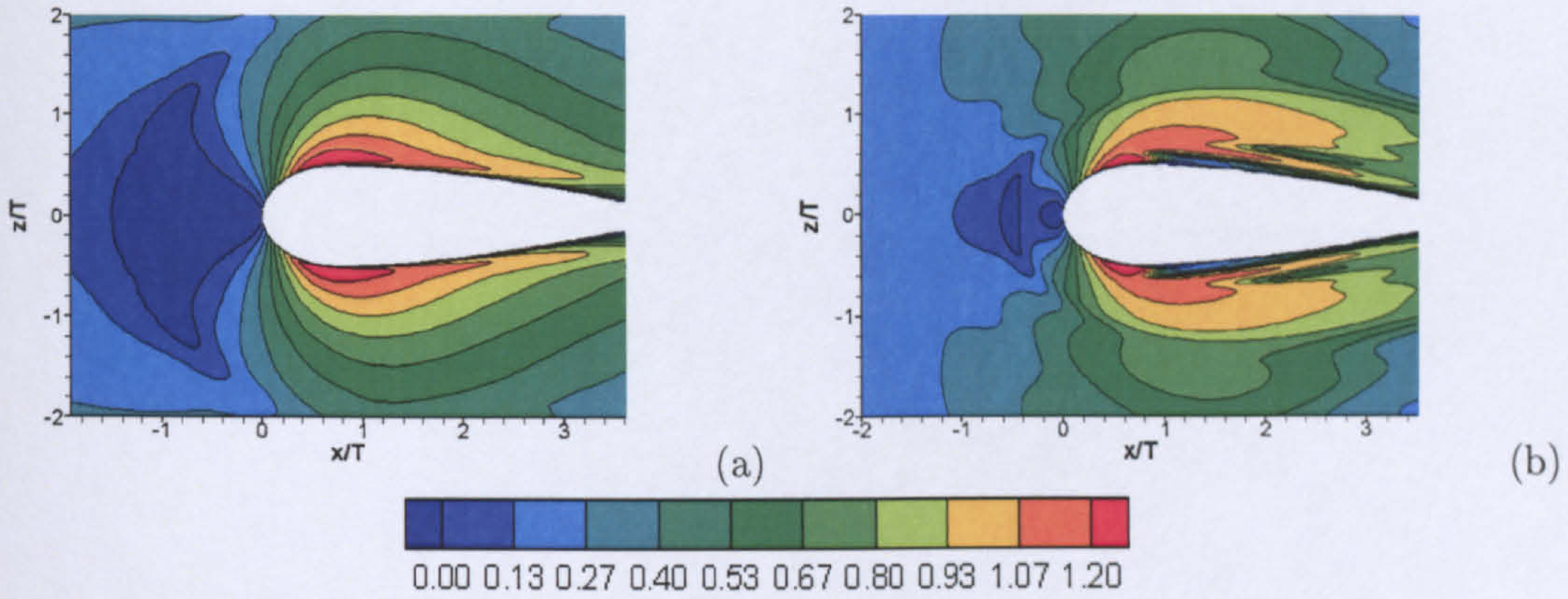

Figure 5.17: Contours of $\frac{U}{U_B}$ at $y = 0.02T$
(a: Smagorinsky model b: $k_{sgs}-$equation model)

Both SGS models over-predicted significantly the recirculation region. The k_{sgs}-equation model gave the largest recirculation region as can be seen on Table 5.1. The same Table shows that the Smagorinsky model gave a better prediction but still considerably larger than the experimental data. In that respect, RANS solution proved to be the most accurate.

Source	Experiment [131]	RANS	LES with Smag.	LES with k_{sgs}-eqn
Recirculation region extent	0.375T	0.3T	2.2T	2.8T

Table 5.1: Recirculation region extend

In the case of the Smagorinsky model results, closer inspection of the recirculation region reveals the presence of three separate vortex cores at the junction region that are close enough to form a larger combined recirculation region. These can be seen in Figure 5.18 (a) where velocity contours and stream traces of the time-averaged flow field in the upstream symmetry plane are presented. Figure 5.18 (a) shows that the primary vortex was predicted at $x = -1.2T$ and the secondary, counter-rotating vortex at $x = -1.4T$. The latter is formed by back-flow fluid that separated from the wall, forming a shear layer that feeds into a primary clockwise-rotated vortex and a secondary anti-clockwise rotated vortical structure. The momentum of this shear layer is such that part of it propagates further upstream only to separate for a second time, forming a third vortex core at $x = -1.8T$.

Systems of vortices such as the one described above have been reported in literature of junction flows. In laminar flow conditions in the range of $Re_D = 3,400$ to $7,300$, using smoke flow visualisation, Baker [8] showed the existence of an oscillating unsteady vortex pattern,

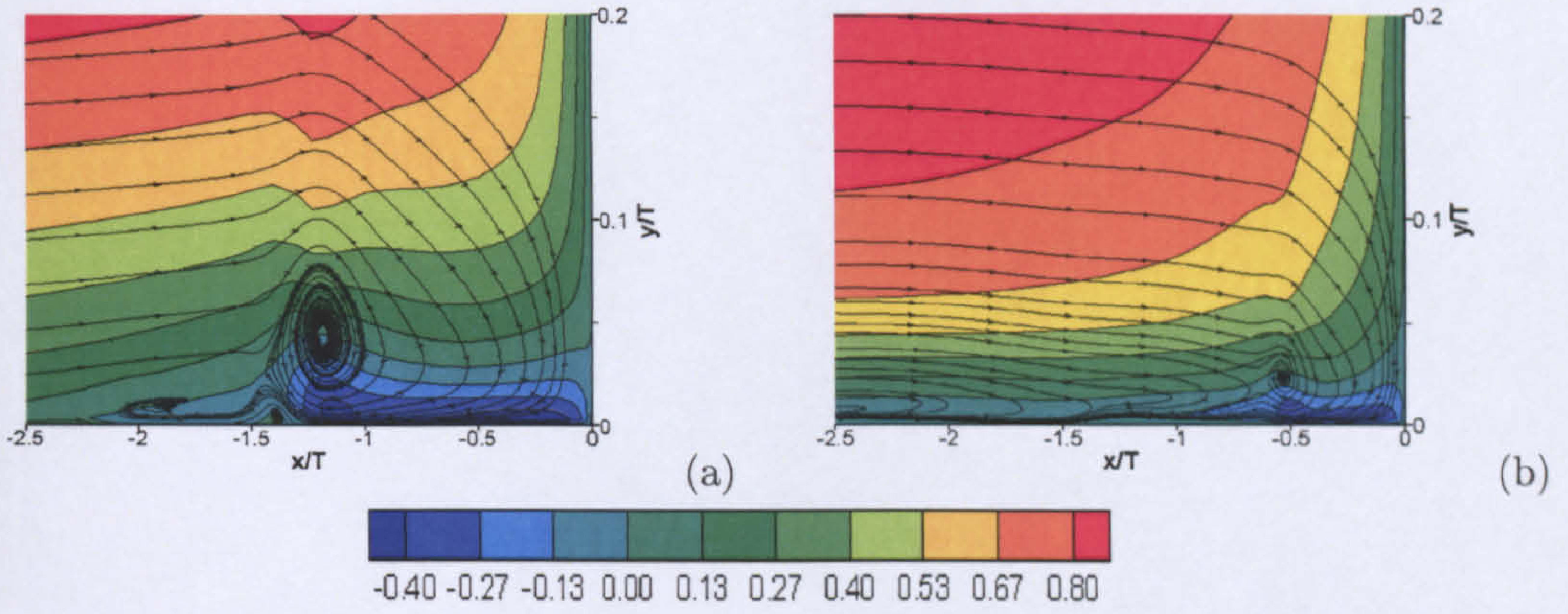

Figure 5.18: Contours of $\frac{U}{U_B}$ and streamtraces in upstream symmetry plane (a: Smagorinsky model b: k_{sgs}−equation model)

which appeared to be a function of Re_D, with more vortices present as Re_D increased, on the junction region upstream of a cylinder of diameter D. In his study on the same test case, in turbulent flow conditions in the range from $Re_D = 4,000$ to $90,000$, Baker [9] used oil-flow visualisation to obtain a system of vortices presented in Figure 5.19. As it can be seen, the system of vortices in Figure 5.19 bears a significant resemblance to this obtained by the Smagorinsky model and presented in Figure 5.18 (a). In his study, Baker [9] concluded that in these conditions a system of four main vortices is always present and that the location of the primary and secondary vortex is a function of D/δ^*, with the location of the vortices moving closer to the junction as D/δ^* increases. This behaviour is also reflected on the LES results obtained by present study, as can be seen in Table 5.2. Table 5.2 shows that in the case of the Smagorinsky model, the value of δ^* at $x = -3.19T$ was larger than the corresponding value given by the k_{sgs}-equation model, resulting in smaller D/δ^* value. As a result, the position of the primary vortex was further away from the junction region, confirming Baker's conclusion.

On a generic wing-body junction geometry, Bain and Fletcher [7] presented a similar system of vortices in the symmetry plane upstream of a generic wing-body junction geometry, whose features were strongly dependent on the Re_T. In all cases studied, a primary vortex was present, downstream of a weak secondary count-rotating vortex and a third vortex was formed as Re_T was increasing. Their relative positions were constant but their distance from the wing leading edge increased with Re_T. Hence, for $Re_T = 3,000$, the location of the primary vortex was at $x \simeq -0.6T$, while for $Re_T = 7,000$ at $x \simeq -0.85T$.

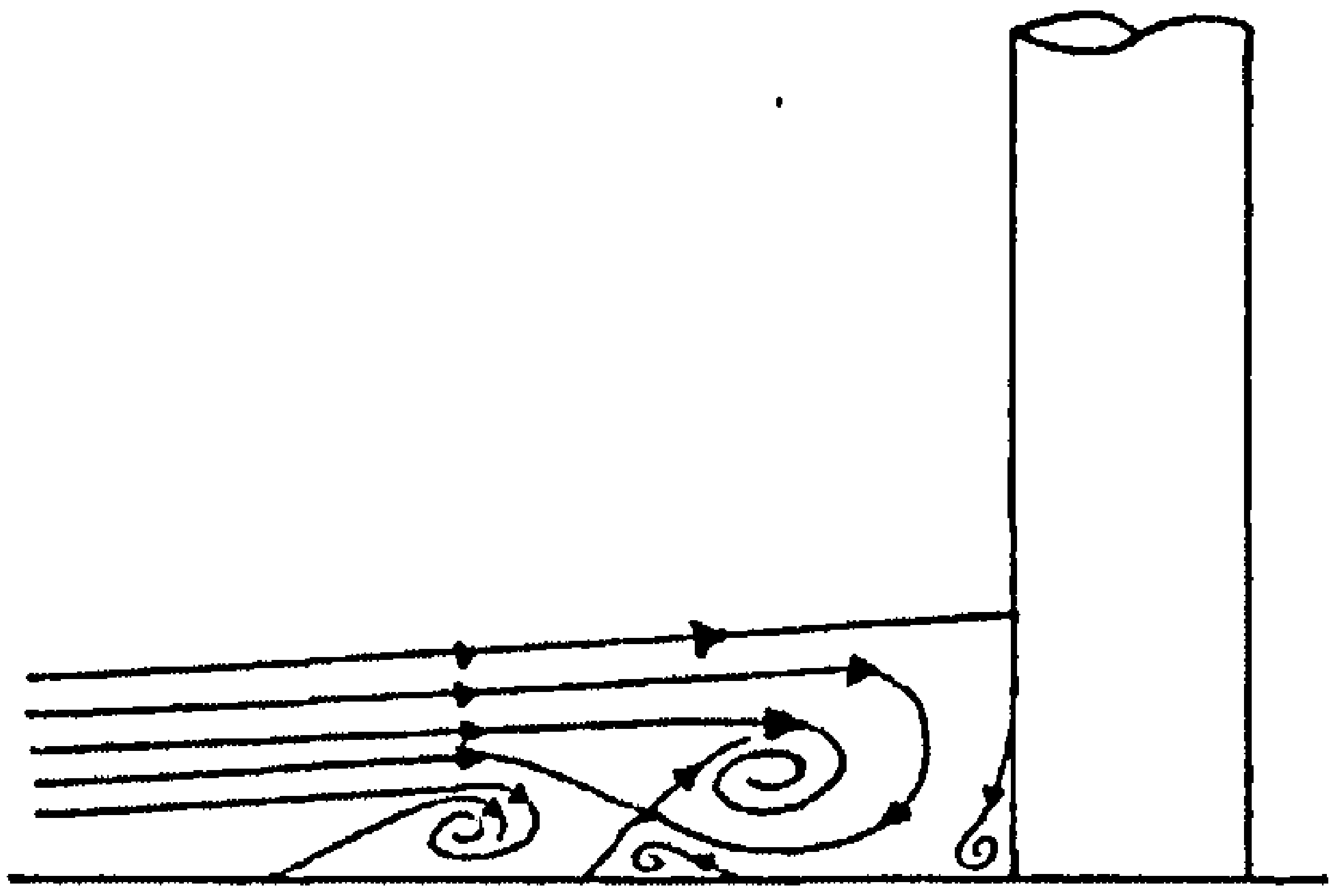

Figure 5.19: System of vortices in upstream symmetry plane of a cylinder (courtesy of Baker[9])

Source	δ^*	θ	H	Re_θ
Experiment[131]	-	-	-	5936
RANS ($k-\varepsilon$)	0.005323	0.004121	1.29	6615
LES (Smagorinsky)	0.006172	0.003545	1.74	5728
LES (k_{sgs}-equation)	0.003701	0.002483	1.49	3970

Table 5.2: Boundary layer characteristics at $x = -1.319T$

Figure 5.18 (b) shows that the time-averaged behaviour predicted by the k_{sgs}-equation model is governed by a single vortex at $x = -0.5T$, which is in close agreement with the experimental data. As the flow further away from the wall reaches the junction region, it moves down-wards and upstream due to the pressure gradients imposed by the wing geometry. This motion generates the back-flow observed in Figure 5.18 (b), which forms the vortical structure present at $x = -0.5T$. It is important to note that on the time-averaged results, the back-flow carries enough momentum to continue further upstream but the dynamics are such that no other vortex is persistent enough to remain present in the region. The existence of this extended back-flow region requires the study of the unsteady behaviour of the flow.

The observation of the instantaneous flow development reveals a very transient behaviour, which can be seen step by step in Figures 5.20 (a) to (l), where stream traces in the upstream symmetry plane are presented for consecutive moments in time separated by 0.01s. When the flow has been fully developed, the back-flow generated by the pressure gradient imposed by the wing geometry results in the formation of three clockwise rotating vortices, thereafter called A, B and C with A being the one further upstream. These vortical structures can be seen in Figure 5.20 (a). The distance between the vortices is of the order of $1T$.

Vortex A and B are moving downstream while vortex C oscillates about a mean position in the region of $x = -0.7T$ to $-0.5T$. The sequential pattern observed starts with the generation of vortex A at $x = -3.0T$. The generation of this vortex is periodic, with period of about 0.03sec. This can be seen by Figures 5.20 (b), (e), (h) and (k). As time comes by, vortex A moves downstream with an average speed of $0.25T/0.01$sec. The periodicity of the vortex generation in combination with the vortex downstream speed results in the coexistence of an average of three vortices in the region of interest. Hence, when vortex A has reached $x = -2.25T$, a new vortex, A', is about to be formed further upstream at $x = 3.0T$ (Figure 5.20 (e)).

When vortex A reaches the region of $x = -2.0T$, the interaction of the flow between vortex A and C increases the rotational motion. As a result, when vortex A reaches $x = -1.5T$, a secondary vortex is formed (Figure 5.20 (g)) which is quickly entrained by vortex A, as the latter moves further downstream (Figure 5.20 (h)).

It is worth noting that the vortex becomes stronger as it moves further downstream. This is because it is continuously fed with high momentum freestream flow on its upper side, and increasing back-flow over its lower side, contributing to an increased rotational motion. The vortex reaches each maximum strength in the region of $x = -0.75T$ to $-0.5T$ (Figures 5.20 (i) and (j)). Then, the vortex size is reduced and the vortex moves upstream only to be entrained by the following oncoming vortex (Figure 5.20 (k) and (l) respectively). It is these last three stages of the vortex life that give the impression of a stable, oscillating vortex C at $x = -0.5T$. The period of this pseudo-oscillation is about 0.03sec.

The vortex deterioration shortly after $x = -0.5T$ can be explained by the existence of high cross-stream pressure gradients imposed by the wing geometry that lead to the stretching and concentration of ω_z [38]. The process described is repeated with an approximate period of 0.11s.

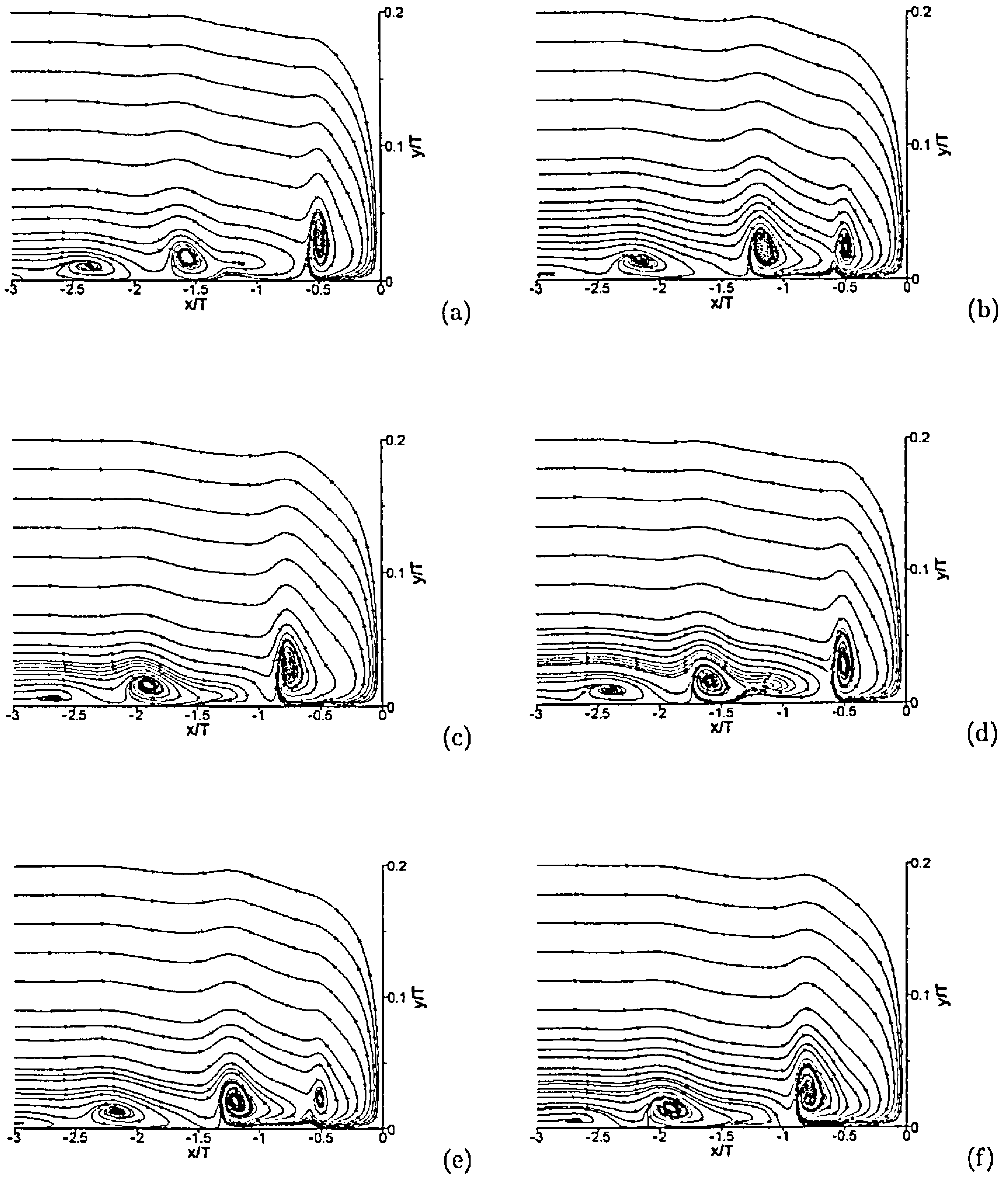

See next page for title.

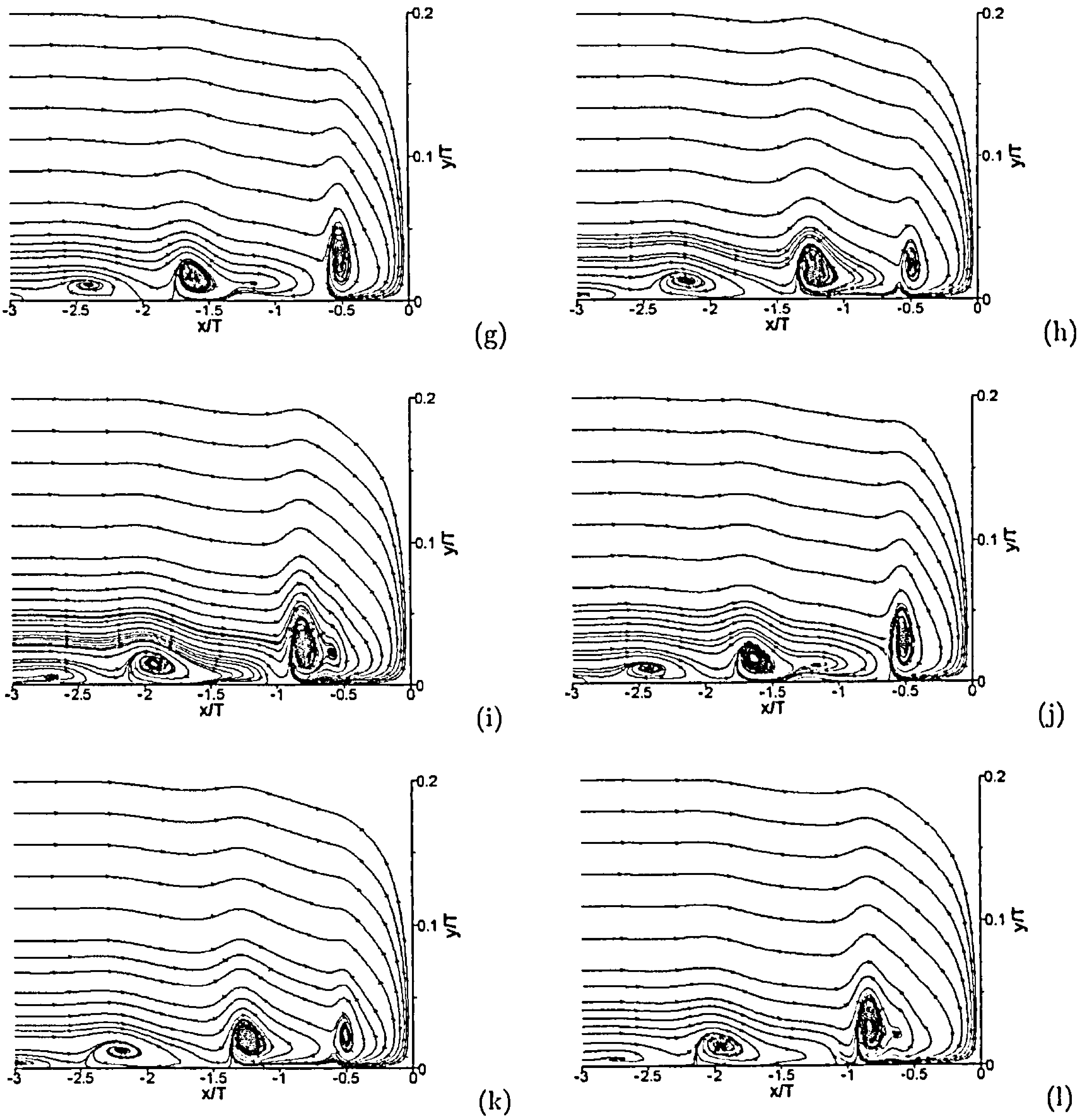

Figure 5.20: Instantaneous streamtraces in upstream symmetry plane separated by 0.01s (k_{sgs}-equation model LES calculation)

Similar transient behaviours to the one described above have been reported in the past by a number of researchers [34, 36, 35, 38]. Devenport and Simpson [38] indicated the presence of a bimodal system of vortices at the junction region of the geometry involved in the present study, at the same flow conditions. In their study, they showed that the instantaneous recirculation region was smaller than the averaged for 20 to 30% of the observation time. During this period, the back-flow associated with the recirculation separated from the wall at about $x = -0.2T$, generating a weak secondary recirculation further upstream, at around $x = -0.3T$. In the rest of the observation time the fluid reversed by the wing does not separate but rather forms a near-wall back-flow jet which only occasionally separates and forms a recirculation much larger than the observed averaged [38]. It is worth noting that the average period of this phenomenon was around 0.02s, based on the provided velocity time history [38], which was close to the period of oscillation of vortex C predicted by the k_{sgs}-equation model LES.

The flow features discussed above indicate that the two SGS models gave rise to two different flow structures. In the case of Smagorinsky model, a steady system of two co-rotating vortices and one counter-rotating vortex is present at $x = -1.2T$. In the case of k_{sgs}-equation model, a periodic generation of vortices rolling downstream gave rise to a single vortex present in the time-averaged flow field, at $x = -0.5T$, in close agreement with the experimental data of Olcmen and Simpson [131], which indicated that the position of the time-averaged bound vortex in the upstream symmetry plane was at $x \simeq -0.2T$. This observation was also in agreement with the measurement taken by Devenport and Simpson [38]. In terms of vortical structures, none of these studies showed the presence of a third vortex that was persistent enough to be seen in the time-averaged results.

The discrepancies between the experimental and the LES results were attributed to two factors that can affect significantly the recirculation region; the state of the upstream boundary layer and the turbulence activity at the junction region. The state of the upstream boundary layer can affect the extent of the back-flow region by imposing an adverse pressure gradient. The turbulence activity in the junction region, which is dictated by both the imposed pressure gradients and the SGS model, can affect the structure of the bound vortex in the upstream symmetry plane and hence the back-flow itself [6, 132].

Figure 5.21 shows the velocity profiles obtained at $x = -3.19T$ by RANS and LES calculations, which is the location corresponding to the station 0.75c upstream of the junction. The displacement and momentum thickness, δ^* and θ respectively, as well as the flatness ratio H and the Re based on θ can be seen in Table 5.2.

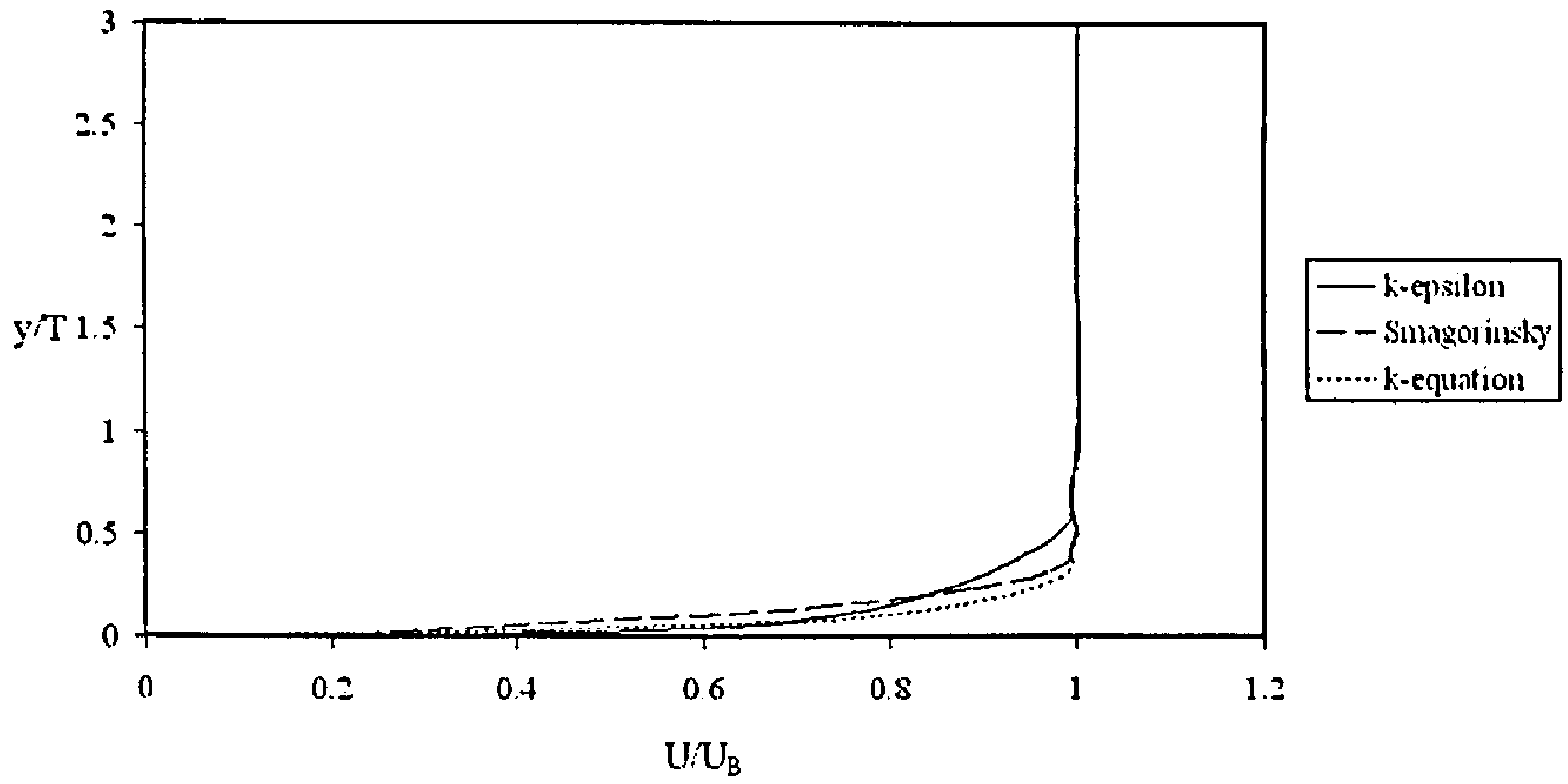

Figure 5.21: Velocity profiles at $x = -3.19T$ obtained by RANS and LES calculations

As it can be seen, there is a substantial variation among the profiles. RANS and k_{sgs}-equation model LES calculations provided more turbulent boundary layers, carrying more momentum closer to the wall while the Smagorinsky model resulted in a more laminar-like velocity profile. This is confirmed by the corresponding values of H, presented in Table 5.2. RANS and k_{sgs}-equation model LES calculations had $H = 1.29$ and 1.49 respectively, which is close to a typical turbulent boundary layer value of 1.4 [146]. The Smagorinsky model resulted in $H = 1.74$ which was significantly closer to the typical laminar boundary layer value of 2.2 [146]. As a result, in the case of the Smagorinsky model, the pressure gradient imposed on the back-flow by the oncoming flow was smaller, leading to a translation of the vortex system further upstream. The strong dependency of the back-flow characteristics and the state of the approaching boundary layer agrees with observations made by a number of junction flow researchers [49, 9, 10], who pointed out the direct relation between the size of the near-wall vortical structures and the near-wall momentum of the oncoming boundary layer.

The second factor that affected the state of the recirculation region was the predicted turbulence activity in the region. The transient state of the vortex structures upstream of the junction are responsible for considerable turbulence activity which is reflected on the Reynolds stress distributions. Devenport and Simpson [33] reported an order of magnitude increase in the levels of turbulence production terms in the region, comparing with regions of the flow further upstream that are remain relatively unaffected by the recirculation region.

In terms of turbulence activity, Figures 5.22 and 5.23 show the normal and shear Reynolds stresses distribution respectively, as predicted by the Smagorinsky model, in the form of contours in the upstream symmetry plane. Figures 5.24 and 5.25 show the corresponding results, as they were obtained by the k_{sgs}-equation model. Comparing with the experimental data, the areas of high normal and shear stresses are translated further upstream, due to the corresponding translation of the bound vortex system described above. It is worth noting however that this translation is significantly reduced in the case of k_{sgs}-equation model calculation, where the first high stress region is laying at $x = -0.5T$, comparing to $x = -1.4T$ predicted by the Smagorinsky model.

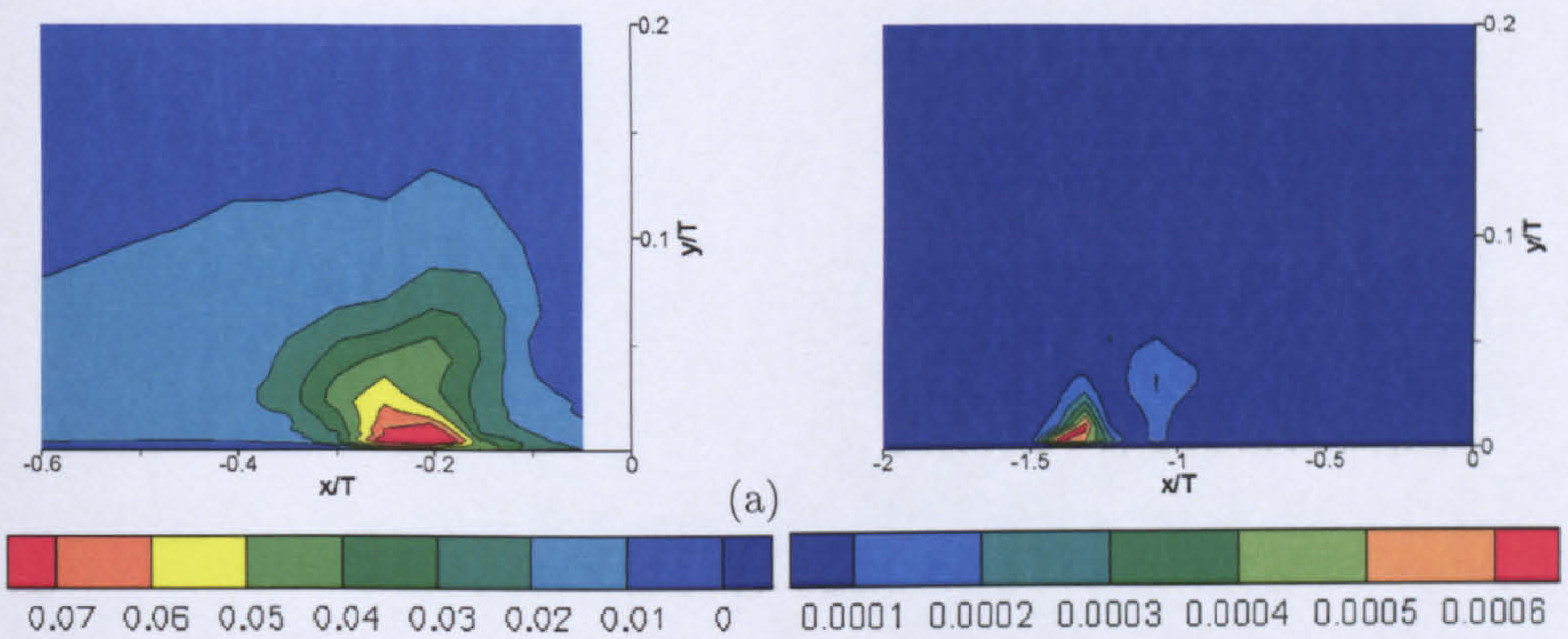

Figure 5.22: $\frac{\overline{u'u'}}{U_B^2}$ contours in upstream symmetry plane
(a: experimental data, b: Smagorinsky model)

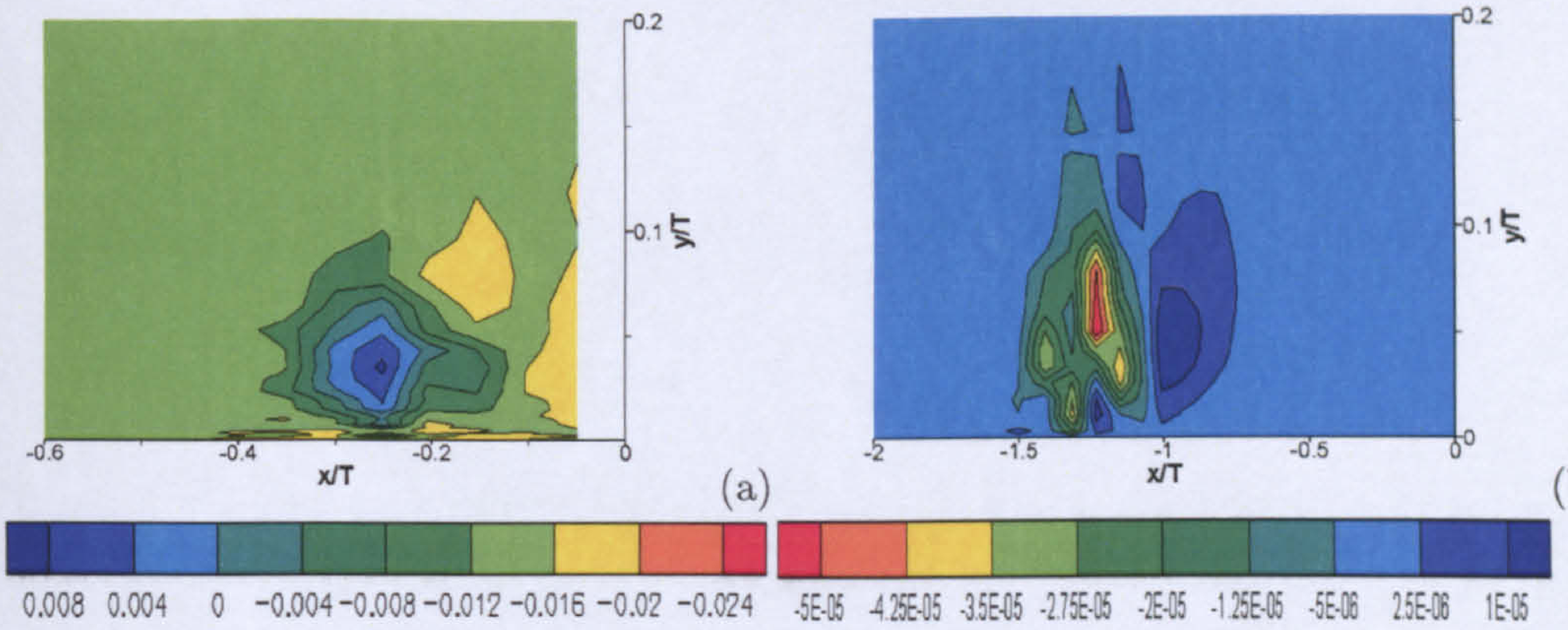

Figure 5.23: $\frac{\overline{u'v'}}{U_B^2}$ contours in upstream symmetry plane
(a: experimental data, b: Smagorinsky model)

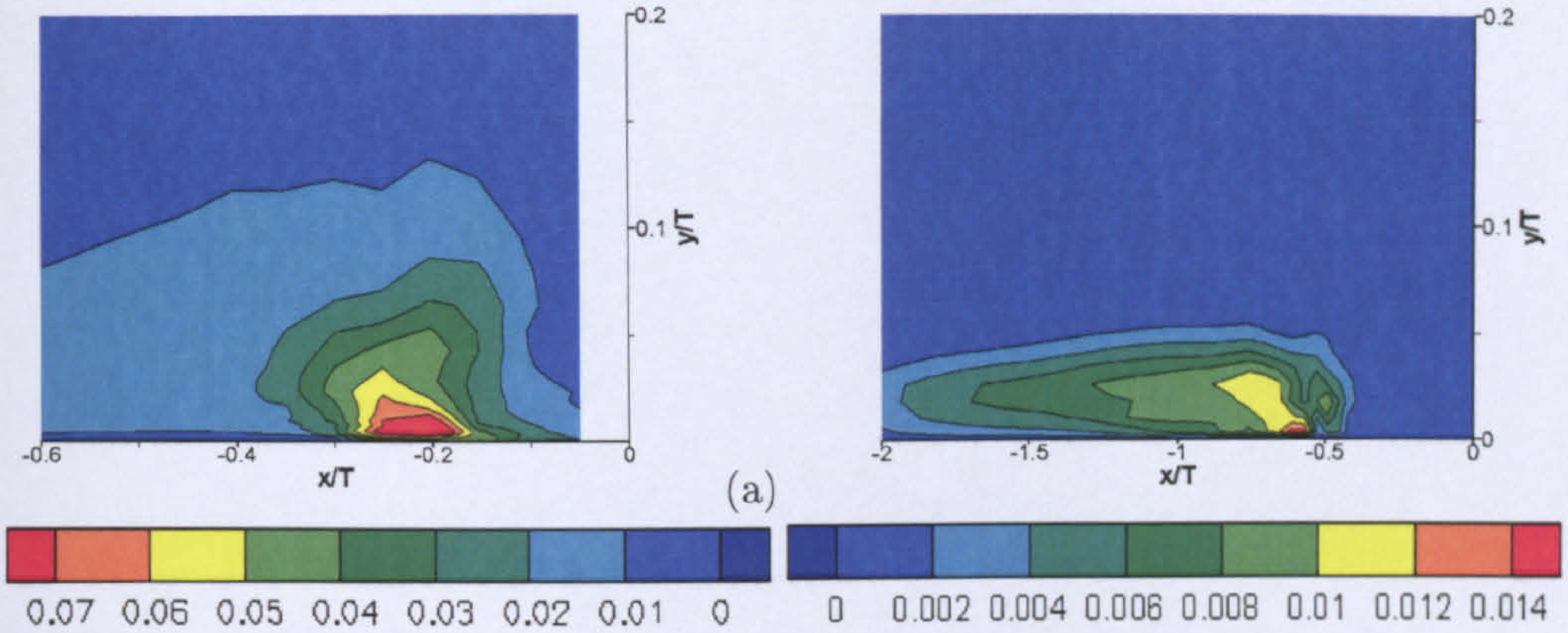

Figure 5.24: $\frac{\overline{u'u'}}{U_B^2}$ contours in upstream symmetry plane
(a: experimental data, b: k_{sgs}-equation model)

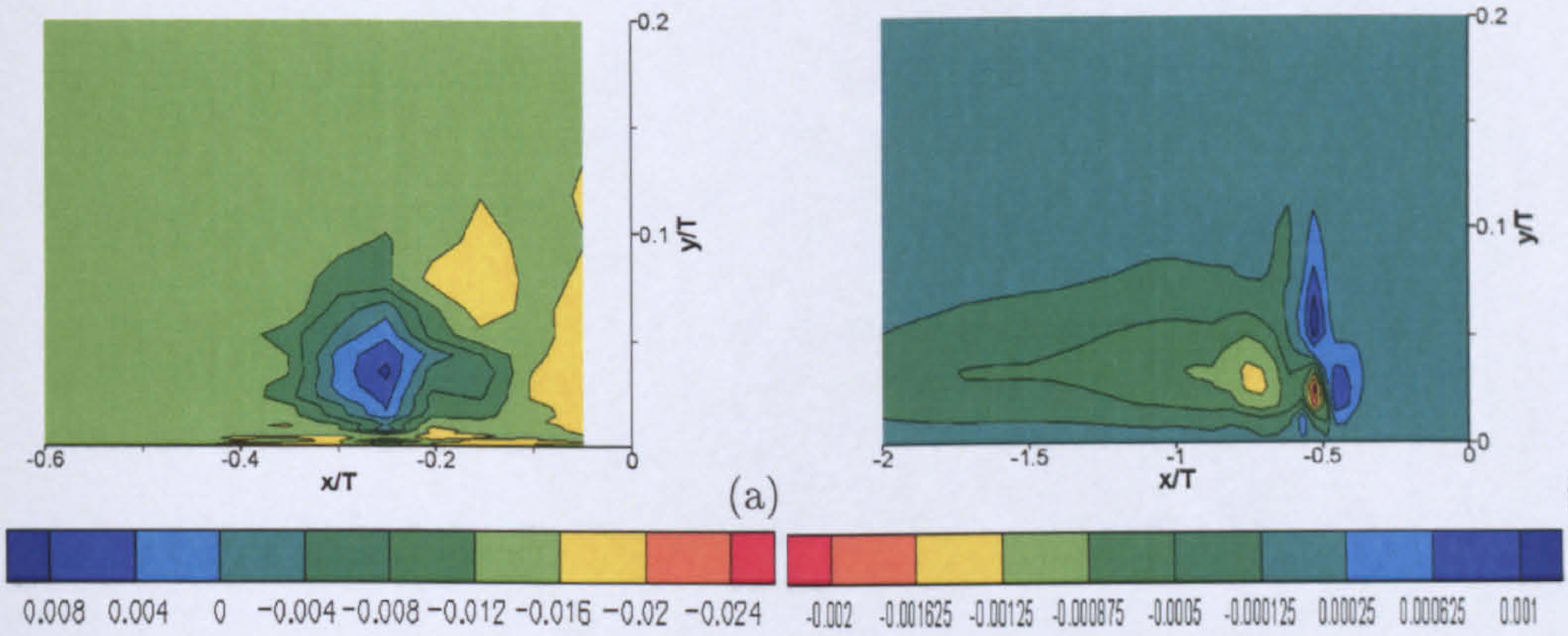

Figure 5.25: $\frac{\overline{u'v'}}{U_B^2}$ contours in upstream symmetry plane
(a: experimental data, b: k_{sgs}-equation model)

In terms of normal stress levels, the Smagorinsky model results show significant reduction in normal stresses compared to the experimental values, indicating that the model produced excessive dissipation that resulted in a suppression of the turbulence activity and the over-prediction of the size of the vortex system developed upstream of the wing-body junction region. This dissipative behaviour was in accordance with observations made previously on channel flows, as described in section 4.2.5. The k_{sgs}-equation model produced normal stress levels that were closer to those obtained in the experiments, although still low, resulting in a more accurate representation of the recirculation region. The dissipation introduced by the k_{sgs}-equation model was lower than in the Smagorinsky case resulting in increased turbulence activity that was reflected in the stress distribution. This strong dependence of the extent and structure of the recirculation region on the modelling approach has also been pointed out for RANS calculations of this flow[6, 132].

The vortical structures present in the region have a direct impact on the shear stress distribution. Figures 5.23 and 5.25 indicate significant differences, reflecting observations made previously regarding the presence of different vortex structures. In the case of the Smagorinsky model, the presence of the primary clockwise-rotating vortex and the secondary anti-clockwise-rotating vortex produces alternating sign shear stress regions, in the corresponding locations. On the other hand, the k_{sgs}-equation model results indicate the presence of a strong clockwise-rotating primary vortex at $x = -0.5T$, in accordance to the observations made on Figure 5.18 (b). In terms of shear stress levels both SGS models under-estimated the shear stresses. It is worth noting that the Smagorinsky results indicate a reduction of 3 orders of magnitude, which was significantly larger than the reduction of 1 order of magnitude predicted by the k_{sgs}-equation model.

From the results presented above, it becomes clear that the stress levels were affected considerably by the SGS model used. Another factor that is believed to have affect significantly the flow field was the local grid resolution. y^+ in the region of $-2.5T \leq x \leq 0.0T$ was in the range of $2.8 \leq y^+ \leq 14.6$ for the Smagorinsky model case and $2.6 \leq y^+ \leq 12.7$ for the k_{sgs}-equation model case. Similarly, the grid resolution around the wing leading edge, in the region $0.0T \leq y \leq 0.2T$ was $2.2 \leq x^+ \leq 11.8$ for the Smagorinsky model case and $2.0 \leq x^+ \leq 11.8$ for the k_{sgs}-equation model case. Hence, in both cases the flow was under-resolved and the calculation was relying on the WW near-wall model to extract all the required information. Still, the k_{sgs}-equation model managed to predict a vortical structure in good agreement with the experiments. The Smagorinsky model seemed to suffer more by the grid resolution, resulting in the flow structure described above.

The position and the strength of the vortex system predicted by the LES calculations in the plane upstream of the wing had an important impact on the prediction of the time-averaged flow field further downstream. This can be seen in the $\frac{U}{U_B}$ contours at $x = 0.76T, 2.72T \text{and} 4.46T$, which are presented in Figures 5.26, 5.27 and 5.28 respectively for the Smagorinsky model, and in Figures 5.29, 5.30 and 5.31 respectively for the k_{sgs}-equation model. Comparing with the experimental data, it can be seen that at $x = 0.76T$, the Smagorinsky results show that the boundary layer is suppressed in area $z = 0.8 - 1.1T$ and it is only further away from the wing surface that it starts to grow. This is due to the presence of the bound vortex in the region, which can be seen in Figure 5.32 (a) where stream traces are presented for the $x = 0.76T$ plane. The vortex generates a down-wash inboard of its rotation axis and an up-wash outboard, due to its anti-clockwise rotation. As a result high momentum fluid is moved down-wards in the region $z \leq 0.8T$, suppressing the boundary layer, and low momentum fluid is moving upwards, in the region $z \geq 0.8T$, increasing the boundary layer thickness.

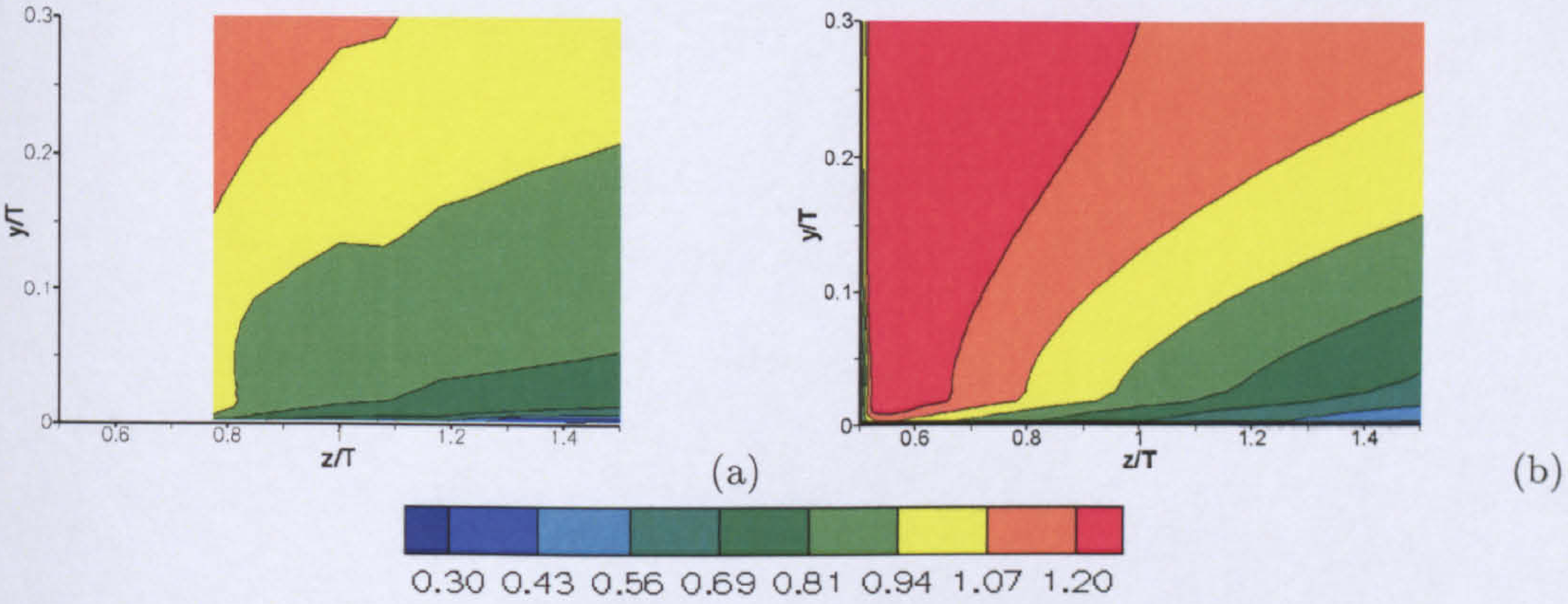

(a) (b)

Figure 5.26: $\frac{U}{U_B}$ contours at $x = 0.76T$
(a: experimental data, b: Smagorinsky model)

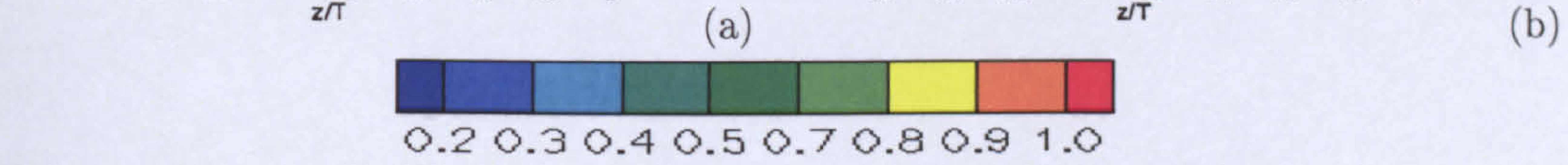

(a) (b)

Figure 5.27: $\frac{U}{U_B}$ contours at $x = 2.72T$
(a: experimental data, b: Smagorinsky model)

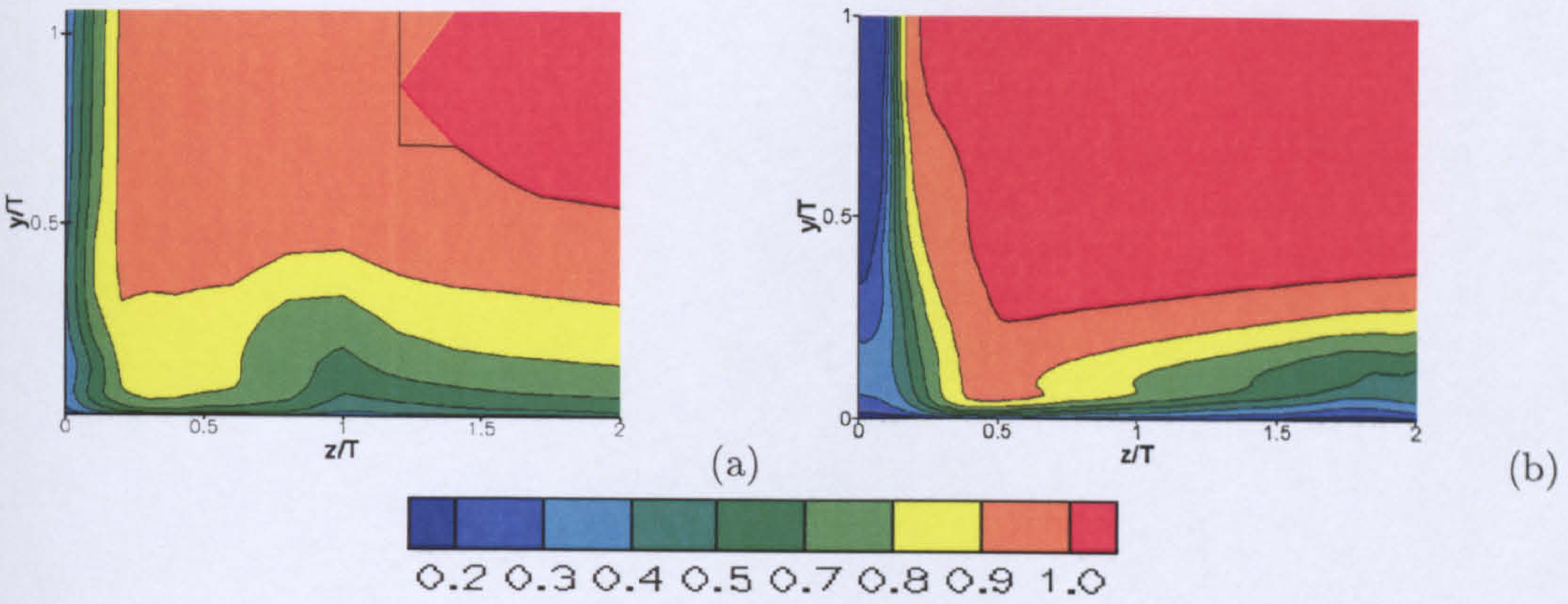

Figure 5.28: $\frac{U}{U_B}$ contours at $x = 4.46T$
(a: experimental data, b: Smagorinsky model)

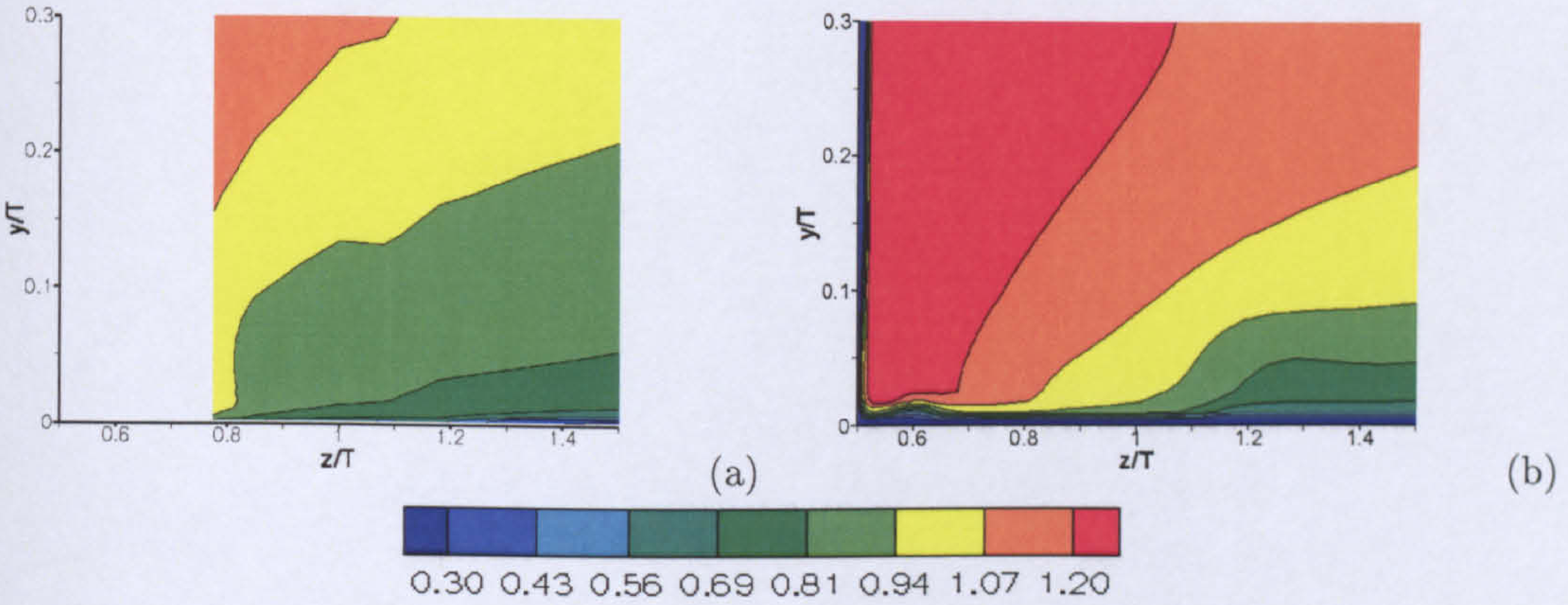

Figure 5.29: $\frac{U}{U_B}$ contours at $x = 0.76T$
(a: experimental data, b: k_{sgs}-equation model)

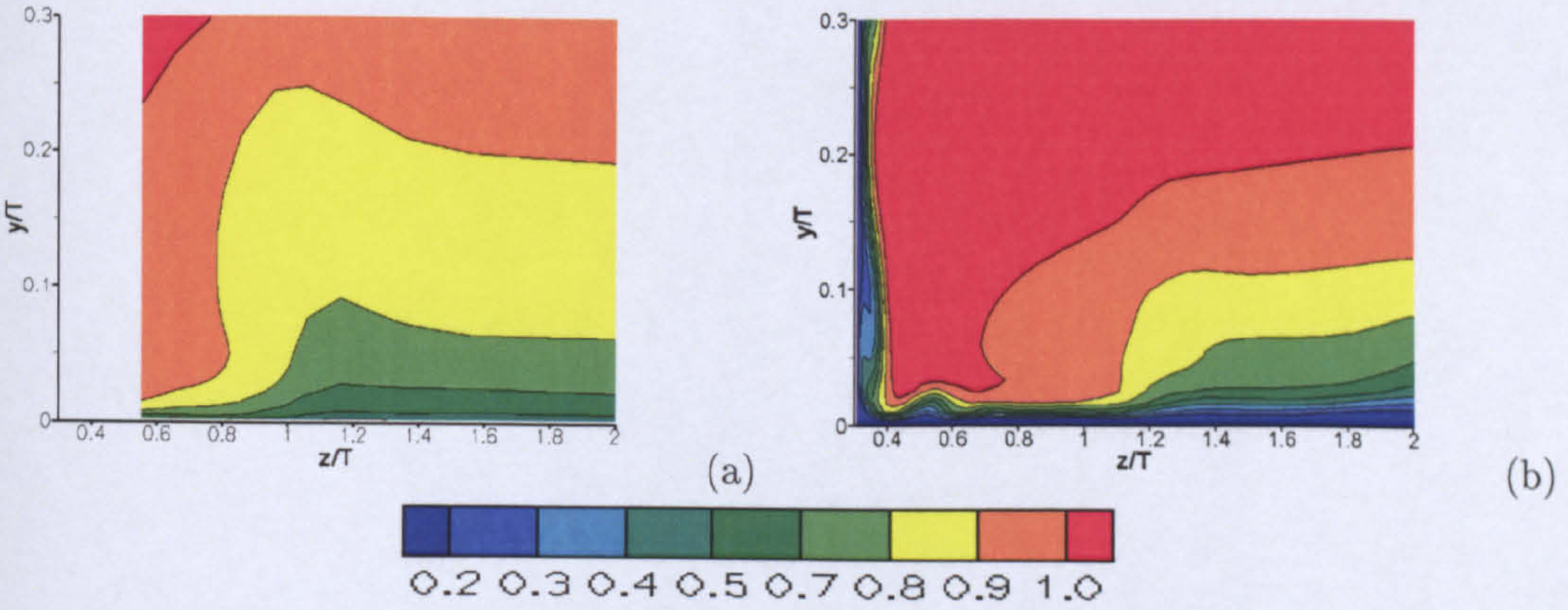

Figure 5.30: $\frac{U}{U_B}$ contours at $x = 2.72T$
(a: experimental data, b: k_{sgs}-equation model)

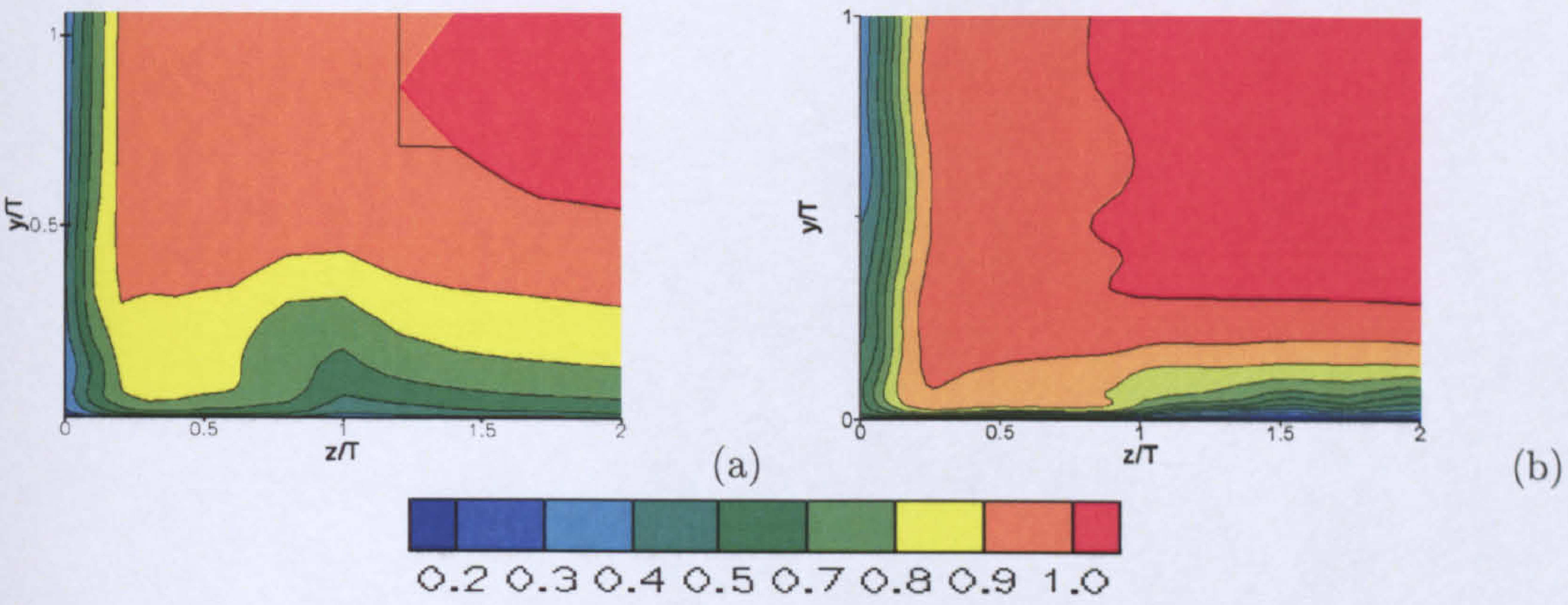

Figure 5.31: $\frac{U}{U_B}$ contours at $x = 4.46T$
(a: experimental data, b: k_{sgs}-equation model)

In the case of the k_{sgs}-equation model, Figure 5.29 shows that the state of the boundary layer formed over the lower wall is different, having larger areas of low momentum fluid carried in the flow closer to the wall. This is because, instead of having a single vortex further away from the bottom wall as in the Smagorinsky model case, a number of vortices are present, much closer to the lower wall. This can be seen in Figure 5.33 (a), where stream traces are presented for the $x = 0.76T$ plane. It appears that the vortical structure present in the upstream plane rolls up downstream to form a bound vortex structure that passes closer to the wing surface than in the Smagorinsky case, at $z = 1.5T$, interacting heavily with the boundary layer. Figure 5.33 (a) shows that a number of secondary vortices are also present, all within the boundary layer region, resulting in an increase of the boundary layer thickness. These might be the remainings of shedding of the transient vortices observed in the upstream symmetry plane.

Figure 5.29 (b) shows that the boundary layer interacts with the junction flow in the region of $z = 0.5 - 0.6T$, leading to a local increase of boundary layer thickness. This is due to the presence of a secondary streamwise vortex that is generated in the junction region along the wing surface, resulting in a redistribution of fluid momentum by transfering low momentum fluid upwards and vice versa. This vortex is located at $z = 0.6T$ and can be seen in Figure 5.33 (a). The presence of such vortical structures has been noted in literature. Pierce and Shin [137] pointed out their existence in the junction region along a streamlined cylinder, in their experiments at Re_θ=12,500. Further away from the wing surface, the boundary layer has a constant thickness up to $z = 1.1T$, and then it increases in the same manner to that observed in the case of Smagorinsky model results.

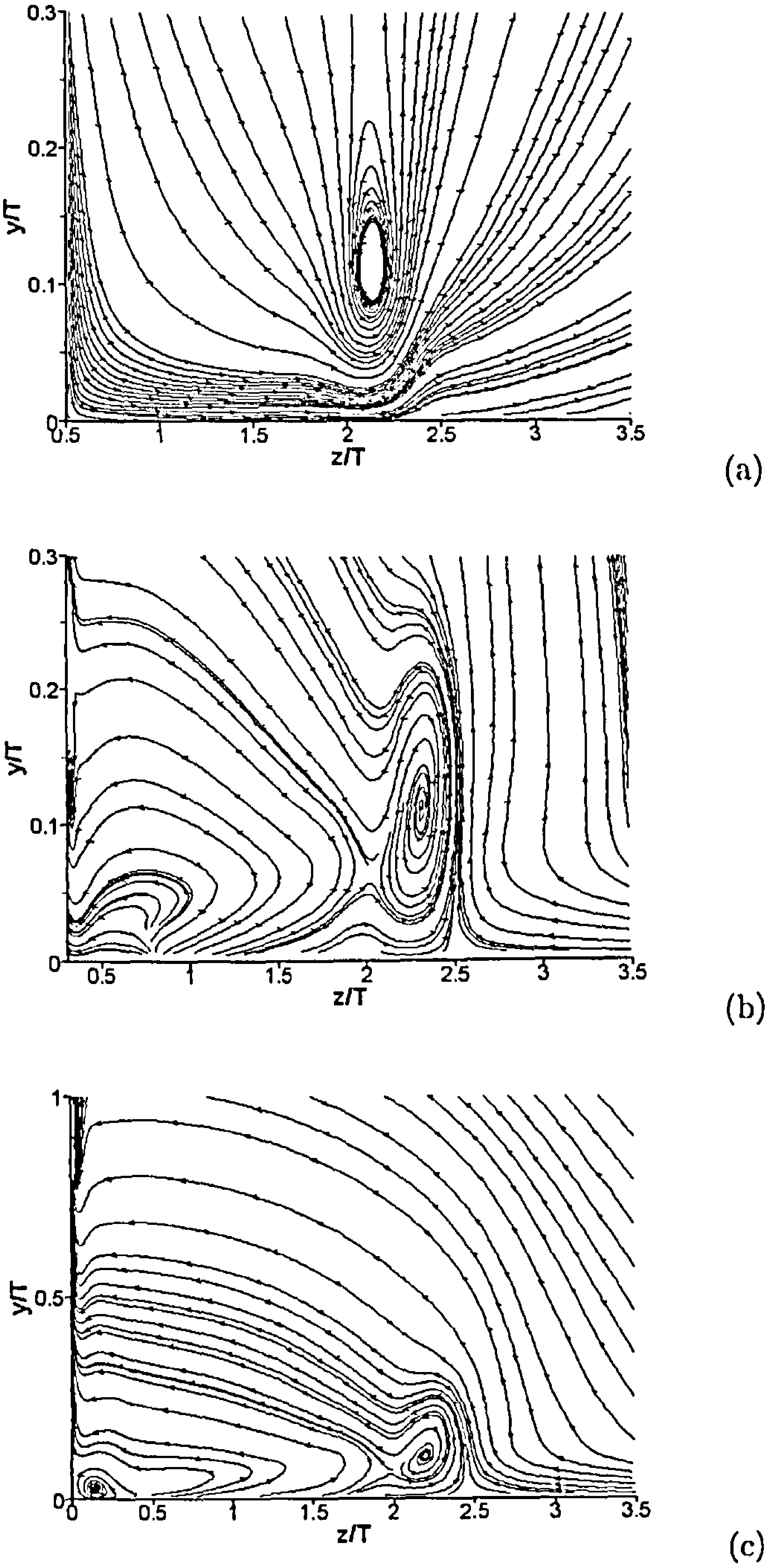

Figure 5.32: Stream traces by the Smagorinsky model on $x = 0.76T$ (a), $x = 2.72T$ (b) and $x = 4.46T$ (c)

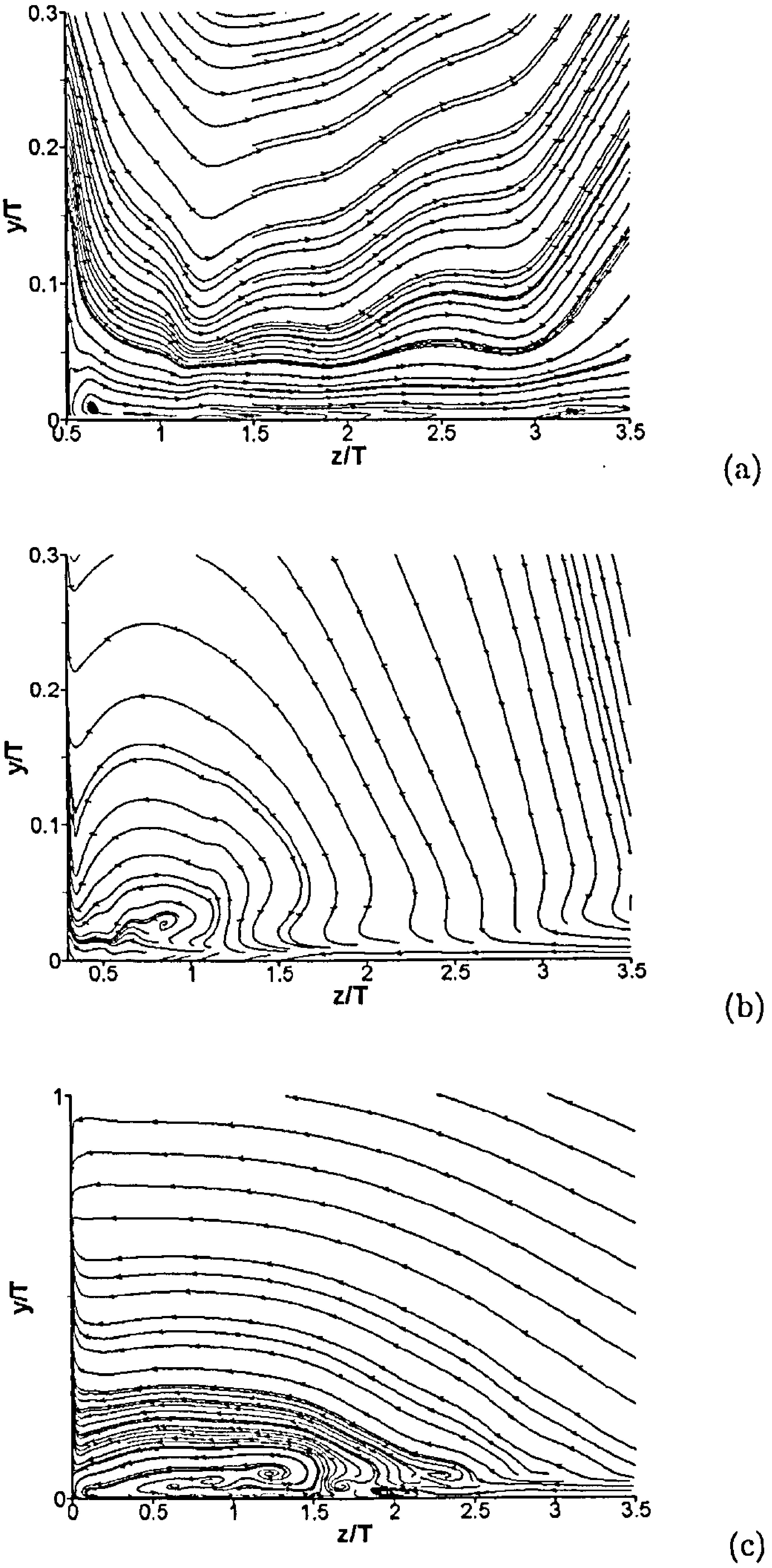

Figure 5.33: Stream traces by the k_{sgs}-equation model on $x = 0.76T$ (a), $x = 2.72T$ (b) and $x = 4.46T$ (c)

A side effect of this vortical structure close to the junction region is the change in the flow direction close to the wing surface, which can be seen in Figure 5.33 (a). The effect of this flow direction is that the boundary layer is under higher strain resulting in an increase of its thickness, as can be seen in Figure 5.29 (b). Note that this feature is not present in the

Smagorinsky model results nor has it been reported in the experiments.

Further downstream, at $x = 2.72T$, the flow structure obtained by the Smagorinsky model calculation is similar to that observed in the experiments, up to $z = 0.8T$, as can be seen in Figure 5.27. However, moving further away from the wing surface, it can be seen that the bound vortex, whose presence is indicated by the transfer of low speed fluid away from the bottom wall, has moved out-wards. This can be confirmed by Figure 5.32 (b), where it can be seen that the vortex core has moved from $z = 2.15T$, in the previous station (Figure 5.32 (a)), to $z = 2.3T$. The interaction of the vortex with the surrounding flow at its new position results in a boundary layer thickness increase in the region of $z = 1.8 - 2.0T$, comparing with $z = 1.2T$ observed in the experiments.

The flow field prediction by the k_{sgs}-equation model is rather different, as can be seen in Figure 5.30. As in the previous streamwise station, the boundary layer appears to be dictated by low momentum fluid, which, due to its interaction with the vortices passing through, moves upwards, causing a thickening of the boundary layer. This effect can be seen in the region $z = 0.4 - 0.65T$ and $z = 1.2 - 2.0T$, indicating a translation of the bound vortex further away from the wing surface. Comparing to the experimental data and the Smagorinsky model results, it can be seen that the bound vortex strength has been under-predicted since the amount of low speed fluid moved further away from the wall is less than in the experimental observations. The position of the bound vortex can be seen in Figure 5.33 (b). Comparing with the Smagorinsky results, the vortex is located further inboard, in closer agreement to the experimental data.

At $x = 4.46T$, the area where an increase of the boundary layer can be observed, is located at $z = 1.75T$ for the Smagorinsky model and $z = 1.5T$ for the k_{sgs}-equation model, comparing with $z = 1.05T$ given by the experiments, as can be seen in Figures 5.28 and 5.31 respectively. This was an indication that both models predicted a vortex position which was further outboard comparing to the experimental observations. In the case of Smagorinsky model, Figure 5.32 (c) shows that the vortex has moved closer to the lower wall and slightly closer to the wing. It is this vortex re-position that results in the increase of the boundary layer thickness at $z = 1.75T$. Another point of interest is that a secondary vortex has been developed close to the junction region, similar to the one observed in the k_{sgs}-equation model results at $x = 0.76T$ (Figure 5.33 (a)). This vortex, whose onset can be traced back to $x = 2.72T$ as Figure 5.32 (b) shows, interacts with the wing wake, increasing the area of momentum deficit downstream of the wing trailing edge, as can be seen in Figure 5.28. A similar mechanism might be also present in the experimental results although it is not clear.

Figure 5.33 (c) shows that in the case of the k_{sgs}-equation model, the vortex present in $x = 2.72T$ section broke down into a number of weaker vortices and a primary vortex, located at $z = 1.5T$. The interaction of the weak vortices with the flow is such that the boundary layer is suppressed up to $z = 0.9T$, while the primary vortex results in the increase of the boundary layer thickness further away from the wing surface, at $z = 1.5T$.

The flow features described above have an important effect on the turbulence activity in the region. Figure 5.34 shows contours of streamwise normal stresses at $x = 4.46T$ for the Smagorinsky model and Figure 5.36 for the k_{sgs}-equation model. Comparing the experimental data with the LES data of Figure 5.34, it becomes clear that the wake structure is completely different both in distribution and in magnitude. Smagorinsky model results indicated two areas of high turbulence activity, very close to the centre line. The upper one belongs to the wake formed over the rear end of the wing, which can be seen in Figure 5.35, where mean flow field D iso-surfaces are presented. The lower high normal stress region on Figure 5.34 belongs to the vortex developed in the junction region, on the side of the wing as discussed earlier. Figure 5.35 shows that this flow structure increases in size and area as it travels further downstream and upwards. The maximum values observed were five times larger than the experimental peak values. Hence, in contrast to the observations made in the upstream symmetry plane, where normal and shear stresses were significantly under-estimated, the turbulence activity in the wake region was over-predicted. It should be noted that no area of high stresses can be seen in the region of the bound vortex due to the scale used.

The k_{sgs}-equation model predicted increased streamwise normal stresses but still at the same levels as those observed in the experiments. As can be seen in Figure 5.36, the stresses distribution indicates high turbulence activity in both the wing wake and the boundary layer of the bottom wall. In contrast to the Smagorinsky model, the area that the bound vortex crosses this streamwise station is shown clearly by the high normal stresses at $z = 1.0 - 2.0T$. This location can also be confirmed by Figure 5.37 which shows mean flow field D iso-surfaces.

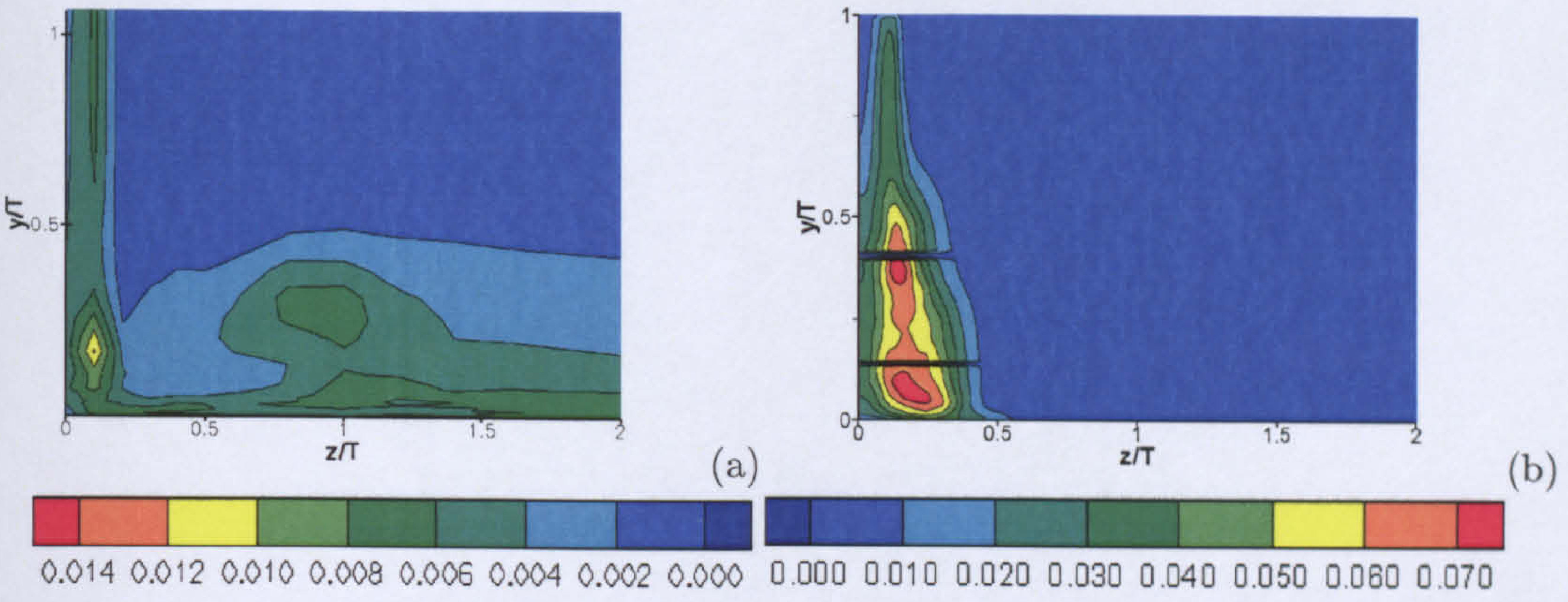

Figure 5.34: $\frac{\overline{u'u'}}{U_B^2}$ contours at $x = 4.46T$
(a: experimental data, b: Smagorinsky model)

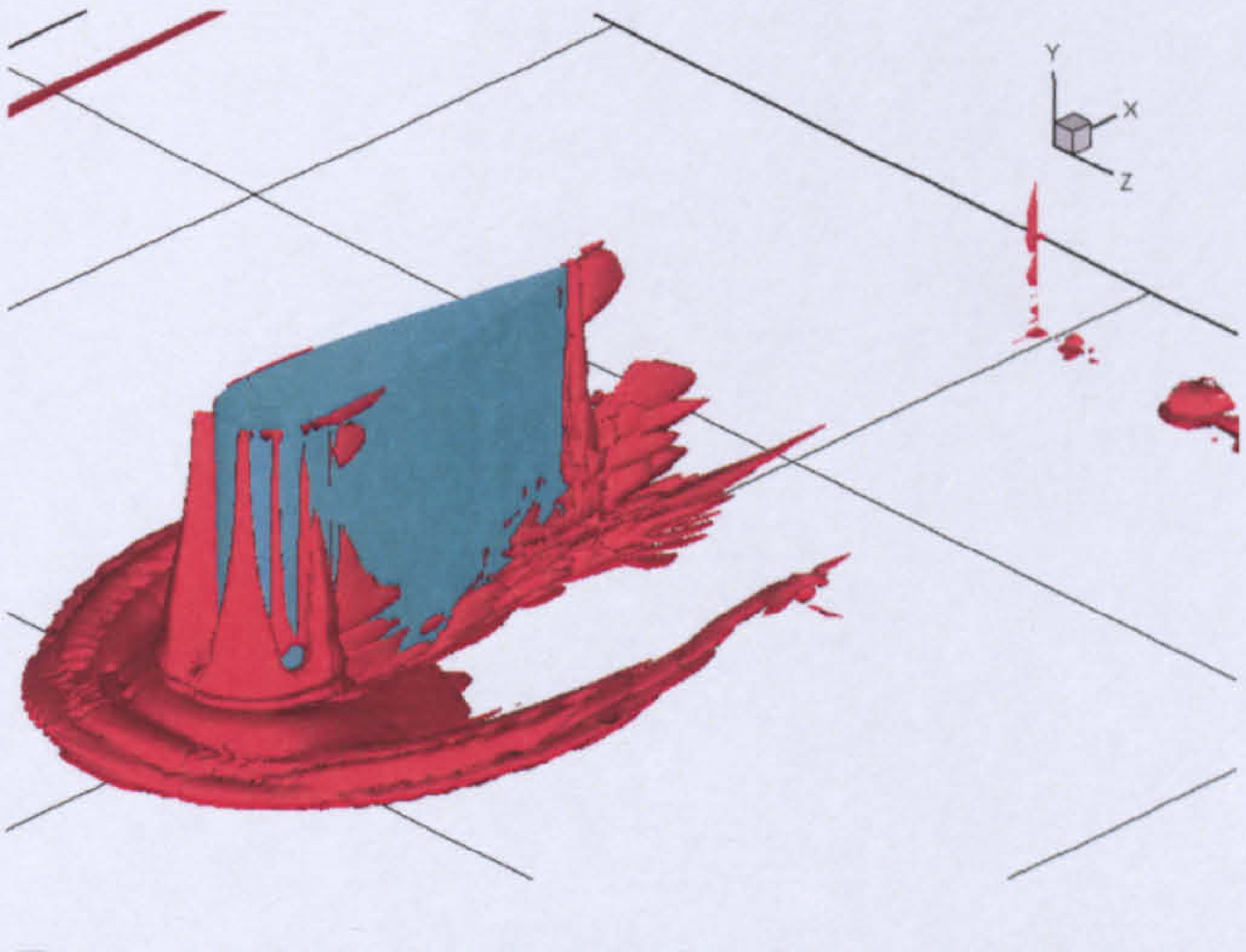

Figure 5.35: Time-averaged flow field D iso-surfaces
(Smagorinsky model)

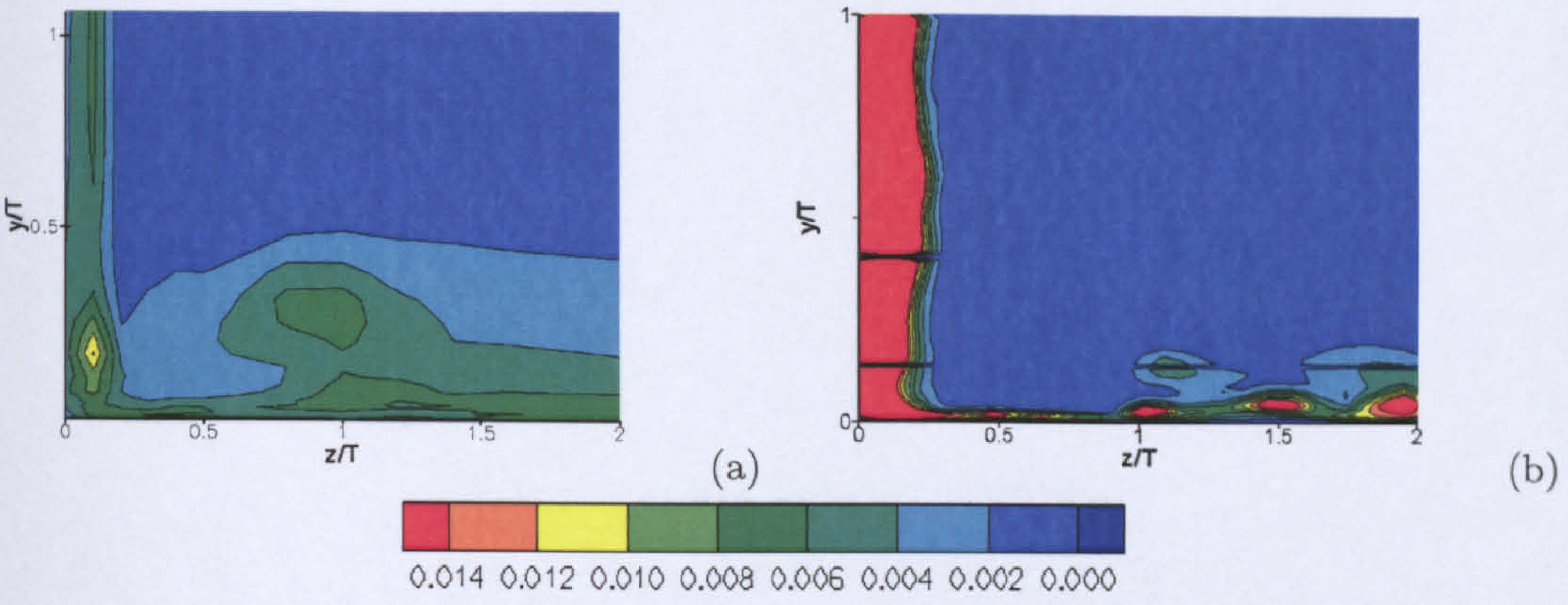

(a)

(b)

Figure 5.36: $\frac{\overline{u'u'}}{U_B^2}$ contours at $x = 4.46T$
(a: experimental data, b: k_{sgs}-equation model)

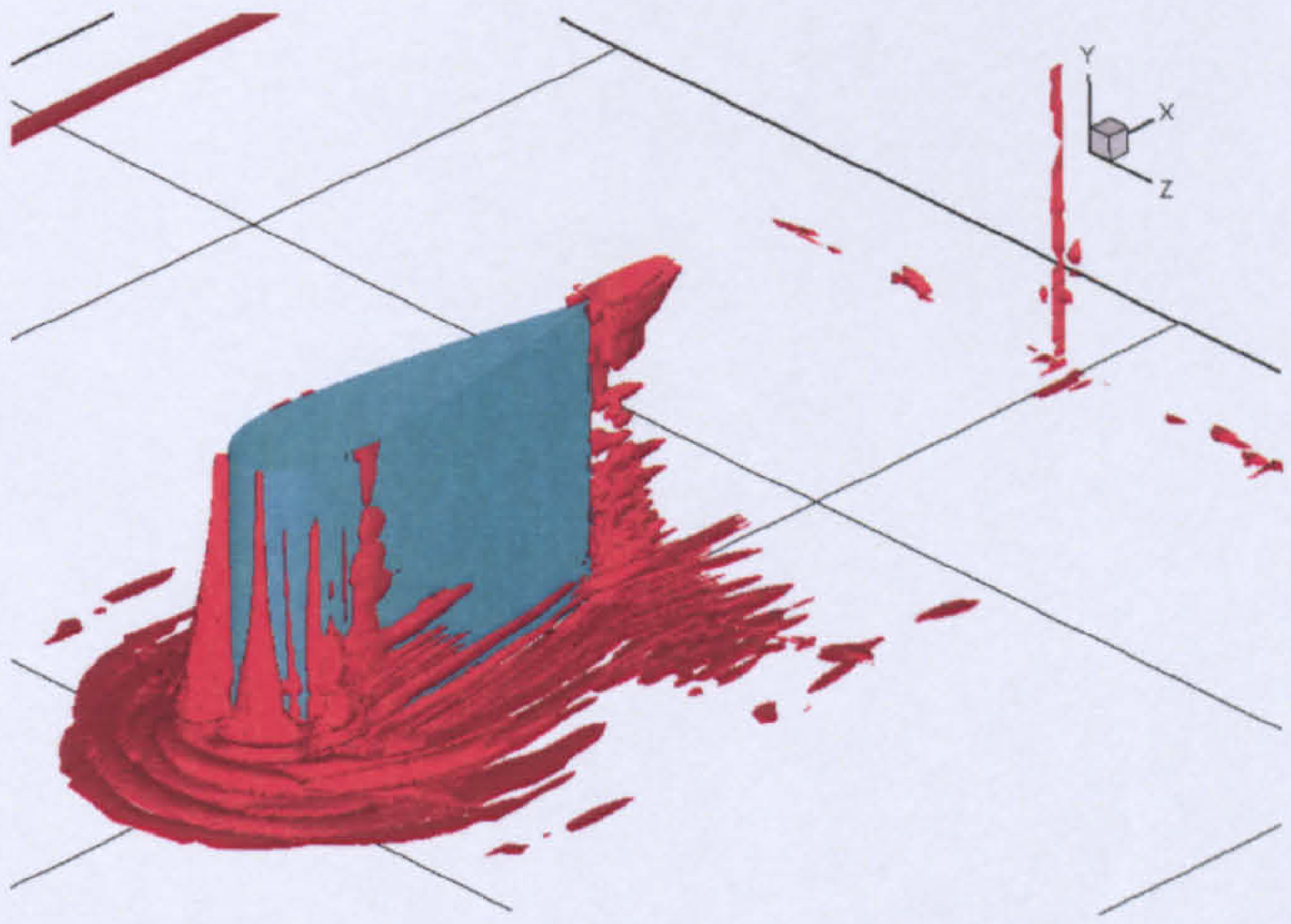

Figure 5.37: Time-averaged flow field D iso-surfaces
(k_{sgs}-equation model)

The flow features presented in Figures 5.35 and 5.37 show the general predicted flow behaviour by each SGS model. Figure 5.35 shows that the Smagorinsky model gives rise to a large steady vortex upstream of the wing, which rolls-up around the wing to form a distinct bound vortex structure similar to that observed in experiments. Comparing to the data of Olcmen and Simpson [131], the location of the vortex in the upstream symmetry plane is further away from the wing and this has an effect on the bound vortex which is also further away from the wing surface.

The k_{sgs}-equation model is less dissipative, leaving more turbulent fluctuations unsuppressed. This results in a significantly more unsteady flow field, which results in a time-average solution with considerable variations from that predicted by the Smagorinsky model. The vortex generated upstream is closer to the wing leading edge, and hence in better agreement with the experimental data by Olcmen and Simpson [131]. As in the case of the Smagorinsky model, this vortex rolls up downstream and forms a horseshoe vortex, which however, is closer to the wing surface, in a more accurate position. The strength of the horseshoe vortex is smaller, leading to a possible break-down into a number of weaker vortices. This process is possibly affected by the development of a secondary vortex, along the side of the wing in the junction region, which can be seen in Figure 5.37. As a result, when the flow reaches the wing trailing edge, the main horseshoe vortex has been further dissipated and coexist with a number of vortices on each inboard side.

Figure 5.38 shows C_P distributions predicted by the two LES calculations, at different wall-normal stations, along the wing surface. Figure 5.38 (a) shows that both simulations predicted that at the leading edge of the wing the flow is slower than that observed in the experiments. The suction region up to the peak value of about $C_P = -1.15$, was predicted in the same manner by both models, indicating that the flow in this region was governed primarily by the pressure gradients imposed by the wing geometry. However, further downstream, the flow development predicted by the two simulations was quite different.

In the case of the Smagorinsky model, moving along the surface downstream, up to $x \simeq 2.0T$, the pressure distribution is in good agreement with the experimental data. Although the suction level predicted was low, the pressure recovery further downstream was more accurate. An interesting characteristic of the C_P distribution is the existence of a pressure plateau, extending from $x = 2.2T$ to $3.0T$. This pressure distribution indicates the presence of a separation bubble. In this region, the flow separates due to the adverse pressure gradient and as it moves to an area of reduced adverse pressure, its velocity remains relatively constant, producing a plateau in the C_P distribution. The shear layer formed due to the separation becomes more turbulent and unsteady as it travels downstream and eventually it reattaches to the surface forming a bubble. This can be seen in Figure 5.39, where the velocity vectors are presented for this region. It is believed that the cause of the flow separation might be associated with the existence of the vortex developed in this region, close to the junction. As shown in Figure 5.32 (b) and (c), this vortex affects significantly the direction of the local flow setting the boundary layer under larger strain. Downstream of the reattachment point, the flow separates again, leading to the formation of a wake near the trailing edge region. This wake can be seen in Figure 5.35. It is the presence of this wake that affects the levels of pressure recovery, which appears to be reduced comparing with the experimental data.

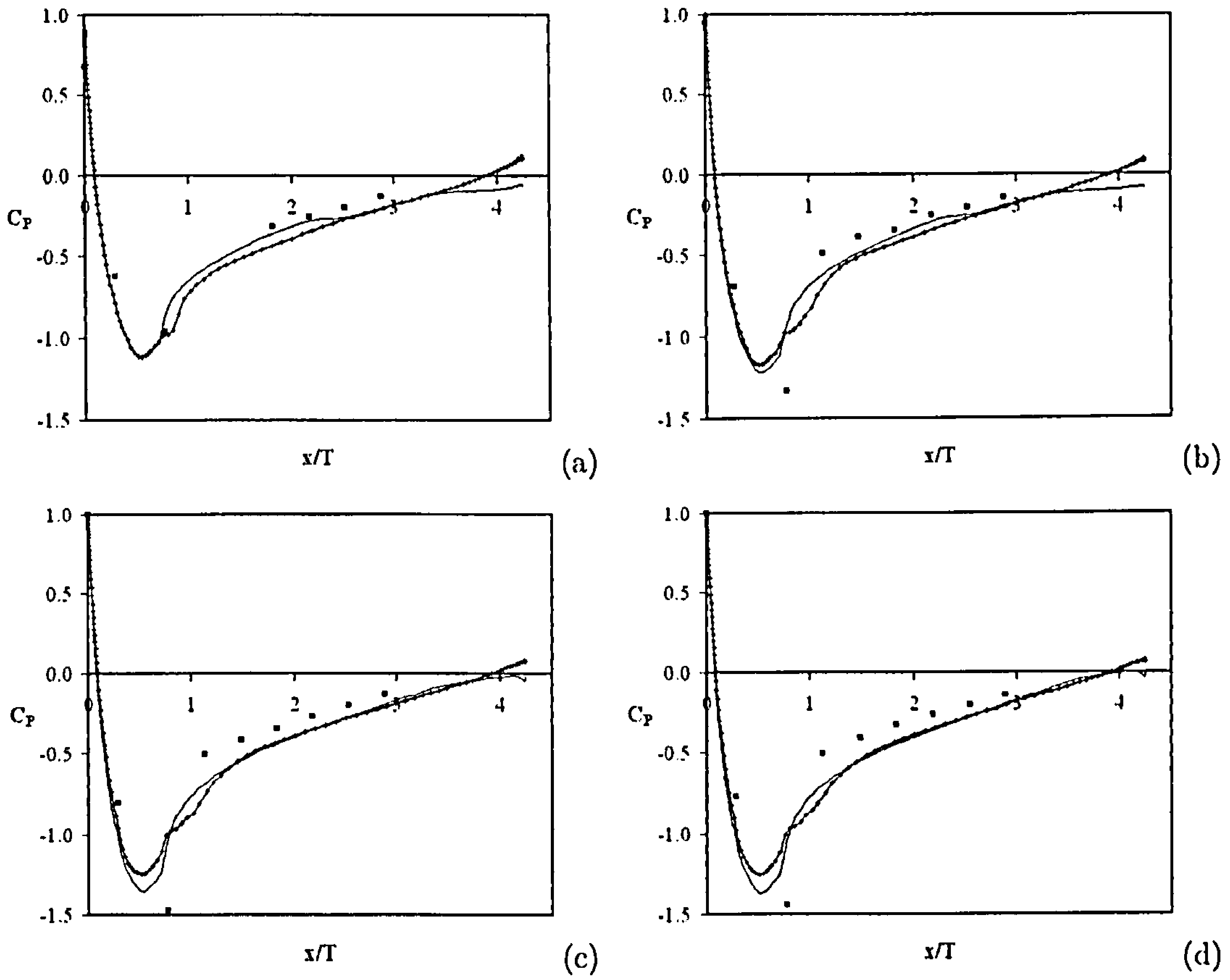

Figure 5.38: C_P distributions along wing surface: solid line, Smagorinsky model, solid line with crosses, k_{sgs}-equation model, squares, experimental data [131, 49] (a: at $y = 0.13279T$, b: at $y = 0.39837T$, c: at $y = 1.4607T$ and d: at $y = 1.7263T$)

In the case of the k_{sgs}−equation model, downstream of the peak suction point, the flow tends to separate but it remains attached. This results in a pressure plateau similar to

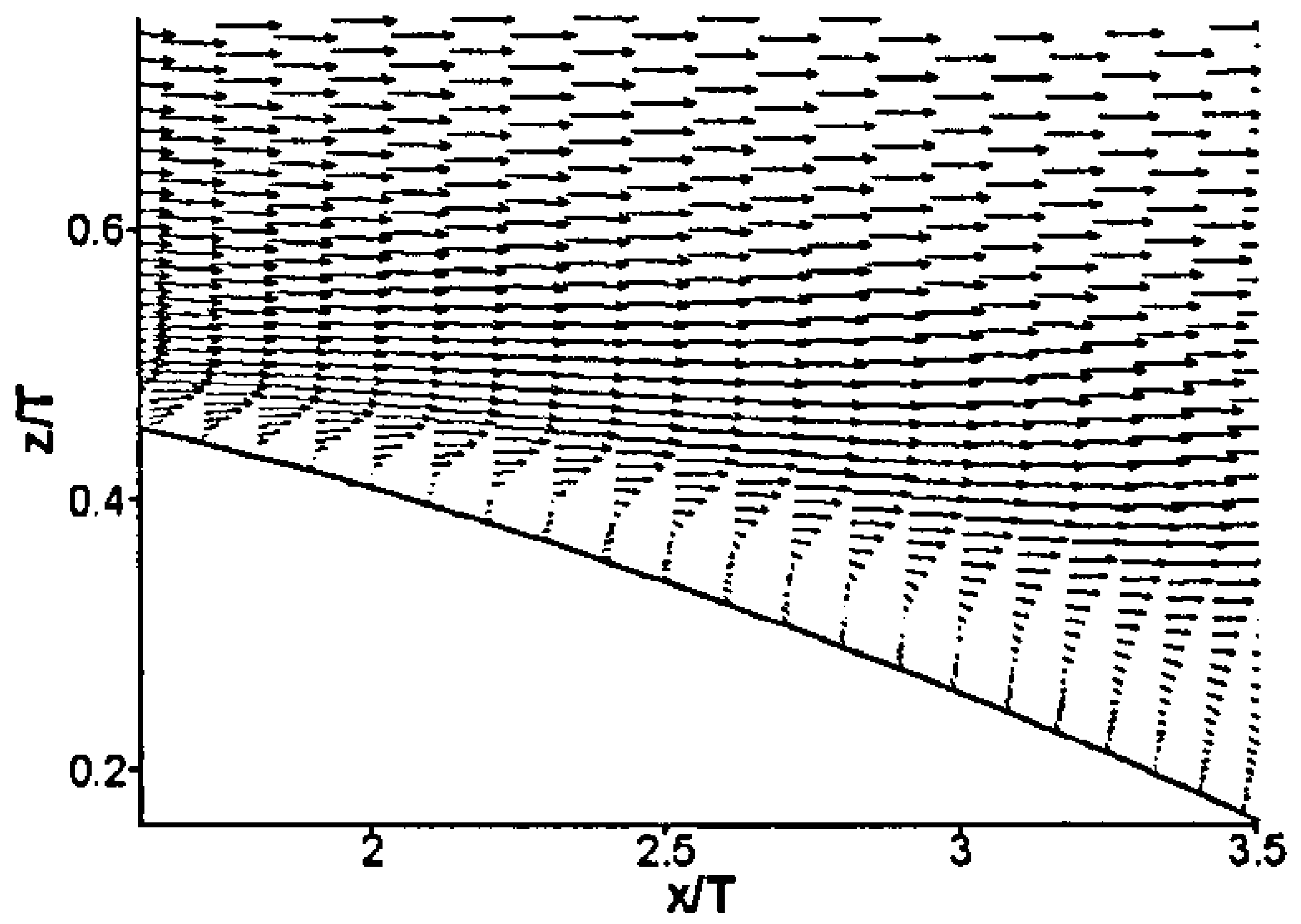

Figure 5.39: Vector field in the separation bubble region at $y = 0.13279T$ (Smagorinsky model)

that observed when a separation bubble was present. This can be seen in Figure 5.38 (a). Downstream of $x = 1.0T$, the flow decelerates in a steady manner, resulting in a constant pressure recovery. As in the case of the Smagorinsky model, the levels of pressure in the region $x = 1.5 - 3.0T$ are reduced compared with the experimental results indicating higher velocities. In contrast to the Smagorinsky model prediction, the flow remains attached longer further downstream, resulting in a continuous pressure recovery. As a result the wake formed downstream of the wing is significantly reduced, as it can be confirmed by Figure 5.37.

At $y = 0.39837T$, the Smagorinsky model under-predicts the peak suction but still, the given distribution is slightly more accurate than the value obtained by the RANS simulation, as can be seen by comparing Figures 5.38 (b) and 5.13 (b). The pressure plateau can still be seen, although reduced, followed by a mild pressure recovery due to the presence of the wake.

In the case of the $k_{sgs}-$ equation model, the peak suction under-prediction is slightly larger than the Smagorinsky model. At $y = 0.39837T$ station, the flow does separate at $x = 0.7T$ and reattaches at $x = 1.6T$ forming a separation bubble. Hence, the same phenomenon as that observed in the Smagorinsky LES calculation is present but in different location. This can be seen in Figure 5.40, which presents the vector field of this region. This separation is attributed to the interaction of the boundary layer with the vortex developed in the junction region, which was pointed out previously and can be seen in Figure 5.33 (a). Finally, the pressure recovery observed downstream of the point of reattachment has remained unaltered.

Moving further away from the bottom wall, Figures 5.38 (c) and (d) show that the change of the predicted peak suction is larger, with the Smagorinsky model providing values closer to the experiments. The presence of the separation bubble region in the k_{sgs}-equation model prediction may be part of the cause of the reduced peak suction since it alters the effective wing shape, modifying the flow field upstream as well as downstream. In terms of pressure recovery downstream of $x = 1.7T$, both models show similar behaviour. In the case of Smagorinsky model, the separated flow region has moved further back, improving the pressure recovery and reducing the wake region. This can be confirmed by Figure 5.35, where it can be seen that the wake region over the trailing edge is reduced with the distance from the bottom wall. The k_{sgs}-equation model results show no change from the distribution predicted in the other two stations over this region.

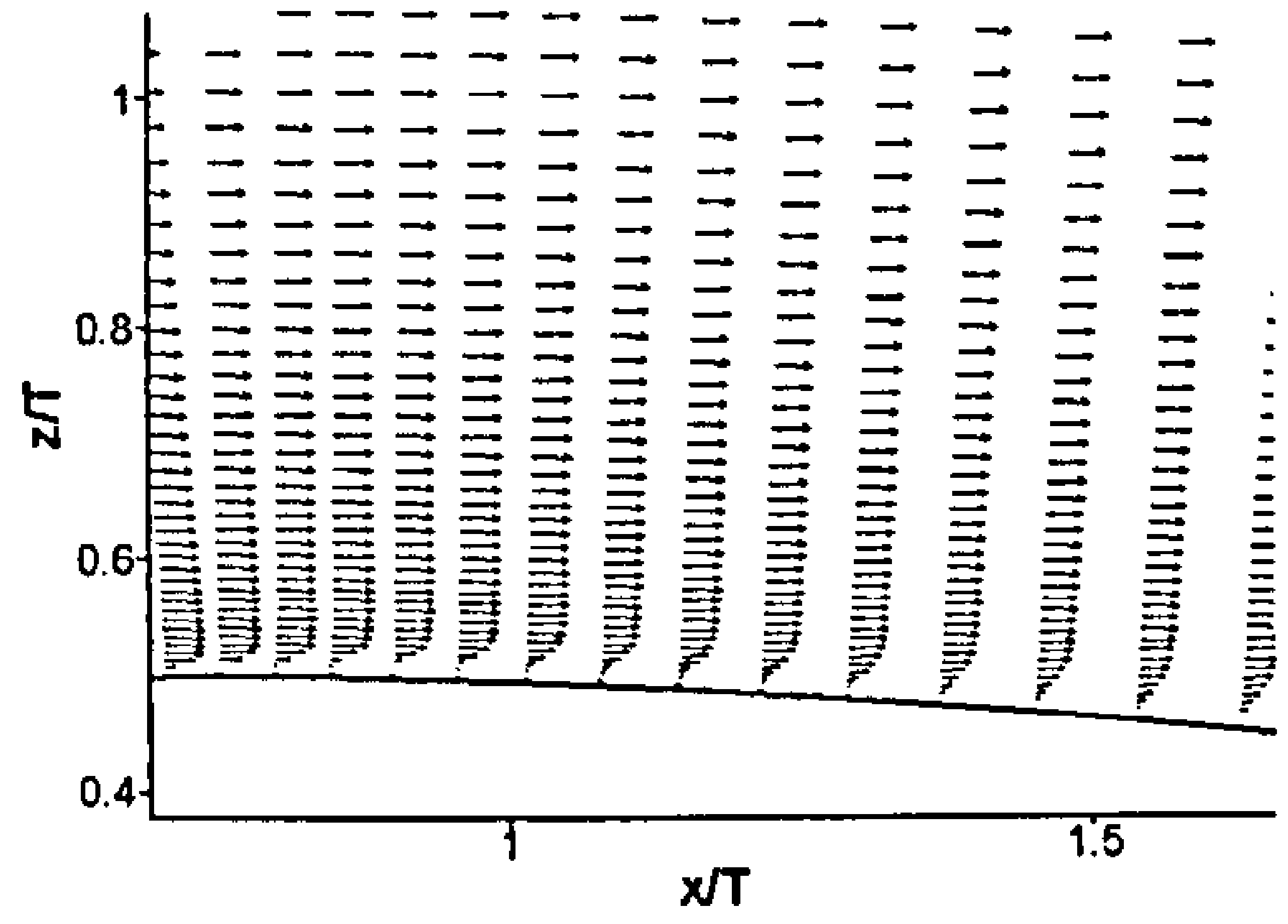

Figure 5.40: Vector field in the separation bubble region at $y = 0.39837T$ (k_{sgs}-equation model)

The distributions discussed above are of particular interest as they indicate that the prediction of the pressure is related to the SGS model used. This is in accordance to observations made by Apsley and Leschziner [6] who pointed out that the turbulence model used in the RANS calculation performed on the same test case affected the near-wall flow structure which had an impact of the rest of the flow field. As a result, the surface pressure distributions predicted by the various models were different [6].

5.7 Wing-body junction flow simulation conclusions

For the purposes of the current study, three simulations of the ERCOFTAC wing-body junction flow case [52] were performed; a RANS simulation with the $k - \varepsilon$ turbulence model, an LES using the Smagorinsky model and an LES using the k_{sgs}-equation model. The results of the three calculations were compared to experimental data by Olcmen and Simpson [131] in terms of mean flow field characteristics, stresses and pressure distributions on the wing surface.

In terms of mean flow features, RANS simulation gave the closest results to experiments with the LES k_{sgs}-equation model calculation following. The Smagorinsky model gave rise to an enlarged recirculated flow region in the plane upstream of the wing-body junction. It is interesting to note that the two SGS models predicted a significantly different instantaneous flow behaviour. The flow structure presented by the Smagorinsky model was quite stable in contrast to the structures developed in the same region during the k_{sgs}-equation model simulation that where unsteady, characterised by a periodic motion.

In terms of turbulent quantities, as expected by previous studies [6, 97], RANS performance with the $k - \varepsilon$ turbulence model was poor with respect to the caption of normal and shear stresses. LES results were better but still characterised by an under-prediction of stresses at the upstream symmetry plane and an over-prediction at the x-plane close to the wing trailing edge. Inflow boundary conditions, grid resolution and the behaviour of the SGS models were considered possible causes of this behaviour.

The differences in the variation of the recirculation region with time had an effect on the bound vortex structure. The Smagorinsky model presented a single core bound vortex further away from the wing, compared to the experiments. k_{sgs}-equation model resulted in a vortex closer to the position described by the experimental data but much weaker than that of the Smagorinsky model, cascading downstream into a number of smaller vortices.

Finally, in terms of pressure distributions, RANS prediction was overall the most accurate. Both LES calculations predicted a separation bubble, at different locations. This affected adversely the accuracy of the results. In all cases, the use of a shear-free upper boundary condition seemed to have an adverse effect on the pressure distribution and in particular over the upper half of the wing.

Chapter 6

Digital Filter Generator of Inflow Conditions

As discussed in section 1.5, one of the main objectives of this study was "the identification and improvement of a cost effective algorithm for the generation of realistic inflow boundary conditions". For these purposes, a Digital Filter based algorithm proposed by Klein et al. [82] was identified. The algorithm makes use of the signal superposition method, which, as discussed in section 1.4.5, appears to have certain advantages over other methods, in terms of convenience of generation of the boundary conditions and computational cost. Furthermore, the algorithm proposed by Klein et al. has already been applied successively on a number of flows [80, 81, 82, 182], where it has been reported to perform well.

The DFG algorithm proposed by Klein et al. [82] generates synthetic LES inflow conditions that are characterised by flow statistics that are given as inputs. These are the profiles of first and second moments (mean values and Reynolds stresses) of the three velocity components over the inlet plane, and length (or time) scales of the turbulence in the 3 co-ordinate directions. These statistical properties can be obtained by either experiment or numerical simulation.

Compared to recycling methods, such as that proposed by Spalart [167] and Lund [108], the Klein et al. DFG approach has the benefit of not requiring flow similarity and/or equilibrium, as required by other methods [77]. Furthermore, no extension of the flow domain is required, as needed by some recycling methods [169], while possible spurious periodicity in the data can be eliminated. Compared to precursor methods it may be more cost effective since no extra simulation would be required. Finally, compared to other synthetic data techniques, the algorithm can be extended to allow for spatially varying turbulence scales instead of a single, modelled spectrum, allowing for generation of anisotropies within the flow field, and hence, for the reconstruction of more realistic synthetic data.

6.1 Theoretical background of the DFG algorithm

The DFG method produces time series of inflow data in two steps. In the first step, a provisional time series for a velocity fluctuating about a zero mean is generated (u_m, where subscript m indicates the digitised time coordinate with time interval Δt). A random data series r_m, defined with $\overline{r_m} = 0$, $\overline{r_m r_n} = \delta_{mn}$, is used to construct u_m from a convolution of the random data series and a digital linear non-recursive filter:

$$u_m = \sum_{n=-N}^{N} b_n r_{m+n} \tag{6.1}$$

where b_n are filter coefficients and N is the extent of the filter support. Due to the statistical properties of a random data series, it follows that:

$$\frac{\overline{u_m u_{m+k}}}{\overline{u_m u_m}} = \frac{\sum\limits_{j=-N+k}^{N} b_j b_{j-k}}{\sum\limits_{j=-N}^{N} b_j^2} \tag{6.2}$$

Eq.6.2 provides a relation between the autocorrelation function of u_m ($R_{uu}(k\Delta t)$ - the left hand side) and the filter coefficients. If a functional form of the autocorrelation is assumed, the values of b_n that will give rise to a time series u_m possessing this autocorrelation may be obtained by inversion of Eq.6.2. For simplicity purposes and in the context of a first approach to the problem, Klein et al. [82] suggested that a non-dimensional form of $R_{uu}(k\Delta t)$ could be deduced by analogy with the 1D spatial autocorrelation $R_{uu}(r)$ observed in homogeneous turbulence, with a turbulence length scale L (r is the spatial separation). Batchelor [13] has shown that in the case of homogeneous turbulence, $R_{uu}(r)$ takes the form:

$$R_{uu}(r) = \exp\left(-\frac{\pi r^2}{4L^2}\right) \tag{6.3}$$

This approximation of a temporal correlation by a spatial correlation form is based on Taylor's hypothesis of "frozen convection" [173], which suggests that temporal variations of u' at a fixed measuring point could be assumed to be due to the passage of a frozen pattern of turbulent motion past the point, provided that $u'/U \ll 1$ [114]. It can been shown [146] that the adoption of this hypothesis can lead to a direct equality between the measured temporal and spatial corelation under homogeneous turbulence conditions.

The accuracy of Taylor's hypothesis depends on the type of the flow and it has been shown that when $u'/U \ll 1$, it is quite accurate [146]. However, in free shear flows Taylor's hypothesis has been shown to fail [176]. In that respect, a DFG algorithm based on such approximation would be expected to perform well in homogeneous turbulence and be less accurate as more shear is introduced to the flow. Still the extent of this approximation's applicability in the context of the DFG has not been demonstrated before.

If we specify L at the point in question, in terms of the local grid spacing, say Δx, and write $L = n_x \Delta x$, the left hand side of Eq.6.2, when converted to a spatial rather than a time dimension, becomes:

$$\frac{\overline{u_m u_{m+k}}}{\overline{u_m u_m}} = R_{uu}(k\Delta x) = \exp\left(-\frac{\pi (k\Delta x)^2}{4(n_x \Delta x)^2}\right) = \exp\left(-\frac{\pi k^2}{4n_x^2}\right) \tag{6.4}$$

Klein et al. [82] show that this results in explicit relations for the filter coefficients:

$$b_k \simeq \frac{\tilde{b}_k}{\left(\sum\limits_{j=-N}^{N} \tilde{b}_j^2\right)^{1/2}} \tag{6.5}$$

where $\tilde{b}_k = \exp\left(-\frac{\pi k^2}{2n_x^2}\right)$.

Klein et al.[82] have suggested that N should take a value of $N \geq 2n$ in order to minimise the error introduced through the approximation of Eq.6.5, thus the grid spacing and non-uniformity, and the local values of length scale have a large influence on the extent of the filter support needed (N) and hence on the computational cost of the method.

The above description has been cast in terms of turbulence length scales. It is, however, convenient to modify the implementation such that for the streamwise flow direction (perpendicular to the LES inlet boundary), a turbulence integral time scale T_x is used instead of a length scale L_x, since this allows direct connection between the streamwise direction and the time marching nature of the LES solution. This implies that the temporal correlation function is modelled via the same exponential form as given in Eq.6.3 transformed into the time domain. The method is otherwise identical, with the integral time scale linked to the LES timestep Δt via $T_x = n_t \Delta t$. Note that the extent of r_m in the streamwise direction is $2N_t + 1$.

The methodology described above, given that a turbulence scale has been specified at each grid point (this and the local grid spacing and timestep define the appropriate value for n) and that R_{uu} has the functional form of Eq.6.3, produces a filter kernel such that, when convoluted with r_m, a time series for u_m is produced which possesses the desired scale. In order to extend the procedure to three dimensions, three 1D filter coefficients are multiplied to produce the final 3D filter coefficient. This requires the provision of three scales (T_x, L_y, L_z), or what is equivalent, three values for n (n_t, n_y, n_z). Eq.6.1 is then used to produce a fluctuating velocity field.

The procedure described above will therefore generate filter coefficients which are stored in a three-dimensional array of the form:

$$b_{tyz} = (-N_t : N_t, -N_y : N_y, -N_z : N_z) \tag{6.6}$$

where N is the extent of the filter and the subscripts denote the co-ordinate of interest. Eq.6.6 shows the direct link between the filter coefficient array size, the turbulence scales to be reproduced, and the grid/timestep used. For a given numerical discretisation, the larger the turbulence scales, the larger the array. It is important to consider carefully the size of the N variables since these have an impact on both memory requirements and computational cost when it comes to the convolution stage of the algorithm.

Although the random data series r_m is defined with $\overline{r_m} = 0$, $\overline{r_m r_n} = \delta_{mn}$, the signal produced by the convolution described by Eq.6.1 is not guaranteed that it will share these properties. This will solely depend on the form of the filter used. Therefore, in general it is necessary to normalise u_m by:

$$u_m^n = \frac{u_m - \langle u_m \rangle}{\sqrt{Var\left(u_m\right)}} \tag{6.7}$$

where $\langle\rangle$ denotes a time-averaged value, $Var\left(\right)$ is the variance and the superscript n denotes a normalised value.

The second step of the DFG procedure is to modify the time series generated in the first step (u_m^n) so that it possesses desired mean values and correlations between different velocity components rather than the zero mean, unity variance and zero cross-correlation implied by the first step. This is achieved by employing Lund's method [108]. The time series from the first step, u_i^n, is guaranteed to satisfy $\overline{u_i^n} = 0$, $\overline{u_i^n u_j^n} = \delta_{ij}$, due to the signal normalisation. The following transformation, used previously by Lund [108] and Zhou and Leschziner [200] generates the final time series $U_i\,(t)$:

$$U_i = \overline{U}_i + a_{ij} u_j^n \tag{6.8}$$

where a_{ij} is the Cholesky decomposition of the Reynolds stress tensor given by:

$$a_{ij} = \begin{pmatrix} \left(\overline{u_1^2}\right)_{in}^{1/2} & 0 & 0 \\ \dfrac{(\overline{u_2 u_1})_{in}}{a_{11}} & \left(\left(\overline{u_2^2}\right)_{in} - a_{21}^2\right)^{1/2} & 0 \\ \dfrac{(\overline{u_3 u_1})_{in}}{a_{11}} & \dfrac{\left((\overline{u_3 u_2})_{in} - a_{21} a_{31}\right)}{a_{22}} & \left(\left(\overline{u_3^2}\right)_{in} - a_{31}^2 - a_{32}^2\right)^{1/2} \end{pmatrix} \tag{6.9}$$

where $\left(\overline{u_i u_j}\right)_{in}$ are the input (prespecified) values of the Reynolds stresses tensor, obtained either from experimental or simulation data, and $U_i\,(t)$ is the velocity time series that now has the desired first and second moments and turbulence scales (and, it should be noted, also the input autocorrelation function).

6.2 Development of the DFG algorithm

The preliminary use of the DFG algorithm brought to the surface two weak points of the approach. The first was related to the lack of the ability of the algorithm to allow for turbulence scale variation. This approach was originally adopted in order to contribute to the simplicity of the method and to restrict the required input data. However, it did impose a limitation to the accuracy of the produced data, especially when the single set of turbulence scales selected was not representative of the scales present in the flow.

Note that if only one set of turbulence scales is used over the entire LES flow inlet boundary, and the grid on the inlet plane is uniform, the use of a single 3D filter coefficient would then suffice for the generation of inlet data, since the parameters N_t, N_y, N_z would be the same at every grid node in the inlet plane. If the turbulence scales vary spatially over the inlet plane or the grid is non-uniform (or both), then the value of n will also vary spatially over the inlet plane ($n_i = L_i/\Delta x_i$) and a number of filter coefficients will be required. This obviously has a potentially significant impact on the accuracy and time cost associated with the DFG procedure. A number of filters can easily be used, corresponding to the range of different n values. In the limit, every grid point could be associated with a separate filter coefficient, corresponding to the particular turbulence scales/grid sizes appropriate to each local point. However, this will increase dramatically the b_{tyx} array, leading to a significant increase of the computational cost.

The second disadvantage of the method was related to the computational cost which could rise significantly with the size of turbulence scales involved, through n_t, n_y and n_z, due to the convolution operation described by Eq. 6.1. This adversely affects the use of the algorithm as a practical tool.

Hence, the development that was carried out aimed to address these two issues. Analytical discussion on these is given in section 6.2.1 and 6.2.2.

6.2.1 Multi-scale approach and implementation

The original algorithm presented by Klein et al. [82] made use of a single turbulence scale for each of the three directions. Hence, the first stage of the algorithm development involved the introduction of many turbulence scales, varied in space. The importance of this new feature to the quality of the generated data is discussed in detail in section 6.4. As a first approach to this idea, it was decided that only the scale variation in the wall-normal direction y would be considered. The introduction of multiple turbulence scales could potentially improve the quality of data produced by incorporating more characteristics present in the real flow.

In order to apply the multi-scale approach, the wall-normal variation of turbulence scales, obtained either from experimental or numerical data, had to be divided into a number of zones. In each zone, turbulence scales would be represented by their mean values, resulting in the "digitisation" of the distribution. Using these mean values and the process described in section 6.1, a number of filter kernels could then be generated, equal to the number of zones the wall-normal distribution had been divided into. Then, during the convolution operation, described by Eq.6.1, the filter kernel used for each point, would be the one corresponding to the zone that the point of interest belonged to.

As a first step, the variation of n can be approximated through a digitised form of its point-by-point distribution, using a number of representative n values over a corresponding number of regions of the inlet plane. In this case, the number of filter coefficients needed will correspond to the number of different regions chosen to represent sufficiently accurately the point-by-point distribution of scales. In this way the filter coefficient array becomes four-dimensional $(b_{ftyz}(f, 2N_{ft}+1, 2N_{fy}+1, 2N_{fz}+1)$, where f is the number of different regions).

This indicates that the employment of a multi-scale DFG approach results in an enlarged filter coefficients array and therefore, an increase of the computational cost. The employment of a multiple turbulence scales approach makes the need for efficient computation even more important. Once the filter coefficients have been computed, Eq.6.1 is used to produce a fluctuating velocity field. In a multi-scale DFG approach, each point in the inlet plane is convoluted with the filter that corresponds to the region to which the point belongs. This is performed through the numerical form of Eq.6.10, given by:

$$u_{jk} = \sum_{t'=-N_{ft}}^{N_{ft}} \sum_{j'=-N_{fy}}^{N_{fy}} \sum_{k'=-N_{fz}}^{N_{fz}} b_{ftyz}\left(f,t',j',k'\right) r\left(f,t',j+j',k+k'\right) \tag{6.10}$$

Note that Eq.6.10 is performed for $j = 1...M_y$, $k = 1...M_z$ and for all regions into which the inlet plane has been divided, i.e. for $f = 1...f_{max}$. M_y and M_z denote the number of grid points in the y and z directions and f_{max} the number of different inlet plane regions.

It is also worth mentioning at this point that different sets of filters applied within different zones of the inlet plane were not observed to produce any unphysical discontinuities close to the zone boundaries as long as the variation of turbulence scales from zone to zone was relatively smooth. If this is the case, there is no mechanism in the algorithm that will produce data with rapid variations across zone boundaries.

An illustration of the implementation of the multi-scale approach can be seen in Figure 6.1. The value of r_m at each location, is convoluted, denoted by '*', by the corresponding filter kernel, which by its turn, corresponds to a pre-specified set of turbulence scales in time, y and z direction, through the procedure described in section 6.1.

6.2.2 Multi-scale frequency domain convolution approach and implementation

The second stage of development of the DFG algorithm was related to the reduction of the computational cost. Veloudis et al. [182] have described a DFG implementation including

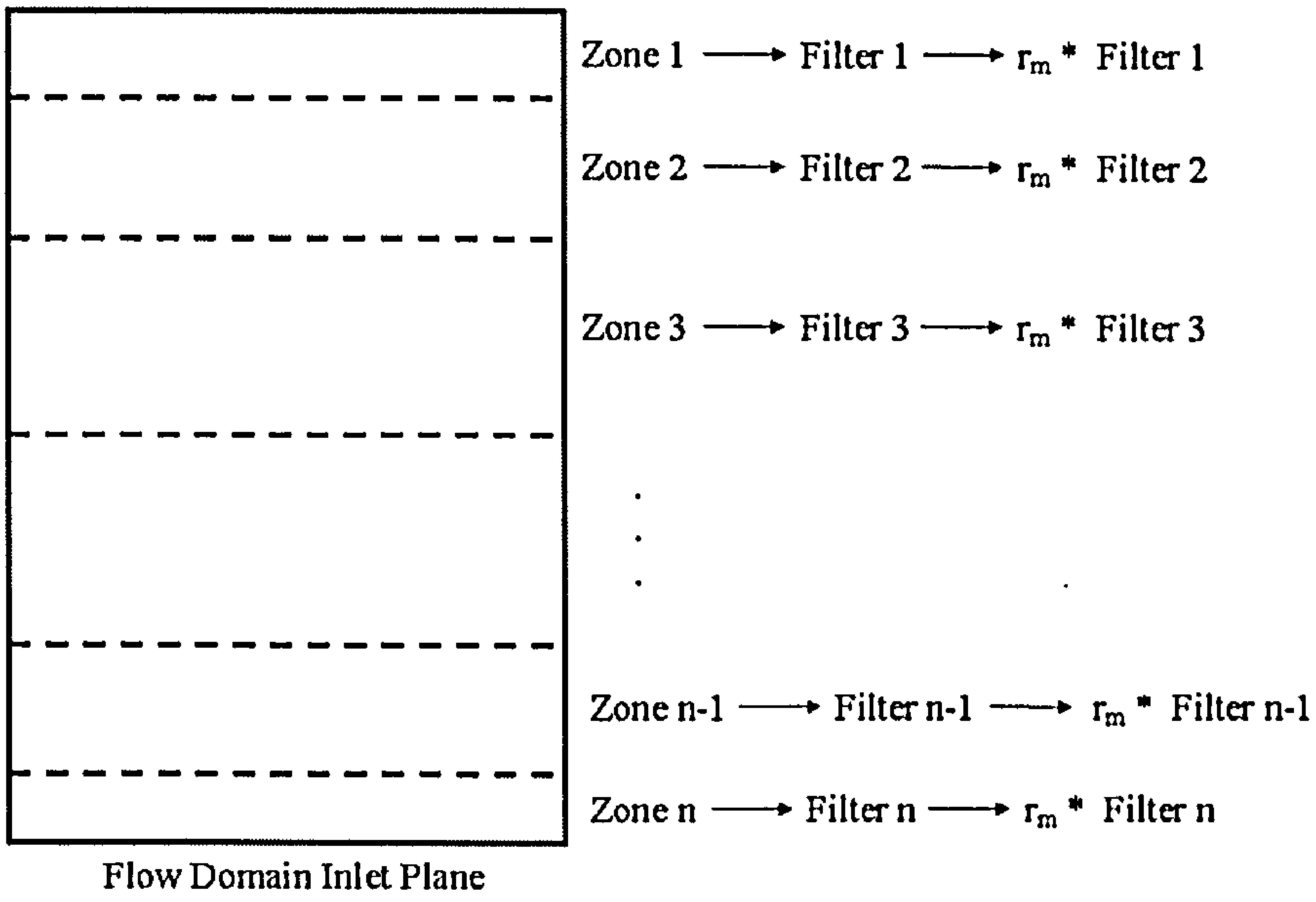

Figure 6.1: Graphic representation of the multi-scale DFG implementation

spatially varying scales and the associated multiple sets of filter coefficients, leading to the employment of six different filters to describe the wall normal variation of the turbulence scales. In that work it was concluded that the use of even only six filters can increase the computational cost of the DFG approach substantially, perhaps even to a prohibitively expensive level. The major part of the computational time is spent in the convolution of the random signal r_m with the digital filter kernel, given by Eq.6.1.

Hence, for the purposes of the present work, the DFG algorithm was modified in order to decrease the computational time required, increasing at the same time the ability to use a larger number of filters with non-proportional increase in computational time. This was achieved in two ways. The first was to perform the signal convolution in the frequency domain and the second was to use data interpolation in time.

In order to perform the signal convolution in the frequency domain, both signals have to be of the same element size. In order to achieve this, the filter kernel was padded with zeros until it reached the same number of elements as r_m, and the length of each was increased to the next largest 2^n size, as required by the Fast Fourier Transform (FFT) algorithm which was then used to transform both signals, r_m and b_m, into the frequency domain as:

$$R_m(\omega) = FFT(r_m(t)) \tag{6.11}$$

and

$$B_m(\omega) = FFT(b_m(t)) \tag{6.12}$$

where ω is the frequency.

In the frequency domain, the convolution of the two signals is given by:

$$u_m(\omega) = R_m(\omega) \cdot B_m(\omega) \tag{6.13}$$

where

$$u_m(\omega) = FFT(u_m(t)) \tag{6.14}$$

The convoluted signal is then returned to the time domain by an inverse FFT and the resulting signal is normalised using Eq.6.7. After normalisation, it is ready to be used in the second stage of the algorithm, as described above.

Despite the fact that three separate calculations are performed, i.e. a forward FFT, a multiplication and an inverse FFT, the overall computational time can be significantly decreased. This is essentially due to the transformation of integration in the time domain into a simple multiplication in the frequency domain, with the corresponding saving in computational cost (an order N^2 operation problem is reduced to $N \log_2 N$). Further details on the computational time reduction will be given below.

A further computational speedup may be achieved by the adoption of a larger timestep in the DFG algorithm (Δt_{DFG}), compared to the LES timestep Δt, and the use of data interpolation between the DFG timesteps, to produce the unsteady data that correspond to the finer timestep of the LES. The LES timestep, Δt, is limited by a CFL constraint but a larger value for Δt_{DFG} may be employed, equal to, for example, 1/10 of the smallest integral time scale required to be reproduced by the algorithm. This simplification results in a significantly smaller working array for r_m and b_{fxyz}, compared to the work reported in [182], since it can considerably reduce N_t. This has a beneficial effect on computational time, whilst providing enough data to describe adequately even the smallest timescales of interest. For the smaller LES Δt, intermediate data sets required were produced 'on the fly' by linear interpolation of the data sets available from the DFG. Note that due to the very small Δt needed for stability reasons by the LES method, the use of temporal interpolation as suggested above does not degrade the temporal accuracy of the results as will be shown in section 5.

In summary, the new implementation of the DFG algorithm can be described by the following steps:

1) Divide the inlet plane into f zones in the wall-normal direction and choose appropriate length scales $L_{fy} = n_{fy}\Delta y$, $L_{fz} = n_{fz}\Delta z$ and a time scale $T_{fx} = n_{ft}\Delta t_{DFG}$ for each of them. Δt_{DFG} can be either equal or multiple of the Δt value used for the LES calculation. Choose a corresponding filter width based on the condition $N_{fi} \geq 2n_{fi}$, $i = t, y, z$.

2) Initialise and store three random fields of the form $r_{ftyz}\,(f, -N_{ft} : N_{ft}, -N_{fy} : N_{fy} + M_{fy}, -N_{fz} : N_{fz} + M_{fz})$, where M_{fy} and M_{fz} denote the dimensions of the computational grid corresponding to each zone of the inflow plane.

3) Calculate the filter coefficients for each zone, using Eq.6.5 and by multiplying the three one-dimensional filters to obtain a three-dimensional filter. The results can be stored in an array of the form $b_{ftyz}(f, -N_{ft} : N_{ft}, -N_{fy} : N_{fy}, -N_{fz} : N_{fz})$.

4) Store the elements corresponding to the first zone to an array of the form $r_{tyz}\,(2N_{1t} + 1, 2N_{1y} + 1 + M_{1y}, 2N_{1z} + 1 + M_{1z})$ and generate its Fourier transform.

5) Store the elements corresponding to the filter to be applied on the first zone, to an array of the form $b_{tyz}\,(2N_{1t} + 1, 2N_{1y} + 1 + M_{1y}, 2N_{1z} + 1 + M_{1z})$ by padding the extra elements with zeros. Then generate its Fourier transform.

6) Perform the convolution of the two signals in the frequency domain using Eq.6.13.

7) The resulted signal is returned to the time domain using inverse Fourier transform and it is normalised using Eq.6.7. It is then stored in an array u_{ftyz} , which has the same form as r_{ftyz}.

8) Repeat steps 4) to 7) for all zones of the inlet plane. At the end of the procedure u_{ftyz} is complete and the transformation given by Eq.6.8 and 6.9 is used to produce the final signal U_i.

9) Store the final signal.

10) Discard the first y,z-plane in r_{ftyx} and shift the whole data as $r_{ftyx}(f,i,j,k) \Rightarrow r_{ftyx}(f,i+1,j,k)$. Fill the plane $-N_{ft}$ with new random numbers.

11) Repeat steps 4) to 10) for each timestep.

6.3 Test case

The testing of the multi-scale DFG involved a series of simulations of a flow passing through a periodic geometry domain. The idea was to perform a fully periodic boundary condition simulation that would not have any requirement for explicit imposing of artificial turbulent data at the inlet. This simulation would provide all the required input data to the DFG algorithm, in terms of first and second moment statistics as well as turbulence scales variation. Furthermore, it would form the "target" flow field for the second series of simulations.

The second series of simulations would make use of inlet data produced by the DFG algorithm, using different levels of description of the wall-normal variation of turbulence scales. These would be called Level 1, Level 2 and Level 3. Hence, the produced flow fields would show the level of the flow sensitivity to the different levels of turbulence scales description.

6.3.1 Description of test case selected

The streamwise repeating constricted channel flow problem studied by Temmerman et al. [174] was selected as the test case for the assessment of the DFG algorithm. This flow case was considered appropriate since it was streamwise and spanwise periodic and it had an attached boundary layer region extending over $0.23h$ downstream of the inlet plane, where h is the constriction height, as can be seen in Figure 6.2. The test case also involved this attached boundary layer separating and forming a turbulent shear layer further downstream, followed by a considerable separated flow region. Such a flow problem has not been previously treated using synthetic inlet data, so was considered a suitable test for the present method.

The flow geometry can be identified in Figure 6.2 with the same dimensionless quantities as those used by Temmerman et al. [174]. The channel height is $l_y = 3.03h$, where h is the constriction height; the length in the streamwise direction is $l_x = 9h$, and in the spanwise direction $l_z = 4.5h$. The Reynolds number of the flow is 10,595, based on h and the bulk velocity U_B at the constriction crest. For the calculations performed, h was set to 0.028m and U_B to 5.53m/s.

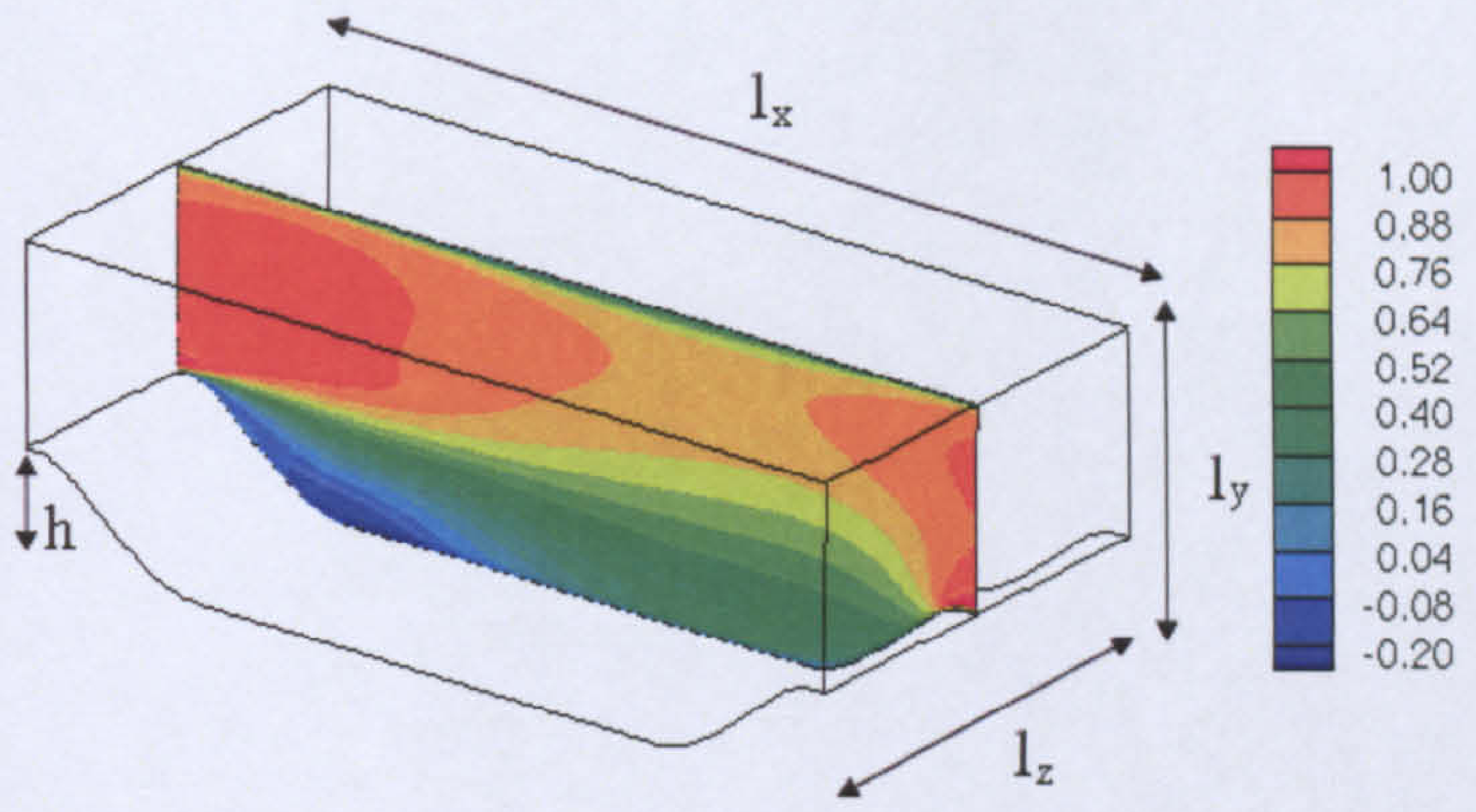

Figure 6.2: Geometry and contours of U/U_B for channel flow with repeated constrictions

A periodic boundary condition (PBC) simulation was first performed to confirm the acceptability of the current LES solution and to obtain the information required for the DFG method. A simulation record length (~1.28 sec) corresponding to around 80,000 timesteps or 28 flow through times (flow through time $T_{FT} = \frac{l_x}{U_B} \simeq 45$msec) was generated by the PBC simulation and was processed to deduce statistically stationary first and second moments of the velocity field. The LES timestep used was $3.51 \times 10^{-4} T_{TF}$ ($\Delta t = 16\mu$sec) corresponding to a maximum CFL number of around 0.2. The grid used for the simulation had 160×64×62 (x, y, z) cells, with constant grid spacing in the streamwise, x, and spanwise, z, directions, while in the wall normal direction, y, it was refined close to the lower wall. Note that this grid (~650,000 cells) is substantially coarser than the 196×128×186 ~5 million cell grid used in the well-resolved simulation of Temmerman et al. [174].

The subgrid scales were modelled with the aid of the Smagorinsky model and the van Driest near-wall damping function [181]. Furthermore, the Werner-Wengle near-wall model [186] was employed since the near-wall grid resolution was not fine enough for no-slip conditions to be applied. Temmerman et al. [174] have also reported results for the same flow problem using exactly the same combination of SGS and near-wall modelling; their results compared well with predictions obtained using alternative SGS models, on a grid similar to the one used in the present study, and the employment of the Smagorinsky model was therefore considered appropriate for the present purposes.

Similarly, in the same study by Temmerman et al. [174], it was noted that although solutions were insensitive to the SGS model employed, more sensitivity was observed for the near-wall treatment. In this respect, the Werner-Wengle model was found to give the best results overall. The sensitivity of the predicted flow to the SGS/near-wall model was mainly concentrated on the reattachment point location; SGS models giving lower ν_t values, returned more accurate resolved stresses (in comparison to the highly resolved simulation performed [174]) and led to a longer reattachment distance.

During the PBC simulation performed for the present study, the average value of ν_t/ν throughout the whole flow domain was of order of 1.0. The maximum value in the region of the lower wall and in the first half of the domain of primary interest here, was 2.3. Furthermore, the ratio of the SGS to resolved shear stresses $\frac{\overline{u'v'}_{sgs}}{\overline{u'v'}_{res}}$ was less than 4% in the majority of the flow domain, with the only exception being the near-wall region of the upper surface, where, due to the coarse grid employed, the maximum value observed was around 25% in a very restricted region. For this reason, only the resolved part of the stresses was considered in the presentation of the results, which focus on flow events near the lower boundary.

As far as boundary conditions were concerned, the inlet and outlet were treated as periodic boundaries, as were the side of boundaries. The same computational setup was used in all simulations performed for the testing of the multi-scale DFG algorithm.

6.3.2 Results of periodic boundary condition simulation

Figure 6.2 presents contours of the mean streamwise velocity component U non-dimensionalised by U_B. The flow separates from the curved surface of the constriction and re-attaches on the lower plane channel wall to form a separation bubble of length 4.08 x/h. Predicted values for separation and re-attachment locations were compared with reference data taken from Temmerman et al. [174] in Table 6.1. U/U_B, $\frac{\overline{u'u'}}{U_B^2}$ and $\frac{\overline{u'v'}}{U_B^2}$ time-averaged profiles in the y direction at $x/h = 0.05$, 2.0 and 5.0 can be seen in Figures 6.3, 6.4 and 6.5, again compared with the Temmerman et al. [174] LES data. The time-averaged results presented here and in subsequent sections were produced by gathering information of ten flow through times.

Figures 6.3 (a) (b) and (c) show that the current PBC simulation compared reasonably well with the results of the reference LES (Temmerman et al. [174]) in terms of the mean axial velocity development. At the inlet plane ($x/h = 0.05$) the profiles were similar, although the present LES showed higher velocities close to the lower wall, and a mass balancing under prediction in the region near the upper wall. The high velocity near the lower wall was a possible cause for the earlier separation shown in Table 6.1. At $x/h = 2.0$, the separation

Table 6.1: Separation bubble data from reference and PBC simulation

Simulation	Separation Point (x/h)	Re-attachment Point (x/h)	Separation Bubble Length (x/h)
Reference data [174]	0.22	4.72	4.50
PBC simulation	0.09	4.17	4.08

bubble features were in close agreement with the reference data. The over-prediction of the axial velocity in the central region and under-prediction close to the upper wall were presumably related to the inlet profile differences. Finally, after re-attachment, the flow developed in a similar manner in the two calculations, except near the lower wall, as can be seen in Figure 6.3 (c). The differences noted are fairly small, and were related to the lack of resolution, compared to the Temmerman et al. grid [174], in the current LES calculation near the lower wall, and the use of a wall function as opposed to a well-resolved LES grid. As noted above, the overall grid size of the current LES was almost a factor of 8 times smaller (half as fine in each grid direction) as the reference LES.

Reasonably close agreement between the predictions of axial normal stress and shear stress from the two calculations can be seen in Figures 6.4 and 6.5. The shape of these profiles was reproduced well at all these conditions, but the insufficient near-wall resolution in the present LES produced errors in near-wall absolute values. However, although there were differences, it was felt that for the present purpose, the benchmarking of the current PBC LES solution against the reference LES data of Temmerman et al. [174] was sufficient to justify the use of the PBC simulation as valid test data for the DFG study which was the main focus of the work reported here.

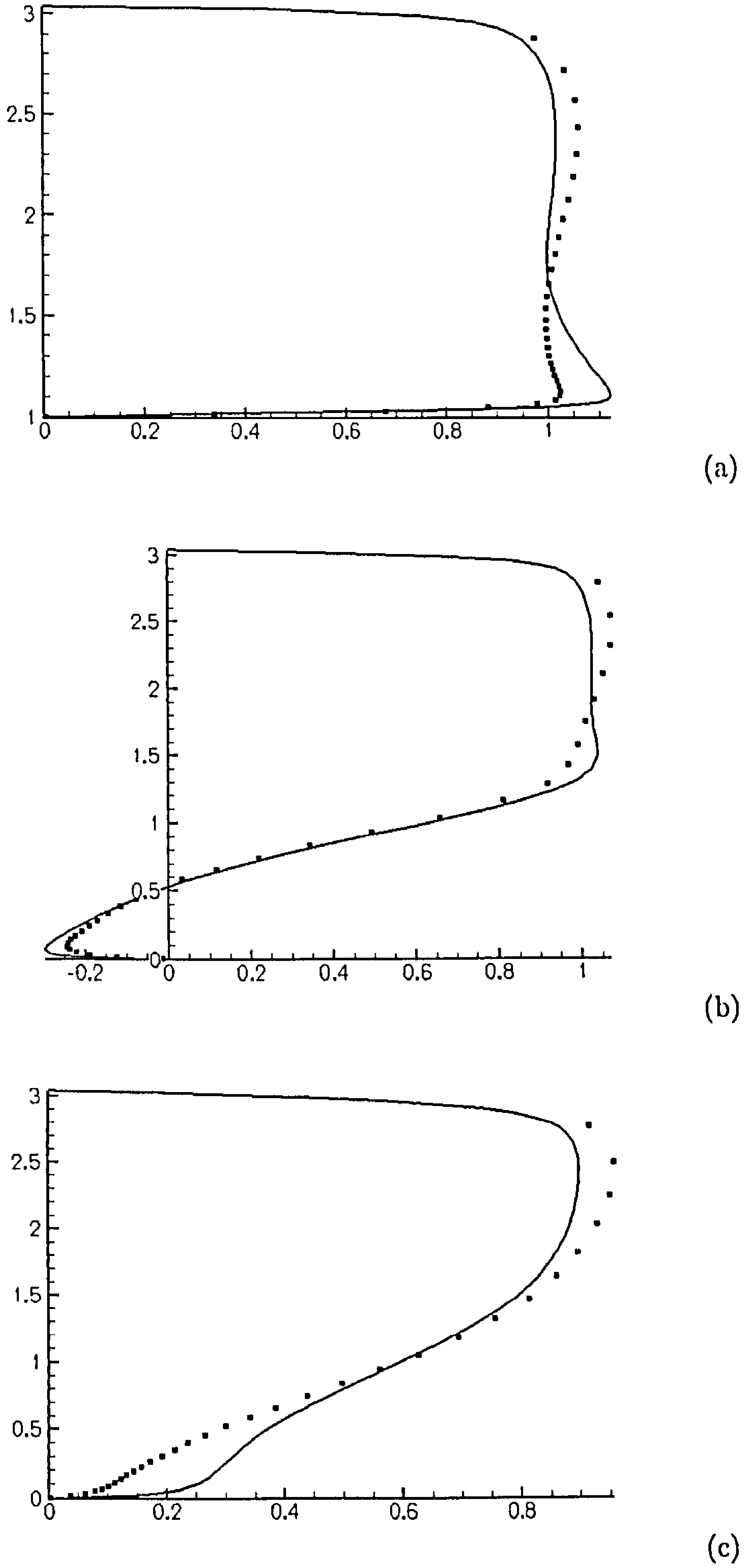

Figure 6.3: $\frac{U}{U_B}$ vs. y/h at $x/h = 0.05$ (a), $x/h = 2.0$ (b), $x/h = 5.0$ (c) (squares: Reference Simulation, solid line: Periodic Flow Simulation)

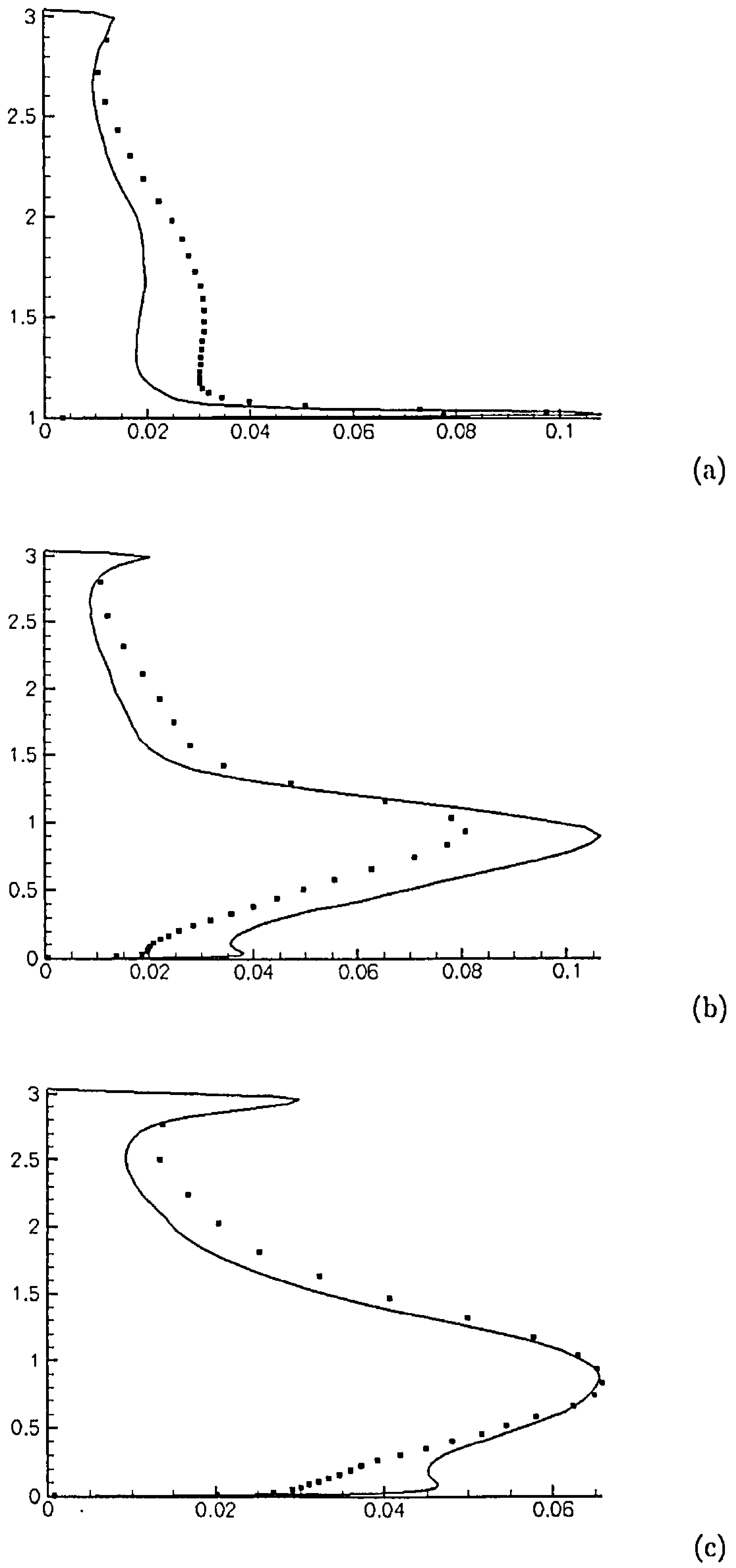

Figure 6.4: $\frac{\overline{u'u'}}{U_B^2}$ vs. y/h at $x/h = 0.05$ (a), $x/h = 2.0$ (b), $x/h = 5.0$ (c) (squares: Reference Simulation, solid line: Periodic Flow Simulation)

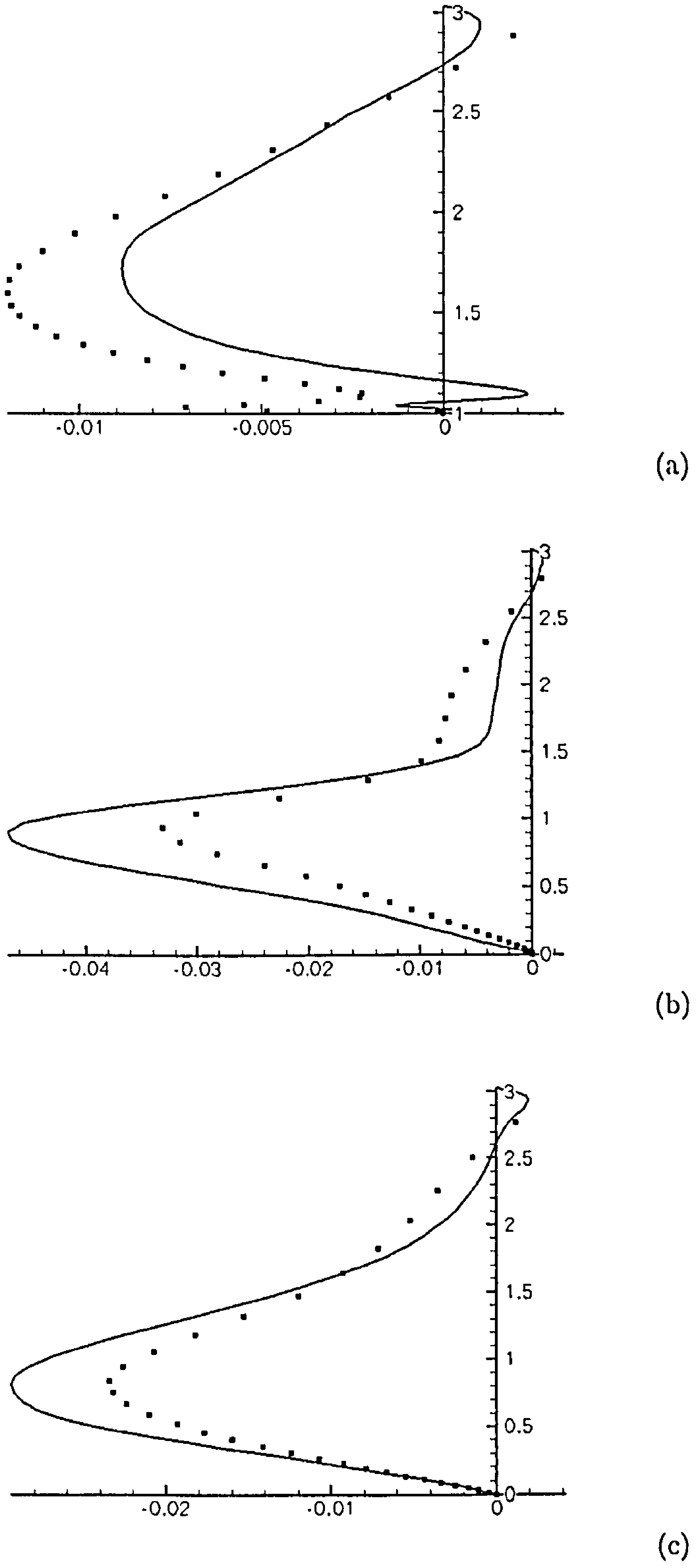

Figure 6.5: $\frac{\overline{u'v'}}{U_B^2}$ vs. y/h at $x/h = 0.05$ (a), $x/h = 2.0$ (b), $x/h = 5.0$ (c) (squares: Reference Simulation, solid line: Periodic Flow Simulation)

6.3.3 Extraction of length and time scales from PBC LES Solution

Using the PBC simulation, time series were extracted at selected points in the (y, z) space covering the inlet plane ($x = x_{in}$). From these time series, a longitudinal integral time scale was calculated from the autocorrelation of the axial velocity according to [146]:

$$T_x(x_{in}, y, z) = \int_0^{\infty} \frac{\overline{u(x_{in}, y, z, t)\, u(x_{in}, y, z, t+\tau)}}{\overline{u(x_{in}, y, z, t)^2}} d\tau \tag{6.15}$$

where τ is the time separation between the samples of interest.

Similarly, lateral integral length scales L_y and L_z were calculated from spatial correlations in the relevant directions, as described by Eq.6.16 and 6.17 respectively:

$$L_y(x_{in}, y, z) = \int_{y_{min}}^{y_{max}} \frac{\overline{v(x_{in}, y, z, t)\, v(x_{in}, y+Y, z, t)}}{\overline{v(x_{in}, y, z, t)^2}} dY \tag{6.16}$$

$$L_z(x_{in}, y, z) = \int_{z_{min}}^{z_{max}} \frac{\overline{w(x_{in}, y, z, t)\, w(x_{in}, y, z+Z, t)}}{\overline{w(x_{in}, y, z, t)^2}} dZ \tag{6.17}$$

The subscripts *min* and *max* denote minimum and maximum values. The resulting time and length scale wall-normal distributions can be seen in Figure 6.6 plotted as absolute dimensional quantities.

Interestingly, the variation of T_x is fairly constant in most of the central region of the inlet plane at around 40% of the mean flow time scale (defined as $\frac{l_y - h}{U_B}$), with two distinctive peaks close to the walls with values closer to 90% (lower wall) and 70% (upper wall) of the mean flow time scale. This shape is related to the flat, low turbulence level in the inlet plane over most of the channel height (see Figure 6.4), and the rapid change in eddy shape, turbulence level and velocity as the walls are approached, particularly on the lower wall. The turbulent eddies become smaller in the wall-normal direction, but elongated (streak-like) in the longitudinal direction, leading to longer turbulent time scales. The transverse length scale peaks at around 20% of the channel height but decreases as expected as the walls are approached, more rapidly again for the lower wall. The spanwise peak length scale is also near the lower wall and is around 15% of the solution domain span; a more typical value is around 5%, confirming the acceptability of the use of periodic boundary conditions in the spanwise direction for the present domain size. The corresponding distributions for n_t, n_y, n_z can be seen in Figure 6.7. Note that the difference between the L_y and n_y profiles is due to the variable cell size in the y direction.

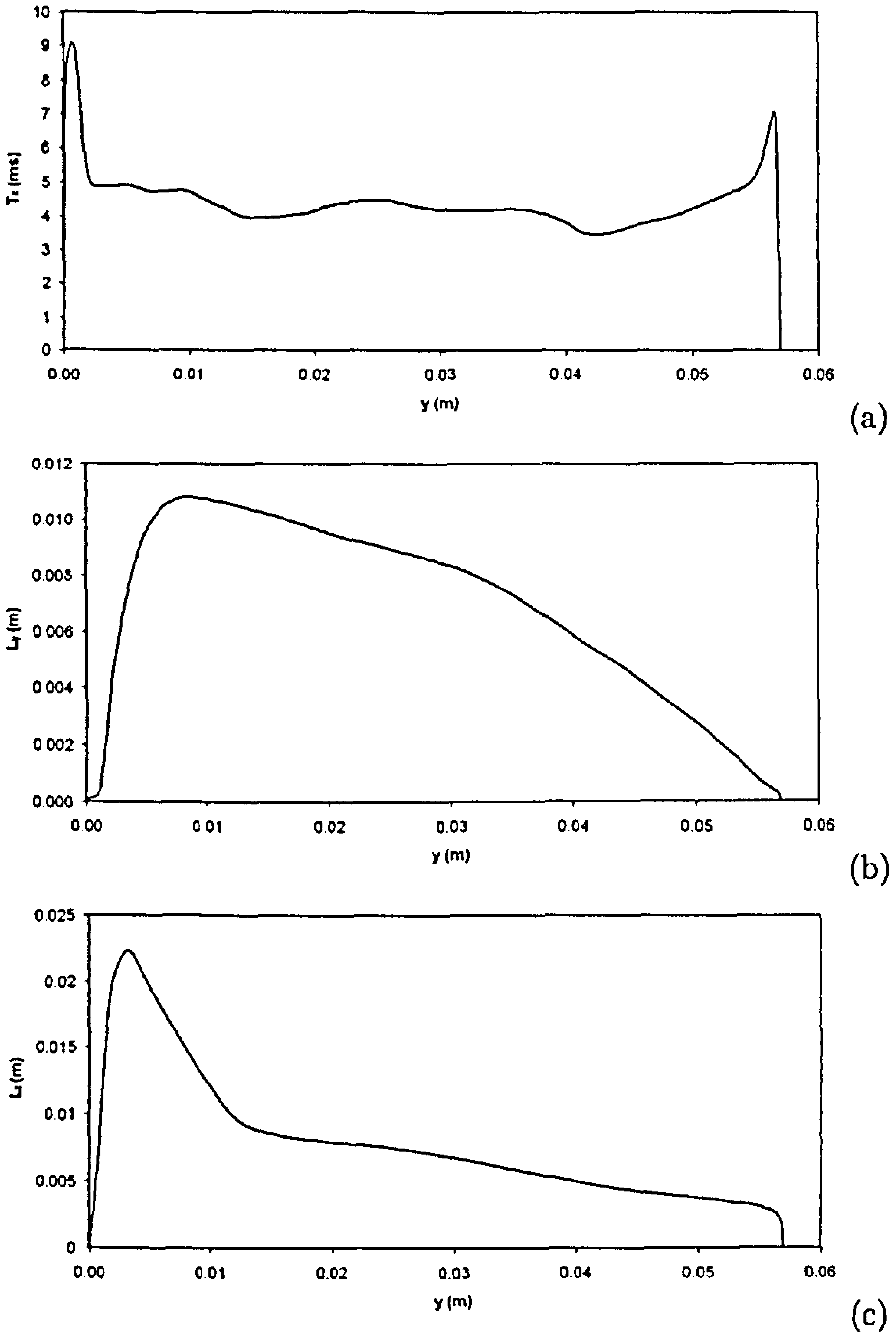

Figure 6.6: Wall-normal distributions of turbulence integral time and length scales (a: time scale, b: wall-normal length scale, c: spanwise length scale)

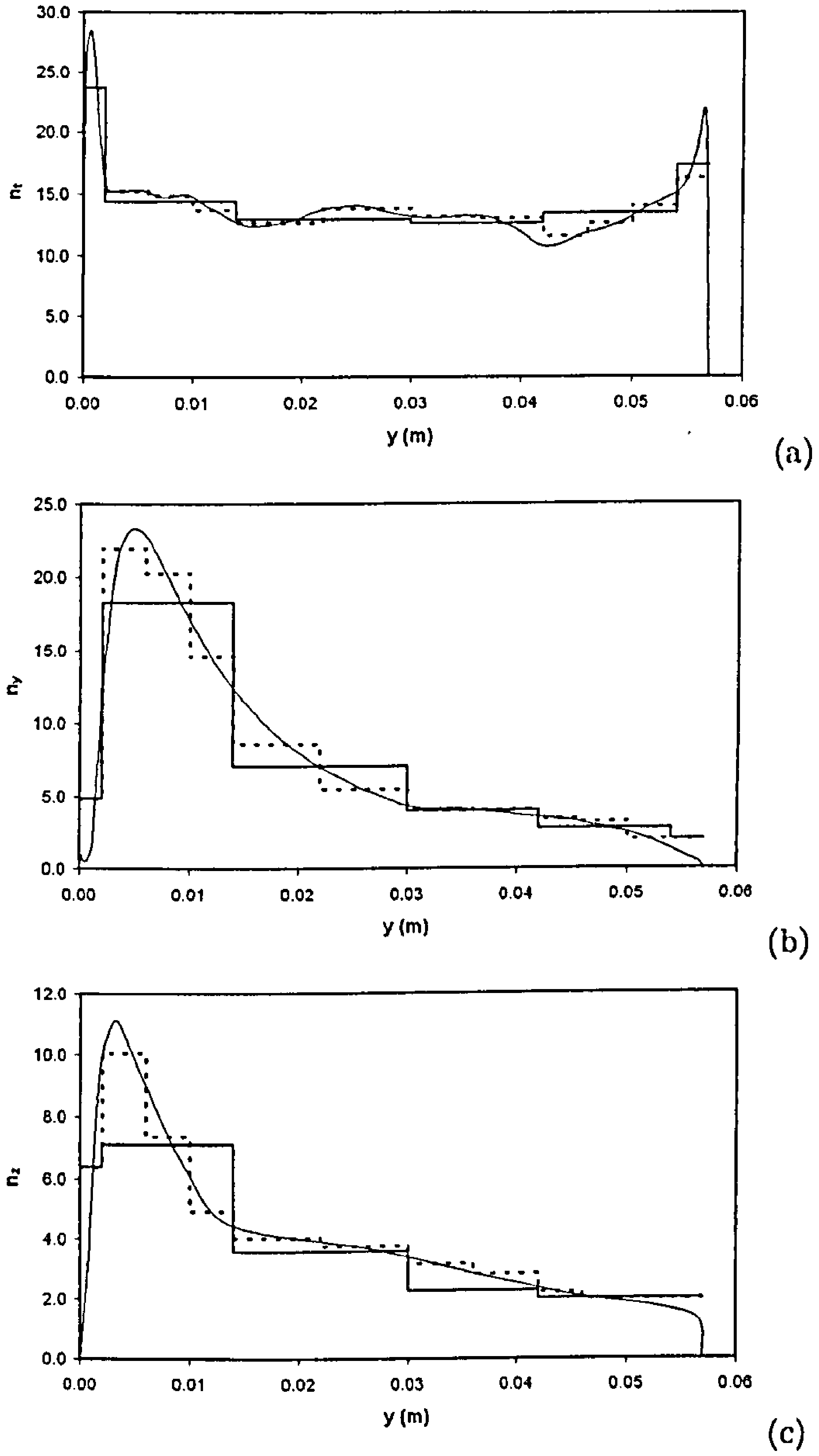

Figure 6.7: Wall-normal distributions of n_t, n_y, n_z
(a: time scale, b: wall-normal length scale, c: spanwise length scale)

For input to the DFG calculation at Level 1 (spatially uniform scales over the inlet plane), the turbulence scales used were calculated as a cell size weighted average over the y-direction, of the turbulence scale distributions computed from the PBC simulation. The values obtained can be seen in Table 6.2 in terms of the DFG timestep ($n_t = T_x/\Delta t_{DFG}$) and mesh spacing ($n_y = L_y/\Delta y, n_z = L_z/\Delta z$). Note that $\Delta t_{DFG} = 0.00032$sec (i.e. 20 times the LES timestep), $0.00026\text{m} \leq \Delta y \leq 0.002\text{m}$ and $\Delta z = 0.002\text{m}$.

Table 6.2: n values for Level 1 simulation

Simulation	n_t	n_y	n_z
Periodic Boundary Conditions	14.66	7.46	5.06

For input to DFG calculations at Level 2 and 3, the PBC extracted scale profiles were digitised into 6 and 12 zones respectively. The digitisation can be seen by the thick solid and dotted line in Figure 6.7. In terms of an ideal turbulence scales wall-normal profile representation, the best achievable resolution would correspond to using the curves shown in Figure 6.7 directly, and lead to the use of a different filter at each cell in the wall-normal direction. However, it was believed this would be prohibitively expensive and unnecessary for a first implementation with spatially varying scales; hence the variation of turbulence scales was digitised using a number of filters that represented the profile satisfactorily, at an acceptable computational cost, and to investigate the effects of this choice, two levels of digitisation were explored.

4,560 timesteps of inlet boundary condition data were generated for Level 1, 2 and 3 simulations, using the DFG algorithm described. When interpolated for the finer LES timestep, these would correspond to 91,200 timesteps, able to provide inlet data for approximately 32 T_{FT}.

6.4 Multi-filter frequency convolution method results and discussion

Before proceeding to the presentation of the Level 1, 2 and 3 results, some comments may be made about the improved realism achievable via the spatially varying scales input into the DFG algorithm. One benefit of this is illustrated in Figure 6.8, which shows autocorrelations of the axial velocity deduced from the PBC simulation at two points with significantly different turbulent scales. The first point is at $y = 0.0012$m, and the second point is at $y = 0.0136$m; as can be seen in Figure 6.6, T_x, L_y and L_z are quite different at these two points. Two observations may be made on the profiles shown in Figure 6.8. The first is to note the shape of the autocorrelation function predicted by the PBC simulation. At neither point does the predicted shape follow precisely the Gaussian shape assumed by the DFG method. The record length used to obtain these autocorrelations is at least 140 integral timescales long (corresponding to 1.28sec), so the PBC predicted shapes are statistically accurate and departures from a Gaussian shape are determined by the local flow physics. Hence, the Klein et al. DFG approach [82] will never be able to reproduce the inlet turbulence structure precisely, since it generates time series that are forced to fit Gaussian correlation functions. Results could potentially be improved by the adoption of other correlation function forms that corresponded closer to observations in inhomogeneous flows, but this aspect has not been addressed here. Note that di Mare et al. [40] have employed a DFG approach using alternative and spatially variable autocorrelation functions to produce data for an attached boundary layer simulation, indicating promising results.

The second point is that the integral time scale at the point nearest to the wall is around twice that of the other point. Hence the Level 1 approximation, which assumes the same turbulence scales at both points, will necessarily introduce errors. Multi-scale approximation, although it will not remove the Gaussian function restriction, will at least allow the autocorrelation to be scaled appropriately at different points. This is illustrated in Figure 6.8 by the DFG produced R_{uu} curves. The red solid line shows the Level 1 generated values. Since the scales at the point further from the wall are close to the cell-averaged uniform value chosen in the Level 1 simulation, the agreement with the PBC R_{uu} curve is reasonable; however, the same curve is used in the DFG Level 1 computation also for the second point and here the agreement with the PBC data is very poor. The DFG Level 3 data is shown in Figure 6.8 as blue solid lines; with even the crude digitisation adopted, the multi-scale implementation shows (within the constraint of the Gaussian function) a good representation of the different turbulence scales between the two points.

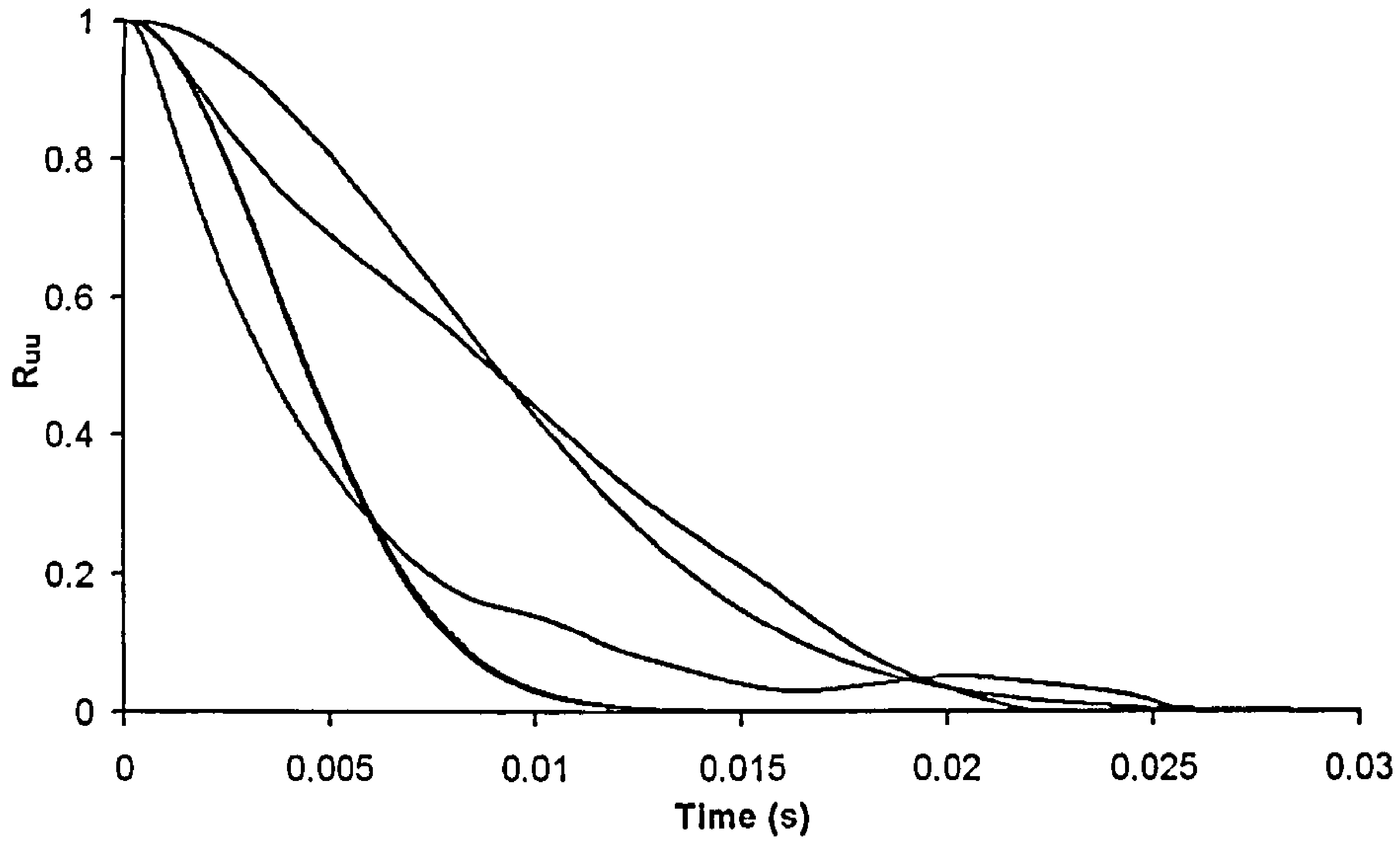

Figure 6.8: R_{uu} at $y = 0.0012$m (upper lines) and at $y = 0.0136$m (lower lines) (black solid lines: PBC R_{uu}, red solid line: DFG Level 1 R_{uu}, blue solid lines: DFG Level 3 R_{uu})

Profiles of U/U_B, $\frac{\overline{u'u'}}{U_B^2}$, $\frac{\overline{v'v'}}{U_B^2}$ and $\frac{\overline{u'v'}}{U_B^2}$, at three streamwise locations, $x/h = 0.0, 2.0, 5.0$ predicted by the PBC, Level 1, Level 2 and Level 3 DFG simulations are shown in Figures 6.9, 6.10, 6.11 and 6.12. At inlet, the agreement of 1^{st} and 2^{nd} order moments of all DFG-driven simulations with the PBC data was very good, as expected since the algorithm was formulated to reproduce this input data. Some discrepancies can be seen for $\frac{\overline{u'v'}}{U_B^2}$ and this is possibly due to the lack of phase information in the present approach which prevents the generated turbulent structures at the inflow from being perfectly physical.

Although the mean velocity profiles within the recirculation region of the flow, at $x/h = 2.0$, were close to the PBC data in all three DFG calculations, further downstream, Level 2 and 3 simulations reproduced the PBC predicted recovery region after the flow re-attachment, much better than Level 1.

Predictions for the normal stresses indicate, interestingly and perhaps surprisingly, that even the use of a single, spatially uniform specification of inlet turbulence scales (Level 1) can produce acceptable results. The profiles of $\frac{\overline{u'u'}}{U_B^2}$ and $\frac{\overline{v'v'}}{U_B^2}$ at $x/h = 2.0$ show that the accuracy of all three DFG simulations is essentially the same at this station, with only some slight improvement very close to the lower wall for the Level 3 data. The conclusion to be drawn here is that although the simulations have started with quite different turbulence scales at the inlet, the calculations have generated a similar (and self consistent) turbulence structure by $x/h = 2.0$. The presence of the recirculation zone and its bounding shear layer has presumably contributed significantly to the generation of the turbulence structures, offsetting to some extent the inlet plane differences. Further downstream, at $x/h = 5.0$, Level 2 and 3 give better results with Level 3 giving the most accurate prediction overall. The profiles for shear stress, as seen in Figure 6.12, indicate that the multi-scale DFG Level 2 and 3 simulations give more accurate results throughout the flow field, with Level 1 data displaying under-predicted peak values.

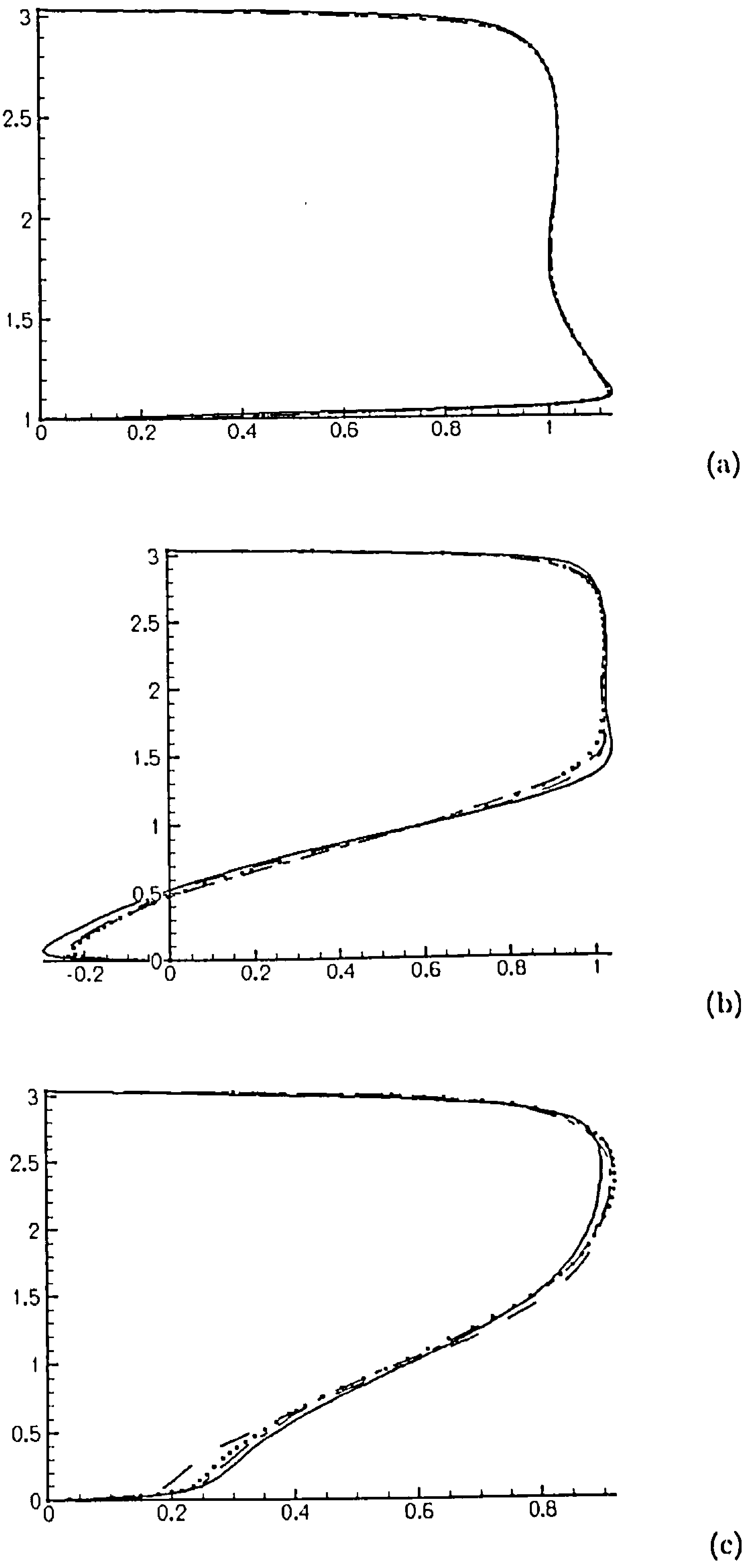

Figure 6.9: $\frac{U}{U_B}$ vs. y/h at $x/h = 0.0$ (a), $x/h = 2.0$ (b), $x/h = 5.0$ (c)
(solid line: Periodic Flow Simulation, dashed line: Level 1, dash-dotted line: Level 2, dotted line: Level 3)

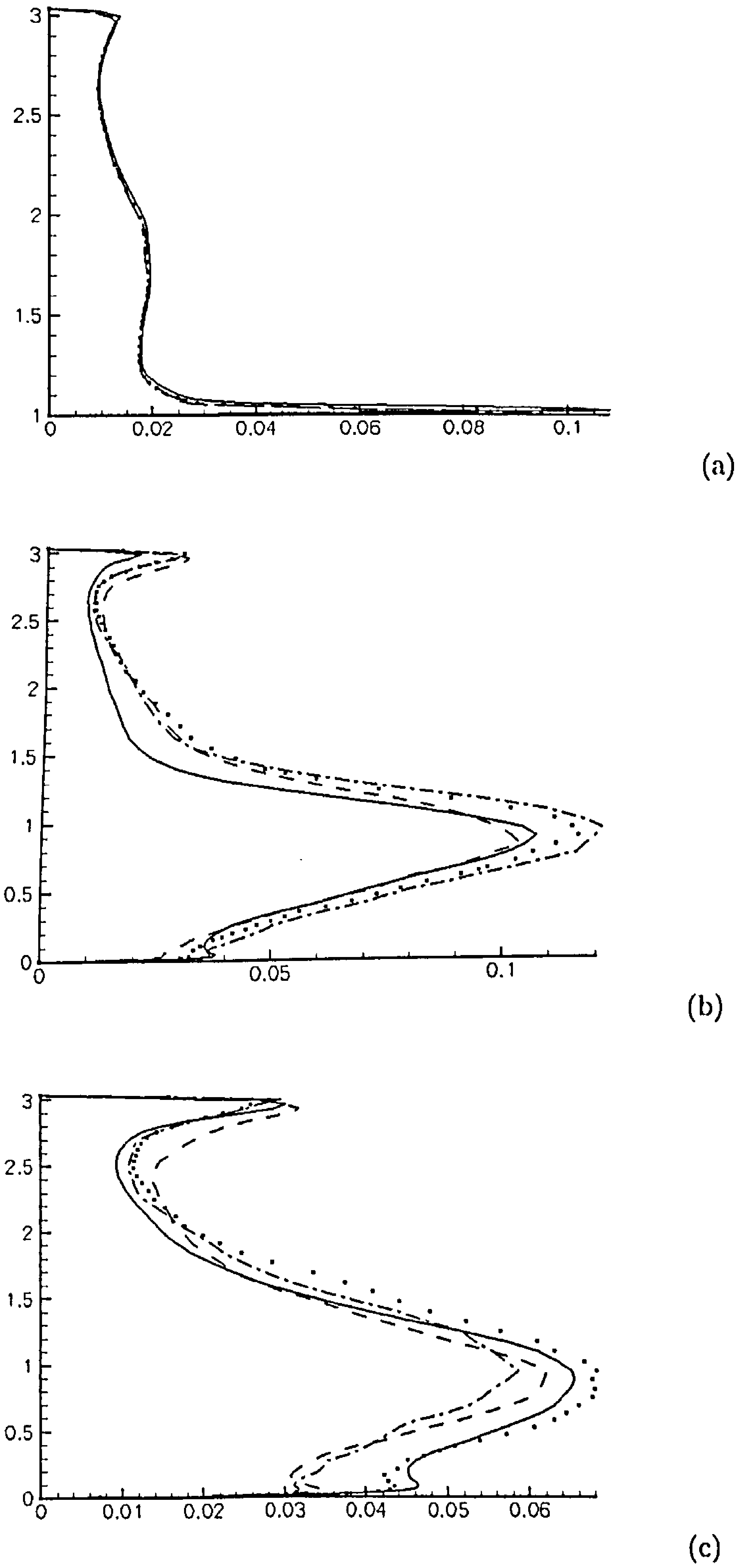

Figure 6.10: $\frac{\overline{u'u'}}{U_B^2}$ vs. y/h at $x/h = 0.0$ (a), $x/h = 2.0$ (b), $x/h = 5.0$ (c)
(solid line: Periodic Flow Simulation, dashed line: Level 1, dash-dotted line: Level 2, dotted line: Level 3)

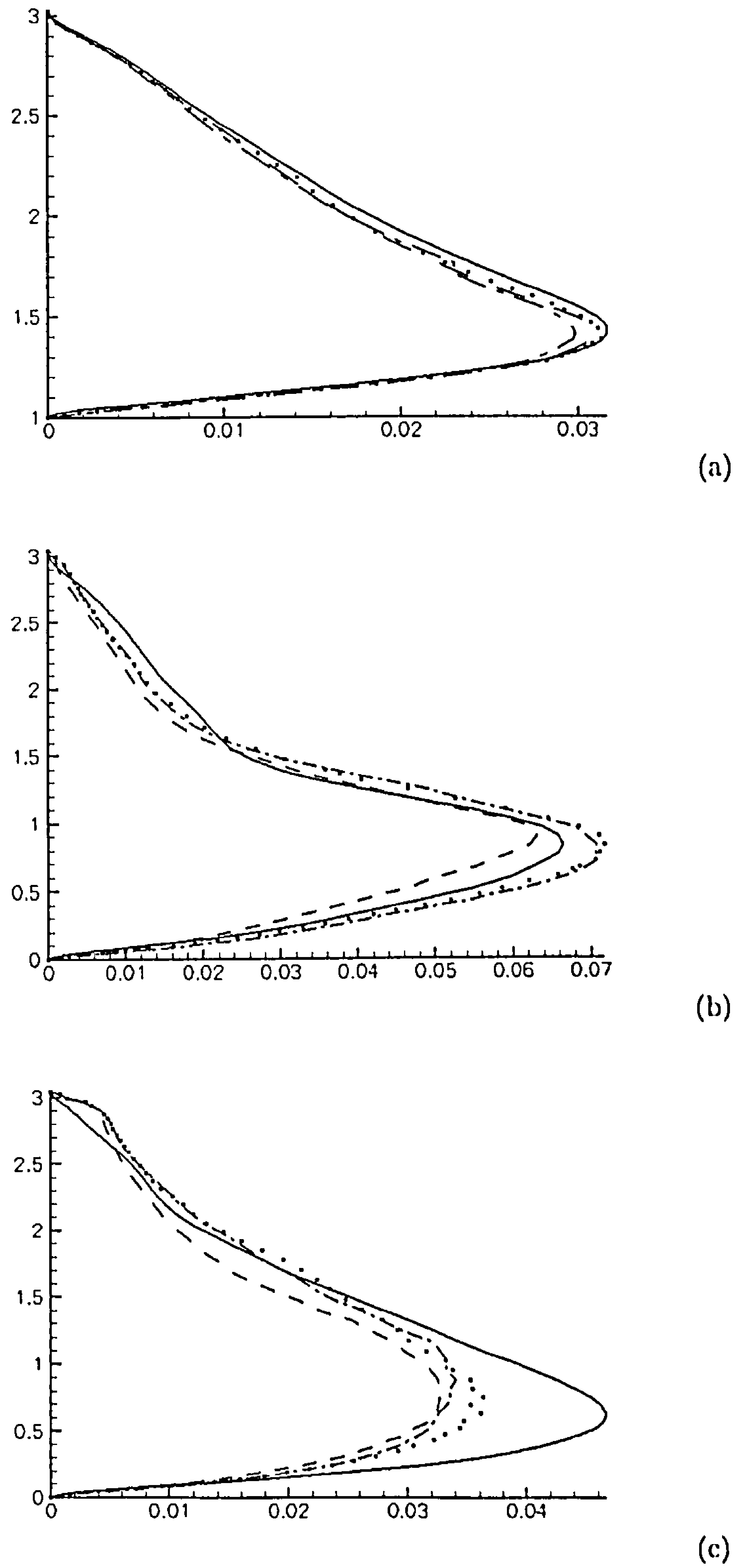

Figure 6.11: $\frac{\overline{v'v'}}{U_B^2}$ vs. y/h at $x/h = 0.0$ (a), $x/h = 2.0$ (b), $x/h = 5.0$ (c)
(solid line: Periodic Flow Simulation, dashed line: Level 1, dash-dotted line: Level 2, dotted line: Level 3)

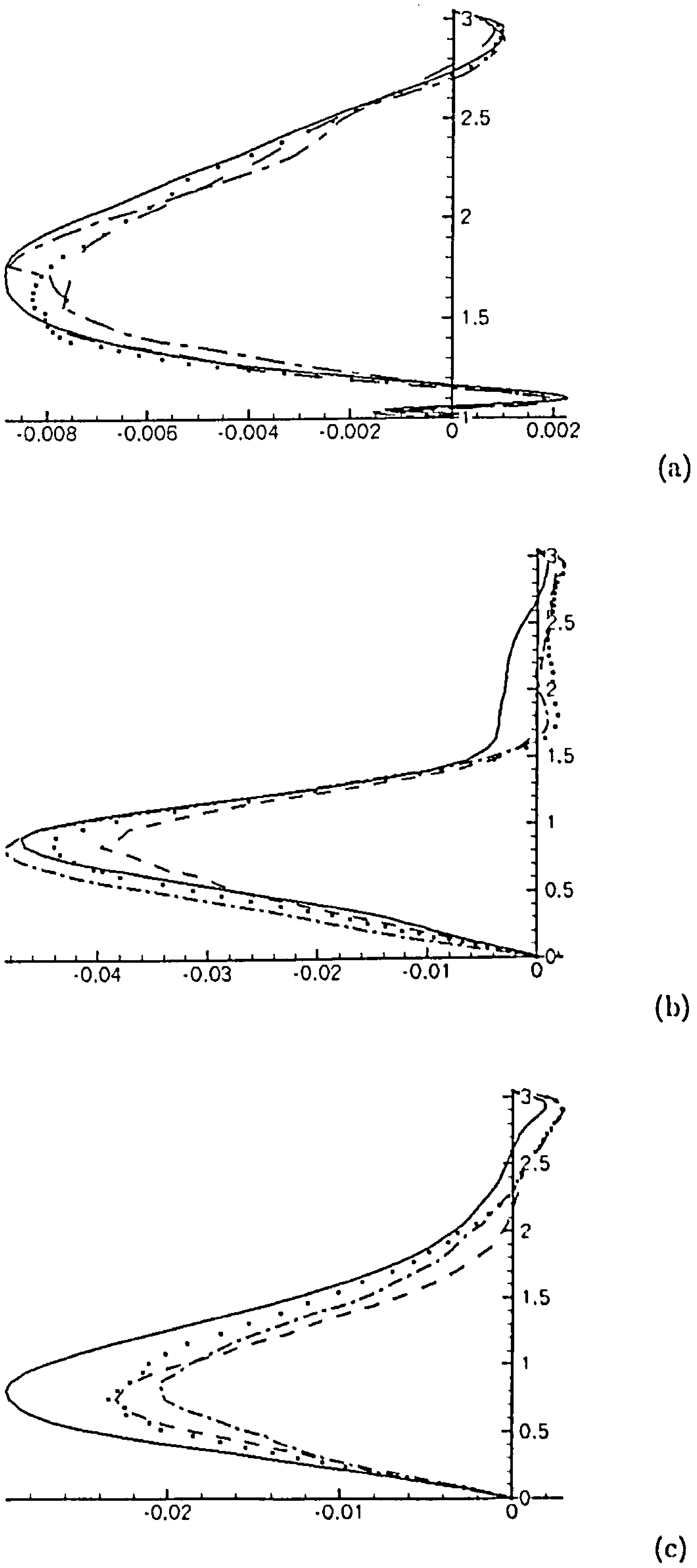

Figure 6.12: $\frac{\overline{u'v'}}{U_B^2}$ vs. y/h at $x/h = 0.0$ (a), $x/h = 2.0$ (b), $x/h = 5.0$ (c) (solid line: Periodic Flow Simulation, dashed line: Level 1, dash-dotted line: Level 2, dotted line: Level 3)

Figures 6.13 (a), (b), (c) and (d) present contours of the resolved turbulence kinetic energy, k, for the PBC, a simulation driven by random disturbance inlet conditions and the DFG Level 1 and 3 simulations. The random disturbance inlet simulation was carried out by imposing the time-averaged velocity profiles obtained by the PBC, with a 3% of mean velocity magnitude white noise disturbance superimposed. This simulation was performed for illustration purposes and the results presented in Figure 6.13 (b) indicate the importance of realistic inlet conditions for the predicted distribution of k. The lack of any correlation in the random disturbance signal causes it to decay rapidly, without promoting any flow turbulence. Hence the flow field becomes essentially laminar in the region near the inlet plane, until natural shear-layer instabilities develop some turbulence further downstream.

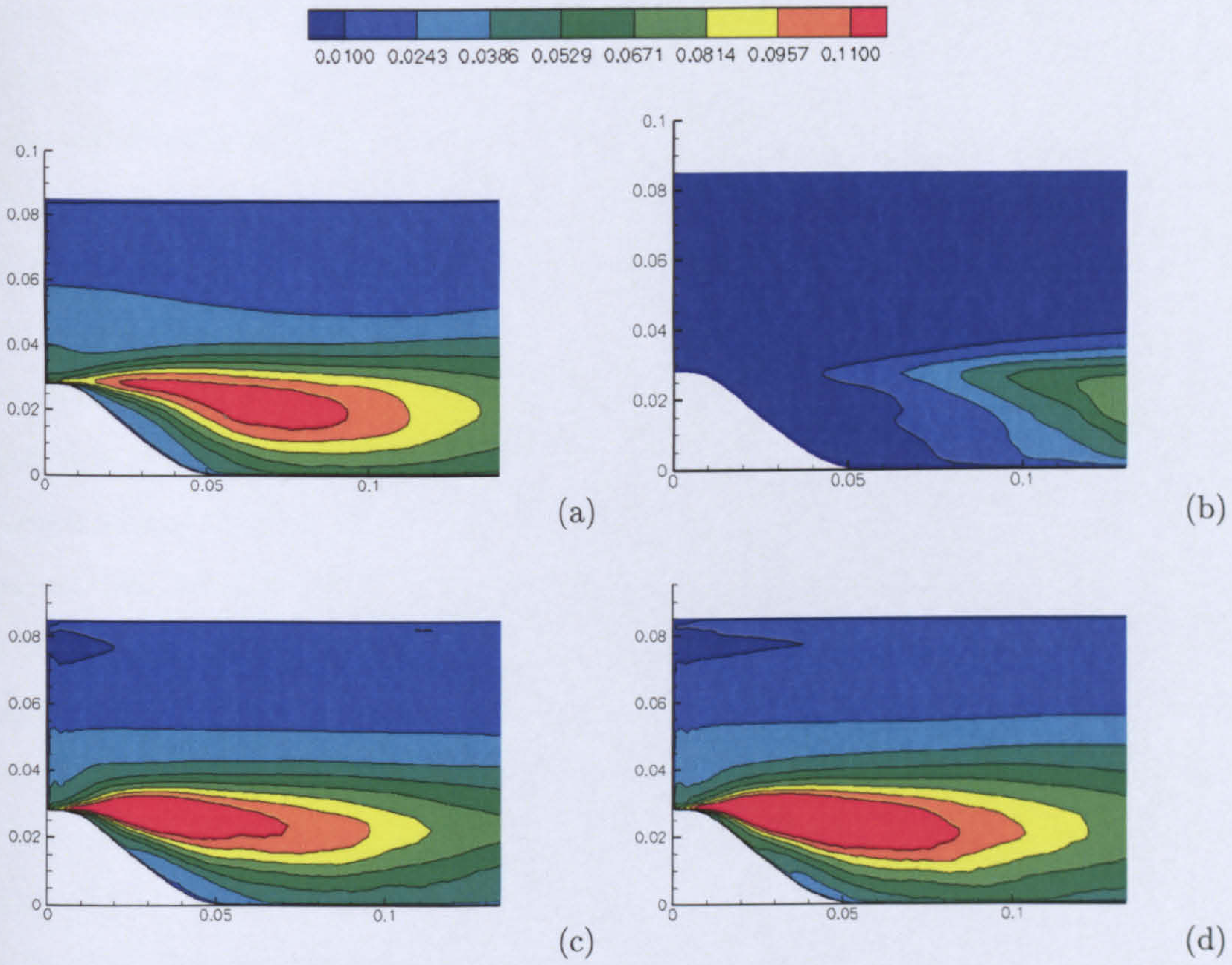

Figure 6.13: k contours of (a) Periodic Flow Simulation,
(b) Random Disturbance Inlet Data simulation
(c) Level 1 and (d) Level 3 simulation, over the first half of flow domain

On the contrary, the use of DFG inlet data results in a prediction of the k field that correlates significantly better with that obtained in the PBC simulation. The Level 1 simulation displays a smaller region over which k achieves its maximum value than in the PBC simulation, and this is improved when multiple turbulence scales are used, as can be seen in

Figure 6.13 (d) for the Level 3 data.

In both Level 1 and Level 3 simulations, the LES results obtained using DFG inlet data have produced a flow field with more rapid growth of turbulence energy and reduced turbulence dissipation in the region close to the inlet than the PBC simulation, resulting in higher levels of turbulence in the flow right from the inlet plane. It is believed that the associated higher rates of momentum mixing between the near-wall flow and the outer flow have made the boundary layer on the lower wall more resistant to the adverse pressure gradient present, causing a delay in the separation of the flow ($x_{sep}/h = 0.09$ for PBC and $x_{sep}/h = 0.27$ for DFG Level 3).

Finally, some comments may be made about the computational cost reduction of the new approach presented here for the DFG implementation. As was mentioned by Veloudis et al. [182], the cost of using a multi-scale DFG approach for LES inlet condition generation increases significantly with the number of turbulence scales used. Using the implementation approach adopted in [82], it was concluded that multi-scale DFG may not be cost effective in many cases, with a computational time required too large to be able to use it for 'on-the-fly' generation of inlet data.

The modification proposed here, of a frequency domain convolution reduces the computational time required per LES timestep significantly. This can be seen in Table 6.3, where the computational time for the previous [82] method and the percentage change in the computational time achieved by the current convolution method are presented. As expected, when the working array size required to generate the filter is relatively small, as in Level 1, the convolution procedure in the time domain can be quicker [164] since the array padding required by the FFT approach leads to inefficiencies. However, when the number of the array filter elements increases, due to the larger number of turbulence scales being used, the time domain method becomes disproportionally slow. At Level 3 the frequency domain method leads to a 70% reduction in time compared to the time-domain method. This reduction in computational time has no adverse effect on accuracy, as can be seen by the the third column of Table 6.3 which shows that the maximum difference recorded between the values calculated for the provisional signal by the two methods was below 1.0% for all cases.

Table 6.3: Signal convolution computational time

Simulation	Previous method [82] (sec)	New method (change in comp. time %)	max Diff. (%)
Level 1	1.84	+100	0.2
Level 2	8.07	-43	0.9
Level 3	44.32	-72	0.9

In addition, as described above, by employing the technique where a longer timestep is used, in the DFG method (Δt_{DFG}), than the LES (Δt), n_t and hence the size of the r_m working array corresponding to the streamwise direction, was reduced considerably. The effect of the associated interpolation to produce data at Δt fine intervals, on the autocorrelation R_{uu} of the produced signal can be seen in Figure 6.14. The data presented in Figure 6.14 were extracted from the point corresponding to $y = 0.0012$m, where Level 2 and Level 3 data sets made use of the same turbulence scales. 'Original' data corresponds to the signal generated by the DFG algorithm and 'Interpolated' data corresponds to the data that was to be used in the Level 1, 2 and 3 simulations. In all cases, it can be seen that the autocorrelation produced by the interpolated signal compares well with that produced by the original signal. The effect of the time interpolation on the generated time scales is a slight increase in all cases. The difference in the produced T_x is 5.42% for the Level 1, 4.03% for the Level 2 and 2.22% for the Level 3 data. Hence, it can be concluded that the differences are relatively small and the time savings achieved using this method outweigh these minor adverse effects.

The frequency domain deconvolution in combination with the data interpolation resulted in significant cost reduction, which was reflected on the total CPU time required. It is worth noting that the total CPU time per flow-through time of the PBC simulation was 43,000 sec and for the simulation with the DFG (Level 3 which was the most expensive) it was 45,600 sec, i.e. only 6.0% more and hence significantly cheaper than the precursor method.

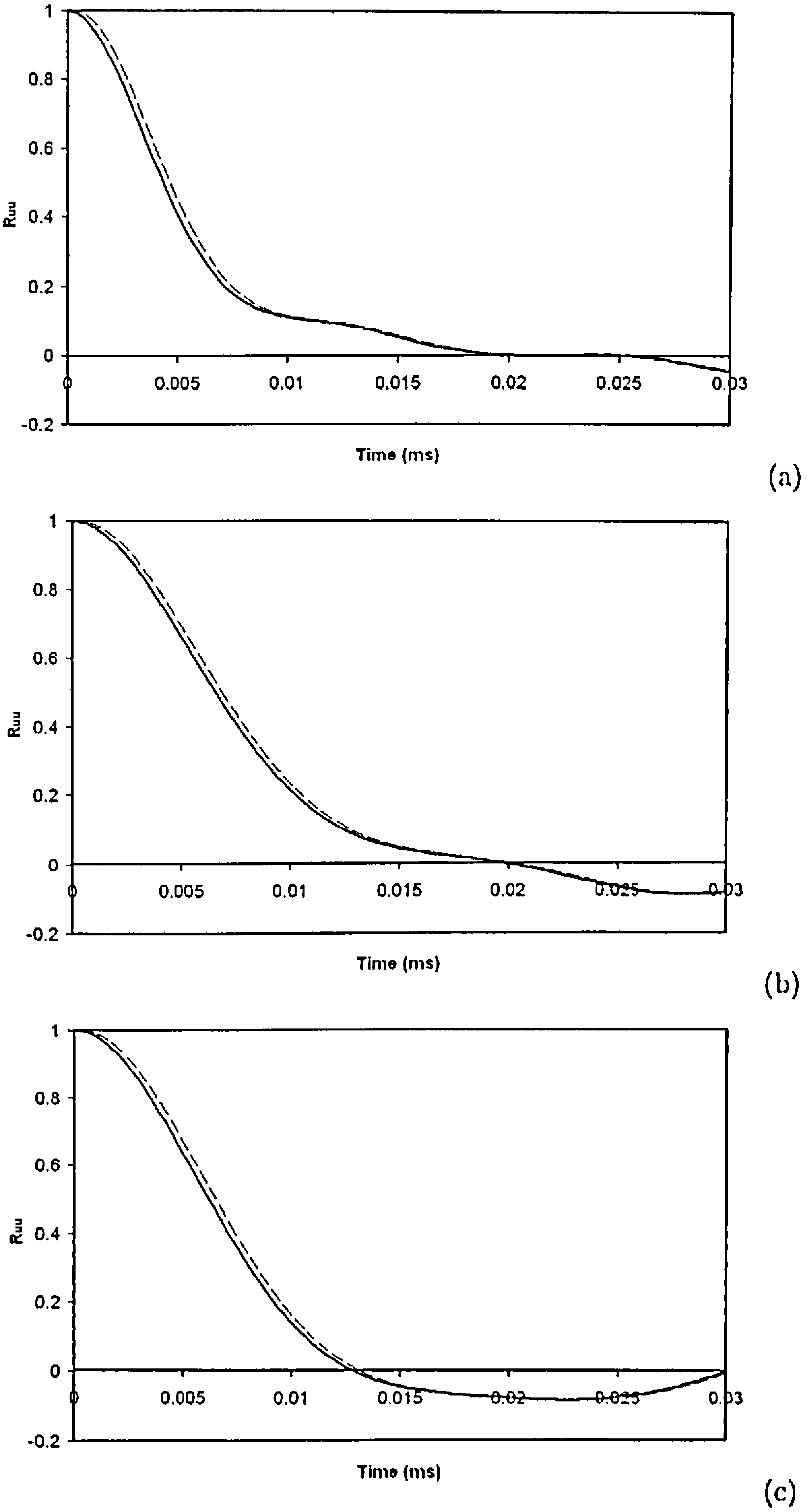

Figure 6.14: R_{uu} of Level 1 (a), Level 2 (b) and Level 3 simulation (c) (solid line: original data, dashed line: interpolated data)

Chapter 7

Conclusions and Future Work

7.1 Review of aim and objectives

The aim of the present study was to explore the possibilities of improvement of SGS modelling and inlet boundary conditions for LES of wall-bounded flows. Based on considerations presented and discussed in section 1.5, the two major tasks were the following:

1. The investigation of the potential of SGS models based on the information directly from the subgrid scales.
2. The identification and development of a cost effective algorithm for the generation of realistic inflow boundary conditions.

The performance of the first task involved the achievement of the following objectives:

1. Implementation of a transport equation model that allows for near-wall effects.
2. Exploration of alternative SGS model formulations and investigation of their potential to improve the accuracy of LES of wall-bounded flows.
3. Testing and comparison of the implemented models with others on a number of flow cases that will indicate the advantages and disadvantages of their use.

Similarly, the objectives set for the second task were:

1. Identification of an appropriate method
2. Identification and development of areas where further improvement is possible.
3. Testing and comparison of the original and final method.

7.2 On SGS modelling

The first objective set for the investigation of SGS modelling based on subgrid scale quantities was met by the implementation of the k_{sgs}-equation model developed by Yoshizawa and Horiuti [195], in combination with a number of near-wall damping functions to allow for the near-wall effects, as described in Chapter 3. The near-wall damping functions implemented in the code were those proposed by van Driest [181], Piomelli [144], Yoshizawa [196] and Inagi [68], covering different approaches including both functions that made use of geometric parameters as well as functions that were based purely on information extracted from the flow field. The study described in section 4.1.3 indicated that k_{sgs}-equation model performed better with the Yoshizawa near-wall damping function [196] and therefore it was employed in combination with this function in the rest of the simulations performed. The same study showed that the Smagorinsky model performed better with the Piomelli near-wall damping function [144].

The second objective was met by the development of a new SGS model, based on the calculation of the rate of energy dissipation directly from an assumed energy spectrum. The development and implementation of this model was presented in section 3.2.3, where it was shown that a k_{sgs}-equation based SGS model can be improved further by the new treatment of the dissipation term. In terms of near-wall treatment, a series of tests indicated that the model performed better with the Inagi near-wall damping function [68] and therefore it was used in combination with this for the rest of the simulations performed.

The third objective was met by the performance of a series of tests in two stages. The first stage involved the use of Smagorinsky, MS, k_{sgs}-equation and ESD model on a series of channel flow cases, covering a Re_{τ} range from 180 to 1,800. The main conclusions drawn from this study were the following:

1) ESD model presented the best results overall, followed by the k_{sgs}-equation model. This confirmed the superiority of the subgrid-scale based models over models based on the resolved scales.

2) MS model proved superior to Smagorinsky in case 2, in agreement with published results on the same case [196]. Furthermore, this agreement was an indication of the correct implementation of the Yoshizawa NW model.

3) In terms of velocity distribution, ESD model proved consistent over the range of

Re_τ considered, giving the most accurate results in the majority of cases. The accurate C_f prediction played an important role as its under-prediction by the rest of the models resulted in an offset of the U^+ distribution.

4) In terms of Reynolds stresses, ESD model's prediction of $\overline{u'u'}$ was more accurate in all cases considered while $\overline{v'v'}$ and $\overline{w'w'}$ were at the same levels as these obtained by the k_{sgs}-equation model. The latter proved more accurate than Smagorinsky model mainly in the prediction of $\overline{v'v'}$ and $\overline{w'w'}$.

5) In terms of coherent structures, the increased dissipation introduced by the Smagorinsky resulted in a decrease of turbulence activity that reflected on the coherent structures present in the flow. Hence, compared with the rest of the models, fewer structures were observed, with geometrical features that were not always consistent with observations made in experiments. In contrast, the coherent structures obtained by ESD and the rest of the models tested were in a good agreement with experimental data.

6) Lumley's triangles confirmed the physical realisability of all models considered.

The second stage of the SGS models testing was based on the results of the first stage, in terms of combinations of SGS models and near-wall damping functions employed. Hence, the Smagorinsky model with Piomelli near-wall damping function [144] and the k_{sgs}-equation model with the Inagi near-wall damping function [68] were selected to be further investigated on a wing body junction case. This case imposed a number of challenges on the SGS models, discussed in section 5.6.3. The main conclusions drawn were the following:

1) Both models predicted the same flow behaviour, dictated by the presence of a bound vortex around the wing geometry. However, each model predicted different flow characteristics due to the different levels of dissipation introduced to the flow by each SGS model. In both cases, the extent of the backflow region was over-predicted.

2) The variation of vortex position in the upstream symmetry plane, with D/δ^* was in accordance to the behaviour observed in the experiments.

3) Smagorinsky model predicted a system of vortices upstream of the wing leading edge, which was statistically stationary in time and in space and similar in pattern

to observation made by Baker [9]. Its position was further upstream compared to experimental data of Olcmen and Simpson [131] and it is believed that this caused the whole formation of the horseshoe vortex to be translated further away from the wing surface. Furthermore, the predicted vortex strength was significantly larger.

4) The k_{sgs}-equation model predicted the periodic generation of vortices upstream of the wing that move downstream to reach their peak at a location that was close to the vortex position observed in the experiments. The time-averaged flow field of this process indicated a vortical structure in the upstream symmetry plane similar to that observed by Olcmen and Simpson [131], at a position close to the experimental value. This vortex resulted in the formation of a bound vortex system that was closer to the wing surface comparing to the Smagorinsky results.

5) The discrepancies between the experimental and LES results were attributed to the state of the oncoming boundary layer and the turbulence activity predicted in the region. The role of the local grid resolution was also pointed out as a parameter that could be improved.

6) Both SGS models under-predicted the normal and shear stresses in the plane upstream of the wing leading edge and over-predicted them at the constant x-plane close to the wing trailing edge. The over dissipative character of Smagorinsky model resulted in an excessive damping of any turbulent fluctuation upstream of the wing resulting in the stable vortical structure described above. On the contrary, the reduced dissipative action of the k_{sgs}-equation model resulted in the maintenance of more unsteadiness in the flow that eventually resulted in a more accurate flow field.

7) In terms of the bound vortex characteristics, in the case of Smagorinsky model, the vortex was further away from both the wing surface and the bottom wall, resulting in a small interaction with the boundary layer. In the case of the k_{sgs}-equation model, the bound vortex was closer to the wing surface and to the lower wall, interacting heavily with the boundary layers. In both cases, secondary vortices were observed in the junction region on the side of the wing surface, resulting in flow separation.

8) Pressure distribution was affected by the flow separation on the side of the wing surface and by the formation of a wake at the rear end of the wing section. In the case of Smagorinsky model, the flow separation over the rear part of the wing and the wake formed further downstream affected adversely the accuracy of the C_P distribution. The early flow separation observed in the k_{sgs}-equation model LES compromised the accuracy of the C_P distribution up to $x = 1.5T$. Further downstream, the results were close to the experimental data.

9) Despite the coarse grid employed, the k_{sgs}-equation model gave a more realistic solution overall. This was an indication of the ability of this type of SGS modelling to reproduce more accurately the turbulent flow field with a coarse grid.

Unfortunately, due to time limitations, the ESD model presented and tested in section 3.2.3 and 4.2 respectively, was not further tested on the wing-body junction.

7.3 On the multi-scale DFG algorithm

The first objective set for the investigation of an inflow conditions generation algorithm was met by the the identification of the DFG algorithm proposed by Klein et al. [82], as the method had the potential to be further developed to allow for generation of inlet conditions for wall-bounded flows. The advantages of this method comparing to other approaches were discussed in the introduction of Chapter 6.

The second objective was met by the identification of areas of further development, discussed and described in section 6.2. These were focused on the ability of the code to produce data that could be used for wall-bounded flows and on the computational cost. Regarding the first area of interest, improvements were made by the adoption of a multi-filtering approach which allowed for the generation of inlet data with spatially varying turbulence scales. However, as discussed in section 6.2.2, this approach increased the computational cost. Therefore, in order to reduce the computational time required, frequency domain convolution was adopted, in combination with the introduction of a simple data interpolation technique. Both of these modifications were described in section 6.2 and discussed in section 6.4.

The new implementation of the DFG-based LES inlet condition approach highlighted the following main points:

1) Considerable savings in computational time can be achieved by the implementation of frequency domain convolution and data interpolation between successive timesteps. This allows for the adoption of a more detailed description of turbulence scales at minor cost increase.

2) Although the strength of spatial variation in the turbulence scales was relatively strong (a factor of 4), this did not prove problematic for the DFG method using a fixed Gaussian correlation function shape.

The third objective was met by the comparison of the original and the modified algorithm on the same test case. The case that was selected was a channel geometry with periodic constrictions, as described in section 6.3.1. A periodic boundary conditions, PBC, LES of the same test case was used to produce the required first and second order statistics and to be used as a reference data. Three sets of inlet data were generated, using the original DFG algorithm, a 6-filter and a 12-filter DFG methodology.

Comparisons between the target PBC LES calculation and three DFG-driven LES calculations of the same flow highlighted the following main points:

1) The DFG-driven LES calculations using spatially varying scales at inlet predicted the test problem better than a constant scale simulation on the evidence of both mean, but particularly turbulence profiles. The selection of a representative constant scale could still produce inlet data of adequate quality, although this outcome will probably be flow dependent.

2) Gaussian autocorrelation shape assumed by the DFG will necessarily differ in general from that determined by the flow physics, and this limits the ability of the DFG method to reproduce turbulence structures at an inlet plane with complete fidelity compared to, say, a precursor calculation.

3) The use of spatially varying turbulence scales in the DFG input cannot remove this restriction, but does allow the integral scale of the Gaussian correlation influenced time-series to match the local turbulence structure.

4) Even the increase of spatial resolution of turbulence scales investigated here did not allow the initial development of the boundary layer evolving from the inlet plane to match with the target PBC simulation. This may well be due to the

use of a Gaussian correlation function shape in the DFG method and it would be worthwhile to explore a modified DFG, which allowed an alternative correlation function shape more suited to strongly inhomogeneous flow.

7.4 Recommendations for future work

The work performed on the present study was focused on two very important subjects for the further development of LES; the use of transport equation models to improve the accuracy of SGS modelling and the employment of algorithms to produce artificial unsteady inlet data appropriate for LES use.

Regarding the first subject, the following recommendations for future work are given:

1) Further testing of the proposed ESD model. Time limitations restricted the testing of the proposed ESD model only to channel flows. A series of further tests involving more complex and transient flow features should be performed to access the performance of the model and identify any areas where further improvements may be required.

2) Further investigation of the ESD model. The model improves the treatment of the dissipation term in the k_{sgs}-equation, which proves to be very important, especially when the model is used on wall-bounded flows. In terms of further investigation, the effects of more realistic energy spectrums should be accounted for by the introduction of Pope's spectrum [146] or by the estimation of the spectrum shape based on flow quantities. However, any development in these two directions should also consider the cost factor since, even in its initial formed presented here, the model is about 50% more expensive than the Yoshizawa and Horiuti k_{sgs}-equation model. In that respect, the use of an alternative root identification algorithm could be beneficial.

3) The current study only considered the use of near-wall model as a viscous wall treatment. Other approaches such as the introduction of extra terms in the k_{sgs}-equation could improve the performance of the model in flow regions where low Reynolds number effects are more pronounced.

4) Due to time limitations and computational resources available, the application of

the Smagorinky model and the k_{sgs}–equation model on the wing-body junction case was limited to the use of a single grid. Further assessment of the two models on refined grids would be beneficial for the evaluation of the grid resolution dependence of the results.

Regarding the second subject, the following recommendations for future work are given:

1) The conclusion of the work performed on the DFG algorithm indicated that the adoption of the Gaussian distribution can limit its accuracy. Therefore it is proposed that at a first stage, future work should involve use of alternative, more realistic autocorrelation distributions. Di Mare and Jones [40] have already shown promising results using alternative forms of the autocorrelation function. At a second stage, variable forms of autocorrelation function should be considered, based on flow properties and location.

2) Extension of the turbulence scale spatial variation in two dimensions. These could make the algorithm more attractive to cases without any periodicity direction.

Appendix

$$\vec{\nabla}\xi_{i,J,K} = \frac{V_{I,J,K}\left(\vec{A}_{i-1,J,K} + \vec{A}_{i,J,K}\right) + V_{I-1,J,K}\left(\vec{A}_{i,J,K} + \vec{A}_{i+1,J,K}\right)}{4V_{I,J,K}V_{I-1,J,K}} \tag{7.1}$$

$$\vec{\nabla}\xi_{I,j,K} = \frac{V_{I,J,K}\left(\vec{A}_{i,J-1,K} + \vec{A}_{i+1,J-1,K}\right) + V_{I,J-1,K}\left(\vec{A}_{i,J,K} + \vec{A}_{i+1,J,K}\right)}{4V_{I,J,K}V_{I,J-1,K}} \tag{7.2}$$

$$\vec{\nabla}\xi_{I,J,k} = \frac{V_{I,J,K}\left(\vec{A}_{i,J,K-1} + \vec{A}_{i+1,J,K-1}\right) + V_{I,J,K-1}\left(\vec{A}_{i,J,K} + \vec{A}_{i+1,J,K}\right)}{4V_{I,J,K}V_{I,J,K-1}} \tag{7.3}$$

where V denotes the cell volume and $\vec{A}$ the area vector. Capital letter indices denote cell centre values and small letter indices cell surface values.

Bibliography

[1] I. E. Abdalla. *Numerical studies of separated boundary layer transition on a first plate with blunt leading edge.* PhD thesis, Loughborough Univerisity, 2004.

[2] R. J. Adrian. On the role of conditional averages in turbulence theory. In G. Pateson and J. Zakin, editors, *Turbulence in Liquids*, pages 322–332, Princeton, NJ, 1977. 4th Biennal Symposium on Turbulence in Liquids, Science Press.

[3] S. R. Ahmed, G. Ramm, and G. Faltin. Some salient features of the time-averaged ground vehicle wake. *SAE Paper*, (840300), 1984.

[4] K. Akselvoll and P. Moin. Large eddy simulation of turbulent confined co-annular jets. *Journal of Fluid Mechanics*, 315:387–411, 1996.

[5] N. Andersson, L. E. Erikson, and L. Davidson. Investigation of an isothermal Mach 0.75 jet and its radiated sound using large-eddy simulation and Kirchhoff surface integration. *International Journal of Heat and Fluid Flow*, 26:393–410, 2005.

[6] D. D. Apsley and M. A. Leschziner. Investigation of advanced turbulence models for the flow in a generic wing-body junction. *Flow, Turbulence and Combustion*, 67:25–55, 2001.

[7] J. G. Bain and C. A. J. Fletcher. Predictions of generic wing-body junction flow behaviour. *Journal of Wind Engineering and Industrial Aerodynamics*, 50:19–30, 1993.

[8] C. J. Baker. The laminar horseshoe vortex. *Journal of Fluid Mechanics*, 95:347–368, 1979.

[9] C. J. Baker. The turbulent horse shoe vortex. *Journal of Wind Engineering and Industrial Aerodynamics*, 6:9–23, 1980.

[10] C. J. Baker. The position of points of maximum and minimum shear stress upstream of cylinders mounted normal to flat plates. *Journal of Wind Engineering and Industrial Aerodynamics*, 18:263–274, 1985.

[11] E. Balaras and C. Benocci. Large eddy simulations of flow in a square duct. University of Missouri Rolla, 1992. 13th Symposium of Turbulence.

[12] J. Bardina, J. H. Ferziger, and W. C. Reynolds. Improved subgrid model for large eddy simulation. *AIAA Journal*, (80-1357), 1980.

[13] G. Batchelor. *The theory of homogeneous turbulence.* Cambridge University Press, Cambridge, UK, 1953.

[14] P. Batten, U. Goldberg, and S. Chakravarthy. Interfacing statistical turbulence closures with Large Eddy Simulation. *AIAA Journal*, 42:485–492, 2004.

[15] L. Belik. The secondary flow about circular cylinders mounted normal to a flat plate. *Aerodynamics Quarterly*, 24:47–54, 1973.

[16] P. Birkby and G. J. Page. Numerical predictions of turbulent underexpanded sonic jets using a pressure-based methodology. *IMECH*, 215 Part G:165–173, 2001.

[17] J. R. Chaznov. Simulation of the Kolmogorov inertial subrange using an improved subgrid model. *Physics of Fluids*, A 3 (1):188–200, 1990.

[18] H. Choi and P. Moin. Effects of the computational time step on numerical solutions of turbulent flow. *Journal of Computational Physics*, 113:1–4, 1994.

[19] J. P. Chollet and M. Lesieur. Parameterisation of small scales of three-dimensional isotropic turbulence utilizing spectral closures. *Journal of Atmospheric Sciences*, 38:2747–2757, 1981.

[20] M. S. Chong, A. E. Perry, and B. J. Cantwell. A general classification of three-dimensional flow fields. *Physics of Fluids*, A 4:765–777, 1990.

[21] R. A. Clark, J. H. Fersiger, and W. C. Reynolds. Evaluation of subgrid-scale models using an accurately simulated turbulent flow. *Journal of Fluid Mechanics*, 91:1–16, 1979.

[22] D. Coles. The law of the wake in the turbulent boundary layer. *Journal of Fluid Mechanics*, 1:191–226, 1956.

[23] G. Comte-Bellot. Ecoulement turbulent ntre deux parois paralleles. Technical Report 419, Publications Scientifiques et Techniques du Ministere de l'Air, 1965.

[24] M. Cook. *Flight Dynamics Principles.* Arnold, 1997.

[25] L. Davidson. Large Eddy Simulations: a note on derivation of the equations for the subgrid turbulent kinetic energies. Intern shrift 97/12, Department of Thermo and Fluid Dynamics, Chalmers University of Technology, Sweden, 1997.

[26] L. Davidson. LES of recirculating flow without any homogeneous direction: a dynamic one-equation subgrid model. In K. Hanjalic and T. W. J. Peeters, editors, *2nd International Symposium on Turbulence Heat and Mass Transfer*, pages 481–490. Delft Univerity Press, 1997.

[27] R. B. Dean. Reynolds number dependence of skin friction and other bulk flow variables in two-dimensional rectangular duct flow. *ASME Journal of Fluids Engineering*, 100:215–223, June 1978.

[28] J W. Deardorff. A numerical study of three-dimensional turbulent channel flow at large Reynolds numbers. *Journal of Fluid Mechanics*, 41:453–480, 1970.

[29] J. W. Deardorff. Three-dimensional numerical study of the height and mean structure of a heated planetary boundary layer. *Boundary-Layer Meteorology*, 7:81–106, 1974.

[30] J. W. Deardorff. Stratocumulus-capped mixed layers derived from a three-dimensional model. *Boundary-Layer Meteorology*, 18:495–527, 1980.

[31] A. Dejoan and R. Schiestel. LES of unsteady turbulence via an one-equation subgrid-scale transport model. *International Journal of Heat and Fluid Flow*, 23:398–412, 2002.

[32] H. Van der Ven. A family of large eddy simulation filters with non-uniform filter widths. *Physics of Fluids*, 7 (5):1171–1172, 1995.

[33] W. J. Devenport and R. L. Simpson. Turbulent structures near the nose of a wing-body junction. In *Proceedings of 19th AIAA Fluid Dynamics and Plasma Dynamics Lasers Conference*, number AIAA-87-1310, Honolulu, 1987. AIAA, AIAA.

[34] W. J. Devenport and R. L. Simpson. LDV measurements in the flow past a wing-body junction. In *Proceedings of 4th International Symposium of Applied Laser Anemometry in Fluid Mechanics*, number 2.3., Lisbon, Portugal, 1988.

[35] W. J. Devenport and R. L. Simpson. Time-dependent structure in wing-body junction flows. In F. Durst, B. Launder, F. Schmidt, and J. Whitelaw, editors, *Turbulent Shear Flows*, volume 6, pages 232–248. Springer, Heidelberg, 1989.

[36] W. J. Devenport and R. L. Simpson. The turbulence structure near an appendage-body junction. In *Proceedings of 17th Symposium of Naval Hydrodynamics*, pages 461–477, The Hague, Netherlands, 1989. Washington DC: Natl. Acad.

[37] W. J. Devenport and R. L. Simpson. An experimental investigation of the flow past an idealized wing-body junction. Final Report VPI-AOE-172, Department of of Aerospace and Ocean Engineering, VPI and SU, 1990.

[38] W. J. Devenport and R. L. Simpson. Time-dependent and time-averaged turbulence structure near the nose of a wing-body junction. *Journal of Fluid Mechanics*, 210:23–55, 1990.

[39] W. J. Devenport and R. L. Simpson. Flow past a wing-body junction - experimental evaluation of turbulence models. *AIAA Journal*, 4(30):873–881, 1992.

[40] L. di Mare and W. P. Jones. Algebraic and operator methods for generation of inlet data for LES and DNS. In *Fourth International Symposium on Turbulence and Shear Flow Phenomena*, number 266, Williamsburg, 2005.

[41] S. C. Dickinson. An experimental investigation of appendage-flat plate junction flow. Technical Report DTNSRDC-886/051, David W. Taylor Naval Ship Research and Development Center, August 1986.

[42] D. Drikakis. Advances in turbulent flow computations using high-resolution methods. *Progress in Aerospace Sciences*, 39:405–424, 2003.

[43] D. Drikakis, F. Gristein, and D. Youngs. On the computation of instabilities and symmetry-breaking in fluid mechanics. *Progress in Aerospace Sciences*, 41:609–641, 2005.

[44] D. Drikakis and W. Rider. *High-Resolution Methods for Incompressible and Low-Speed Flows.* Computational Fluid and Solid Mechanics. Springer, 1st edition, 2004.

[45] P. Druault, S. Lardeau, J. P. Bonnet, F. Coiffet, J. Delville, E. Lamballais, J.F. Largeau, and L. Perret. Generation of three-dimensional turbulent inlet conditions for large eddy simulation. *AIAA Journal*, 42 (3):447–456, 2004.

[46] F. Ducros, P. Comte, and M. Lesieur. Large eddy simulation of transition to turbulence in a boundary layer developing spatially over a flat plate. *Journal of Fluid Mechanics*, 326:1–36, 1996.

[47] J. K. Eaton and J. P. Johnston. Turbulent flow reattachment: an experimental study of the flow and structure behind a backward-facing step. Technical Report MD-39, Stanford University, 1980.

[48] J. H. Ferziger and M. Peric. *Computational methods for fluid dynamics.* Springer, 3rd edition.

[49] J. L. Fleming, R. L. Simpson, J. E. Cowling, and W. J. Devenport. An experimental study of a turbulent wing-body junction and wake flow. *Experiments in Fluids*, 14:366–378, 1993.

[50] R. Friedrich, T. J. Huttl, M. Manhart, and C. Wagner. Direct numerical simulation of incompressible turbulent flows. *Computers and Fluids*, 30:555–579, 2001.

[51] R. Friedrich and F. Nieuwstadt. LES of pipe flows. In *ERCOFTAC Bulletin*, volume 22, pages 19–25. 1994.

[52] Retrieved from. cfd.me.umist.ac.uk, accessed on May 2005.

[53] C. Fureby, N. Alin, N. Wikstrom, S. Menon, N. Svanstedt, and L. Persson. Large Eddy Simulation of high-Reynolds-number wall-bounded flows. *AIAA Journal*, 42(3):457–468, March 2004.

[54] M. Germano. Turbulence: The filtering approach. *Journal of Fluid Mechanics*, 238:325–336, 1992.

[55] M. Germano, U. Piomelli, P. Moin, and W. H. Cabot. A dynamic subgrid-scale eddy viscosity model. *Physics of Fluids*, 3 (7):1760–1765, 1991.

[56] M. Germano, U. Piomelli, P. Moin, and W. H. Cabot. A dynamic subgrid-scale eddy viscosity model. In *Procedures of Summer Workshop*, Stanford CA, 1991. Centre of Turbulence Research.

[57] S. Ghosal. An analysis of the numerical errors in large eddy simulations of turbulence. *Journal of Computational Physics*, 125 (1):187–206, 1996.

[58] S. Ghosal, T. Lund, P. Moin, and K. Akselvoll. A dynamic localization model for Large Eddy Simulation of turbulent flows. *Journal of Fluid Mechanics*, 286:229–255, 1995.

[59] P. A. Gnoffo. An upwind-biased, point-implicit relaxation algorithm for viscous, compressible prefect gas flows. Technical Paper 2953, NASA, 1990.

[60] T. Goutorbe, D. Laurence, and V. Maupu. A priori test of a subgrid scale stress tensor model including anisotropy and backscatter effects. In P. R. Voke, L. Kleiser, and J. P. Chollet, editors, *Direct and Large Eddy Simulation*, volume 1, pages 121–131. Kluwer, 1994.

[61] G. Grotzbach. Direct numerical and large eddy simulations of turbulent channel flows. In N. P. Chereminisoff, editor, *Encyclopaedia of Fluid Mechanics*, volume 6, pages 1337–1391. Gulf, 1987.

[62] Bob Haimes. *VISUAL3 User's and Programmer's Manual.* Massachusetts Institute of Technology, rev. 2.35 edition, December 1998.

[63] C. Hartel and L. Kleiser. Analysis and modelling of subgrid-scale motions in near-wall turbulence. *Journal of Fluid Mechanics*, 356:327–352, 1998.

[64] C. Hartel, L. Kleiser, F. Unger, and R. Friedrich. Subgrid-scale energy transfer in the near wall region of turbulent flows. *Physics of Fluids*, 6 (9):3130–3143, 1994.

[65] S. Hassid and M. Poreh. A turbulent energy model for flows with drag reduction. *Journal of Fluids Engineering*, (75-FE-H).

[66] K. Horiuti. Large Eddy Simulation of turbulent channel flow by one-equation modelling. *Journal of the Physical Society of Japan*, 54 (8):2855–2865, 1985.

[67] J. Hunt, A Wray, and P. Moin. Eddies, stream and convergence zones in turbulent flows. Technical Report CTR-S88, Center for Turbulence Research, Stanford, USA, 1988.

[68] M. Inagi, T. Kondoh, and Y. Nagano. A mixed-time-scale SGS model with fixed model-parameters for practical LES. *ASME Journal of Fluids Engineering*, 127:1–13, 2005.

[69] K. Iwamoto. Database of fully developed channel flow. THTLAB Internal Report ILR-0201, Department of Mechanical Engineering, The University of Tokyo, Hongo, Bunkyo-ku, Tokyo 113-8656, Japan, June 2002.

[70] J. Jeong, F. Hussain, W. Schoppa, and J. Kim. Coherent structures near the wall in a turbulent channel flow. *Journal of Fluid Mechanics*, 332:185–214, 1997.

[71] J. Jimenez and P. Moin. The minimal flow unit in near-wall turbulence. *Journal of Fluid Mechanics*, 225:213–240, 1991.

[72] J. Jimenez and A. Pinelli. The autonomous cycle of near-wall turbulence. *Journal of Fluid Mechanics*, 389:335–359, 1999.

[73] J. Jimenez and M. P. Simens. Low-dimensional dynamics of a turbulent wall flow. *Journal of Fluid Mechanics*, 435:81–91, 2001.

[74] J. Jovanovic. *The statistical dynamics of turbulence.* Springer Verlag, 2004.

[75] H. J. Kaltenbach. Large Eddy Simulation of flow in a plane, assymetric diffuser. In *Annual Research Briefs*, pages 101–. Center of Turbulence Research, Stanford University, Center of Turbulence Research, Stanford University, 1993.

[76] H. J. Kaltenbach and H. Choi. Large eddy simulation of flow around an airfoil on a structured mesh. Annual research briefs, Cetre for Turbulence Research, Stanford, CA, *1995.*

[77] A. Keating and U. Piomelli. Synthetic generation of inflow velocities for large eddy simulation. In *34th AIAA Fluid Dynamics Conference*, pages 2004–2547. AIAA, 2004.

[78] J. Kim, P. Moin, and R. Moser. Turbulence statistics in fully developed channel flow at low Reynolds number. *Journal of Fluid Mechanics*, 177:133–166, 1987.

[79] W. W. Kim and S. Menon. An unsteady incompressible Navier-Stokes solver for large eddy simulation of turbulent flows. *International Journal of Numerical Methods in Fluids*, 31:983–, 1999.

[80] M. Klein, A. Sadiki, and J. Janicka. Influence of boundary conditions on the direct numerical simulation of a plane turbulent jet. In *Proceedings of TSFP2*, volume 1, pages 401–406, 2001.

[81] M. Klein, A. Sadiki, and J. Janicka. Influence of the inflow conditions on the direct numerical simulation of primary break-up of liquid jets. In *Proceedings of ILASS-17-Europe*, volume 1, pages 475–480, 2001.

[82] M. Klein, A. Sadiki, and J. Janicka. A digital filter based generation of inflow data for spatially developing direct numerical or large eddy simulations. *Journal of Computational Physics*, 186:652–665, 2003.

[83] L. S. G. Kovasznay. Spectrum of locally isotropic turbulence. *Journal of Aeronautical Sciences*, 15:745–753, 1948.

[84] R. H. Kraichnan. Eddy viscosity in two and three dimensions. *Journal of Atmospheric Sciences*, 33:1521–1536, 1976.

[85] S. Krajnovic and L. Davidson. Large-eddy simulation of the flow around a surface-mounted cube using adynamic one-equation subgrid model. In S. Banerjee and J. Eaton, editors, *The First International Symposium on Turbulence and Shear Flow Phenomena*, pages 741–746, New York, Wallingford, UK, 1999. Begell House Inc.

[86] S. Krajnovic and L. Davidson. Large eddy simulation of the flow around a three-dimensional bluff body. In *39th AIAA Aerospace Sciences Meeting and Exhibit*, number 2001-0432, Reno, Nevada, USA, 2001.

[87] S. Krajnovic and L. Davidson. A mixed one-equation subgrid model for large eddy simulation. *International Journal of Heat and Fluid Flow*, 23:413–425, 2002.

[88] S. Krajnovic, D. Mueller, and L. Davidson. Comparison of two one-equation subgrid models in recirculating flows. In P. V. Voke, N. D. Sandham, and L. Kleiser, editors, *Direct and Large Eddy Simulation*, volume 3, pages 63–74. Kluwer, 1999.

[89] C. K. G. Lam and K. Bremhorst. Modified form of the k-epsilon model for predicting wall turbulence. *ASME Journal of Fluids Engineering*, 103:456–460, 1981.

[90] C. De Langhe, B. Merc, K. Lodefier, and E. Dick. Very-large-eddy simulation subgrid modelling using the statistical mechanics renormalization group. Sendai, 2003. 3rd International Symposium on Turbulence and Shear Flow Phenomena.

[91] B. E. Launder and B. I. Sharma. Application of the energy-dissipation model of turbulence to the calculation of flow near a spinning disk. *Letters on Heat Mass Transfer*, 1:131–138, 1974.

[92] B. E. Launder and D. B. Spalding. The numerical computation of turbulent flows. *Computer Methods in Applied Mechanical Engineering*, 3:269–289, 1974.

[93] H. Le, P. Moin, and J. Kim. Direct numerical simulation of turbulent flow over a backward-facing step. *Journal of Fluid Mechanics*, 330:349–374, 1997.

[94] S. Lee, S. K. Lele, and P. Moin. Simulation of spatially evolving turbulence and the application of Taylor's hypothesis in compressible flow. *Physics of Fluids*, A 4 (7):1521–1530, 1992.

[95] C. E. Leith. Stochastic backscatter in a subgrid scale model: Plane shear mixing layer. *Physics of Fluids*, A 2 (3):297–299, 1990.

[96] A. Leonard. Energy cascade in large eddy simulation of turbulent fluid flow. *Advances in Geophysics*, 18A:237–248, 1974.

[97] M. A. Leschziner and D. D. Apsley. Advanced turbulence modelling of the flow in a generic wing-body junction. In *European Congress on Computational Methods in Applied Sciences and Engineering*, Barcelona, 11-14 September 2000. ECCOMAS.

[98] M. Lesieur. *Turbulence in fluids.* Kluwer, 3rd edition, 1997.

[99] M. Lesieur, P. Begou, P. Comte, and O. Metais. Vortex recognition in numerical simulations. *ERCOFTAC Bulletin*, 46:25–28, 2000.

[100] D. K. Lilly. The representation of small-scale turbulence in numerical simulation experiments. In *Proceedings of the IBM Scientific Computing Symposium on Environmental Sciences*, Yorktown Heights, USA, 1967.

[101] D. K. Lilly. A proposed modification on the Germano subgrid-scale closure method. *Physics of Fluids*, A 4:633–635, 1992.

[102] S. Liu, C. Meneveau, and J. Katz. On the properties of similarity subgrid scale models as deduced from measurements in turbulent jet. *Journal of Fluid Mechanics*, 275:83–119, 1994.

[103] J. Lumley. The structure of inhomogeneous turbulent flows. In A. M. Yaglon, V. I. Tatarski, and Nauka, editors, *Atmospheric Turbulence and Radio Wave Propagation*, pages 166–178. Moscow, 1967.

[104] J. L. Lumley. Computational modelling of turbulent flows. In *Advances in applied mechanics*, volume 18, pages 123–176, New York, 1978. Academic Press, Inc.

[105] J. L. Lumley. Coherent structures in turbulence. In *Transition and turbulence*, pages 215–242. Academic Press, University of Wisconsin, October 1980.

[106] T. S. Lund, S. Ghosal, and P. Moin. Numerical experiments with highly variable eddy viscosity models. In S. A. Ragale and U. Piomelli, editors, *Engineering applications of large eddy simulation*, volume 162 of *FED*. 1993.

[107] T. S. Lund and P. Moin. Large eddy simulation of a concave wall boundary layer. *International Journal of Heat and Fluid Flow*, 17:290–, 1996.

[108] T. S. Lund, X. Wu, and K. D. Squires. Generation of turbulent inflow data for spatially developing boundary layer simulations. *Journal of Computational Physics*, 140:233–258, 1998.

[109] P. Majander and T. Siikonen. Evaluation of Smagorinsky-based subgrid-scale models in a finite-volume computation. *International Journal of Numerical Methods in Fluids*, 40:735–774, 2002.

[110] T. Maruyama. On the influence of turbulence characteristics at an inlet boundary for large eddy simulation of a turbulent boundary layer. In *Proceedings of ETMM4*, Corsica, 1999.

[111] T. Maruyama, W. Rodi, Y. Maruyama, and H. Hiroaka. Large eddy simulation of the turbulent boundary layer behind roughness elements using an artificially generated inflow. *Journal of Wind Engineering and Industrial Aerodynamics*, 83:381–392, 1999.

[112] P. J. Mason and D. J. Thomson. Stochastic backscatter in large eddy simulations of boundary layers. *Journal of Fluid Mechanics*, 242:51–78, 1992.

[113] O. Matais and M. Lesieur. Spectral large eddy simulation of isotropic and stably stratified turbulence. *Journal of Fluid Mechanics*, 265:157–194, 1992.

[114] W. D. McComb. *The physics of fluid turbulence.* Clarendon Press, 1990.

[115] O. J. McMillan and J. H. Fersiger. Direct testing of subgrid-scale models. *AIAA Journal*, 17:1340–1346, 1979.

[116] O. J. McMillan and J. H. Fersiger. Tests on new subgrid scale models in strained turbulence. *AIAA*, (80-1339), 1980.

[117] C. P. Mellen, J. Frohlich, and W. Rodi. Lessons from LESFOIL project on large eddy simulation of flow around an airfoil. *AIAA Journal*, 41(4):573–582, 2003.

[118] C. Meneveau and J. Katz. Scale invariance and turbulence models for large eddy simulation. *Annual Review of Fluid Mechanics*, 32:1–32, 2000.

[119] C. Meneveau, T. S. Lund, and W. H. Cabot. A Langrangian dynamic subgrid-scale model for turbulence. *Journal of Fluid Mechanics*, 319:353–385, 1996.

[120] S. Menon and W. W. Kim. High Reynolds number flow simulations using a localized dynamic subgrid-scale model. In *34th Aerospace Sciences Meeting*, number 96-0425. AIAA, 1996.

[121] P. Merati, H. M. McMahon, and K. M. Yoo. Experimental modelling of a turbulent flow in the junction and wake of an appendage flate plate. In *Proceedings of 1st National Fluid Dynamics Congress*, Cincinnati, OH, 1988.

[122] C. Moeng. A large-eddy-simulation model for the study of planetary boundary layer turbulence. *Journal of the Atmospheric Sciences*, 41 (13):2052–2062, 1984.

[123] P. Moin and J. Kim. Numerical investigation of turbulent channel flow. *Journal of Fluid Mechanics*, 118:341–377, 1982.

[124] P. Moin and K. Manesh. Direct numerical simulation: a tool in turbulence research. *Annual Review of Fluid Mechanics*, 30:539–578, 1998.

[125] Y. Morinishi, T. S. Lund, O. V. Vasilyev, and P. Moin. Fully conservative higher order finite difference schemes for incompressible flow. *Journal of Computational Physics*, 143(CP985962):90–124, 1998.

[126] R. D. Moser, J. Kim, and N. N. Mansour. Direct numerical simulation of turbulent channel flow up to Ret=590. *Physics of Fluids*, 11 (4):943–945, 1999.

[127] Y. Na and P. Moin. Direct numerical simulation of turbulent boundary layers with adverse pressure gradient and separation. Technical report, Thermosciences Division, Department of Mechanical Engineering, Stanford University, Stanford, CA 94305, 1996.

[128] F. M. Najjar and D. K. Tafti. Study of discrete test filters and finite difference approximations for the dynamic subgrid scale stress model. *Physics of Fluids*, 8 (4):1076–1088, 1996.

[129] J. Nikuradse. Stromungsgesetze in rauhen rohren. Forschungsheft 361, VDI, 1933.

[130] L. H. Norris and W. C. Reynolds. Turbulent channel flow with a moving wavy boundary. Report FM-10, Department of Mechanical Engineering, Stanford University, Stanford, CA, U.S.A, 1975.

[131] S. M. Olcmen and R. L. Simpson. An experimental study of a three-dimensional pressure-driven turbulent boundary layer. *Journal of Fluid Mechanics*, 290:225–262, 1995.

[132] R. Paciorri, A. Bonfiglioli, A. D. Mascio, and B. Favini. RANS simulations of a junction flow. *International Journal of Computational Fluid Dynamics*, 19(2):179–189, February 2005.

[133] G. J. Page. *Delta User's Guide*. Loughborough University, Department of Aeronautical and Automotive Engineering, Loughborough University, UK, release 2.1 edition, May 1999.

[134] G. J. Page. Influence of nozzle modelling in LES of turbulent free jets. In *Proceedings of 11th AIAA/CEAS Aeroacoustics Conference*, number AIAA 2005-2883, Monterey, California, USA, May 2005. AIAA.

[135] G. J. Page, J. J. McGuirk, N. J. Hughes, M. Hossain, and M. T. Trumper. A computational and experimental investigation of serrated coaxial nozzles. In *Proceedings of 8th AIAA/CEAS Aeroacoustics Conference*, number AIAA Paper No. 2002-2554, pages 1–11, Breckinridge, Colorado, June 2002. AIAA.

[136] Y-H. Pao. Structure of turbulent velocity and scalar fields at large wavenumbers. *Physics of Fluids*, 8:1063–1075, 1965.

[137] F. J. Pierce and J. Shin. The development of a turbulent junction vortex system. *Journal of Fluids Engineering*, 114:559–565, 1192.

[138] U. Piomelli. High Reynolds number calculations using the dynamic subgrid-scale stress model. *Physics of Fluids*, A 5:1484–1490, 1993.

[139] U. Piomelli. Large eddy simulation: achievements and challenges. *Progress in Aerospace Sciences*, 35:335–362, 1999.

[140] U. Piomelli, J. H. Ferziger, P. Moin, and J. Kim. New approximate boundary conditions for large eddy simulations of wall-bounded flows. *Physics of Fluids*, A 1 (6):1061–1068, 1989.

[141] U. Piomelli and L. Junhui. Large Eddy Simulation of rotating channel flow using a localized dynamic model. *Physics of Fluids*, 7:839–848, 1995.

[142] U. Piomelli, A. Scotti, and E. Balaras. Large-eddy simulations of turbulent flows, from desktop to supercomputer. VECPAR 2000, 2001.

[143] U. Piomelli, X. Yunfang, and R. J. Adrian. Subgrid scale energy transfer and near-wall turbulence structure. *Physics of Fluids*, 8 (1):215–224, 1996.

[144] U. Piomelli, T. A. Zang, C. G. Speziale, and M. Y. Hussaini. On the Large Eddy Simulation of transitional wall-bounded flows. *Physics of Fluids*, A 2 (2):257–265, 1990.

[145] Pointwise. *GridGen User Manual, Version 14*.

[146] S. B. Pope. *Turbulent Flows*. Cambridge University Press, 2000.

[147] S. B. Pope. Ten questions concerning the large-eddy simulation of turbulent flows. *New Journal of Physics*, 6:1–24, 2004.

[148] W. H. Press, S. A. Teukolsky, W. T. Vetterling, and B. P. Flannery. *Numerical Recipes in Fortran 77: The Art of Scientific Computing (Vol. 1ofFortranNumericalRecipes)*. Press Syndicate of the University of Cambridge, 2nd edition, 2001.

[149] L. P. Purtell, P. S. Klebanoff, and F. T. Buckley. Turbulent boundary layer at low Reynolds number. *Physics of Fluids*, 24 (5):802–811, 1981.

[150] M. M. Rai and P. Moin. Direct numerical simulation of transition and turbulence in a spatially evolving boundary layer. *Journal of Computational Physics*, 109:169–, 1993.

[151] S. Rajagopalan and R. A. Antonia. Some properties of the large structure in a fully developed turbulent duct flow. *Physics of Fluids*, 22 (4):614–622, 1979.

[152] C. M. Rhie and W. L. Chow. Numerical study of the turbulent flow past an aerofoil with trailing edge separation. *AIAA Journal*, 21:1525–1535, 1983.

[153] S. K. Robinson. The kinematics of the turbulent boundary layer structure. Technical Memo TM 103859, NASA, 1991.

[154] P. Sagaut. Simulation of separated flows with subgrid models. In *La Recherche Aerospatiale*, volume 1, pages 51–63. 1996.

[155] P. Sagaut. *Large Eddy Simulation for incompressible flows, an introduction*. Springer, 2nd edition, 2003.

[156] P. Sagaut, E. Montreuil, and O. Labbe. Assesment of some self adaptive SGS models for wall bounded flows. *Aerospace Science and Technology*, 3 (6):335–344, 1999.

[157] H. Salman, G. J. Page, and J. J. McGuirk. Prediction of lobed mixer vortical structures with a k-e turbulence model. *AIAA Journal*, 41 (5):878–887, May 2003.

[158] U. Schumann. Subgrid scale model for finite difference simulations of turbulent flows in plane channels and annuli. *Journal of Computational Physics*, 12:376–404, 1975.

[159] U. Schumann. Boundary conditions at walls - the unresolved problem. Not published, 1995.

[160] A. Scotti, C. Meneveau, and D. K. Lilly. Generalised Smagorinsky model for anisotropic grids. *Physics of Fluids*, A 5:2306–2309, 1993.

[161] K. B. Shah and J. H. Ferziger. A new non-eddy viscosity subgrid-scale model and its application to channel flow. Annual Research Briefs, Center of Turbulence Research, 1995.

[162] R. L. Simpson. Junction flows. *Annual Review of Fluid Mechanics*, 33:415–443, 2001.

[163] J. Smagorinsky. General circulation experiments with the primitive equations: 1. The basic experiment. *Monthly Weather Review*, 91:90–164, 1963.

[164] S. W. Smith. *The Scientist's and Engineer's Guide to Digital Signal Processing*. California Technical Publishing, 2nd edition, 1999.

[165] A. Sohankar, L. Davidson, and C. Norberg. Erratum. *ASME: Journal of Fluids Engineering*, 122 (3):643, 2000.

[166] A. Sohankar, L. Davidson, and C. Norberg. Large eddy simulation of flow past a square cylinder: comparison of different subgrid scale models. *ASME: Journal of Fluids Engineering*, 122 (1):39–47, 2000.

[167] P. R. Spalart. Direct simulation of a turbulent boundary layer up to Re=1410. *Journal of Fluid Mechanics*, 187:61–, 1988.

[168] P. R. Spalart and S. R. Allmaras. A one-equation turbulence model for aerodynamic flows. *La Recherche Aerospatiale*, 1:5–21, 1994.

[169] P. R. Spalart and J. H. Watmuff. Experimental and numerical study of a turbulent boundary layer with pressure gradients. *Journal of Fluids Mechanics*, 249:337–371, 1993.

[170] A. Spille-Kohoff and H. J. Kaltenbach. Generation of turbulent inflow data with a prescribed shear stress profile. In Liu, Sakell, and Beutner, editors, *DNS/LES Progress and Challenges*, pages 319–326. Greyden Press, 2001.

[171] S. Stanley and S. Sarkar. Influence of nozzle conditions and discrete forcing on turbulent planar jets. *AIAA Journal*, 38:1615–1623, 2000.

[172] G. Tang, J. J. McGuirk, Z. Yang, and G. J. Page. Large eddy simulation of fully developed channel flow. Technical report, Loughborough University, 2000.

[173] G. I. Taylor. The spectrum of turbulence. In *Proceedings of Royal Society of London*, number A 164, pages 476–490, 1938.

[174] L. Temmerman, M. A. Leschziner, C. P. Mellen, and J. Frohlich. Investigation of wall function approximations and subgrid scale models in large eddy simulation of separated flow in a channel with streamwise periodic constrictions. *International Journal of Heat and Fluid Flow*, 2001.

[175] C. Tenaud and L. T. Phuoc. Large Eddy Simulation of unsteady, compressible, separated flow around NACA 0012 Airfoil. *Computational Fluid Dynamics*, pages 1100–1106, 1996.

[176] C. Tong and Z. Warhaft. Passive scalar dispersion and mixing in a turbulent jet. *Journal of Fluid Mechanics*, 292:1–38, 1995.

[177] A. A. Townsend. On the fine-scale structure of turbulence. In *Proceedings of Royal Society*, volume A, pages 534–542.

[178] A. A. Townsend. *The Structure of Turbulent Shear Flow.* Cambridge University Press, Cambridge, 2nd edition, 1976.

[179] M. Tsubokura. Proper representation of the subgrid-scale eddy viscosity for the dynamic procedure in large eddy simulation using finite difference method. *Physics of Fluids*, 13 (2):500–504, 2001.

[180] F. Unger and R. Friedrich. Large-eddy simulation of fully-developed turbulent pipe flow. In E. H. Hirschel, editor, *Flow Simulation of High Performance Computers*, volume 1 of *NNFM*. Vieweg-Verlag, 1994.

[181] E. R. van Driest. On turbulent flow near a wall. *Journal of Aerospace Sciences*, 23:1007–1011, 1956.

[182] I. Veloudis, Z. Yang, J. J. McGuirk, and G. Page. Assessment of the digital filter approach for generating large eddy simulation inlet conditions. In W. Rodi, editor, *Proceedings of TETMM 6*, Sardinia, 2005. ERCOFTAC.

[183] P. R. Voke. Low Reynolds number subgrid-scale models. Technical report, Department of Mechanical Engineering, University of Surrey, Guildford GU2 5XH, UK, October 4 1994.

[184] T. von Karman. Mechanishe ahnlichkeit und turbulenz. In *Proc. Third Int. Congr. Applied Mechanics*, pages 85–105, Stockholm, 1930.

[185] T. Wei and W. W. Willmarth. Reynolds-number effects on the structure of a turbulent channel flow. *Journal of Fluid Mechanics*, 204:57–95, 1989.

[186] H. Werner and H. Wengle. Large-eddy simulation of turbulent flow over and around a square cube in a plate channel. In *8 th Symposium on Turbulent Shear Flows*, pages 155–168, 1991.

[187] J. H. Williamson. Low-storage Runge-Kutta schemes. *Journal of Computational Physics*, 35:48–56, 1980.

[188] V. C. Wong. A proposed statistical-dynamic closure method for the linear or non-linear subgrid scale stresses. *Physics of Fluids*, A 4 (5):1080–1082, 1992.

[189] X. Wu, I. H. Tristanto, G. J. Page, and J. J. McGuirk. Influence of nozzle modelling in LES of turbulent free jets. In *Proceedings of 11th AIAA/CEAS Aeroacoustics Conference*, number 2005-2883, pages 1–8, Monterey, California, USA, May 2005. AIAA.

[190] V. Yakhot and S. A. Orszag. Renormalization group analysis of turbulence.i. basic theory. *Journal of Scientific Computing*, 1:3–51, 1986.

[191] Z. Yang and I. E. Abdalla. Effects of free-stream turbulence on large-scale coherent structures of separated boundary layer transition. *International Journal for Numerical Methods in Fluids*, 49:331–348, June 2005.

[192] F. W. Yao and N. D. Sandham. DNS of turbulent flow over a bump with shock/boundary layer interactions. In W. Rodi and Fueyo, editors, *Proceedings of the Fifth Engineering Turbulence Modelling and Measurements*, 2002.

[193] A. Yoshizawa. A statistically-derived subgrid scale model for the large-eddy simulation of turbulence. *Thysics of Fluids*, 25 (9):1532–1538, September 1982.

[194] A. Yoshizawa. Statistical analysis of the deviation of the reynolds stress from its eddy viscosity representations. *Physics of Fluids*, 27 (6):1377–1387, June 1984.

[195] A. Yoshizawa and K. Horiuti. A statistically-derived subgrid scale kinetic energy model for the Large Eddy Simulation of turbulent flows. *Journal of the Physical Society of Japan*, 54 (8):2834–2839, August 1985.

[196] A. Yoshizawa, K. Kobayashi, T. Kobayashi, and N. Taniguchi. A non-equilibrium fixed-parameter subgrid-scale model obeying the near-wall asymptotic constraint. *Physics of Fluids*, 12 (9):2338–2344, 2000.